



REFERENCE ONLY

UNIVERSITY OF LONDON THESIS

Degree

PhD

Year

2006

Name of Author

MIGLIORANZI
SILVIA

COPYRIGHT

This is a thesis accepted for a Higher Degree of the University of London. It is an unpublished typescript and the copyright is held by the author. All persons consulting the thesis must read and abide by the Copyright Declaration below.

COPYRIGHT DECLARATION

I recognise that the copyright of the above-described thesis rests with the author and that no quotation from it or information derived from it may be published without the prior written consent of the author.

LOAN

Theses may not be lent to individuals, but the University Library may lend a copy to approved libraries within the United Kingdom, for consultation solely on the premises of those libraries. Application should be made to: The Theses Section, University of London Library, Senate House, Malet Street, London WC1E 7HU.

REPRODUCTION

University of London theses may not be reproduced without explicit written permission from the University of London Library. Enquiries should be addressed to the Theses Section of the Library. Regulations concerning reproduction vary according to the date of acceptance of the thesis and are listed below as guidelines.

- A. Before 1962. Permission granted only upon the prior written consent of the author. (The University Library will provide addresses where possible).
- B. 1962 - 1974. In many cases the author has agreed to permit copying upon completion of a Copyright Declaration.
- C. 1975 - 1988. Most theses may be copied upon completion of a Copyright Declaration.
- D. 1989 onwards. Most theses may be copied.

This thesis comes within category D.

☐

This copy has been deposited in the Library of

UCL

☐

This copy has been deposited in the University of London Library, Senate House, Malet Street, London WC1E 7HU.

Beauty photoproduction at HERA II with the ZEUS experiment

Silvia Miglioranza

London

2006



PhD Thesis

Thesis Submitted to University College London
in accordance with the requirements of degree of
Doctor of Philosophy in the Faculty of Science

UMI Number: U592150

All rights reserved

INFORMATION TO ALL USERS

The quality of this reproduction is dependent upon the quality of the copy submitted.

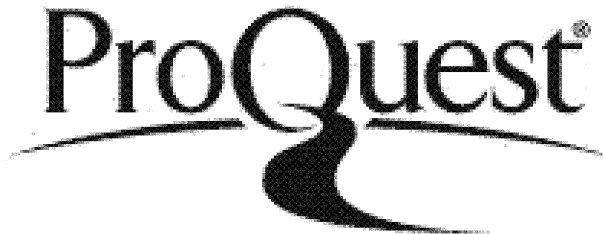
In the unlikely event that the author did not send a complete manuscript and there are missing pages, these will be noted. Also, if material had to be removed, a note will indicate the deletion.



UMI U592150

Published by ProQuest LLC 2013. Copyright in the Dissertation held by the Author.
Microform Edition © ProQuest LLC.

All rights reserved. This work is protected against
unauthorized copying under Title 17, United States Code.



ProQuest LLC
789 East Eisenhower Parkway
P.O. Box 1346
Ann Arbor, MI 48106-1346

Declaration

I confirm that the work presented in this thesis is my own. Where information has been derived from other sources, I confirm that this has been indicated in the thesis.

Abstract

In this thesis the beauty photoproduction cross section has been measured with the ZEUS detector at HERA II using e^+p data collected in 2004 corresponding to an integrated luminosity of 33 pb^{-1} . Beauty production has been studied in the photoproduction regime, in which the boson exchanged between the proton and the positron is an almost real photon (virtuality, $Q^2 \simeq 0 \text{ GeV}^2$). Events were selected in which a $b\bar{b}$ pair is produced and at least one of the pair decays semi-leptonically into a muon. The beauty content of the sample was extracted using a combination of P_T^{rel} (transverse momentum of the muon with respect to the closest jet) and impact parameter (distance of closest approach of the muon track to the primary vertex) methods. Measurements of the total and differential cross sections for beauty production were made.

The measured cross sections are in good agreement with NLO QCD predictions and with the HERA I results that were obtained from a luminosity ~ 3 times larger than that of the present measurement, using only the P_T^{rel} variable to separate the beauty signal from charm and light flavours and fixing the charm-to-light-flavour ratio from external measurements. An external constraint for the charm contribution is not needed in this analysis since its fraction is extracted from the fit to these data.

Contents

Declaration	2
Abstract	3
List of Figures	9
List of Tables	22
Introduction	23
1 Quantum chromodynamics and lepton-proton interactions	26
1.1 Deep Inelastic Scattering (DIS)	26
1.2 Kinematics at HERA: lepton-nucleon interactions	28
1.3 Parton model	30
1.4 Structure functions in QCD	32
1.5 Fragmentation functions	37
1.6 Photoproduction	38
1.6.1 Direct photoproduction	39
1.6.2 Resolved photoproduction	40
1.7 Photoproduction generalized model	41
1.8 The photon structure	43
1.9 Two-jet photoproduction results at HERA	45
2 Heavy quark production mechanisms	48
2.1 Introduction	48
2.2 Heavy quark production at HERA	49
2.3 Heavy quark production in perturbative QCD	50
2.4 Massive scheme	51

2.5	Massless scheme	52
2.6	Beauty production in the global context	54
2.6.1	Fixed target experiments	54
2.6.2	Measurements at the $Spp\bar{p}S$	56
2.6.3	Measurements at the Tevatron	57
2.6.4	$\gamma\gamma$ interactions	58
2.7	Beauty results at HERA	58
2.7.1	Beauty photoproduction from semileptonic decays to muons	58
2.7.2	Beauty production in DIS	61
2.7.3	Lifetime tagging	63
2.7.4	Double tagging of beauty: $D^* - \mu$ correlations and dimuon studies	65
3	HERA and the ZEUS detector	69
3.1	The HERA collider	69
3.1.1	The HERA injection system	71
3.2	The HERA luminosity upgrade	73
3.3	The ZEUS detector	75
3.4	The Central Tracking Detector (CTD)	79
3.4.1	Measurement of dE/dx	81
3.5	The Uranium-scintillator Calorimeter (UCAL)	82
3.6	The muon detectors	85
3.6.1	The Forward MUON detector (FMUON)	86
3.6.2	The Barrel and Rear MUON detector (B/RMUON)	88
3.6.3	The Backing Calorimeter (BAC)	89
3.7	The luminosity measurement	90
3.8	Background	91
3.9	The ZEUS trigger system	92
4	The ZEUS Microvertex Detector (MVD)	95
4.1	Barrel and forward micro vertex detector	97
4.2	Readout electronics	99
4.3	Preliminary test results	100
4.4	Radiation monitor	102

5	Physics simulation and NLO QCD predictions	104
5.1	General structure of an event generator	104
5.2	The HERWIG Monte Carlo	106
5.3	The PYTHIA Monte Carlo	108
5.4	The detector simulation	110
5.5	Monte Carlo samples	111
5.5.1	Beauty event simulation	111
5.5.2	Charm event simulation	113
5.5.3	Light quark event simulation	114
5.6	NLO QCD predictions	115
6	Analysis overview	118
6.1	Definition of the measurement	118
6.2	Beauty flavoured hadrons and their semi-muonic decay	119
6.3	Choice of decay channel	122
6.4	Background processes	123
6.5	Analysis observables	126
6.5.1	Mass signature: the P_T^{rel} method	126
6.5.2	Lifetime signature: the impact parameter method	128
6.6	Experimental requirements and analysis strategy	131
7	Event reconstruction and selection	133
7.1	Reconstruction of tracks and vertices	133
7.1.1	Pattern recognition	134
7.1.2	Track fit	135
7.1.3	Vertex finding	137
7.1.4	MVD information	138
7.2	Beam spot	141
7.3	Jet algorithm	141
7.4	Reconstruction of the hadronic system	144
7.4.1	Reconstruction of Energy Flow Objects (EFOs)	145
7.4.2	Correction of the cone islands	149
7.4.3	Correction for the presence of a muon	150
7.5	Muon reconstruction	152

7.5.1	Forward muon reconstruction: MPMATCH	152
7.5.2	Barrel and rear muon reconstruction: BREMAT	154
7.6	Trigger chain for online data selection	158
7.7	Offline data selection	159
7.8	Photoproduction selection	159
7.8.1	Veto on reconstructed electrons	159
7.8.2	Reconstruction of y with the Jaquet-Blondel method . . .	160
7.9	Final selection	161
7.9.1	Control distributions	164
7.10	Muon efficiency corrections	164
8	Primary vertex determination	171
8.1	Event selection and beam spot position	171
8.2	Time and z dependence	174
8.2.1	Time dependence	175
8.2.2	Z dependence	176
8.3	Summary	177
9	Smearing of the Monte Carlo impact parameter distribution	181
9.1	Selection	181
9.2	Double convolution fit	182
9.3	After smearing	188
10	Extraction of the beauty fraction	190
10.1	Extraction of the beauty fraction from the P_T^{rel} fit	190
10.2	P_T^{rel} corrections	192
10.2.1	P_T^{rel} fit	194
10.3	Impact parameter fit	195
10.3.1	Combined fit	197
11	Cross section measurement	202
11.1	Definition of the visible cross section	202
11.2	Visible and differential cross sections	203
11.3	Systematic errors	206
11.4	Discussion of results	209

A	Vertex fitting mathematics	210
A.1	Introduction	210
A.2	Vertex fit: general theory	210
A.3	The “perigee” parametrization	
	$q=(\epsilon, z_p, \theta, \phi_p, \rho)$	213
A.4	The “simple” vertex fitting	216
B	General characteristics of a silicon strip detector	218
	Bibliography	220

List of Figures

1.1	<i>DIS kinematics at HERA.</i>	28
1.2	<i>Neutral current (γ or Z^0 exchange) and charged current (W^\pm exchange) interactions.</i>	29
1.3	<i>Diagrams of QCD processes at first order in α_s: a) and b) QCD Compton Scattering, c) boson-gluon fusion.</i>	33
1.4	<i>Proton structure function measured in electromagnetic scattering of electrons (H1 and ZEUS) and muons, within the kinematic domain of HERA data. In the figure it is possible to observe the scaling violation at low x.</i>	34
1.5	<i>Feynman diagrams of quark and gluon splitting processes. The associated P_{jk} functions are indicated.</i>	35
1.6	<i>Parton evolution diagram showing the gluonic emission ordered according to k_t.</i>	37
1.7	<i>LO processes of direct dijet photoproduction a) QCD Compton scattering b) Boson-gluon fusion.</i>	40
1.8	<i>Direct dijet photoproduction event as detected by ZEUS.</i>	41
1.9	<i>Resolved photoproduction LO processes.</i>	42
1.10	<i>Three-jet resolved photoproduction event at ZEUS.</i>	43
1.11	<i>Direct and resolved LO photoproduction processes; the dashed lines represent the border between the hard process (perturbatively calculated) and the non perturbative part.</i>	44

1.12	<i>Distribution of x_γ^{obs} variable in two-jet events; the data are compared with MC HERWIG+MI (solid line), HERWIG-MI (dotted line) and PYTHIA+MI (dashed line) where MI are the Multiple Interactions. The shaded area represents all the direct events generated by HERWIG, the vertical line defines the experimental cut used to divide the direct-enriched processes from the resolved-enriched ones.</i>	46
1.13	<i>Angular cross section for the resolved (full dots) and direct (empty circles) processes compared with LO and NLO QCD predictions and with HERWIG and PYTHIA Monte Carlo.</i>	47
2.1	<i>Examples of Feynman diagrams for beauty production. In a) the direct Boson-Gluon Fusion process; in b) c) d) examples of resolved photoproduction processes are displayed.</i>	50
2.2	<i>Comparison between massive (FMNR) and massless (PFF) scheme calculations for the differential cross section distribution versus the transverse momentum of charm in photoproduction, taken from [28], adopting HERA-like kinematics with fixed photon energy. . .</i>	54
2.3	<i>Cross section measurement (in nb) for $b\bar{b}$ from fixed target (see Table 2.1) and collision experiments as a function of the centre-of-mass energy \sqrt{s}. The measurements are compared to predictions from PYTHIA for $pp \rightarrow b\bar{b}$ with its default setting scaled up by an empirical factor of $k=1$, $k=2$, or $k=3$.</i>	55
2.4	<i>Inclusive single beauty quark cross section for $\eta < 1.5$ and $P_T > P_T^{\text{min}}$ from UA1. Presented are the cross section measurements extracted from single muon events and dimuon events originating from different beauty quarks and from beauty chain decays as well as measurements extracted from single muon events originating from J/ψ from beauty quarks and the comparison to a next-to-leading order calculation [32].</i>	56
2.5	<i>Cross section as a function of the transverse momentum of the beauty quark measured at CDF; the recent MC@NLO and FONLL theoretical results are also shown [38].</i>	57
2.6	<i>Beauty and charm production cross section measured by L3 at LEP. In the figure the NLO QCD prediction results are also shown. . . .</i>	59

- 2.7 *Beauty production differential cross sections as a function of the muon pseudorapidity η^μ and of the muon transverse momentum, P_T^μ measured at ZEUS [42]. The 96-00 data are compared with PYTHIA and CASCADE Monte Carlo models and with NLO QCD predictions. 60*
- 2.8 *Comparison of the beauty production differential cross sections as a function of the muon pseudorapidity η^μ and of the muon transverse momentum, P_T^μ , obtained by ZEUS and H1. Slightly different pseudorapidity regions and theoretical NLO QCD predictions were adopted by the two experiments as reported in the figure. The bars on the NLO predictions show the results obtained varying the b mass between 4.5 GeV and 5.0 GeV and the renormalization and factorization scales between $m_T/2$ and $2m_T$, where $m_T = \sqrt{P_T^2 + m_b^2}$ 61*
- 2.9 *Differential cross section as a function of x_{jets} measured by ZEUS [42]. The muon spectrum (obtained with PYTHIA) was used to extrapolate the observable cross section to the process $ep \rightarrow \text{dijet } \mu^\pm X$ 62*
- 2.10 *Differential cross section as a function of Q^2 measured at (a) ZEUS and (b) H1 in DIS events [45] [44]. Data are compared in both cases with NLO QCD predictions. 63*
- 2.11 *Significance distributions using the b , c and uds -fractions from the fit to the subtracted significance distributions of the data [48]. $S1$ of tracks (left) in jets with exactly one track, $S2$ of tracks (right) with the second highest significance in jets with two or more tracks are shown. 64*
- 2.12 *Differential beauty cross sections as a function of transverse momentum P_T^{jet} (a) and the pseudorapidity η^{jet} (b) of the leading jet [48]. 65*

2.13	<i>Muon transverse momentum distribution (a) for both high and low mass dimuon pairs in the non isolated unlike sign sample [52]. Two muons are entered for each event. The breakdown into the expected contributions from different processes is also shown. In (b) the cross section $d\sigma/d\Delta\phi^{\mu\mu}$ for dimuon events from $b\bar{b}$ decays in which each muon originates from different $b(\bar{b})$ quarks [52]; the data (solid dots) are compared to the scaled sum of the predictions by the leading order plus parton shower (LO+PS) generators PYTHIA and RAPGAP (histogram) and the NLO prediction from FMNR (band).</i>	66
2.14	<i>Summary of all the latest cross section measurements using double tagging techniques obtained by ZEUS and H1. The measurements are compared to NLO QCD predictions.</i>	67
2.15	<i>Summary of the ZEUS and H1 cross section measurements. The ratio DATA/NLO as a function of Q^2 is shown.</i>	68
3.1	<i>The Hamburg Volkspark showing the DESY site. The location of the HERA and PETRA rings are shown. Also illustrated are the locations of the two colliding-beam experiments, ZEUS and H1, together with the single-beam experiments HERMES and HERA-B.</i>	69
3.2	<i>HERA injection system.</i>	72
3.3	<i>HERA integrated luminosity.</i>	73
3.4	<i>ZEUS coordinate system.</i>	76
3.5	<i>ZEUS longitudinal section ($z - y$).</i>	77
3.6	<i>ZEUS transversal section ($x - y$).</i>	77
3.7	<i>Planar drift chambers (left) and straw tubes (right) constituting the Forward Tracking Detector (FDET).</i>	78
3.8	<i>Transverse cross section of one octant of the CTD. The sense wires are indicated with dots.</i>	80
3.9	<i>The energy lost by different particles, as reconstructed by the CTD, as a function of the particle momentum [67].</i>	82
3.10	<i>Production of showers inside ZEUS calorimeter.</i>	83
3.11	<i>Section of an FCAL module.</i>	84
3.12	<i>FMUON longitudinal section.</i>	87
3.13	<i>Layout of the barrel and rear muon detector.</i>	89

3.14	<i>The layout of the ZEUS Luminosity Monitor. The nominal interaction point is located at (0,0).</i>	91
3.15	<i>ZEUS trigger chain</i>	94
4.1	<i>Longitudinal MVD section. There are 3 layers in the barrel region and the 4 wheels in the forward section.</i>	96
4.2	<i>BMVD section: 3 superlayers around beam pipe are shown.</i>	97
4.3	<i>Impact parameter resolution on tracks at $\eta = 0$ as a function of the momentum. The measurements are for tracks crossing 3 layers of half modules [80].</i>	98
4.4	<i>Half modules and ladders mounted on the support.</i>	98
4.5	<i>FMVD 4 wheels.</i>	99
4.6	<i>Schematic view of the analog HELIX chip.</i>	100
4.7	<i>Schematic view of the device used with the test beam.</i>	101
4.8	<i>Intrinsic resolution as a function of the incident angle, measured with the three different algorithms [85].</i>	103
5.1	<i>General structure of the leading-order plus parton-shower PYTHIA MC generator.</i>	105
5.2	<i>A schematic diagram of ZEUS data and Monte Carlo reconstruction chain.</i>	111
6.1	<i>Gluon density distribution as a function of x. The threshold for beauty production is shown [102].</i>	121
6.2	<i>Muonic b quark decay: (a) prompt, (b) charm cascade.</i>	121
6.3	<i>Peterson fragmentation function from beauty (full line) and charm (dashed line), where the values for the fragmentation parameter ϵ have been chosen according to [104].</i>	122
6.4	<i>ZEUS beauty candidate event with 2 jets and 2 associated muons. The muons have impact parameters relative to the beam spot of 250 and 330 μm as well as high P_T^{rel} with respect to the jets of 1.24 and 2.05 GeV. The dimuon pair has an invariant mass of 5.5 GeV.</i>	124
6.5	<i>Normalized distributions of (left) the transverse momentum and (right) the transverse momentum relative to the direction of the parent hadron for muons from charm decays (full line) and beauty decays (dashed line) as predicted by PYTHIA.</i>	127

6.6	<i>The transverse muon momentum P_T^{rel} relative to an associated jet.</i>	128
6.7	<i>Normalized distributions of the impact parameter for muons originating from charm decays (full line) and beauty decays (dashed line) as predicted by PYTHIA</i>	130
6.8	<i>Sketch of the impact parameter, δ, of a muon track. If the muon track intercepts the jet axis downstream the primary vertex (beam position, see Chapter 8) the impact parameter has positive sign, otherwise it is negative.</i>	131
7.1	<i>Parametrization used in Pattern Recognition in VCTRAK. The reference point for the trajectory is (x_0, y_0); (a_1, a_2) are the two fit parameters in the XY plane.</i>	135
7.2	<i>Example of a track segment inside the CTD built using 8 hits. . .</i>	136
7.3	<i>VCTRAK parametrization used in the track fit.</i>	137
7.4	<i>Distributions of the coordinates QD_H (top) and Z_H (bottom) of distance of closest approach (in cm) used in the fit; in the left column plots only the CTD info was used, in the right column MVD hit info was also taken into account [110].</i>	139
7.5	<i>Distributions of the primary vertex coordinates in a beauty photo-production Monte Carlo event sample; on the left column (a),c) and e)) only the CTD information was used. In the right column (b),d) and f)) the MVD hit information was also taken into account [111].</i>	140
7.6	<i>Resolution from single particle MC simulation. The track transverse momentum resolution in the CTD (open markers) and the CAL energy resolution (full markers) are shown [112].</i>	144
7.7	<i>The relative resolution of the CTD and BCAL for reconstructing the energy of (a) an electron, E_e and (b) a charged hadron, E_h, as a function of E_e and E_h and polar angle, θ_e and θ_h, for electrons and hadrons, respectively. The contours show the rate at which one reconstruction improves the other [117].</i>	145
7.8	<i>A schematic diagram showing how cell-islands are formed.</i>	146

- 7.9 *Reconstruction of EFOs by a match between CAL cells clustered into cone islands (HAC cell 1 and EMC cell 2 and 3 are joined to form a cone island) and tracks. The different match categories of a charged particle (track is matched to cone island 4), neutral particle (no track is matched to cone island 5) and unmatched track are shown. 147*
- 7.10 *Distribution of the inactive material in front of the UCAL in units of the radiation length, X^0 , in the $\theta - \phi$ plane, as implemented in the simulation of the detector [118]. 150*
- 7.11 *Energy loss of a muon in the CAL as a function of the polar angle θ (full circles) and the energy fractions in the electromagnetic (crosses) and hadronic (open squares) calorimeter sections [119]. . 151*
- 7.12 *The resolution, $(E_T^{\text{jet}}(\text{rec}) - E_T^{\text{jet}}(\text{true})) / E_T^{\text{jet}}(\text{true})$ (left) and $E_T^{\text{jet}}(\text{rec})$ vs $E_T^{\text{jet}}(\text{true})$ (right), plotted for a beauty MC sample. The reconstructed $E_T^{\text{jet}}(\text{rec})$ is calculated taking as input the EFOs, after applying all the corrections described in the text. The sample was obtained by mixing Monte Carlo samples (direct, resolved and excitation) normalising them according to their predicted luminosities. 153*
- 7.13 *The resolution, $(\eta_{\text{jet}}^{\text{rec}} - \eta_{\text{jet}}^{\text{true}})$ (left) and $\eta_{\text{jet}}^{\text{rec}}$ vs $\eta_{\text{jet}}^{\text{true}}$ (right), plotted for a beauty MC sample. The reconstructed $\eta_{\text{jet}}^{\text{rec}}$ is calculated taking as input the EFOs, after applying all the corrections described in the text. The sample was obtained by mixing Monte Carlo samples (direct, resolved and excitation) normalising them according to their predicted luminosities. 153*
- 7.14 *The resolution, $(P_T^\mu(\text{rec}) - P_T^\mu(\text{true})) / P_T^\mu(\text{true})$ (left) and $P_T^\mu(\text{rec})$ vs $P_T^\mu(\text{true})$ (right), plotted for a beauty MC sample. The reconstructed $P_T^\mu(\text{rec})$ is calculated taking as input the EFOs, after applying all the corrections described in the text. The sample was obtained by mixing Monte Carlo samples (direct, resolved and excitation) normalising them according to their predicted luminosities. 157*

- 7.15 The resolution, $(\eta^\mu(\text{rec}) - \eta^\mu(\text{true})) / \eta^\mu(\text{true})$ (left) and $\eta^\mu(\text{rec})$ vs $\eta^\mu(\text{true})$ (right), plotted for a beauty MC sample. The reconstructed $\eta^\mu(\text{rec})$ is calculated taking as input the EFOs, after applying all the corrections described in the text. The sample was obtained by mixing Monte Carlo samples (direct, resolved and excitation) normalising them according to their predicted luminosities. 157
- 7.16 The resolution, $(y_{JB}(\text{rec}) - y_{JB}(\text{true})) / y_{JB}(\text{true})$ (left) and $y_{JB}(\text{rec})$ vs $y_{JB}(\text{true})$ (right), plotted for a beauty MC sample. The reconstructed y_{JB} is calculated taking as input the EFOs, after applying all the corrections described in the text. The sample was obtained by mixing Monte Carlo samples (direct, resolved and excitation) normalising them according to their predicted luminosities. 161
- 7.17 Distribution of y_{JB} for beauty PYTHIA MC. The sample was obtained by mixing Monte Carlo samples (direct, resolved and excitation) normalising them according to their predicted luminosities. The continuous line shows the total distribution of this variable in the photoproduction event sample considered, no cuts are applied. The dashed line indicates the events selected with no electron found in the event and a cut on the z vertex coordinate $|z_{\text{vtx}}| < 40$ cm. The final subsample of events considered is indicated by the dashed area. 162
- 7.18 Control plots for the muon and jet (associated to the muon) variables. In the upper plots, the muon momentum, P_T^μ , (left) and pseudorapidity, η_μ , (right) are displayed. The lower plots show the analogous variables related to the jet associated to the muon, P_T^{jet} (left) and η_{jet} (right). In all the plots the data (dots) are compared to the fitted distribution (black continuous line) obtained by summing the beauty and charm-plus-light-flavour contributions in the fractions given by the $P_T^{\text{rel}} - \delta$ fit (see Chapter 10). The fitted distribution is area-normalized to the data. The dashed area represents the contribution coming from beauty events. 165

- 7.19 Control plots for several event variables. In a) Y_{JB} , b) Y_{el} , c) E_T of the two FCAL inner rings, d) number of fitted tracks, e) P_T of the event and f) P_T/E_T of the event. In all the plots the data (dots) are compared to the fitted distribution (black continuous line) obtained by summing the beauty and charm plus light flavour contributions in the fractions given by the $P_T^{rel} - \delta$ fit (see Chapter 10). The fitted distribution is area-normalized to the data. The dashed area represents the contribution coming from beauty events. 166
- 7.20 Control plots for track-related variables. In a) Z coordinate of the primary vertex, b) P_T of the tracks, c) distance of closest approach DH of the track to $x = y = 0$ in the transverse plane, d) Z coordinate of closest approach to $x = y = 0$, e) number of Super Layers of the CTD crossed by the tracks and f) number of MVD hits used in the reconstruction of the track. In all the plots the data (dots) are compared to the fitted distribution (black continuous line) obtained by summing the beauty and charm plus light flavour contributions in the fractions given by the $P_T^{rel} - \delta$ fit (see Chapter 10). The fitted distribution is area-normalized to the data. The dashed area represents the contribution coming from beauty events. 167
- 7.21 Event display of a $J/\psi \rightarrow \mu^+\mu^-$ event. 168
- 7.22 Muon efficiency corrections for the forward, barrel and rear regions. In the left-hand column the corrections are shown as a function of the momentum p and in the right-hand column the corrections are shown as a function of θ [129]. 170
- 8.1 Distribution of the primary vertex coordinates in an example run (~ 5000 events were selected after applying the background rejection and quality cuts). A Gaussian fit was used to extract the mean beam spot values, restricting the fit range to $\pm 2\sigma$ 172
- 8.2 Comparison between the beam spot measurements obtained using the VCTRAK vertexing package (circles) and KFTRAK vertexing package (triangles) in a subsample of the 2004 data sample. 173

- 8.3 *HERA (grey) and H1 (black) vertical (top) and horizontal (bottom) beam position measurements (in mm) as a function of time (months). The periodic structure of the plot reflects the different machine fills. 174*
- 8.4 *Distribution on the vertex position in x (top, left), y (top, right) and z (bottom) in bins of approximately 500 events for one single 2004 run. Each of the measurements (triangles) corresponds to 200 events. The variation observed in x and y is of the order of $\sim \pm 20 \mu\text{m}$ 175*
- 8.5 *Straight line fit for the x vs z (left) and y vs z (right) distributions. Only the central region around the mean value of the Z coordinate ($|Z| < 20 \text{ cm}$) is shown. 176*
- 8.6 *Fit parameters for the x coordinate. On the left the off-set, on the right the slope coming from a linear fit. 177*
- 8.7 *Fit parameters for the y coordinate. On the left the off-set, on the right the slope coming from a linear fit. 177*
- 8.8 *The x (top) and y (bottom) coordinates of the beam spot for all 2004 data. 179*
- 8.9 *The x (top) and y (bottom) size of the beam spot for all 2004 data. 180*
- 9.1 *The MC impact parameter distributions (histograms) compared with 2004 data (black crosses), in different P_T bins (the P_T range considered is $0.5 < P_T < 5 \text{ GeV}$, the P_T bin size is 0.5 GeV). . . . 183*
- 9.2 *χ^2 of the fit plotted as a function of the σ of the Gaussian ($\times 10^{-4} \text{ cm}$) and the Γ of the Breit-Wigner ($\times 10^{-3} \text{ cm}$) in the different P_T bins specified in Fig. 9.1. 184*
- 9.3 *Example of a two-dimensional plot of the χ^2 distribution in the first bin of P_T of Fig. 9.2. On the right the distribution of the χ^2 is plotted as a function of the Gaussian σ ($\times 10^{-4} \text{ cm}$), keeping the value of the Breit-Wigner Γ constant at its minimum. On the left the distribution of the χ^2 is plotted as a function of the Breit-Wigner Γ ($\times 10^{-3} \text{ cm}$), keeping the value of the Gaussian σ constant at its minimum. In both distributions a horizontal line at $\chi^2 = 50$ is drawn, corresponding to the expected χ^2 if the fit and the errors were correct. Another line at $\chi^2 = \chi^2_{\text{min}} \times 1.5$ is drawn. 185*

- 9.4 Contour plots of the 2d-histograms of fig. 9.2. The χ^2 distributions as a function of the Breit-Wigner width ($\times 10^{-3}$ cm) and Gaussian width ($\times 10^{-4}$ cm) are plotted in bins of P_T . The contour lines refer to iso- χ^2 regions between $\chi^2 = 50$ and $\chi^2_{\min} \times 1.5$. The minima obtained using the Bayesian approach are identified by the empty ellipses, the minima extracted using the likelihood method are identified by the full dark ellipses. 186
- 9.5 Distribution of the Breit-Wigner gamma ($\times 10^{-3}$ cm, top) and Gaussian sigma ($\times 10^{-4}$ cm, bottom) in bins of P_T . The distributions were fitted with a combination of an exponential (top) and a constant function and with a constant function (bottom). Both the minima estimated using a likelihood (circles) and bayesian (squares) approach are shown. 187
- 9.6 The MC impact parameter distributions (histograms) compared with 2004 data (black crosses), in different P_T bins, after the Monte Carlo smearing has been applied (the P_T range considered is $0.5 < P_T < 5$ GeV, the P_T bin size is 0.5 GeV). 188
- 10.1 P_T^{rel} distribution for a) data and b) beauty, c) charm and d) light flavour Monte Carlo samples. All the MC samples are a mixture of the different direct, resolved and excitation processes and are normalized according to their luminosity. 191
- 10.2 P_T^{rel} ratio data/MC. 193
- 10.3 Ratio between data and MC in each muon P_T bin. 193
- 10.4 P_T^{rel} distribution for the data a) and Monte Carlo beauty b), charm c) and light flavour d) samples. All the MC samples are a mixture of the different direct, resolved and excitation processes and are normalized according to their luminosity. The charm and light flavour MC are corrected for the P_T^{rel} shape corrections. 194
- 10.5 Result of the single P_T^{rel} fit. The different Monte Carlo contributions are shown and their sum is compared with the 2004 data sample. 195

10.6	<i>Impact parameter distribution for the data a) and Monte Carlo beauty b), charm c) and light flavour d) samples. All the MC sample are a mixture of the different direct, resolved and excitation processes and are normalized according to their luminosity.</i>	196
10.7	<i>Combined (P_T^{rel}, δ) distributions for the data a) and Monte Carlo beauty b), charm c) and light flavour d) samples. All the MC samples are a mixture of the different direct, resolved and excitation processes and are normalized according to their luminosity.</i>	197
10.8	<i>Correlation plot P_T^{rel} vs δ for a) data b) beauty c) charm and d) light flavours.</i>	198
10.9	<i>Result of the two-dimensional fit. The different Monte Carlo contributions are shown and their sum is compared with the 2004 data sample.</i>	199
10.10	<i>Contours of 68% probability in the plane defined by the beauty and the charm fractions. The blue line shows the contour from the two-dimensional P_t^{rel}-impact parameter distribution. The green and red lines show the contour for the one dimensional distributions in P_T^{rel} and impact parameter respectively. The triangle shows the physical region in which f_b, f_c and f_l are positive.</i>	200
10.11	<i>Distribution of P_T^{rel} (top) and δ (bottom) for the data and for the MC mixture of beauty, charm and light flavours. The different MC components are also shown independently. The dashed area indicates the beauty contribution, the continuous grey line is charm, the dashed line is the light flavours and the continuous black line is the sum of the MC contributions. The black dots are the data.</i>	201
11.1	<i>Acceptance (top), purity (middle) and efficiency (bottom) distributions as a function of P_T^μ.</i>	204
11.2	<i>Acceptance (top), purity (middle) and efficiency (bottom) distributions as a function of η^μ.</i>	205

11.3	<i>Differential cross section as a function of the muon P_T for $Q^2 < 1 \text{ GeV}^2$, $0.2 < y < 0.8$, $P_T^{jet1,2} > 7,6 \text{ GeV}$, $\eta_{jet1,2} < 2.5$ and $-1.6 < \eta_\mu < 2.3$. The black circles show the results from this analysis while the grey circles show the previous HERA-I measurement. The inner error bars are statistical uncertainties while the external bars show the statistical and systematical uncertainties summed in quadrature. The band represents the NLO QCD prediction and hadronisation.</i>	206
11.4	<i>Differential cross section as a function of the muon η for $Q^2 < 1 \text{ GeV}^2$, $0.2 < y < 0.8$, $P_T^{j1,j2} > 7,6 \text{ GeV}$, $\eta_{j1,j2} < 2.5$ and $-1.6 < \eta_\mu < 2.3$. Only the statistical error is included in the error bars.</i>	207
A.1	<i>Relation between q_i and (V, P_i) in the vertex fit.</i>	211
A.2	<i>Perigee parameters in the $x - y$ projection.</i>	214

List of Tables

2.1	<i>Collection of $b\bar{b}$ production cross sections at fixed target experiments (p - A) [30]; $x_F = p_{\text{parton}}/p_{\text{nucleon}}$ denotes the fractional momentum of the partons inside the nucleon.</i>	55
3.1	<i>HERA design parameters [59][60].</i>	71
5.1	<i>Cross sections and luminosities of the PYTHIA MC sample used in this thesis.</i>	116
6.1	<i>Examples of beauty and charm-flavoured hadrons and their properties [101].</i>	119
7.1	<i>Values of the muon efficiency corrections applied in the analysis. .</i>	170
11.1	<i>Total acceptance, purity and efficiency for the selection applied in the analysis.</i>	204
11.2	<i>Summary of the differential cross section values obtained as a function of P_T^μ and η^μ.</i>	207
11.3	<i>Summary of the systematic errors taken into account.</i>	208
A.1	<i>D and E matrix components.</i>	215

Introduction

The measurement of beauty quark production is an important subject since its cross section, measured in $p\bar{p}$ collisions at Tevatron [1], in $\gamma\gamma$ interactions at LEP [2] and in γp and *deep inelastic scattering* at HERA, has tended to be higher than the theoretical predictions based on calculations exploiting QCD (*Quantum Chromodynamics*) at the second perturbative order in α_s (NLO, Next to Leading Order) [3]. Theoretical predictions are expected to be more accurate the higher the quark mass involved, since the theory becomes asymptotically free above a mass scale ≈ 0.2 GeV; the beauty mass (~ 5 GeV) establishes a scale well above that.

In this thesis a study of events in which beauty quarks are produced in positron-proton interactions is reported. The study is based on the analysis of ~ 30 pb^{-1} of data collected in 2004 by the ZEUS experiment at HERA, a lepton-proton collider working at a centre-of-mass energy of $\sqrt{s} = 318$ GeV.

Beauty production has been studied in the photoproduction regime, in which the photon emitted by the scattered positron and interacting with the proton is almost real ($Q^2 \simeq 0$ GeV²). The measurement of beauty cross sections requires a reliable identification of beauty quarks exploiting their heavy mass or long lifetime. A well established procedure for the identification is the P_T^{rel} method which statistically exploits the harder spectrum of the transverse momentum of the muon from semi-leptonic beauty quark decay relative to the originating quark compared to that from lighter quarks. An additional method exploiting the long lifetime of the beauty quark has become possible after the upgrade of the ZEUS detector in 2000/2001 in preparation for the HERA II programme. With the integration of a Micro Vertex Detector (MVD) in ZEUS, a precise measurement of the impact parameter of the muon with respect to the interaction origin can statistically identify semi-leptonic beauty decays by the asymmetry of

the beauty impact parameter spectrum compared with the symmetric spectrum of light quarks. For both methods the same HERA II data sample was used. Events were selected in which a $b\bar{b}$ pair is produced and at least one quark of the pair decays semi-leptonically into a muon. The experimental signature of the process under investigation is the presence in the final state of at least two high transverse energy jets, coming from the hadronization of the b quarks, and a muon from the b semi-leptonic decay:

$$e p \rightarrow b \bar{b} X \rightarrow \text{dijet } \mu X .$$

In the event selection, the muon was required to be in the acceptance region of the ZEUS muon detectors, whose performances are well understood.

The visible beauty photoproduction cross section has been measured in a kinematic region where the acceptance of the detectors was well determined. In the same kinematic region the differential cross sections $d\sigma/dP_T^\mu$ and $d\sigma/d\eta^\mu$ were also determined. The obtained results have been compared to theoretical predictions from next-to-leading order QCD calculations.

The outline of this thesis is described below. In Chapter 1 a theoretical overview of lepton-proton interactions is discussed. In Chapter 2 an introduction to beauty production mechanisms is reported, together with a summary of the experimental results obtained so far, in particular at HERA. Chapter 3 describes the HERA accelerator and the ZEUS detector, with particular emphasis on the detector components relevant for this analysis. In Chapter 4 the MVD, which plays a central role in this analysis, is described in detail. In Chapter 5 a brief description of the Monte Carlo generator used in this work is reported. Chapter 6 gives a brief introduction about the motivations and strategies followed in this analysis. In Chapter 7 the reconstruction of the events is described in detail; resolution of kinematic variables and control plots produced to validate this analysis are also shown. In Chapter 8 a precise determination of the primary vertex of the event is presented; this measurement, optimized for this analysis, was then made available to the collaboration. Chapter 9 presents the Monte Carlo tuning necessary to have a good description of the data and to extract the beauty content from the selected sample. In Chapter 10 the extraction of the beauty events from the selected data sample is presented. The discrimination between beauty and background events is

performed by analysing the muon and jet dynamics and exploiting the large mass of the b quark. Chapter 11 reports the results regarding the beauty visible and differential cross sections, compared to NLO QCD predictions. At the end, the summary of the work is reported. Appendix A describes in detail the vertexing procedure used for this thesis; in Appendix B the general characteristics of a silicon strip detector are outlined.

Chapter 1

Quantum chromodynamics and lepton-proton interactions

1.1 Deep Inelastic Scattering (DIS)

During the 1960s the discovery of many hadronic resonances, suggested that the mesonic and baryonic states found were not elementary particles but systems made up of constituent fundamental particles.

In 1964 Gell-Mann and Zweig postulated that these particles were composed of a family of spin 1/2 entities which they called quarks, each carrying a fractional charge and subject to the SU(3) symmetry group transformations which affect the flavour and isospin quantum numbers [4]. According to this new vision of the hadronic system, each particle consists of 3 quarks (baryons) or of a $q\bar{q}$ pair (mesons). The properties of the observed hadrons were therefore described by the flavour of their components. Nevertheless since a direct observation of quarks was missing, the new entities were considered as purely mathematical objects rather than observable particles.

Clear support for this model, and its subsequent re-interpretation arrived in 1968 from the results of a deep inelastic scattering (DIS) experiment performed at SLAC [5] where electrons were scattered at high momentum transfer from a hydrogen fixed target. The inclusive process studied was $ep \rightarrow eX$, where X is the hadronic system produced in the final state. The cross section in this case is the product of a kinematic factor times an elastic cross section (Rutherford) modulated by a set of so-called structure functions which describe the internal

structure of the proton. So-called Bjorken scaling was observed: the proton structure function is independent of the momentum transfer when the latter increases. At large momentum transfer the lepton behaved as if it were scattered by a point-like constituent inside the proton. These components (termed *partons* by Feynman) were soon associated with the quarks of Gell-Mann and Zweig. In spite of the apparent success of the Quark Parton Model (QPM), many important problems remained to be solved; one of the more relevant being the violation of Pauli's exclusion principle in the Δ^{++} resonance: this baryon was apparently composed of 3 quarks in the same spin state. The success of the renormalization of $U(1) \times SU(2)$ gauge theory of the electroweak interactions led to the idea that the strong interaction could be explained through a gauge theory as well. The introduction of a new strong charge (the *colour* charge) which can assume 3 different values allows the antisymmetrization of the hadronic wave functions, thereby solving the Δ^{++} problem. The requirement of invariance under $SU(3)$ local gauge transformations (which affect the colour), led to the birth of Quantum Chromodynamics (QCD). This theory describes the dynamics of the constituent hadrons considering the interactions between quarks as mediated by 8 massless gauge bosons called *gluons*. Due to the non-abelian property of the $SU(3)$ colour group, these gauge fields (the gluons) also carry the colour charge. This property yields the asymptotic freedom of the theory whereby the strength of the interaction between quarks, characterized by α_s , increases with the distance (low momenta transfer); conversely when the gap between the two quarks becomes small (large momenta transfer) the quarks behave like non-interacting fermions¹. This kind of behaviour is in agreement with the (postulated) property of *confinement* implying quarks always remain bound inside the hadron even if they behave like free particles when they interact with a current as in DIS experiments. Asymptotic freedom allows the calculation of all the quantities involved through a perturbative expansion in the α_s coupling. The QCD cross section can be factorized in a "hard" component, σ_i , which can be perturbatively determined, and a "soft" non-perturbative component, f_h . This cross section can be represented by a convolution of the form:

¹ $\alpha_s \sim 1/\log(Q/\Lambda)$, where Q identifies the energy scale and Λ is a parameter with value $\simeq 0.2$ GeV which characterizes distances comparable with the hadron size.

$$\sigma = \sum_i f_i^h \otimes \sigma_i \quad (1.1)$$

where the sum runs over all the partons inside the hadron h .

The quantities f_i^h are known as parton distribution functions and contain information about the non-perturbative part of the interaction, while the σ_i contain the dynamics of the hard scattering and can be calculated using perturbative QCD. The f_i^h are related to the distribution of the parton i inside the hadron h . The cross sections σ_i are independent of the interacting hadrons and the parton distributions are independent of the hard interaction and are therefore considered the same for all the interactions which involve hadrons. This property is known as “*hadronic universality*”.

1.2 Kinematics at HERA: lepton-nucleon interactions

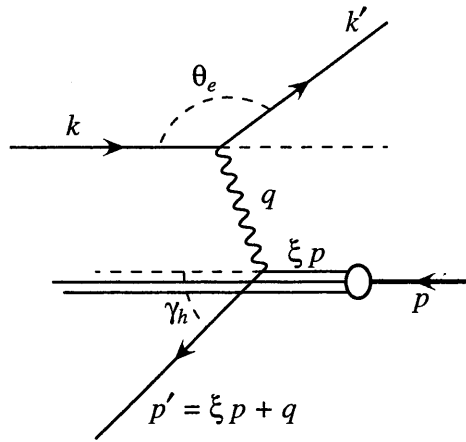


Figure 1.1: *DIS kinematics at HERA.*

In a DIS process (shown in Fig. 1.1), the incoming lepton is scattered from the hadronic system via the exchange of a virtual gauge boson; if the transferred four-momentum between the lepton and proton is high enough, the exchanged boson can resolve the pointlike constituents inside the proton. The fundamental

process, at leading order in lepton-proton scattering is mediated through both electromagnetic and weak forces via the exchange of a photon, in the former case, and Z^0 , W^\pm in the latter. The final state consists of the appropriate lepton (e^- , $\bar{\nu}_e$) and the hadronic state (X) produced by the fragmentation of the nucleon. The process considered could therefore be divided into two classes (see Fig. 1.2):

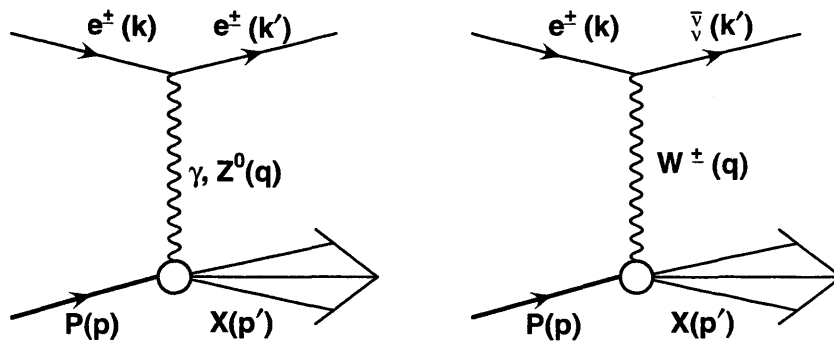


Figure 1.2: *Neutral current (γ or Z^0 exchange) and charged current (W^\pm exchange) interactions.*

- neutral current interactions (NC) where the mediator boson is a photon or a Z^0 ;

$$e^\pm + P \longrightarrow e^\pm X . \quad (1.2)$$

- charged current interactions (CC) where a W^\pm boson is exchanged;

$$e^+(e^-) + P \longrightarrow \bar{\nu}(\nu) X . \quad (1.3)$$

If $k(= E, \vec{k})$ and $k'(= E', \vec{k}')$ are the incoming and outgoing lepton four-momenta respectively (see Fig. 1.1 and 1.2), and $p(= E_p, \vec{p})$ the proton and $q(= E_\gamma, \vec{q})$ the mediator boson four-momenta, then the kinematics of the electron-proton scattering can be completely defined using two of the following Lorentz invariant quantities:

$$Q^2 = -q^2 = -(k - k')^2, \quad (1.4)$$

$$y = \frac{k' \cdot p}{k \cdot p} \quad \text{and} \quad x = \frac{Q^2}{2p \cdot q} . \quad (1.5)$$

Q^2 is the relativistic square of the transferred 4-momentum (with negative sign) of the exchanged boson defining its “virtuality”. In the proton rest frame, y (inelasticity) is the fraction of energy transferred from the lepton to the proton, i.e. $y = \frac{E-E'}{E} = \frac{E_\gamma}{E}$. In the parton model, x is the fraction of the momentum carried by the interacting quark (in a reference system where the proton is moving very fast) and corresponds to the Bjorken scaling variable. The quantities are related as follows:

$$Q^2 = sxy, \quad (1.6)$$

where s is the square of centre-of-mass energy ($\sqrt{s} = \sqrt{(k+p)^2}$) and masses are neglected.

The variable Q^2 can be thought of as a measure of the resolving power of the photon since the wave length of the virtual photon λ is given by:

$$\lambda = \frac{h}{|q|} \quad (1.7)$$

and as Q^2 increases, the ability for the photon to resolve smaller objects increases. At low Q^2 ($Q^2 \ll M_{Z,W}^2$) the contribution from photon exchange is dominant; for $Q^2 \approx M_{Z,W}^2$ the contribution of the Z^0 and W^\pm bosons become significant such that the charged and neutral current cross sections become comparable. For Q^2 much larger than $\Lambda_{QCD} \simeq 0.2$ GeV, where Λ_{QCD} is characteristic of the nucleon size, perturbative calculations are expected to be valid [6].

The deep inelastic regime (DIS) is defined for $Q^2 \gg \Lambda_{QCD}^2$, while for photoproduction $Q^2 \simeq 0$ i.e. the virtuality of the exchanged photon is small. In this case the electron is scattered at very small angles with respect to the incident direction and the incoming electron beam can be thought of as a source of real photons. In photoproduction Q^2 cannot be used to define a hard scale: this can be accomplished by other quantities such as the transverse momentum of the jet in the final state or the mass of the quark for heavy quark production.

1.3 Parton model

As seen in the previous section, the hadronic vertex interaction is assumed to be an elastic scattering between a current and a point-like constituent inside the proton. The cross section will therefore be expressed in terms of the elastic

scattering with a parton and the probability to find this parton inside the proton, as already mentioned in Eq. 1.1.

The ep cross section corresponds to the incoherent sum of the electron-parton scattering processes which is justified in a reference system in which the proton has a very high momentum in order to have all the constituents moving along its direction and the masses neglected. In such a reference system the proton will “appear” to the ingoing lepton as relativistically “contracted” into a thin disc; moreover the time dilation places the parton-parton interactions on a larger time scale than the current-parton interaction (“impulse” approximation). In this reference system, the 4-momentum conservation yields (Fig. 1.1):

$$0 \approx m^2 = (\xi p + q)^2 = \xi^2 p^2 - Q^2 + 2\xi p \cdot q \quad \text{and}$$

$$\xi = \frac{Q^2}{2p \cdot q} = x ,$$

where the i^{th} parton has been considered to carry a fraction ξ of the proton longitudinal momentum (so that $p_i = \xi p$), and to be on-shell both before and after the interaction.

In this way, the Bjorken scaling variable x is identified in the parton model with the fraction of the proton longitudinal momentum ξ , carried by the parton participating in the interaction. At this point, in order to calculate the cross section, it is necessary to multiply the elementary parton-photon scattering cross section with a probability density f_i which describes the probability of finding the i^{th} parton with a momentum fraction between x and $x + \delta x$, and then sum over all the partons inside the proton. Although these probability density functions are not predicted by the model, they have to obey certain sum rules which guarantee, for instance, the correct number of valence quarks ² inside the proton, and momentum conservation. The latter condition can be written as:

$$\sum_i \int_0^1 dx f_i(x) = 1 . \quad (1.8)$$

The general cross section for an electromagnetic DIS process, can be written as:

$$\frac{d\sigma^2}{dx dQ^2} = \frac{4\pi\alpha^2}{xQ^4} \left[(1-y)F_2(x, Q^2) + \frac{1}{2}y^2 2xF_1(x, Q^2) \right] , \quad (1.9)$$

²The hadron valence quarks are those characterizing the quantum numbers of the hadron.

where only two structure functions F_1 and F_2 are involved since parity is conserved in electromagnetic interactions. The scaling property and its interpretation in the parton model can be written as:

$$F_2(x, Q^2) = \sum_i e_i^2 x f_i(x) \quad \text{and} \quad (1.10)$$

$$F_1(x, Q^2) = \frac{1}{2x} F_2(x, Q^2), \quad (1.11)$$

where the Callan-Gross relation,

$$F_L(x) = F_2(x) - 2xF_1(x) = 0, \quad (1.12)$$

is a consequence of the partons being fermions with spin $s = 1/2$. As already observed in (1.8) the sum of the momenta carried by the partons inside the proton has to correspond to the total proton momentum. From the definition of $F_2(x)$ it can be seen that the sum runs over the momentum fractions of all the *charged* partons (e_i^2 in eq 1.10 is the squared charge of the i^{th} -parton).

Experimental measurements performed at SLAC clearly showed the existence of non-charged partons inside the proton carrying approximately 50% of the proton momentum. These were identified as gluons, which are the 8 QCD gauge bosons which mediate the strong colour force. Direct evidence of these neutral particles occurred in 1979 with the observation of three-jet events in e^+e^- annihilation processes at DESY [8]. Under the influence of the strong colour force a quark can radiate gluons both before and after the interaction; on the other hand the gluons can also produce a $q\bar{q}$ pair, each of these quarks having the possibility to interact with the virtual photon. Fig. 1.3 shows a few diagrams of first order QCD processes in α_s .

The introduction of QCD interactions in the quark parton model leads to scaling violations and this was demonstrated by the experimental observation of a logarithmic Q^2 dependence of $F_2(x, Q^2)$.

1.4 Structure functions in QCD

As previously mentioned, the possibility of gluon radiation (by quarks) is one of the causes of scaling violations i.e. structure functions depend on Q^2 as well as

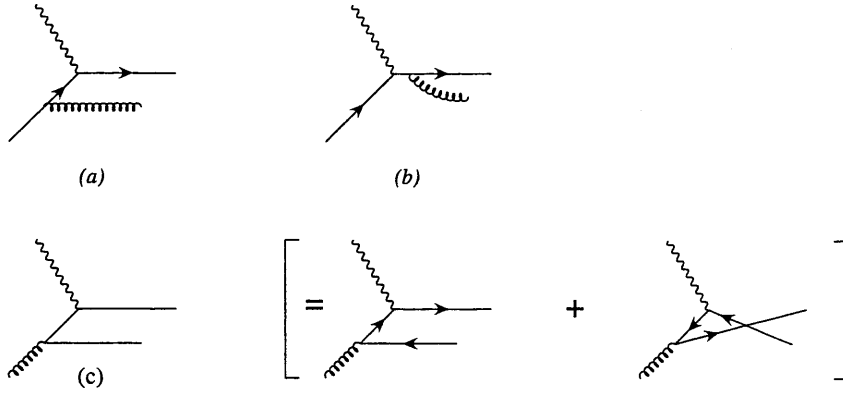


Figure 1.3: *Diagrams of QCD processes at first order in α_s : a) and b) QCD Compton Scattering, c) boson-gluon fusion.*

x . In other words, at high Q^2 a quark can radiate a gluon and its momentum fraction x , decreases. At low Q^2 the photon can resolve the proton substructure in terms of valence quarks. Therefore at high values of x , where the valence quark contribution is dominant, the quark density (F_2) decreases for increasing Q^2 . At low x the number of sea quarks ($q\bar{q}$ pairs originating from gluons) and of gluons is higher, leading to an increasing of F_2 as a function of Q^2 . As Q^2 increases, the photon starts to “see” evidence of the point-like valence quarks within the proton. If the quark were non-interacting, no further structure would be resolved as Q^2 increases and exact scaling would set in. However, QCD predicts that on increasing the resolution (high Q^2), the photon “sees” that each quark is itself surrounded by a cloud of partons and the number of resolved partons which share the proton’s momentum increases with Q^2 . There is an increased probability of finding a quark at small x and a decreased chance of finding one at high x , because high-momentum quarks lose momentum by radiating gluons [7]. This dependence was experimentally tested at HERA [9, 10] as shown in Fig. 1.4 for F_2 plotted against Q^2 .

In QCD, equation 1.9 is modified and the evolution of F_2 , taking into account gluon emission, is predicted to be given by:

$$\frac{F_2(x, Q^2)}{x} = \sum_q e_q^2 \int_x^1 \frac{dy}{y} q(y) \left(\delta \left(1 - \frac{x}{y} \right) + \frac{\alpha_s}{2\pi} P_{qq} \left(\frac{x}{y} \right) \log \frac{Q^2}{\mu^2} \right), \quad (1.13)$$

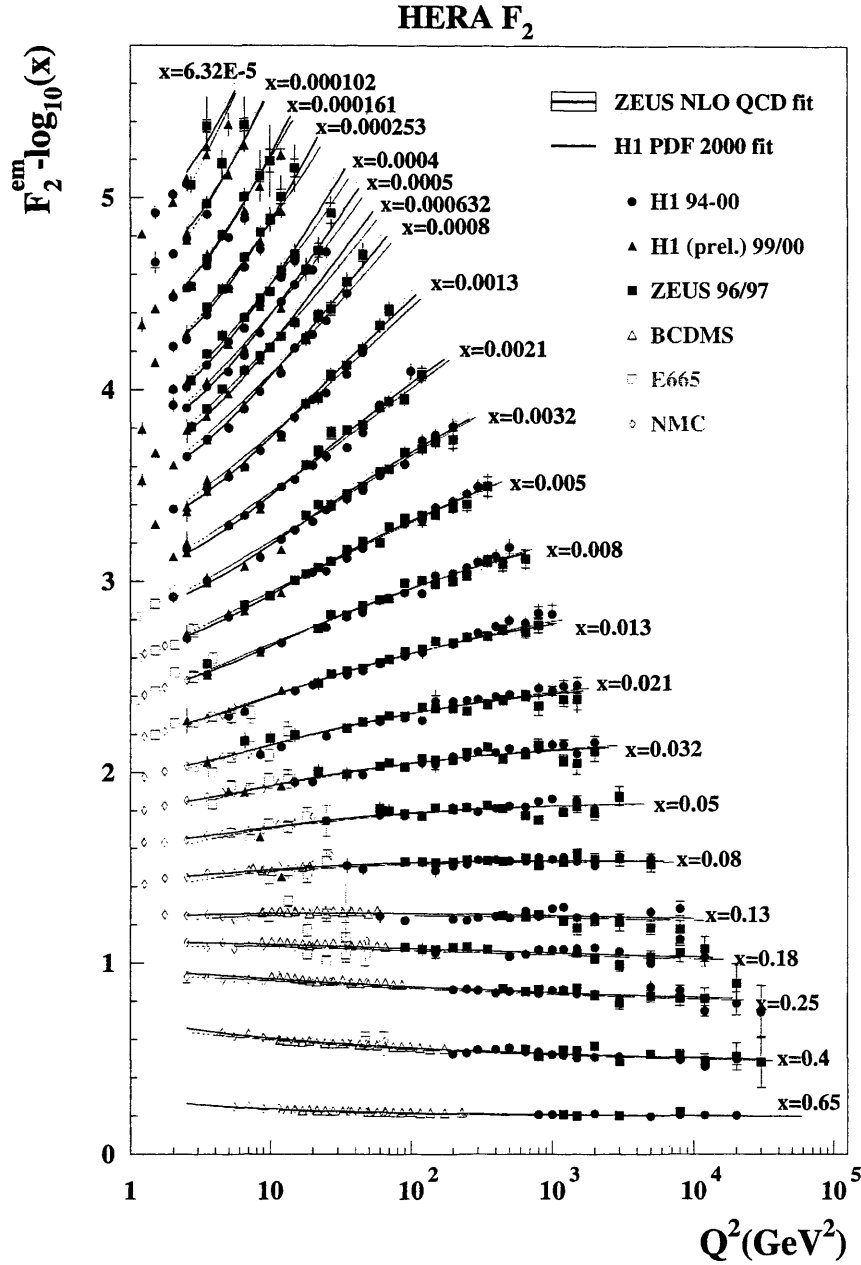


Figure 1.4: *Proton structure function measured in electromagnetic scattering of electrons (H1 and ZEUS) and muons, within the kinematic domain of HERA data. In the figure it is possible to observe the scaling violation at low x .*

where $q(y) = f_q(y)$ represents the distribution function of quark q , μ is the lower limit on the transverse momentum fixed in order to “regulate” the infrared divergences (i.e. where the square of the transverse momentum Q^2 tends to zero)

while $P_{qq}(\frac{x}{y})$ is the probability that a quark carrying a fraction y of the momentum radiates a gluon with momentum fraction x (*splitting function*).

The quark distribution functions can be calculated for any value of Q^2 , once a reference value is known, through the evolution equation:

$$\frac{dq(x, Q^2)}{d \ln Q^2} = \frac{\alpha_s}{2\pi} \int_x^1 \frac{dy}{y} q(y, Q^2) P_{qq}\left(\frac{x}{y}\right). \quad (1.14)$$

The quark density probability evolution is further modified by the possibility that the quark belongs to the pair originating from a gluon; also when a gluon is generated from a quark or from a gluon the respective gluon density distributions must be modified; the above mentioned processes can be visualised with the diagrams of Fig. 1.5.

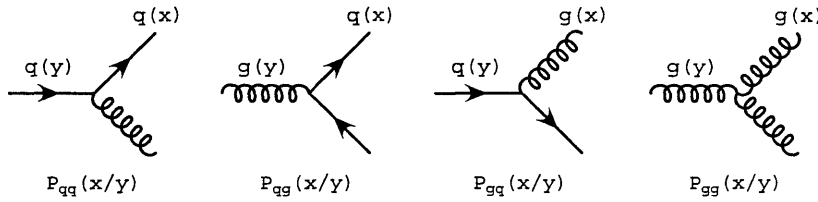


Figure 1.5: *Feynman diagrams of quark and gluon splitting processes. The associated P_{jk} functions are indicated.*

The picture also shows the splitting functions $P_{jk}\left(\frac{x}{y}\right)$, which, as already mentioned, represent the probability that a parton k , carrying a momentum fraction y , radiates a parton j with momentum fraction x . Taking into account all these effects, in QCD there are a set of equations which describe the evolution of quark and gluon distributions inside a hadron as a function of the interaction scale Q^2 :

$$\frac{dq_i(x, Q^2)}{d \ln Q^2} = \frac{\alpha_s}{2\pi} \int_x^1 \frac{dy}{y} \left[q_i(y, Q^2) P_{qq}\left(\frac{x}{y}\right) + g(y, Q^2) P_{qg}\left(\frac{x}{y}\right) \right] \text{ and } \quad (1.15)$$

$$\frac{dg(x, Q^2)}{d \ln Q^2} = \frac{\alpha_s}{2\pi} \int_x^1 \frac{dy}{y} \left[\sum_i q_i(y, Q^2) P_{gq}\left(\frac{x}{y}\right) + g(y, Q^2) P_{gg}\left(\frac{x}{y}\right) \right], \quad (1.16)$$

where $q_i(y, Q^2)$ is the density function for the i^{th} quark and $g(y, Q^2)$ is the density function of the gluon. These equations are better known as *DGLAP* equations (Dokshitzer-Gribov-Lipatov-Altarelli-Parisi) and have been formulated on the basis of the factorization theorem [11]. Given a specific renormalization and factorization scheme, these splitting functions $P_{jk}\left(\frac{x}{y}\right)$ are obtained in QCD through a perturbative expansion in α_s :

$$P_{jk}\left(\frac{x}{y}\right) = P_{jk}^{(0)}\left(\frac{x}{y}\right) + \frac{\alpha_s}{2\pi} P_{jk}^{(1)}\left(\frac{x}{y}\right) + \dots \quad (1.17)$$

The first two terms of the expansion define the NLO DGLAP evolution. In this scheme the parton evolution can be seen as the sum of ladder diagrams where each “rung” corresponds to a gluon emission as in Fig. 1.6. Each diagram with n gluon emissions of momentum $k_{T_i}^2$ represents a term in $(\alpha_s \log Q^2)^n$, where $\alpha_s \log Q^2 \sim 1$, which is dominant at large x and Q^2 . In this regime, each contribution is ordered in transverse momentum such that,

$$k_{T_1}^2 \ll k_{T_2}^2 \ll \dots \ll k_{T_{n-1}}^2 \ll k_{T_n}^2 \ll Q^2.$$

With the knowledge of the x dependence at a minimum Q^2 , Q_0^2 , the evolution equations can be solved to give the parton distributions as a function of x for all Q^2 . This minimum value Q_0^2 cannot presently be calculated so relies on an experimental determination. These evolution equations describe the physics at high x and Q^2 ignoring terms involving $\log(1/x)$ whose importance arises at low x . The terms at low x can be taken into account by summing $(\alpha_s \log(1/x))^n$ gluon emission terms which are now not ordered in transverse momentum resulting in the Balitzky-Fadin-Kuraev-Lipatov (BKFL) equations [12].

In the logarithmic approximation of the dominant term the splitting functions P_{ij} can be parameterized as follows:

$$P_{gq}(z) = \frac{1}{2}[z^2 + (1-z)^2], \quad (1.18)$$

$$P_{qq}(z) = \frac{4}{3} \left[\frac{1 + (1-z)^2}{z} \right] \text{ and} \quad (1.19)$$

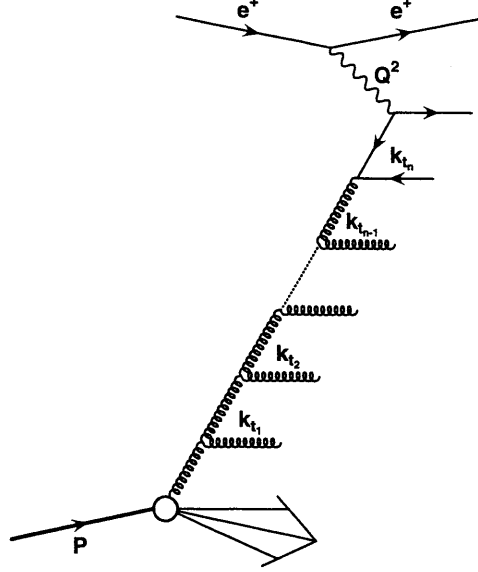


Figure 1.6: *Parton evolution diagram showing the gluonic emission ordered according to k_t .*

$$P_{gg} = 6 \left[\frac{z}{(1-z)} + \frac{(1-z)}{z} + z(1-z) + \left(\frac{11}{12} + \frac{N_f}{18} \right) \delta(1-z) \right], \quad (1.20)$$

where N_f is the number of flavours involved.

1.5 Fragmentation functions

Perturbative QCD can reasonably describe the strong interactions which involve large transferred momenta, but is not able to make predictions at low Q^2 when the partons combine to form observable hadrons. The properties of the hadrons (produced in the quark fragmentation process) to produce jets of observable particles can be described through dimensionless functions which define the single particle's distribution in the final state. These fragmentation functions are conveniently defined for e^+e^- collisions where the total fragmentation function for hadrons h for a given centre-of-mass energy \sqrt{s} can be written as:

$$F^h(x, s) = \frac{1}{\sigma_{tot}} \frac{d\sigma}{dx} (e^+e^- \rightarrow hX), \quad (1.21)$$

where $x = \frac{E_h}{E_p} < 1$, E_h and E_p are the hadron and proton energy, respectively. If we integrate over x the average *multiplicity* of the hadron h is obtained:

$$n_h(s) = \int_0^1 dz F^h(x, s). \quad (1.22)$$

The function in Eq. (1.22) can be decomposed into the contributions of the different partons which are involved in the process, obtaining:

$$F^h(x, s) = \sum_{i=u,d,\dots} \int_x^1 \frac{dz}{z} C_i(s; z, \alpha_s) D_i^h(x/z, s). \quad (1.23)$$

The function $D_i^h(x/z, s)$ represents the probability that the parton i produces an hadron h , with a fraction of energy x and the coefficient functions C_i , for $s < M_Z$, correspond to $C_i = g_i(s)(1-z)$, where $g_i(s)$ is the electroweak coupling. The fragmentation functions D_i^h cannot be calculated in perturbative theory; moreover their determination is more complicated in photoproduction than for e^+e^- collisions [13].

1.6 Photoproduction

In the DIS regime (Eq. 1.9) we have seen that the cross section shows a $1/Q^4$ dependence due to the photon propagator. Therefore the dominant contribution to the total cross section will originate from the photon exchange with very low virtuality. The average lifetime of the exchanged photon varies approximately like $\sim E_\gamma/Q^2$ hence, for very low virtuality, this time appears long with respect to the characteristic time of the hard subprocess. At HERA the electron beam scattered through very small angles can produce collinear, almost real, photons, which results effectively in a $\gamma - p$ collider. The total cross section, σ_{tot}^{ep} can be factorized as the total photon-proton cross section contribution $\sigma_{tot}^{\gamma p}$ times the flux factor $f_{e \rightarrow \gamma}(y)$, which defines the probability to produce a photon with energy $E_\gamma = yE_e$. Since in the $Q^2 \rightarrow 0$ limit, the photon can be polarized only transversely, it is a good approximation to write:

$$\frac{d^2 \sigma^{ep}}{dy dQ^2} \sim f_{e \rightarrow \gamma_T}(y, Q^2) \sigma_{tot}^{\gamma p}(y, Q^2), \quad (1.24)$$

where the photonic flux, $f_{e \rightarrow \gamma_T}(y, Q^2)$, can be written as:

$$f_{e \rightarrow \gamma_T}(y, Q^2) = \frac{\alpha}{2\pi} \frac{1}{Q^2} \left[\frac{1 + (1-y)^2}{y} - 2 \frac{1-y}{y} \frac{Q_{min}^2}{Q^2} \right]. \quad (1.25)$$

In the above equation Q_{min}^2 represents the lower kinematic limit and is given by:

$$Q_{min}^2 = m_e^2 y^2 / (1-y). \quad (1.26)$$

In general this is known as the *equivalent photon approximation (EPA)*. If the Q^2 dependence of the γp cross section is neglected, then integrating over the photon virtuality from the lower kinematic limit to a particular Q_{max}^2 we obtain:

$$f_{e \rightarrow \gamma}^{WWA}(y) = \frac{\alpha}{2\pi} \left[\frac{1 + (1-y)^2}{y} - 2 \frac{1-y}{y} \ln \frac{Q_{max}^2}{Q_{min}^2} - 2 \frac{1-y}{y} \left(1 - \frac{Q_{min}^2}{Q_{max}^2} \right) \right] \quad (1.27)$$

which is known as the Weizsäcker-Williams approximation (WWA) [14].

The photon fluctuation to free states $\bar{l}l$ is described by quantum electrodynamics, while the fluctuation to $q\bar{q}$ pairs is “further complicated” by the strong interactions between quarks. In photoproduction [78] the photon lifetime is long enough to allow the fluctuation into low virtuality $q\bar{q}$ states. This means that the photon behaves in this case as a source of partons and it is therefore possible to use a formalism already developed for hadron-hadron interactions.

1.6.1 Direct photoproduction

The process in which the photon *directly* interacts in the hard subprocess is called direct photoproduction. The photon acts like a pointlike object interacting with the parton inside the proton, a property which distinguishes it from hadron-hadron scattering. Since all the photon energy is available in the collision with the parton, the final state of the process is expected to be characterized by a higher transverse momentum with respect to hadronic interactions in which only a part of the photon is involved.

The dominant processes at HERA are shown in Fig. 1.7. The elementary diagrams shown in the figure are similar to those for DIS at $O(\alpha_s)$; in that case the perturbative scale was fixed by the photon virtuality, while in photoproduction the Q^2 is small and the scale is determined by the internal propagator. In

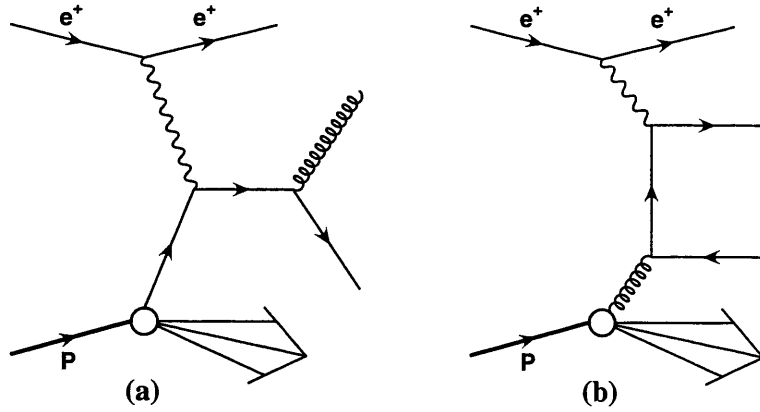


Figure 1.7: *LO processes of direct dijet photoproduction a) QCD Compton scattering b) Boson-gluon fusion.*

jet events with high transverse energy E_T^j in the final state, for instance, the perturbative scale is fixed by E_T^j . In contrast to inclusive DIS, direct photoproduction is sensitive to the proton gluon density at Leading Order (LO). A direct dijet photoproduction event, as “seen” inside the ZEUS detector (see Chapter 3), is shown in Fig. 1.8. Together with the proton fragmentation there are two jets of high transverse momentum which are generated by the two outgoing partons in the hard subprocess, which approximately balance the transverse energy E_T and are in a back-to-back configuration.

1.6.2 Resolved photoproduction

In resolved photoproduction processes, the photon acts like a source of partons, one of them interacting in the hard subprocess with a parton inside the proton. Fig. 1.9 shows some examples of resolved photoproduction LO diagrams.

In Fig. 1.9 a), a gluon from the photon interacts with a gluon from the proton (gluon-gluon fusion), while in Fig. 1.9 b) a quark from the photon interacts with the gluon from the proton. The resolved photoproduction final state differs from the direct one since the fragmentation products of the photon are present in the event. A resolved photoproduction event, as seen by the ZEUS detector is shown in Fig. 1.10.

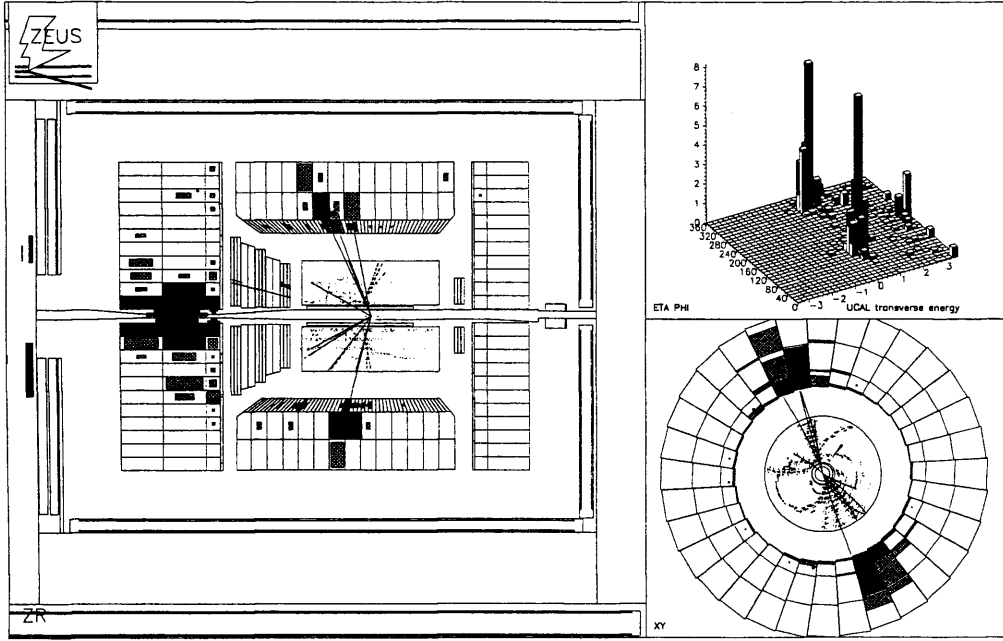


Figure 1.8: *Direct dijet photoproduction event as detected by ZEUS.*

1.7 Photoproduction generalized model

The direct and resolved photoproduction diagrams can be generalized, as shown in Fig. 1.11, to describe jet production. The dashed lines in the figure represent the separation between the hard process which can be perturbatively calculated and the non-perturbative part described through the parton distribution functions. The factorization scales, μ_P and μ_γ , are in general chosen as $\mu_p = \mu_\gamma \sim E_T$, allowing the incoming parton to have a wide phase space region in which to evolve.

The differential cross section for the generalized model can be separated into a direct and a resolved component:

$$d\sigma_{\gamma p \rightarrow cd} = d\sigma_{\gamma p \rightarrow cd}^{dir} + d\sigma_{\gamma p \rightarrow cd}^{res}, \quad (1.28)$$

where the two components can be written as:

$$d\sigma_{\gamma p \rightarrow cd}^{dir} = \sum_b \int_{x_p} dx_p f_{p \rightarrow b}(x_p, \mu_p^2) d\sigma_{\gamma b \rightarrow cd} \quad (1.29)$$

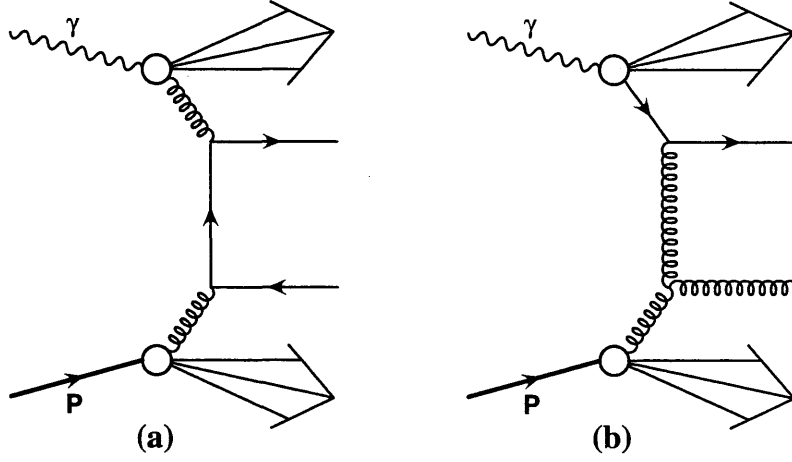


Figure 1.9: *Resolved photoproduction LO processes.*

and

$$d\sigma_{\gamma p \rightarrow cd}^{\text{res}} = \sum_{ab} \int_{x_p} dx_p \int_{x_\gamma} dx_\gamma f_{p \rightarrow b}(x_p, \mu_p^2) f_{\gamma \rightarrow a}(x_\gamma, \mu_\gamma^2) d\sigma_{\gamma b \rightarrow cd}. \quad (1.30)$$

where $d\sigma_{\gamma b \rightarrow cd}$ represents the elementary $2 \rightarrow 2$ cross section of the perturbatively calculable scattering, while $f_{p \rightarrow b}$ and $f_{\gamma \rightarrow a}$ are the photon and proton structure functions respectively.

At the Next-to-Leading-Order, (NLO), there are contributions from the parton scattering $2 \rightarrow 3$ which are dependent on the factorization scale. In fact, increasing μ_γ the amount of the processes $2 \rightarrow 3$ at NLO and the fraction of processes defined at LO decreases; in particular an ambiguity between the direct NLO processes and the resolved LO processes arises and this depends on μ_γ . The advantage of the NLO with respect to the LO has therefore to be traced to the reduction of the factorization scale dependence. The distinction between “direct” and “resolved-photon” processes, whilst an intuitive and useful concept, is valid only at LO.

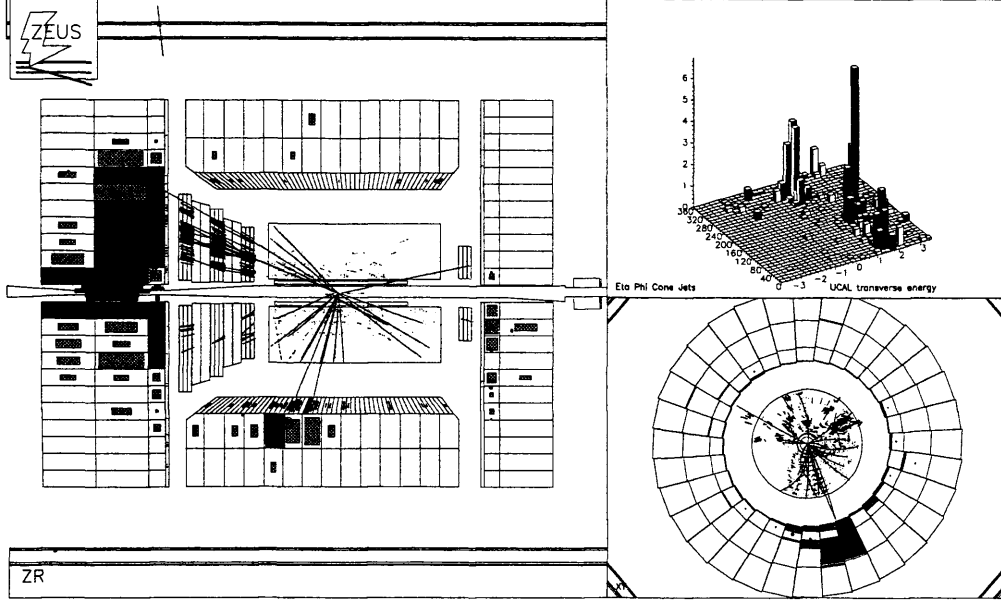


Figure 1.10: *Three-jet resolved photoproduction event at ZEUS.*

1.8 The photon structure

In $e\gamma$ ³ deep inelastic scattering, the cross section for the “probe” photon of virtuality $Q^2 \equiv -q^2$ which interacts with a target made of a real photon with virtuality $P^2 \simeq 0$ generating a final state X , is written as:

$$\frac{d\sigma_{e\gamma \rightarrow eX}^2}{dx dy} = \frac{2\pi\alpha^2 s}{Q^4} [(1 + (1 - y)^2)F_2^\gamma(x, Q^2) - y^2 F_L^\gamma(x, Q^2)] \quad (1.31)$$

where $x \equiv Q^2/(2p \cdot q)$ and $y \equiv Q^2/(sx)$, \sqrt{s} being the centre-of-mass energy.

The advantage of the $e\gamma$ cross section with respect to the ep one is that the photon structure functions can be calculated with the Quark Parton Model. Unfortunately the result depends on the constituent quark masses which are not well defined in quantum field theory. Nevertheless, analogously to the ep scattering, the F_2^γ structure function can be written in terms of the $q_i^\gamma(x, Q^2)$ densities, obtaining (at LO):

$$F_2^\gamma(x, Q^2) = 2x \sum_i e_{q_i}^2 q_i^\gamma(x, Q^2), \quad (1.32)$$

³This scattering was experimentally studied in e^+e^- colliders through the $e^+e^- \rightarrow e^+e^-X$ process, where one of the leptons in the final state is scattered at very small angles with respect to the incoming direction.

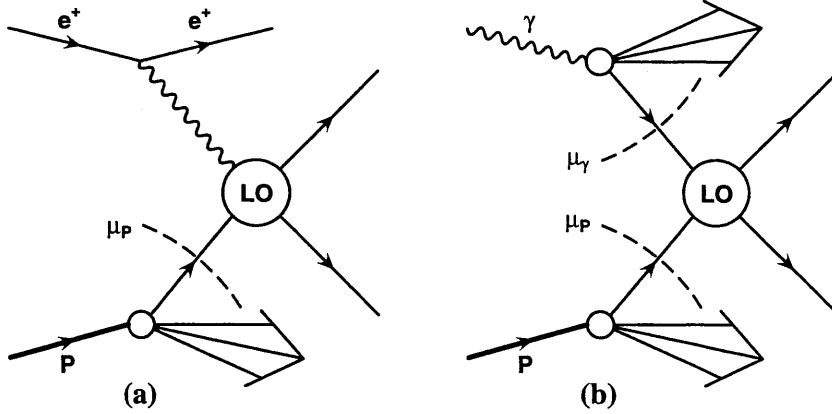


Figure 1.11: *Direct and resolved LO photoproduction processes; the dashed lines represent the border between the hard process (perturbatively calculated) and the non perturbative part.*

where the sum runs over all the quark flavours of charge e_{q_i} ; the factor of 2 takes into account the presence of quarks and antiquarks.

The Q^2 dependence of the photon parton densities obeys the evolution equations:

$$\frac{dq_i(x, Q^2)}{d\log Q^2} = a(x) + \frac{\alpha_s(Q^2)}{2\pi} \int_x^1 \frac{dy}{y} \left[P_{qq} \left(\frac{x}{y} \right) q_i(y, Q^2) + P_{qg} \left(\frac{x}{y} \right) g(y, Q^2) \right], \text{ and} \quad (1.33)$$

$$\frac{dg(x, Q^2)}{d\log Q^2} = a(x) + \frac{\alpha_s(Q^2)}{2\pi} \int_x^1 \frac{dy}{y} \left[P_{gq} \left(\frac{x}{y} \right) \sum_i^f q_i(y, Q^2) + P_{gg} \left(\frac{x}{y} \right) g(y, Q^2) \right], \quad (1.34)$$

where

$$a(x) = 3e_i^2 \frac{\alpha}{2\pi} [x^2 + (1-x)^2] \quad (1.35)$$

takes into account the splitting process $\gamma \rightarrow q\bar{q}$ and is known as the “anomalous” component, while the P_{jk} are already defined in section 1.4.

1.9 Two-jet photoproduction results at HERA

As stated above, the distinction between resolved and direct processes is a well defined concept at LO, while at higher orders the discrimination between the two different contributions is ambiguous. The contribution of the two processes in photoproduction events with two jets in the final state was studied in fixed target experiments in 1979 [15]. It was found that the fraction of resolved photon events was small. At HERA the observation of resolved photon processes was unequivocally proved through the observation of large energy deposits in the rear region (along the electron direction), consistent with the presence of photon fragmentation products. Moreover the distinction between the two components [16] was determined and an experimental separation of the two processes was defined. This separation is based on the photon energy fraction observation, x_γ , which participates in the interaction. For the QCD LO diagrams previously discussed, the momentum and energy conservation, for a two parton scattering, yields:

$$x_\gamma^{LO} = \frac{\sum_i E_T^i e^{-\eta^i}}{2yE_e}, \quad (1.36)$$

where yE_e represents the initial photon energy. For direct photon events $x_\gamma = 1$, while for resolved photon events $x_\gamma < 1$, since only part of the photon energy is involved in the scattering. For an experimentally measurable quantity, the sum in Eq. 1.36 should run over the jets instead over the partons. Equation 1.30 is therefore changed to:

$$x_\gamma^{obs} = \frac{\sum_{jets} E_T^{jets} e^{-\eta^{jets}}}{2yE_e}, \quad (1.37)$$

where the sum runs over the two highest transverse energy jets. Due to hadronization and higher order effects, the x_γ^{obs} value is no longer equal to one for the direct process, but it is nevertheless true that such process will “populate” the highest regions in the distribution of the x_γ^{obs} variable. In Fig.1.12 the data fit using Monte Carlo simulations for both direct-enriched and resolved-enriched processes is shown.

The regions characterizing the two different processes can be clearly distinguished. Experimentally a process can be defined as belonging to the resolved photon category when $x_\gamma^{obs} < 0.75$.

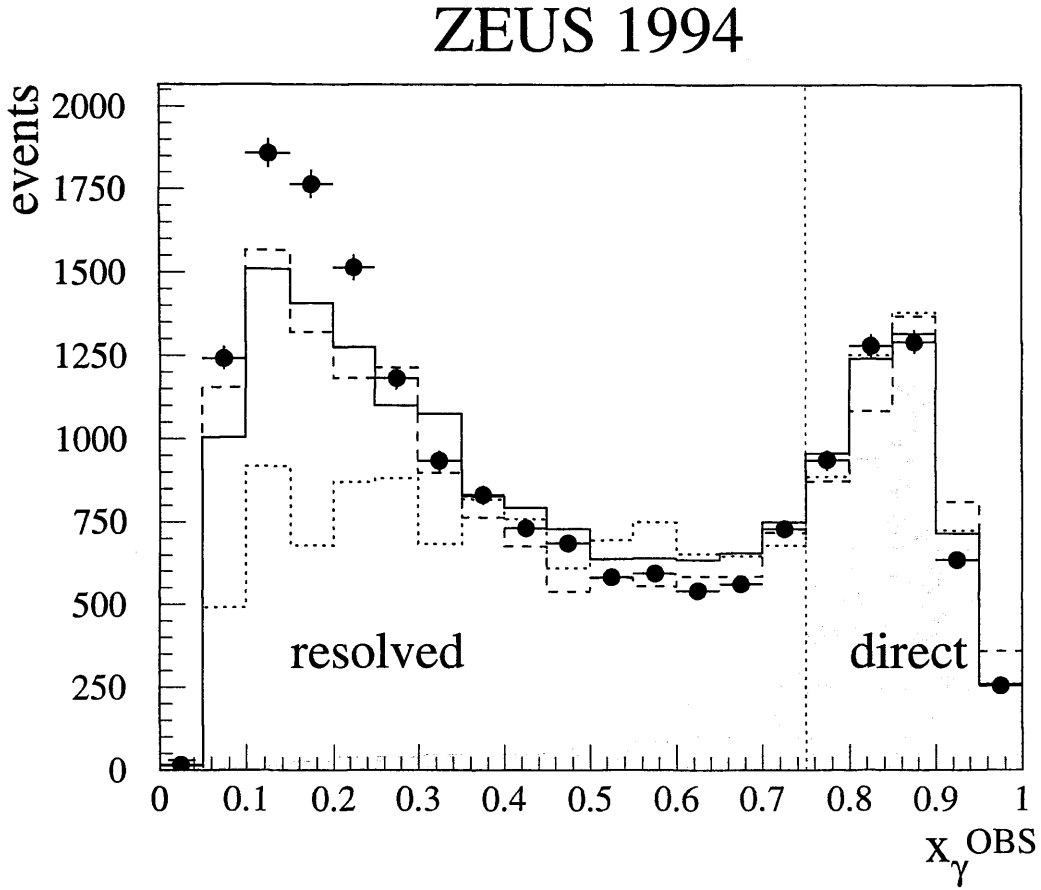


Figure 1.12: Distribution of x_{γ}^{obs} variable in two-jet events; the data are compared with MC HERWIG+MI (solid line), HERWIG-MI (dotted line) and PYTHIA+MI (dashed line) where MI are the Multiple Interactions. The shaded area represents all the direct events generated by HERWIG, the vertical line defines the experimental cut used to divide the direct-enriched processes from the resolved-enriched ones.

Once the existence of the two kinds of process is determined, it is possible to distinguish inside the same class of events the contribution of the different subprocesses described by the diagrams of Fig 1.7 and Fig. 1.9. This distinction can be determined by studying the 2-jet angular distribution, which depends on the spin carried by the process propagator. The angle between the jet-axis and the beam-axis, θ^* , calculated in the centre-of-mass frame of the 2-jet system is:

$$\cos \theta^* = \tanh \left(\frac{\eta^{jet1} - \eta^{jet2}}{2} \right), \quad (1.38)$$

where η^{jet1} and η^{jet2} are the pseudorapidities⁴ of the two jets with highest transverse energy. At LO the direct process involves a quark propagator (fig 1.7) while the resolved process can have a quark or a gluon. A quark propagator, with spin-1/2, leads to an angular dependence $\propto (|1 - \cos \theta^*|)^{-1}$ while a spin-1 gluon will show an angular dependence which varies $\propto (|1 - \cos \theta^*|)^{-2}$. Therefore different angular dependences are expected for the direct and resolved processes. This trend was confirmed in 2-jet photoproduction at ZEUS [17] measuring the angular distribution for direct and resolved events as depicted in Fig. 1.13.

ZEUS 1994

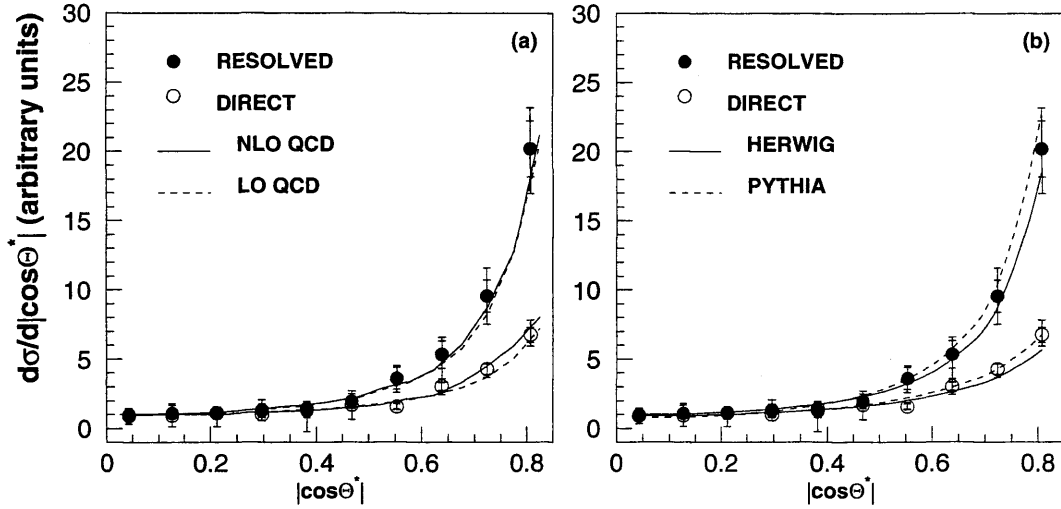


Figure 1.13: Angular cross section for the resolved (full dots) and direct (empty circles) processes compared with LO and NLO QCD predictions and with HERWIG and PYTHIA Monte Carlo.

⁴The pseudorapidity η is defined through $\eta = -\ln(\tan(\frac{\theta}{2}))$ where θ is the polar angle.

Chapter 2

Heavy quark production mechanisms

2.1 Introduction

Heavy quark production processes provide a powerful insight into understanding quantum chromodynamics. The large mass of the heavy quark ($m_q \gg \Lambda_{QCD}$) can make perturbative calculations reliable, even for total cross sections where no other hard scales are involved, by cutting off infrared singularities and by setting a large scale at which the strong coupling can be evaluated. In the first part of this chapter the theoretical aspects of heavy flavour production will be discussed.

The measurements of $b\bar{b}$ production cross sections is a long-standing and important project in the framework of the *Standard Model* carried out over decades. Started in 1977 with the discovery of the beauty quark pair bound state Υ in a fixed target experiment [18], the beauty cross section was measured at different centre-of-mass energies in fixed target experiments shifting the focus to open beauty production (B mesons). The significantly increased centre-of-mass energy of collider experiments continued this program. The photoproduction and hadronic production data obtained from the fixed target experiments showed a reasonable agreement with QCD predictions; nevertheless this compatibility was in the end more qualitative than quantitative because substantial deviations, not yet explained, still remain [19]. At HERA heavy quark production is possible both in photoproduction and DIS reactions, the latter having a dramatically smaller

cross section.

The most recent b results at the Tevatron and the $SppS$ ($p\bar{p}$ interactions), LEP ($\gamma\gamma$ interactions) and fixed target experiments will be discussed in the second part of this chapter.

The chapter will conclude with the experimental results obtained at the HERA collider in the last few years, for both the photoproduction ($Q^2 \sim 0 \text{ GeV}^2$) and DIS ($Q^2 > 1 \text{ GeV}^2$) kinematic regimes.

2.2 Heavy quark production at HERA

Studying beauty production offers advantages at the theoretical level; as already mentioned, its mass ($m_q \gg \Lambda_{QCD}$) ensures greater reliability for calculations, compared to charm production, where corrections $\propto (\Lambda_{QCD}/m_q)^n$ could become non-negligible. Top quark production through boson-gluon fusion is not possible at HERA due to the large mass of this quark, thus heavy quark production in the context of this thesis means always charm and beauty production. The dominant process at LO for heavy quark production in DIS and direct photoproduction is the Boson-Gluon Fusion (BGF) mechanism (Fig. 2.1 a)):

$$\gamma g \rightarrow Q\bar{Q} . \quad (2.1)$$

At LO the BGF process is directly sensitive to the gluonic content of the proton. In resolved photoproduction it is necessary to consider also quark excitation diagrams (Fig. 2.1 c) and d)):

$$Qg \rightarrow Qq , \quad (2.2)$$

where the heavy quarks originate from the photon, and the gluon-gluon fusion process (Fig. 2.1 b)):

$$gg \rightarrow Q\bar{Q} . \quad (2.3)$$

In photoproduction heavy quark production receives contributions from both the direct and resolved components. In the next sections heavy quark photoproduction and the theoretical approaches based on perturbative QCD will be discussed

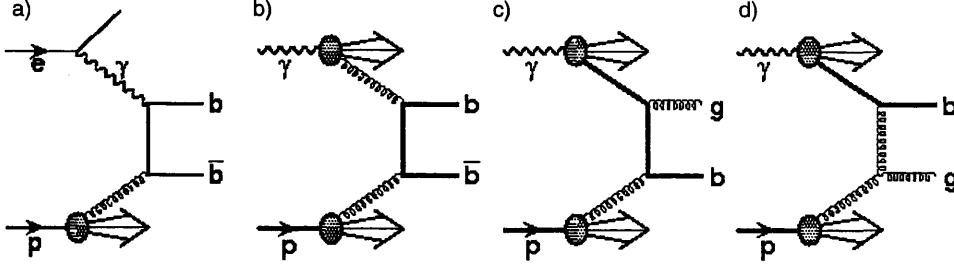


Figure 2.1: *Examples of Feynman diagrams for beauty production. In a) the direct Boson-Gluon Fusion process; in b) c) d) examples of resolved photoproduction processes are displayed.*

in detail.

2.3 Heavy quark production in perturbative QCD

The inclusive production of a heavy quark, Q , with momentum, p , and energy, E , in the process:

$$\gamma(p_1) + H(p_2) \rightarrow Q(p) + X \quad (2.4)$$

has been calculated to $O(\alpha_s^2)$ [20]; in Eq. 2.4 the incoming γ and hadron have four-momenta p_1 and p_2 respectively. The total cross section for a centre-of-mass energy, \sqrt{S} , of this photon-hadron system is given by:

$$\sigma(S) = \sum_j \int dx \sigma_{\gamma j}(xS, m^2, \mu^2) F_j^H + \sum_{i,j} dx_1 dx_2 \sigma_{ij}(x_1 x_2 S, m^2, \mu^2) F_i^\gamma(x_1, \mu) F_j^H(x_2, \mu), \quad (2.5)$$

where F_j^H and F_i^γ are the parton densities of the hadron and photon respectively and μ is the factorization scale. The short distance cross section, for a photon-parton collision is given by:

$$\sigma_{\gamma j}(xS, m^2, \mu^2) = \frac{\alpha \alpha_s(\mu^2)}{m^2} f_{\gamma j}(\rho, \mu^2/m^2), \quad (2.6)$$

where $\rho = 4m^2/s$ (m is the mass of the produced heavy quark) and s is the square of the γ -parton centre-of-mass energy. Eq 2.6 is analogous to the definition of the short-distance cross section for the hadroproduction of heavy quarks:

$$\sigma_{ij}(s, m^2, \mu^2) = \frac{\alpha_s^2(\mu^2)}{m^2} f_{ij}(\rho, \mu^2/m^2) . \quad (2.7)$$

The dimensionless function $f_{\gamma j}$ has the following perturbative expansion:

$$f_{\gamma j}(\rho, \mu^2/m^2) = f_{\gamma j}^0(\rho) + g^2(\mu^2) [f_{\gamma j}^1(\rho) + f_{\gamma j}^{1-}(\rho) \log(\mu^2/m^2)] + O(g^4) , \quad (2.8)$$

and, similarly for f_{ij} we have:

$$f_{ij}(\rho, \mu^2/m^2) = f_{ij}^0(\rho) + g^2(\mu^2) [f_{ij}^1(\rho) + f_{ij}^{1-}(\rho) \log(\mu^2/m^2)] + O(g^4) . \quad (2.9)$$

Details about these functions can be found in [20] [21]; in 2.8 and 2.9 g is the coupling strength ($\alpha_s = g^2/4\pi$). From the perturbative expansion of the equations 2.8 and 2.9 it can be seen that the expansion parameter is the mass of the quark, m_Q , emphasising the fact that this value fixes the hard scale.

The aforementioned equations are calculated for a single particle inclusive cross section but they have been extended in [22] to supply an exclusive cross section which allows a better comparison with the data. Usually for this kind of calculation the massive or massless schemes are used, which are described in the next sections.

2.4 Massive scheme

In the massive scheme of Frixione et al. (FMNR) [23, 24], the gluons and the light quarks are considered the only active partons inside the photon, whilst the heavy quarks do not contribute to the evolution of the coupling nor to the proton and photon structure functions. The photon density function F_i^γ (in Eq.2.5) at LO is given by:

$$F_i^\gamma = N_c e_i^2 (x^2 + (1-x)^2) \quad (2.10)$$

where $N_c = 3$ is the number of colours and e_i is the electric charge of the parton in units of the charge of the electron (for gluons $e_i = 0$). The number of active flavours in the initial state is $n_f=3$, whilst the massive quark appears only in the final state.

The heavy quark is dynamically produced in the hard subprocess, therefore there are only two kinds of resolved process at LO:

$$gg \longrightarrow Q\bar{Q}, \quad q\bar{q} \longrightarrow Q\bar{Q}, \quad (2.11)$$

where the first process is predicted to be dominant with respect to the second by a factor 3-4 [25].

In this scheme the mass of the heavy quark is used to “regularize” the collinear divergences in the initial state and those due to the collinear emission from the quark itself, together with the other soft divergences which annihilate if both the real and virtual contributions are considered; in this way heavy quark production is associated only to the hard subprocess.

In heavy quark photoproduction at HERA, the use of this scheme absorbs the divergent mass terms like m_Q^2/P_T^2 . In fact in the mass perturbative expansion at high p_T , the terms like $\log(p_T^2/m_Q^2)$ become larger and the series diverges. So far it is still not clear at which scale these logarithmic terms become important, recent theories [26] indicating $P_T^2 \sim 25m_Q^2$. This means their contribution becomes non-negligible at ~ 7 GeV for the charm production, whilst for beauty this threshold is much larger, ~ 22 GeV, so it should be safe to neglect them. This scheme is not valid when the P_T involved is much larger than the mass of the quark, $P_T \gg m_Q$, in this case massless calculations are adopted (see next section). As beauty photoproduction is studied in this thesis, the quark mass provides an energy scale which is large enough (Q^2 and P_T in this case are not “competitive” scales) to allow perturbative calculations using a massive scheme.

2.5 Massless scheme

The massless scheme of Cacciari et al. [27] treats the heavy quark as an additional flavour component active above a certain threshold. Below this threshold, estimated as $\mu^2 \sim m_Q^2$, the quark remains an inactive flavour.

This scheme allows the fragmentation functions to be re-defined as a convolution

of a perturbative part $D^Q(x, \mu)$ which describes the fragmentation of a massless parton into a massive quark, and a non-perturbative part, which describes the transition from the heavy quark to the meson. For heavy flavours the terms $\log(p_T^2/m_Q^2)$ are re-absorbed in the perturbative part of the fragmentation functions. A larger number of resolved processes at LO with respect to the massive scheme has to be considered, such as $gQ \rightarrow gQ$, $qQ \rightarrow qQ$ processes, which are classified as flavour excitation processes (for an example see Fig. 2.1 c) d)). These processes are present in the massless scheme as part of the photon structure.

The fragmentation functions, D_k^Q , can be evaluated in perturbative QCD at the scale defined by the mass of the heavy quark and subsequently evolved up to the factorization scale through the DGLAP equations. They are given by:

$$D_Q^Q(x, \mu^2) = \delta(1-x) + \frac{\alpha_s(\mu)C_F}{2\pi} \left[\frac{1+x^2}{1-x} \left(\log \frac{\mu^2}{m^2} - 2 \log(1-x) - 1 \right) \right], \quad (2.12)$$

$$D_g^Q(x, \mu^2) = \frac{\alpha_s(\mu)T_F}{2\pi} (x^2 + (1-x)^2) \log \frac{\mu^2}{m^2}, \quad (2.13)$$

where the massive logarithms are contained in the fragmentation functions as previously mentioned. The colour factors which appear in the above formulae are $C_F = 4/3$ and $T_F = 1/2$ and the splitting functions from the light to heavy quarks are equal to zero. A comparison between the massive and massless schemes has been already performed [28] showing very similar results. Considering a fixed photon energy and HERA-like kinematics, the two components, direct and resolved, and their sum were separately compared (see Fig. 2.2). The sum of direct and resolved showed good agreement between the two calculations whereas the comparison of either the direct or the resolved process is not so good.

The charm and the beauty masses ($m_b, m_c \gg \Lambda_{QCD}$) provide energy scales which are large enough to allow perturbative calculations using a massive scheme. All QCD processes involving heavy quarks should thus be reliably calculable. However, these mass scales often compete with other scales occurring in the same process, such as the transverse momentum (P_T) of the heavy quarks, or the virtuality of the exchanged photon, Q^2 . Since the perturbative expansion cannot be optimized for all scales at once, additional theoretical uncertainties enter which reduce the reliability of the predictions. If one of the competing scales (P_T^2, Q^2) is much larger than the quark mass, approximations in which the heavy

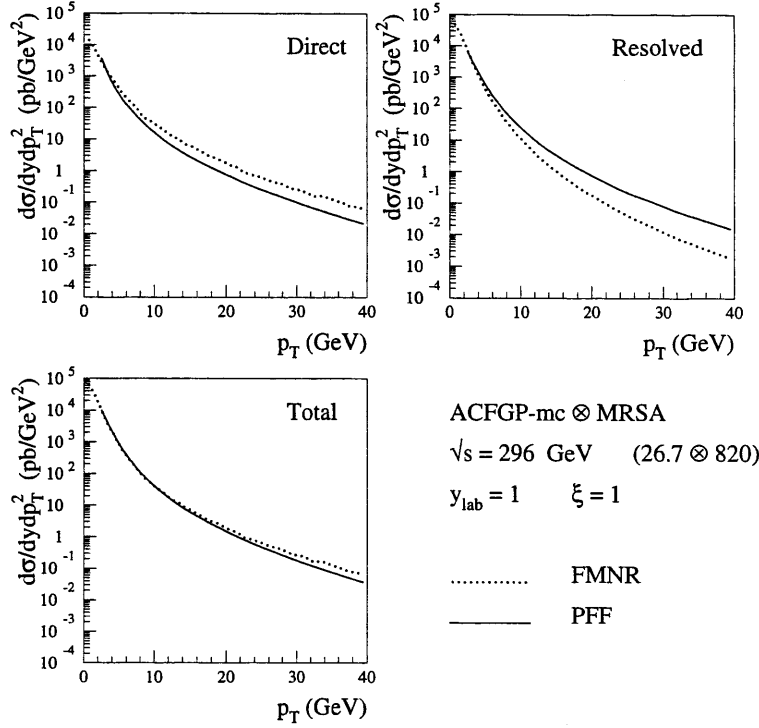


Figure 2.2: Comparison between massive (FMNR) and massless (PFF) scheme calculations for the differential cross section distribution versus the transverse momentum of charm in photoproduction, taken from [28], adopting HERA-like kinematics with fixed photon energy.

quarks are treated as massless can improve the reliability. Mixed schemes are also possible [29]. Understanding and resolving these difficulties should contribute to the understanding of multi-scale problems in general.

Both the massive and massless scheme calculations are available at NLO at HERA.

2.6 Beauty production in the global context

2.6.1 Fixed target experiments

A selection of beauty quark production measurements from fixed target experiments [30] is shown in Table 2.1.

The cross sections are compared to predictions from PYTHIA (see Chap. 5)

Exp.	Target(s)	$b\bar{b}$ evts	$\sigma(b\bar{b})$ in nb at 920 GeV	tag	phase space
p - A					
E789	Au	19	$8.1 \pm 2.2 \pm 1.9$	J/ψ	$0 < x_F^{J/\psi} < 0.1, P_T^{J/\psi} < 2 \text{ GeV}$
E771	Si	15	$61^{+38}_{-24} \pm 11$	J/ψ	$x_F < -0.25$
HERA-B	C, W	83	$14.4 \pm 2.2 \pm 2.3$	J/ψ	$-0.25 < x_F^{J/\psi} < 0.15$

Table 2.1: Collection of $b\bar{b}$ production cross sections at fixed target experiments (p - A) [30]; $x_F = p_{\text{parton}}/p_{\text{nucleon}}$ denotes the fractional momentum of the partons inside the nucleon.

using its default settings in pp collisions (see Fig. 2.3). In the figure the

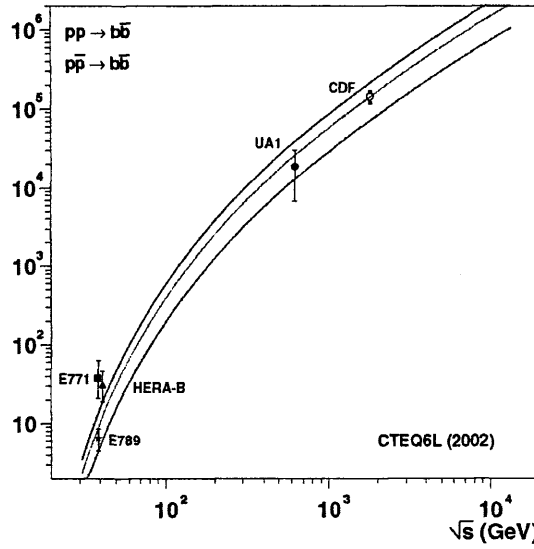


Figure 2.3: Cross section measurement (in nb) for $b\bar{b}$ from fixed target (see Table 2.1) and collision experiments as a function of the centre-of-mass energy \sqrt{s} . The measurements are compared to predictions from PYTHIA for $pp \rightarrow b\bar{b}$ with its default setting scaled up by an empirical factor of $k=1$, $k=2$, or $k=3$.

production cross section measurements presented belong to the complete picture of the investigation of the beauty quark and show how they developed covering the centre-of-mass energies from the fixed target regime up to $\sqrt{s}=1.8 \text{ TeV}$ in $p\bar{p}$ collisions. The prediction is scaled by an empirical factor which is varied between $k = 1$ and $k = 3$. The production of $b\bar{b}$ pairs in $p\bar{p}$ collisions at the quoted centre-of-mass energy is dominated by gluon-gluon-fusion processes and the valence quark distributions are less important. Therefore, the beauty quark cross sections measured in $p\bar{p}$ collisions can be compared to the predictions from

PYTHIA simulating pp collisions. A reasonable description of the measured cross sections is provided by PYTHIA over many order of magnitude.

2.6.2 Measurements at the $Spp\bar{S}$

The UA1 collaboration pioneered the measurement of beauty quark cross sections in single muon and dimuon events in $p\bar{p}$ collisions [31]. The UA1 detector was used to identify beauty quarks by their semileptonic decay into muons at the $Spp\bar{S}$ collider at CERN at a centre-of-mass energy of $\sqrt{s} = 630$ GeV. Muons were selected with a cut on the transverse momentum of the muon $P_T^\mu > 6$ GeV for single muons and $P_T^\mu > 3$ GeV for dimuons. The dimuon system was restricted to $m_{\mu\mu} < 35$ GeV and beauty quarks were identified using the P_T^{rel} method.

The measured single inclusive beauty quark cross section in a η range of $|\eta| < 1.5$ (Fig. 2.4) is compared to a next-to-leading order QCD prediction in the massive scheme [32] and found to be in good agreement.

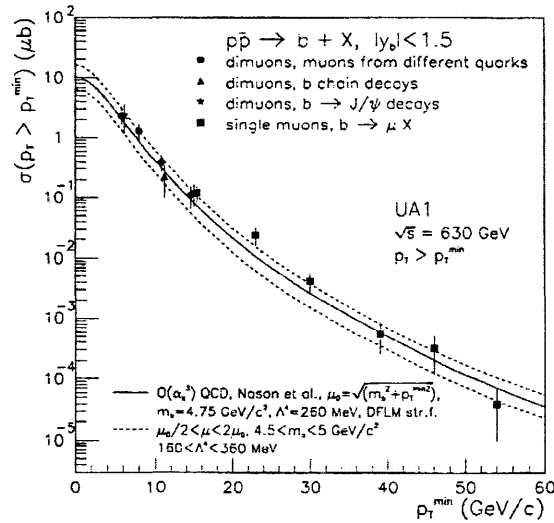


Figure 2.4: *Inclusive single beauty quark cross section for $|\eta| < 1.5$ and $P_T > P_T^{min}$ from UA1. Presented are the cross section measurements extracted from single muon events and dimuon events originating from different beauty quarks and from beauty chain decays as well as measurements extracted from single muon events originating from J/ψ from beauty quarks and the comparison to a next-to-leading order calculation [32].*

The cross sections extracted using single muons from beauty quark events, as well as dimuon events from subsequent J/ψ decays [33] are also well described by the

NLO calculation.

2.6.3 Measurements at the Tevatron

Studying heavy flavour production is a very active research topic for the CDF and D0 experiments at the Tevatron $p\bar{p}$ collider at Fermilab. The CDF and D0 groups measured the cross section for the process $p\bar{p} \rightarrow b + X$ using Run-I data and obtaining results above the NLO QCD predictions [34, 35, 36]. Since then new data from Run-II have become available (a factor four higher in luminosity) and many theoretical developments have been introduced, including full NLO calculations, resummation of $\log(P_T/m_b)$ terms, substantial changes in the fragmentation functions and improved parton density functions. Comparison of this new theory (*FONLL* [37]) with Run-II data at CDF [38] has shown a good agreement as can be seen in Fig. 2.5. In the same figure the data set was also compared with the *MC@NLO* [39] predictions, a Herwig-based programme which combines NLO QCD calculations with parton shower Monte Carlo; a good agreement was also observed in this case.

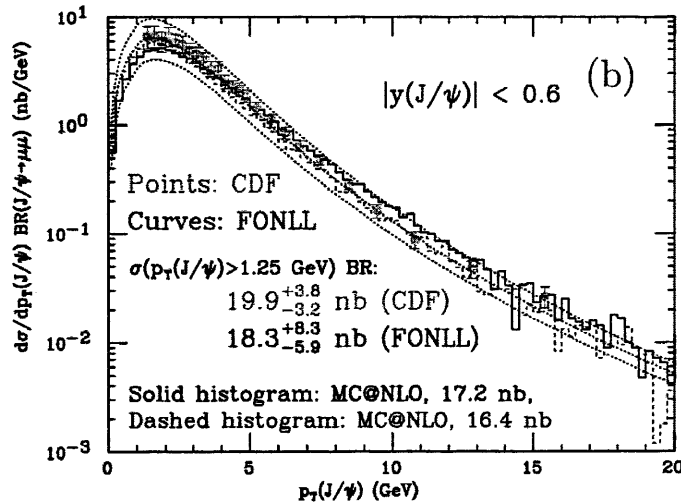


Figure 2.5: Cross section as a function of the transverse momentum of the beauty quark measured at CDF; the recent *MC@NLO* and *FONLL* theoretical results are also shown [38].

2.6.4 $\gamma\gamma$ interactions

The production of beauty has also been studied with the L3 and OPAL detectors at the LEP collider; the latest L3 results refer to a data sample corresponding to an integrated luminosity of 627 pb^{-1} in a centre-of-mass energy range between 189 GeV and 209 GeV (LEP-II data) [2]. Hadronic states containing beauty (and charm) quarks were isolated by tagging electrons and muons originating from their semileptonic decay. The cross section was measured by exploiting the spectra of the muon and the electron transverse momentum with respect to the nearest jet axis; only leptons with momentum higher than 2 GeV were considered (in the muon case this requirement relies on the fact that these particles must have a momentum which allows them to penetrate the calorimeter and reach the muon chambers). The resulting cross sections are:

$$\sigma(e^+e^- \longrightarrow e^+e^-b\bar{b}X)_{\text{muons}} = 13.0 \pm 2.4(\text{stat.}) \pm 2.3(\text{syst.})\text{pb}$$

$$\sigma(e^+e^- \longrightarrow e^+e^-b\bar{b}X)_{\text{electrons}} = 12.6 \pm 2.4(\text{stat.}) \pm 2.3(\text{syst.})\text{pb}$$

The combination of the results using muons and electrons yields the value:

$$\sigma(e^+e^- \longrightarrow e^+e^-b\bar{b}X)_{\text{combined}} = 12.8 \pm 1.7(\text{stat.}) \pm 2.3(\text{syst.})\text{pb}$$

In Fig. 2.6 NLO QCD predictions are also shown and it can be seen that the measurements are higher than the prediction by around 3-4 standard deviations. This is a particularly surprising result as a large part of the cross section, $\gamma\gamma \rightarrow b\bar{b}$, is precisely predicted by QED theory.

2.7 Beauty results at HERA

2.7.1 Beauty photoproduction from semileptonic decays to muons

Both the ZEUS and H1 collaborations have published measurements of b quark production in the photoproduction regime [40] [41] ; the most recent ZEUS results are b production cross section measurements obtained selecting two jets plus μ

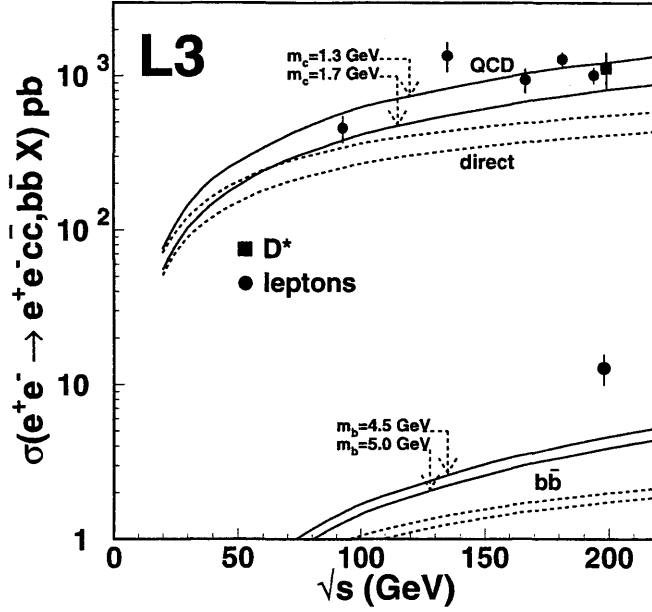


Figure 2.6: *Beauty and charm production cross section measured by L3 at LEP. In the figure the NLO QCD prediction results are also shown.*

events [42].

$$e^+ + p \rightarrow \text{dijet } \mu^\pm X.$$

The fraction of events originating from beauty was extracted using the P_T^{rel} method, in the kinematic region defined by:

$$Q^2 < 1 \text{ GeV}^2,$$

$$0.2 < y < 0.8,$$

$$P_T^{jet1(2)} > 7(6) \text{ GeV},$$

$$|\eta^{jet1(2)}| < 2.5,$$

$$P_T^\mu > 2.5 \text{ GeV},$$

$$-1.6 < \eta^\mu < 2.3,$$

where y is the inelasticity, P_T^{jet} is the jet transverse momentum, $\eta^{jet1(2)}$ is the jet pseudorapidity, and P_T^μ and η^μ are the transverse momentum and the

pseudorapidity of the muon (shown in Fig. 2.7). The H1 collaboration has made similar measurements supplementing the P_T^{rel} method with the impact parameter method; Fig. 2.8 shows the comparison between the differential cross sections (with respect to η^μ and P_T^μ variables) and the QCD predictions considering similar phase space regions.

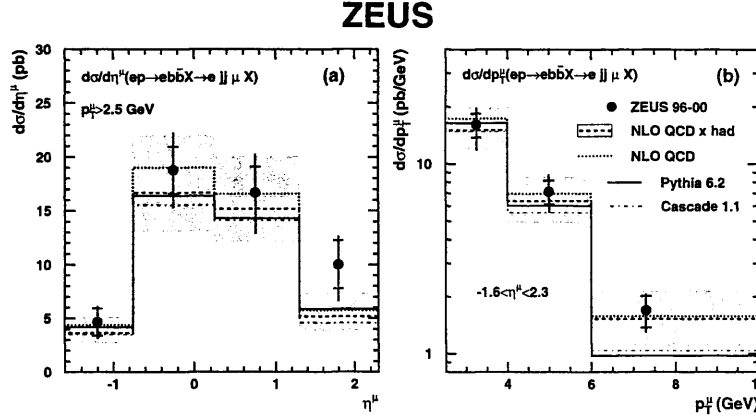


Figure 2.7: Beauty production differential cross sections as a function of the muon pseudorapidity η^μ and of the muon transverse momentum, P_T^μ measured at ZEUS [42]. The 96-00 data are compared with PYTHIA and CASCADE Monte Carlo models and with NLO QCD predictions.

These predictions are based on fixed order perturbative calculations, which implement the FMNR program [23], with hadronization modelled by the Peterson function.

The results from both collaborations are in good agreement with the theoretical predictions although the H1 results are generally higher by around 40% (although still compatible within the theoretical uncertainties and the experimental errors). In Fig. 2.9 the differential cross section is plotted as a function of the variable x_γ^{jets} , defined as the $E - p_z$ fraction of the hadronic system carried by the two jets with highest P_T :

$$x_\gamma^{jets} = \frac{(E - p_z)_{jet1} + (E - p_z)_{jet2}}{(E - p_z)_h}.$$

The importance of this variable is due to the fact that at LO in QCD, x_γ^{meas} is the photon energy fraction which takes part in the hard process: events with *direct* photons are characterized by a $x_\gamma^{meas} \simeq 1$, whilst *resolved* events populate the

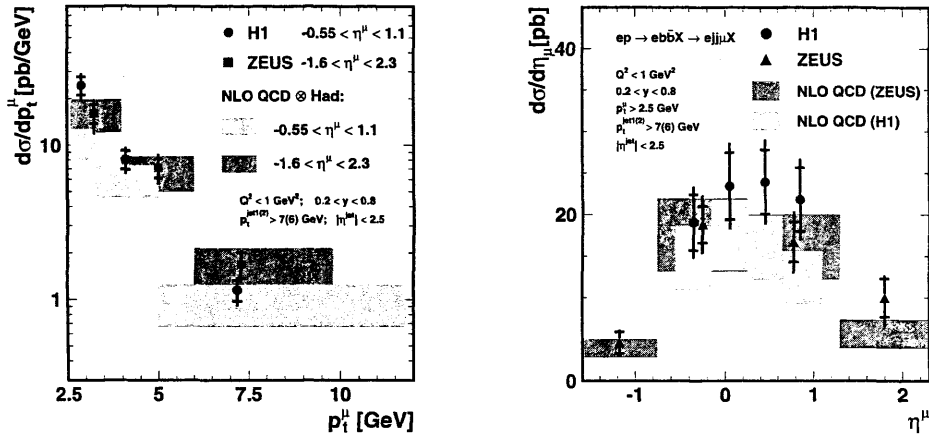


Figure 2.8: Comparison of the beauty production differential cross sections as a function of the muon pseudorapidity η^μ and of the muon transverse momentum, P_T^μ , obtained by ZEUS and H1. Slightly different pseudorapidity regions and theoretical NLO QCD predictions were adopted by the two experiments as reported in the figure. The bars on the NLO predictions show the results obtained varying the b mass between 4.5 GeV and 5.0 GeV and the renormalization and factorization scales between $m_T/2$ and $2m_T$, where $m_T = \sqrt{P_T^2 + m_b^2}$.

regions at low x_γ^{meas} (see section 1.9).

Using the PYTHIA Monte Carlo [43] to extrapolate the cross sections for the part not covered by the muon measurement and for the branching ratio, the cross section was calculated for the reaction:

$$e^+ + p \rightarrow b \bar{b} X \rightarrow \text{jet jet } X.$$

In this case $\sigma^{dijet} = 733 \pm 61 \pm 104$ pb, which is larger by a factor 2 than the prediction $\sigma^{NLOQCD} = 381_{-78}^{+117}$ pb. This demonstrates that further studies are needed in order to investigate the origin of this 2σ discrepancy. In particular a wider muon phase space and/or more inclusive measurements are desirable.

2.7.2 Beauty production in DIS

Results on b production in the DIS kinematic region have been produced by the H1 [44] and ZEUS [45] collaborations. In ZEUS the events have been selected

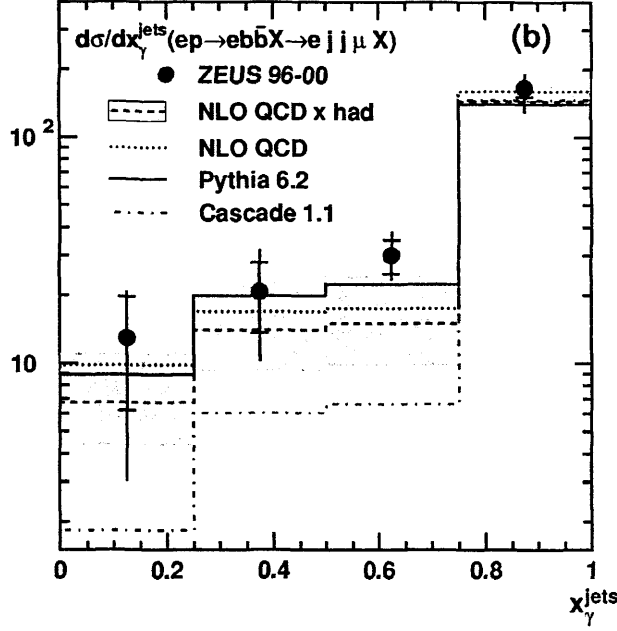


Figure 2.9: Differential cross section as a function of x_{jets} measured by ZEUS [42]. The muon spectrum (obtained with PYTHIA) was used to extrapolate the observable cross section to the process $ep \rightarrow \text{dijet } \mu^\pm X$.

considering a muon in the final state and a jet in the Breit frame¹. A visible cross section $\sigma^{vis} = 40.9 \pm 5.7^{+6.0}_{-4.4}$ pb was measured for the process:

$$e + p \rightarrow e b \bar{b} X \longrightarrow e \text{ jet } \mu X$$

in the kinematic region :

$$Q^2 > 2 \text{ GeV}^2,$$

$$0.05 < y < 0.7, P^\mu > 2 \text{ GeV}$$

$$30^\circ < \theta^\mu < 160^\circ$$

and a jet in the Breit frame with $E_T^{Breit} > 6 \text{ GeV}$ and $-2 < \eta^{LAB} < 2.5$, where θ^μ is the polar angle of the muon track, E_T^{Breit} is the jet transverse energy and η^{LAB}

¹In the Breit frame, defined by $\vec{\gamma} + 2x\vec{P} = \vec{0}$, where $\vec{\gamma}$ is the momentum of the exchanged photon, x is the Bjorken scaling variable and \vec{P} is the proton momentum, a space-like photon collides “head-to-head” with a proton. In the quark-parton model, a DIS interaction $\gamma^* q \rightarrow q$ does not have any jet in the Breit frame.

is the pseudorapidity calculated in the lab frame. Again the method used was the P_T^{rel} one and the results were compared with the massive NLO QCD predictions obtained implementing the HVQDIS program [46](Fig. 2.10 a)).

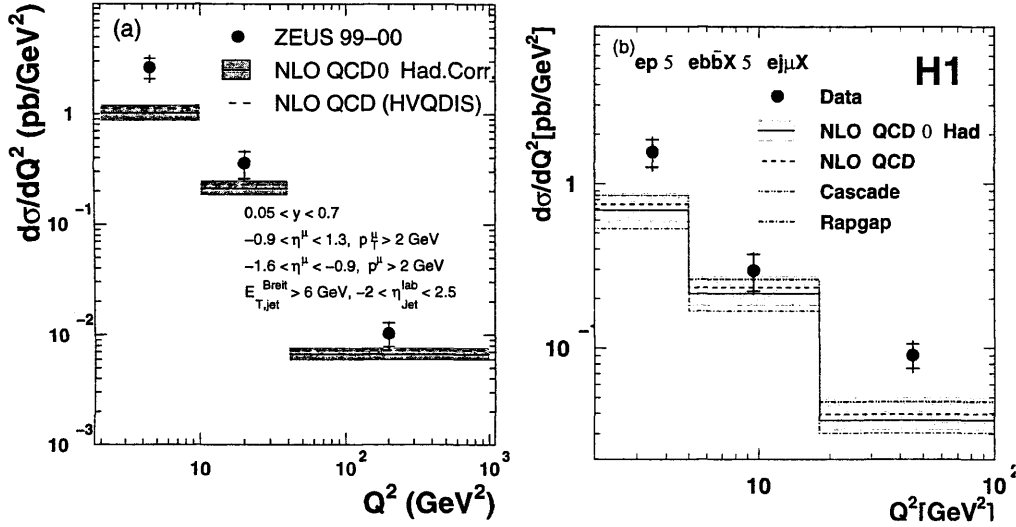


Figure 2.10: Differential cross section as a function of Q^2 measured at (a) ZEUS and (b) H1 in DIS events [45] [44]. Data are compared in both cases with NLO QCD predictions.

The Peterson fragmentation function was used for the b fragmentation to a meson whilst the muon momentum spectrum was extracted using the RAPGAP Monte Carlo ² [47]. Figure 2.10 b) shows the differential cross section as a function of Q^2 obtained by H1; the data are compared with NLO QCD calculations and MC predictions. For both the collaborations general agreement with the experimental values, within the errors, can be observed even if a discrepancy at low Q^2 is noticeable.

2.7.3 Lifetime tagging

H1 has recently measured charm and beauty cross sections using a fit to the lifetime signature of charged particles in jets [48]. This inclusive method yields measurements of differential cross sections that extend to larger values of transverse momenta than in previous HERA analyses in which leptons from

²A Monte Carlo program which simulates both resolved and direct events; it uses the Lund string model for the hadronization phase (see Chapt. 5).

beauty quark decays were used to measure beauty cross sections. Events with two jets in the final state are selected to measure the photoproduction dijet charm or beauty cross section:

$$\sigma(e^+p \rightarrow e^+ (c\bar{c} \text{ or } b\bar{b}) X \rightarrow e^+ + jj + X).$$

The jets are required to have a large transverse momentum, $P_t^{jet(1)2} > 11,8 \text{ GeV}$, considering a central pseudorapidity range $-0.88 < \eta < 1.3$, with $0.15 < y < 0.8$ and $Q^2 < 1 \text{ GeV}^2$. An inclusive sample of tracks with $P_T > 500 \text{ MeV}$ was selected thus obtaining a larger sample to study with respect to a reconstructed D meson or lepton analysis. In order to discriminate between signal and background, two different significances were calculated for these tracks:

- significance of the track associated to a jet in an event where only 1 track was associated to the jet (S1 distribution in Fig. 2.11 right)
- significance of the second highest significance track in event with at least 2 tracks associated to the jet (S2 distribution in Fig. 2.11 left).

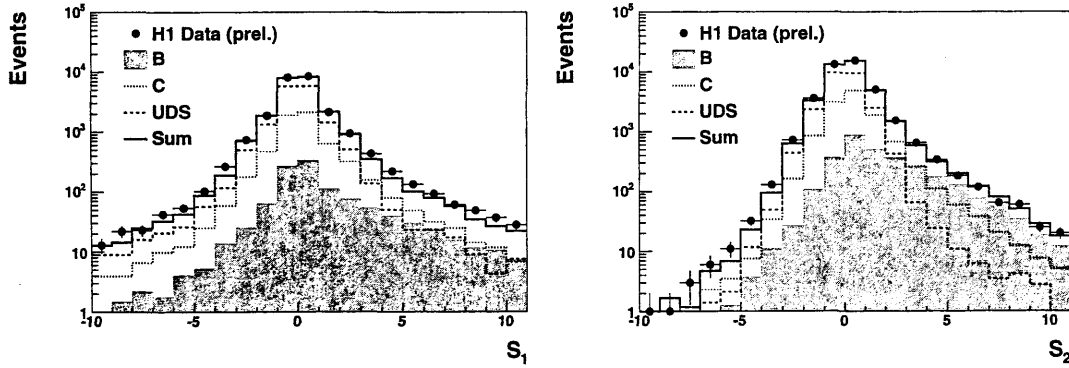


Figure 2.11: *Significance distributions using the b , c and uds -fractions from the fit to the subtracted significance distributions of the data [48]. S_1 of tracks (left) in jets with exactly one track, S_2 of tracks (right) with the second highest significance in jets with two or more tracks are shown.*

The b and c fractions were extracted fitting the subtracted significance distributions.

In Fig. 2.12 the differential cross sections as a function of the P_T and pseudorapidity η of the leading jet are shown. The main difference between the

beauty data and NLO QCD predictions is observable in the positive rapidity and low P_T region where large contributions to the cross sections from resolved photon events are expected. The Monte Carlo generators PYTHIA and CASCADE [49] describe the shape of the charm and beauty data. However, for beauty the PYTHIA(CASCADE) predictions fall below in normalization by a factor ~ 1.8 (~ 1.6).

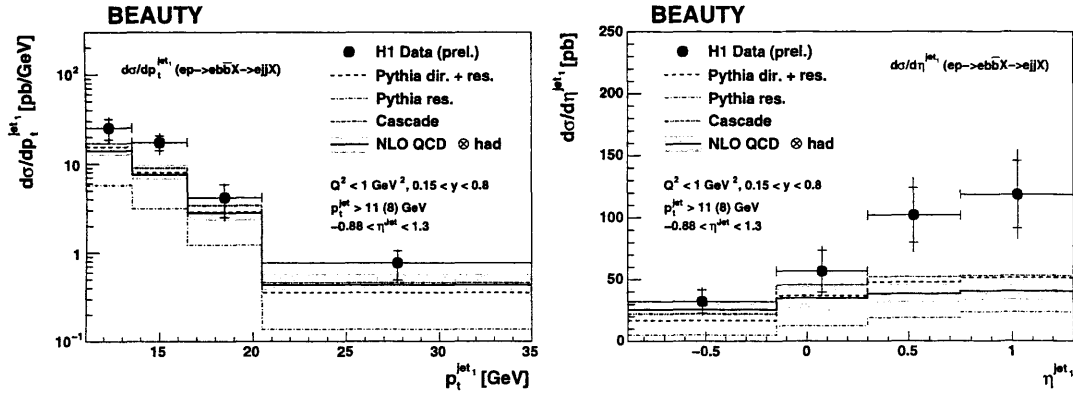


Figure 2.12: Differential beauty cross sections as a function of transverse momentum P_T^{jet} (a) and the pseudorapidity η^{jet} (b) of the leading jet [48].

2.7.4 Double tagging of beauty: $D^* - \mu$ correlations and dimuon studies

Recent results were published by both H1 [50] and ZEUS [51, 52] using $D^* + \mu$ and dimuon (only ZEUS) samples, studying the processes:

$$e + p \rightarrow b \bar{b} X \longrightarrow \mu^- \mu^+ X \text{ and} \quad (2.14)$$

$$e + p \rightarrow b \bar{b} X \longrightarrow D^* \mu^- X. \quad (2.15)$$

These analyses are characterised by a low background due to the requirement of a double tag in the final state. For the dimuon channel, the separation of the sample into high and low mass, isolated and non isolated, like and unlike sign muon pairs further improves the signal to background ratio.

Due to the low P_T threshold for muon identification and to the large rapidity cov-

erage offered by the ZEUS muon system, an almost full phase space for beauty production is covered allowing a direct measurement of the total $b\bar{b}$ cross section without applying any cuts [52].

In Fig.2.13 a) the spectrum of the muon momentum P_T^μ obtained by ZEUS using a dimuon sample is shown where all the different background contributions are shown. Charm pair production contributes to the unlike sign muon sample only and was estimated from the $D^* + \mu$ analysis whilst fake muon background was removed by taking the difference between like-sign and unlike-sign samples (the light flavour contribution cancels out). The remainder is the beauty signal.

The visible cross section obtained is $\sigma^{vis} = 63.0 \pm 7.0^{+20.2}_{-17.6}$ pb. Fig.2.13 b) shows

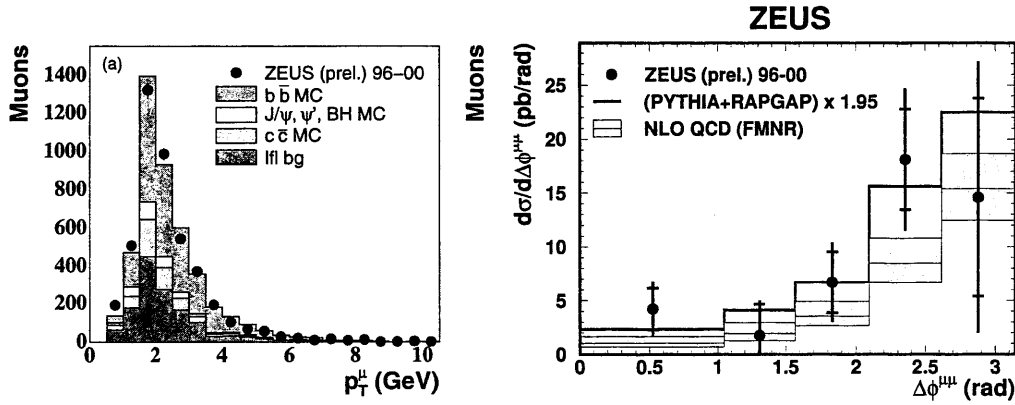


Figure 2.13: Muon transverse momentum distribution (a) for both high and low mass dimuon pairs in the non isolated unlike sign sample [52]. Two muons are entered for each event. The breakdown into the expected contributions from different processes is also shown. In (b) the cross section $d\sigma/d\Delta\phi^{\mu\mu}$ for dimuon events from $b\bar{b}$ decays in which each muon originates from different $b(\bar{b})$ quarks [52]; the data (solid dots) are compared to the scaled sum of the predictions by the leading order plus parton shower (LO+PS) generators PYTHIA and RAPGAP (histogram) and the NLO prediction from FMNR (band).

the differential cross section with respect to the azimuthal distance between the muons $\Delta\phi_{\mu\mu}$ requiring $-2.2 < \eta < 2.5$ and $P_T^\mu > 1.5$ GeV. At the true level the muons were required to originate from different beauty quarks whilst at the reconstruction level a cut on the mass $m_{\mu\mu} > 3.5$ GeV was applied.

The separation of the beauty from the charm signal can be performed also by analysing the angular and charge correlations of the D^* mesons with respect to

the muons in the process 2.15.

Of particular interest is the configuration in which the muon and the D^* originate from the same B meson yielding opposite charged $D^* - \mu$ pairs inside the same hemisphere. Using the same strategy and considering a kinematic domain very similar to that of ZEUS, H1 extracted cross sections for beauty and charm production [50]; the measured values confirm the previous results overshooting the Monte Carlo model predictions based on LO calculations followed by a parton shower.

ZEUS measured the cross section $\sigma_b^{vis} = 214 \pm 52^{+96}_{-84}$ pb, in the kinematic domain ($P_T^{D^*} > 1.9$ GeV, $|\eta^{D^*}| < 1.5$, $P_T^\mu > 1.4$ GeV, $-1.75 < \eta^\mu < 1.3$); this is in good agreement with the H1 results ($\sigma_b^{vis} = 206 \pm 53 \pm 35$ pb, analogous kinematic domain).

Fig. 2.14 shows a summary of the latest cross section measurements obtained by both the experiments using double-tagging techniques.

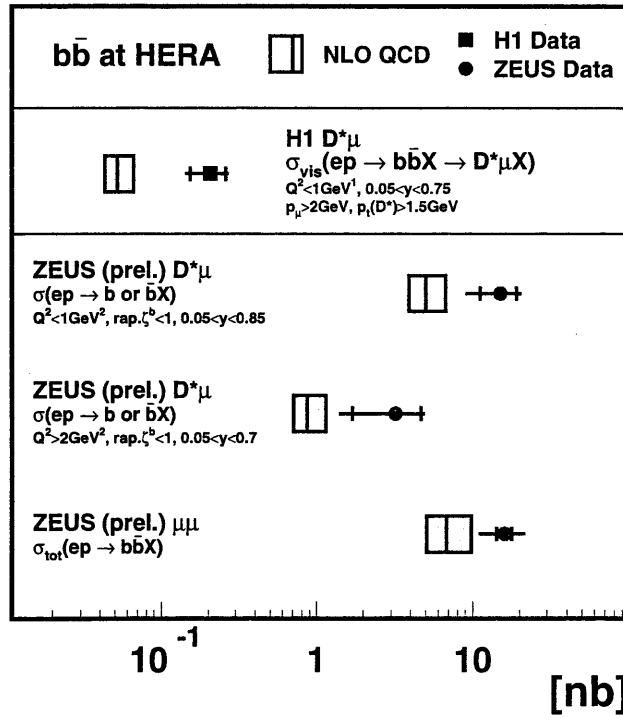


Figure 2.14: Summary of all the latest cross section measurements using double tagging techniques obtained by ZEUS and H1. The measurements are compared to NLO QCD predictions.

In Fig. 2.15 all the measurements available so far for the b production at HERA

are plotted in terms of the ratio measurement/theory; the shown results exploit different kinds of extrapolations.

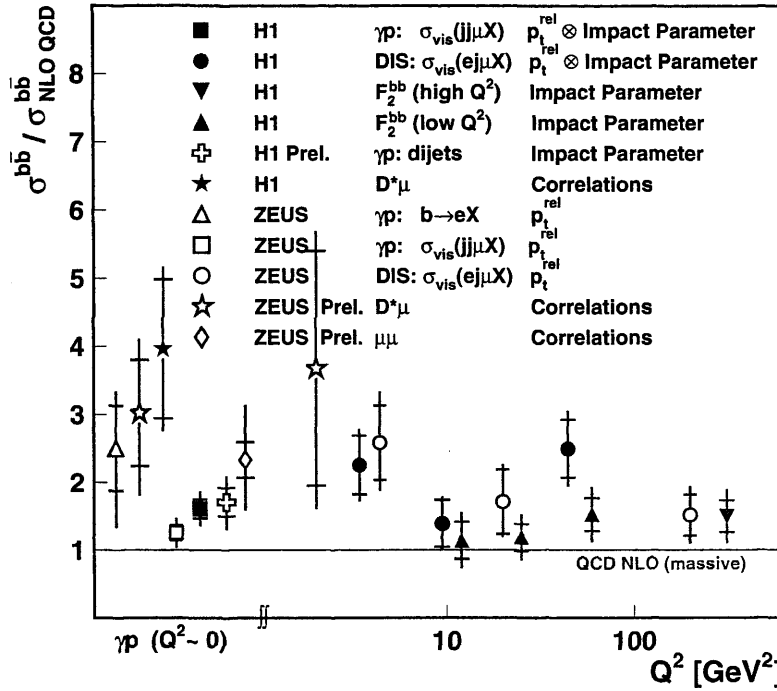


Figure 2.15: Summary of the ZEUS and H1 cross section measurements. The ratio DATA/NLO as a function of Q^2 is shown.

In general we can observe that, while the visible cross sections are in good agreement with the predictions, this agreement is getting worse every time an extrapolation is involved. Both in the partonic extrapolation, where the corresponding correction factors are extracted from Monte Carlo, and in the case of an extrapolation to a kinematic region not covered by measurements, the ratio data/NLO ~ 2 .

Chapter 3

HERA and the ZEUS detector

In this chapter the HERA accelerator and the ZEUS detector are described briefly, giving particular emphasis on the parts of the detector used in the analysis described in this thesis. A detailed description of the ZEUS detector can be found in [54].

3.1 The HERA collider

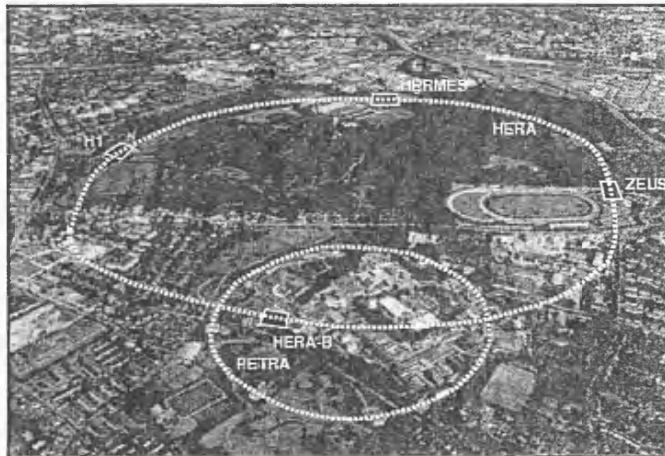


Figure 3.1: *The Hamburg Volkspark showing the DESY site. The location of the HERA and PETRA rings are shown. Also illustrated are the locations of the two colliding-beam experiments, ZEUS and H1, together with the single-beam experiments HERMES and HERA-B.*

The HERA (Hadron Elektron Ring Anlage) collider is a unique particle accelerator for the study of high-energy electron-proton (ep) collisions [55]. It is located at the DESY (Deutsches Elektronen SYnchrotron) laboratory in Hamburg, Germany, and has been in operation since 1992. The HERA ring is located 15-30 m under ground level and has a circumference of 6.3 km. Fig 3.1 shows an aerial view of the tunnel area in Hamburg and the position of the different experiment halls (the ring has 4 linear sections linked at their extremities by 4 arcs of 779 m radius.)

The HERA machine collides electrons and positrons, accelerated to an energy of 27.5 GeV, with 820 (920) GeV protons (the energy of the proton beam was changed at the beginning of 1998 from 820 to 920 GeV). The resulting centre-of-mass energy is 300 (318) GeV, more than an order of magnitude higher than previous fixed-target lepton-nucleon experiments, allowing a new and wider kinematic region in x and Q^2 to be explored.

Four experiments are located in four experimental halls placed along the HERA ring (Fig. 3.1). The two beams are brought into collision every 96 ns at zero crossing angle at two interaction points, one in the North Hall where the H1 experiment is located, the other in the South Hall where the ZEUS experiment is placed. In the East Hall the Hermes experiment studies the spin structure of the nucleon using the collisions of longitudinally polarized leptons on an internally polarized gas target (H, ^2D or ^3He). The HERA-B experiment, located in the West Hall was used until 2003 to collide the proton beam halo with a wire target to study B-meson production.

Built between 1984 and 1990, the HERA collider started operation in 1992 in its initial configuration with 820 GeV protons and 26.7 GeV electrons. In 1994 it was realized that the electron beam current was limited by positively ionized dust particles in the beam pipe through the pumps, reducing the lifetime of the beam. For this reason HERA switched to positrons in July 1994, achieving a more stable lepton beam and a significant increase in the integrated luminosity of the collected data. During the 1997-98 shutdown period, new pumps were installed in the lepton beam to improve the electron beam lifetime, and during 1998 and part of 1999 HERA was run again with electrons. In 1998 the energy of the proton beam was raised from 820 to 920 GeV, switching back to positron-proton

Running period	1993-1997		1998-2000		2003-2004	
Luminosity	$1.6 \cdot 10^{31} \text{ cm}^{-2} \text{ s}^{-1}$		$1.6 \cdot 10^{31} \text{ cm}^{-2} \text{ s}^{-1}$		$7.0 \cdot 10^{31} \text{ cm}^{-2} \text{ s}^{-1}$	
Center-of-mass energy	300 GeV		318 GeV		318 GeV	
	lepton	proton	lepton	proton	lepton	proton
Energy (actual)	27.5 GeV	820 GeV	27.5 GeV	920 GeV	27.5 GeV	920 GeV
Max number of bunches	210	210	210	210	180	180
Beam current	58	163	58	163	58	140
Particles per bunch	$3.65 \cdot 10^{10}$	10^{11}	$3.65 \cdot 10^{10}$	10^{11}	$4.18 \cdot 10^{10}$	10^{11}
Beam width (σ_x)	0.286 mm	0.280 mm	0.286 mm	0.280 mm	0.118 mm	0.118 mm
Beam height (σ_y)	0.060 mm	0.058 mm	0.060 mm	0.058 mm	0.032 mm	0.032 mm

Table 3.1: *HERA design parameters [59][60].*

collisions in 1999.

Although a lot of interesting measurements have already been performed at HERA, the desire was expressed by the experiments for an increase in the luminosity. The motivations for this increase were studied in a one-year workshop held between 1995 and 1996, when it was concluded that having $\sim 1 \text{ fb}^{-1}$ of integrated luminosity would open up the possibility of new interesting measurements [56].

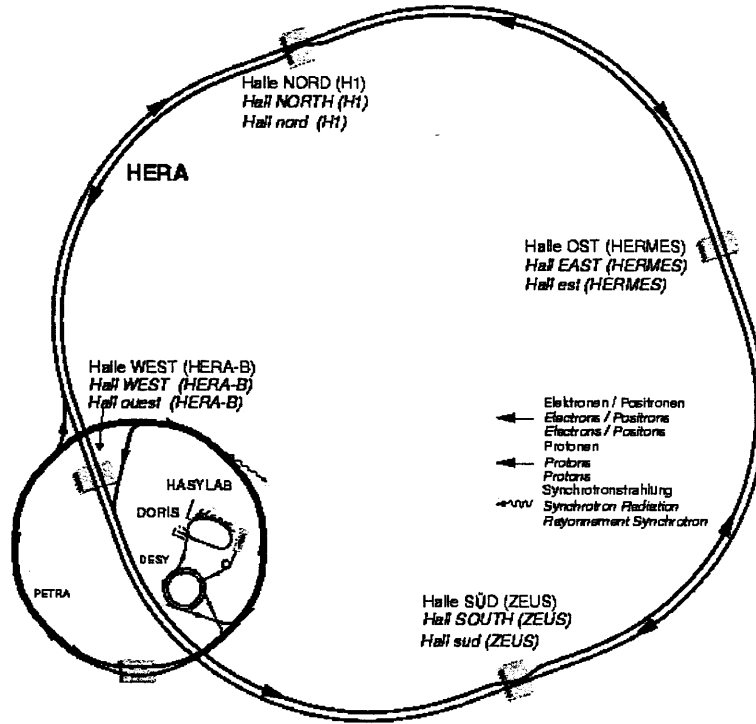
During the shutdown 2000/2001, the HERA collider was upgraded to achieve a five times higher specific luminosity at the collision point [57]. In addition spin rotators were included to rotate the spin of the leptons such that the lepton beam is longitudinally polarized at all interaction regions. A further longer shutdown was necessary in the middle of 2003 to solve severe background problems [58]. Since October 2003, HERA provided stable beam operations and delivered a total luminosity of 290 pb^{-1} .

A summary of HERA design parameters during the running periods 1993-1997 and 1998-2000 and 2003-2004 can be found in Table 3.1.

3.1.1 The HERA injection system

HERA provides two different injection systems for the beams, shown in Fig. 3.2.

The proton acceleration chain starts with negative hydrogen ions (H^-) accelerated in a LINAC to 50 MeV. The electrons are then stripped off the H^- ions to obtain protons, which are injected into the proton synchrotron DESY III and accelerated up to 7.5 GeV in 11 bunches with a temporal gap of 96 ns, the same as the main HERA ring; these bunches are then transferred to PETRA, where

Figure 3.2: *HERA injection system.*

they are accelerated to 40 GeV. Finally they are injected into the HERA proton storage ring, and the injection stops when the ring contains 210 bunches. Through the radiofrequency generated in resonant cavities, the proton beam is then accelerated up to 920 GeV.

Pre-acceleration of the electrons (positrons) starts in two cascaded linear accelerators, LINAC I and LINAC II, where the leptons are accelerated up to 250 and 450 MeV respectively. The leptons are then injected into DESY II, accelerated to 7.5 GeV and then transferred to PETRA II, where they reach an energy of 14 GeV in bunches separated by 96 ns gaps. They are then injected into HERA where they reach the nominal lepton beam energy of 27.5 GeV, again until the main ring is filled with 210 bunches. Some of these bunches are kept empty (pilot bunches) in order to study the background conditions. When either the lepton or the proton bunch is empty, the beam related background, originating from the interaction of the lepton or the proton beam with the residual gas in the beam pipe, can be studied, whereas when both the bunches are empty the

non-beam-related background, such as cosmic ray rates, can be estimated.

3.2 The HERA luminosity upgrade

HERA started delivering data in June 1992. Since then the luminosity has continuously increased, as shown in Fig. 3.3.

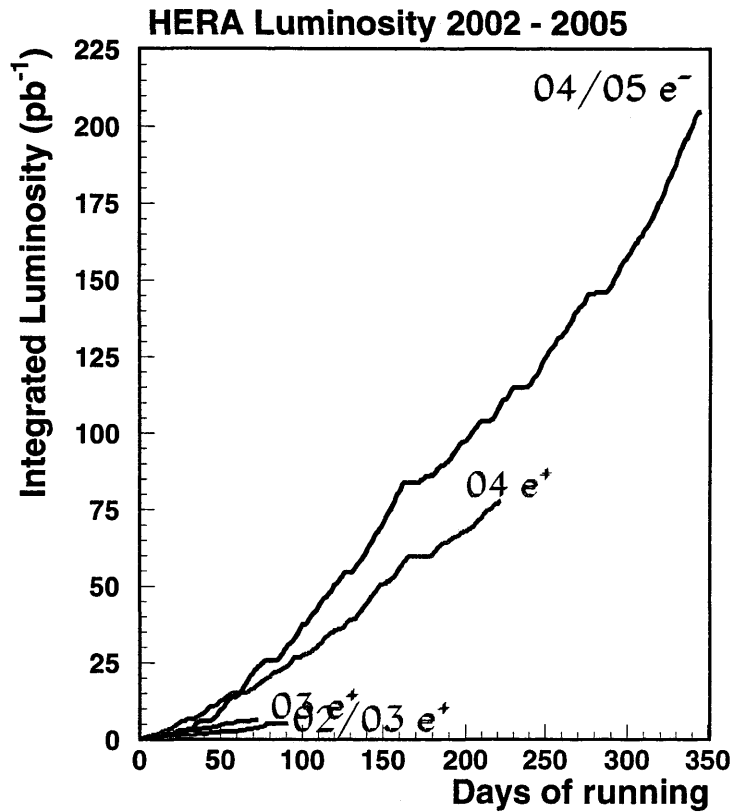


Figure 3.3: *HERA integrated luminosity.*

The data collected so far were used to explore the proton structure and to test more and more precisely QCD theory; nevertheless the physics studied so far was predominantly low- Q^2 physics relative to the electroweak scale $Q^2 = m_W^2$. HERA was built to also explore this energetic region since phenomena such as the electron polarization and the capability to compare electron and positron running becomes relevant only in the electroweak regime. With the luminosity upgrade new and important tests will be carried out to study the electroweak and strong interactions. Moreover, new phenomena which go beyond the standard

model will be investigated; luminosity of the order of an inverse femtobarn will allow the search for particle states in an unexplored kinematic region above 200 GeV. The F_2 structure function will be more precisely measured, allowing the extraction of a gluonic density with a precision of 1%, which will allow more efficient testing of the validity of the QCD evolution equations over a large range in x and Q^2 . Moreover the HERA capability to use both electron and positron beams will allow the determination of F_3 , and hence the distribution of the valence quarks inside the proton. Studies of diffraction will significantly improve with the larger statistics available. Jet studies will be performed at high E_T allowing α_s measurements at different scales. Also important is the possibility of obtaining more precise measurements of the cross sections which can be calculated through QCD, providing a good test for this theory.

At HERA the luminosity is effectively defined as:

$$L = \frac{I_e \cdot N_p \cdot \gamma_p}{4\pi e \epsilon_N \sqrt{\beta_{xp}^* \beta_{yp}^*}} \quad (3.1)$$

where I_e represents the total leptonic current (only considering the colliding bunches), N_p is the number of protons in each bunch, ϵ_N is the normalized emittance of the proton beam, γ_p is the Lorentz factor for the protons, e is the elementary charge, while β_{xp}^* and β_{yp}^* are the horizontal and vertical beta functions at the interaction point.

Increasing the intensities of the beams to substantially improve the luminosity would have required a huge financial cost (the currents of the leptonic beam could only have been incremented increasing in an almost proportional way the power of the radiofrequency cavity). Rather the luminosity was increased by making the interaction cross-section smaller by reducing the beta functions at the interaction point. These functions are limited by chromatic effects and limitations on the “opening” of the low beta quadrupoles. In order to increase the luminosity up to $\sim 7.4 \cdot 10^{-31} \text{cm}^{-2} \text{sec}^{-1}$ new superconducting magnets [61] close to the interaction point (inside the calorimeter volume), absorption system for the synchrotron radiation and for the vacuum were installed in the interaction region.

During the break, planned in order to upgrade the accelerator, the Micro Vertex Detector (MVD) was positioned inside the cavity between the beam pipe and the inner wall of the Central Tracking Detector (CTD).

3.3 The ZEUS detector

ZEUS is a multi-purpose, magnetic detector designed to study electron/positron-proton collisions. It measures $12 \times 10 \times 19 \text{ m}^3$, weighs 3600 tonnes and it is quasi-hermetic covering most of the 4π solid angle, with the exception of the small region around the beam pipe.

As a result of the asymmetric beam energies, most of the final state particles are boosted in the proton beam direction. Consequently, the sub-detectors of ZEUS are coaxial but asymmetric with respect to the interaction point. The detector can measure energies from a few tens of MeV to hundreds of GeV in the forward region. For low momentum particles the tracking in the magnetic field is very precise, while high energy particles are well measured by the calorimetric system (see sections 3.4 and 3.5).

Particle identification is needed in a wide momentum range to achieve the physics goals. In Neutral Current (NC) DIS events the scattered lepton has to be identified and measured with high precision and the identification of electrons, positrons and muons is also needed in order to study the semi-leptonic decay of heavy quarks and exotic processes involving leptons.

In Charged Current (CC) DIS processes a hermetic detector is needed in order to reconstruct the missing transverse momentum carried by the outgoing neutrino. In these kinds of events, and also in untagged photoproduction events, the precise reconstruction of the final state is important in order to determine the event kinematics.

The ZEUS coordinate system is a right-handed, cartesian system with the origin defined as the nominal Interaction Point (IP) ¹. The positive z -axis points in the direction of the proton beam and is often referred to as the “forward” region. The x -axis points from the IP towards the centre of HERA ring and the y -axis lies at 90° to the other two axes and points approximately vertically upwards. Since the proton-beam axis has a slight tilt, the y -axis does not precisely coincide with the vertical. The actual IP varies from event to event, and the run average and proton tilt varies on a fill-by-fill basis (see Chapter 8). However, the nominal IP is close to the geometric centre of the detector.

Polar angles are defined with respect to the proton-beam direction in the forward

¹ $x = y = 0$, defined in ZEUS by the geometrical centre of the central tracking detector, and $z = 0$ defines the nominal IP [62]

region ($\theta = 0$) and the leptonic-beam is therefore at $\theta = \pi$. The azimuthal angles ϕ are measured with respect to the x -axis.

The pseudorapidity variable is often used in event analysis; this quantity is an approximation at high energies of the particle rapidity given by $y = \log \frac{E+P_z}{E-P_z}$, and is defined by $\eta = -\log(\tan \frac{\theta}{2})$, where θ is the polar angle. The ZEUS coordinate system is illustrated in Fig. 3.4.

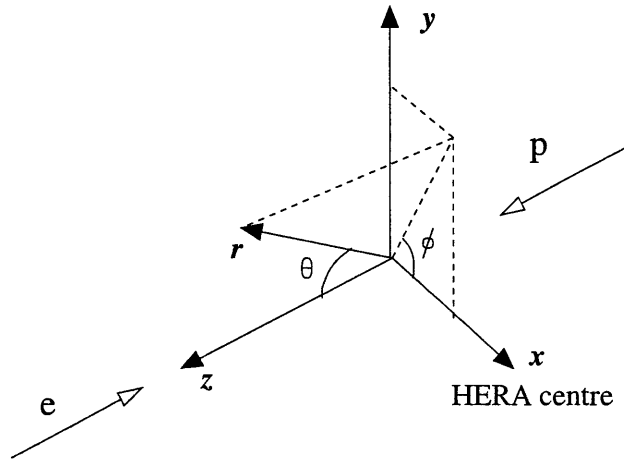


Figure 3.4: ZEUS coordinate system.

A brief outline of the various detector components is given below and a more detailed description of the sub-detectors relevant to the present analysis will be given later in this chapter. A complete description of ZEUS and its components can be found in [54]. The two projection views of the detector in the $x-y$ and $z-y$ planes (Figs. 3.5 and 3.6) help to understand how the different components are placed in the different angular regions. At the centre of ZEUS, surrounding the beam pipe, lie the inner charged particle tracking detectors. The main tracking device is the CTD (Central Tracking Detector) placed in a solenoidal magnetic field ($B=1.43$ T) generated by a thin superconducting solenoid. In 2001, a silicon-strip Micro Vertex Detector (MVD) replaced the Vertex Detector (VXD) which was part of the initial configuration and removed during the 1995-1996 shutdown. The CTD is supplemented in the forward direction by three sets of planar drift chambers (FTD) with interleaved Transition Radiation Detectors (TRD) (labelled FDET in Fig. 3.7).

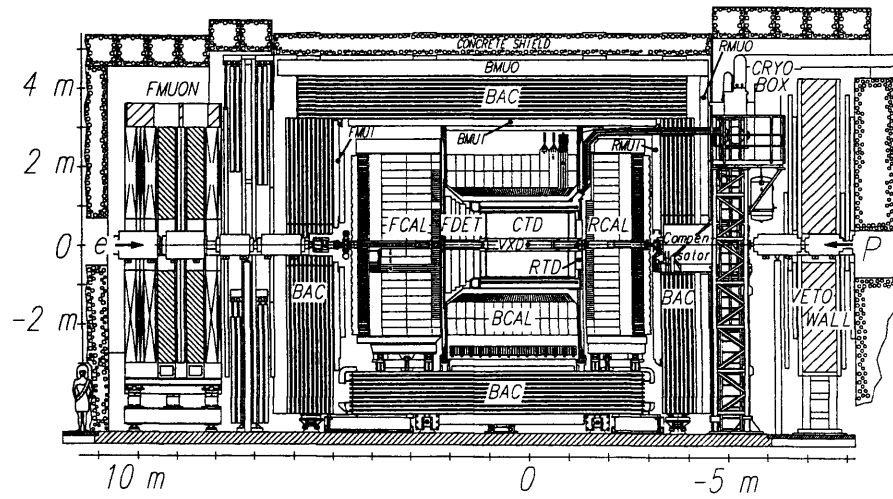


Figure 3.5: ZEUS longitudinal section ($z - y$).

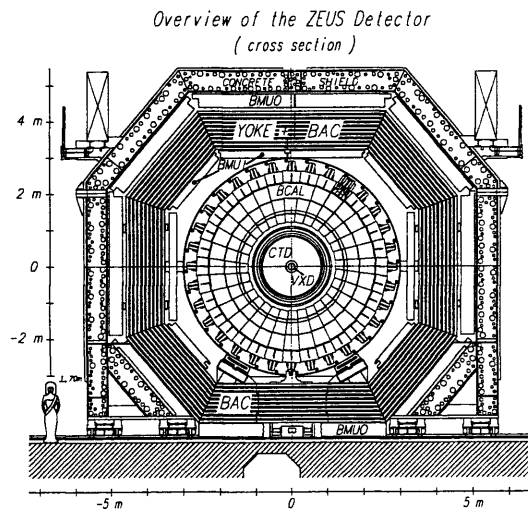


Figure 3.6: ZEUS transversal section ($x - y$).

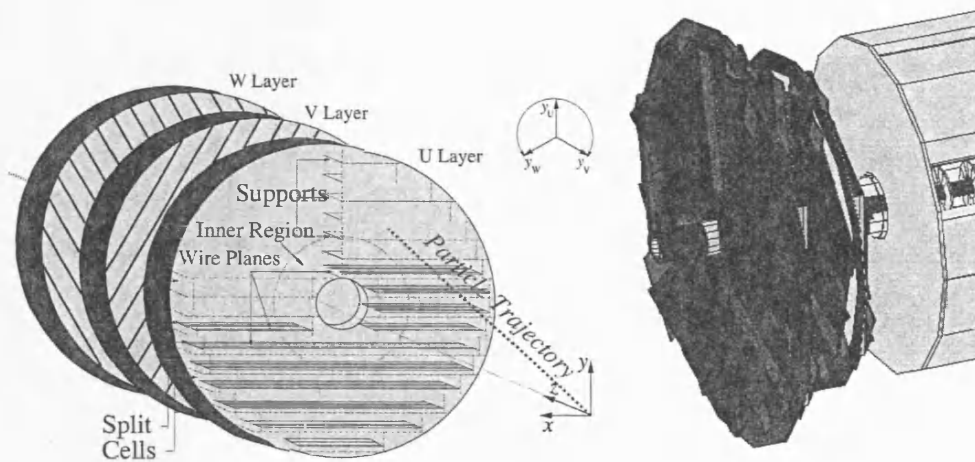


Figure 3.7: Planar drift chambers (left) and straw tubes (right) constituting the Forward Tracking Detector (FDET).

In 2001 the TRD system was replaced by a Straw Tube Tracker (STT) consisting of two modules built of straw tube layers filling the gaps between the three FTD chambers. Commissioning of the STT is still under way. The rear direction is supplemented by one planar drift chamber consisting of three layers (RTD). Although technically part of the calorimeter, the Small Rear Tracking Detector (SRTD) provides improved position resolution for particles and is particularly useful for the identification of the scattered lepton in the rear direction not intercepted by the rear part of the calorimeter. Together, the tracking detectors offer an angular acceptance of $10^\circ < \theta < 160^\circ$ for charged particles.

The tracking system is surrounded by a compensating high resolution uranium-scintillator sampling calorimeter (UCAL, see section 3.5) which is used as the main device for energy measurements; it is divided into three sections: the Forward (FCAL), Barrel (BCAL) and Rear (RCAL) CALorimeters. The iron yoke, which provides the return path for the solenoidal magnetic field flux, is equipped with a set of proportional tubes and serves as a calorimeter (BAC) for the detection of shower tails not completely “contained” by UCAL; this device acts also as a tracking device for muon detection.

Dedicated muon identification detectors (see section 3.6) are located inside (FMUI, BMUI and RMUI) and outside the iron yoke (FMUO, BMUO and

RMUO); for the inner muon chambers the iron of the yoke is magnetized with a toroidal field (with strength $B \simeq 1.7$ T) in order to analyse the muon momentum.

Other detectors are located several metres away from the main detector along the beam pipe. The VETO wall is located in the rear direction at about $z = -7.5$ m from the interaction point. It consists of an iron wall supporting scintillator hodoscopes and is used to reject background from beam gas interactions. The LUMI detector (see section 3.7) is made of two small lead-scintillators calorimeters at $z = -35$ m and $z = -(104-107)$ m and detects electrons and photons from bremsstrahlung events for the luminosity measurement.

3.4 The Central Tracking Detector (CTD)

The Central Tracking Detector (CTD) [63] is a cylindrical wire drift chamber used to measure the direction and momentum of the charged particles and to estimate the energy loss dE/dx which provides information for particle identification. The inner radius of the chamber is 18.2 cm, the outer is 79.4 cm, and its active region covers the longitudinal interval from $z = -100$ cm and $z = 104$ cm, resulting in a polar angle coverage of $15^\circ < \theta < 164^\circ$. The chamber is flushed, close to atmospheric pressure, with a gas mixture of argon (Ar), carbon dioxide (CO_2) and ethane (C_2H_6) in the proportion 90:8:2. An alcohol/ H_2O mixture (77 /23 %) is injected into the gas.

The CTD consists of 72 radial layers of sense wires, divided in groups of eight groups of nine *superlayers* (SL). A group of eight radial sense wires with associated field wires in one superlayer makes up a *cell*. The sense wires are $30\ \mu\text{m}$ thick while the field wires have differing diameters. A total of 4608 sense wires and 19584 field wires are contained in the CTD.

The CTD is designed to operate in a magnetic field to allow the momentum measurement of charged particles. The field wires are tilted at 45° with respect to the radial direction in order to obtain a radial drift under the influence of the electric and magnetic fields. One octant of the CTD is shown in Fig. 3.8.

A charged particle traversing the CTD produces ionisation of the gas in the chamber. Electrons from the ionization drift towards the positive sense wires, whilst the positive ions are repelled and drift towards the negative field wires.

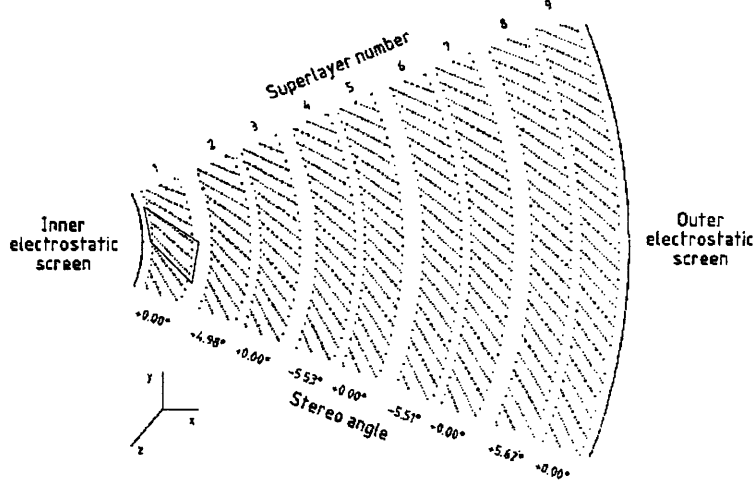


Figure 3.8: *Transverse cross section of one octant of the CTD. The sense wires are indicated with dots.*

The drift velocity of the electrons is approximately constant and equal to $50 \mu\text{m/ns}$. An avalanche effect occurs close to the wire giving an amplification factor on the electrons of $\sim 10^4$ so that a measurable pulse is induced on the sense wires.

The superlayers are numbered 1 to 9 from the innermost to the outermost SL. Odd-numbered (axial) SLs have wires parallel to the z direction, while wires in even-numbered (stereo) SLs are at a small stereo angle of $\pm 5^\circ$ to achieve a better resolution in z . The achieved resolution is $\sim 100 - 120 \mu\text{m}$ in the $r - \phi$ plane and 1.4 mm in the z coordinate.

The three inner axial superlayers (SL1, SL3, SL5) are additionally instrumented with the z -by-timing system. This estimates the z -position of a hit by measuring the difference in arrival time of the pulses on the sense wires at each end of the detector. Although the resolution achieved ($\sim 3\text{cm}$) is much cruder than that obtained using the full axial and stereo wire information, it is a relatively fast method and used predominantly for trigger and track seed-finding.

As mentioned in section 1.2, the CTD is contained within a superconducting solenoid which provides a magnetic field of 1.43 T. This field causes charged

particles to travel in a circular path of radius, R , given by:

$$R = P_T / QB \quad (\text{S.I. units}) \quad (3.2)$$

where Q is the charge of the particle (Coulombs), B is the strength of the magnetic field (Tesla) and P_T is the transverse momentum (kg m s^{-1}). This allows an accurate determination of the P_T of the charged particle. The resolution on the transverse momentum P_T , for tracks fitted to the interaction vertex and passing at least three CTD superlayers, and with $P_T > 150$ MeV, is given by [64]:

$$\sigma(P_T)/P_T = 0.0058P_T \oplus 0.0065 \oplus 0.0014/P_T \quad (3.3)$$

where P_T is expressed in GeV. The error includes the hit position resolution (first term) and the multiple scattering before and inside the volume of the chamber (second and third terms), where the symbol \oplus indicates the quadratic sum.

Since the installation of the MVD in 2001, the resolution has changed and the influence of new detector components on the resolution of the tracking system is still under investigation. It is expected that the influence from multiple scattering is larger (more material) but that the hit resolution is better compared to the resolution quoted above due to the inclusion of MVD hits. Latest results including the MVD in the global track reconstruction indicate the momentum resolution is [65]:

$$\sigma(P_T)/P_T = 0.0026P_T \oplus 0.0104 \oplus 0.0019/P_T \quad (3.4)$$

where all terms having the same interpretation as above.

3.4.1 Measurement of dE/dx

The CTD is also used to estimate the ionization energy loss of a particle in the gas, in order to have additional information on the particle identification. The ionization energy loss is parametrized by the Bethe-Bloch equation [66]:

$$-dE/dx = 4\pi N_A r_e^2 m_e c^2 z^2 \frac{Z}{A} \frac{1}{\beta^2} \left[\ln \left(\frac{2m_e c^2 \gamma^2 \beta^2}{I} \right) - \beta^2 - \frac{\delta}{2} \right] \quad (3.5)$$

3.5. THE URANIUM-SCINTILLATOR CALORIMETER (UCAL) 82

for a particle with charge ze passing through a medium with atomic number Z and mass number A ; in the formula N_A is the Avogadro's constant, r_e is the classical electron radius and δ is the density correction. The energy loss is a function of the velocity, $c\beta$, of the particle: for low β the ionization loss decreases steeply, down to a minimum for $\gamma = (1 - \beta)^{-0.5} \simeq 3$, and then rises as a logarithm up to a plateau at very high γ . At low momenta, $p = \beta\gamma m$, the energy loss is different for different particle masses. The behaviour as observed by the CTD is shown in Fig. 3.9.

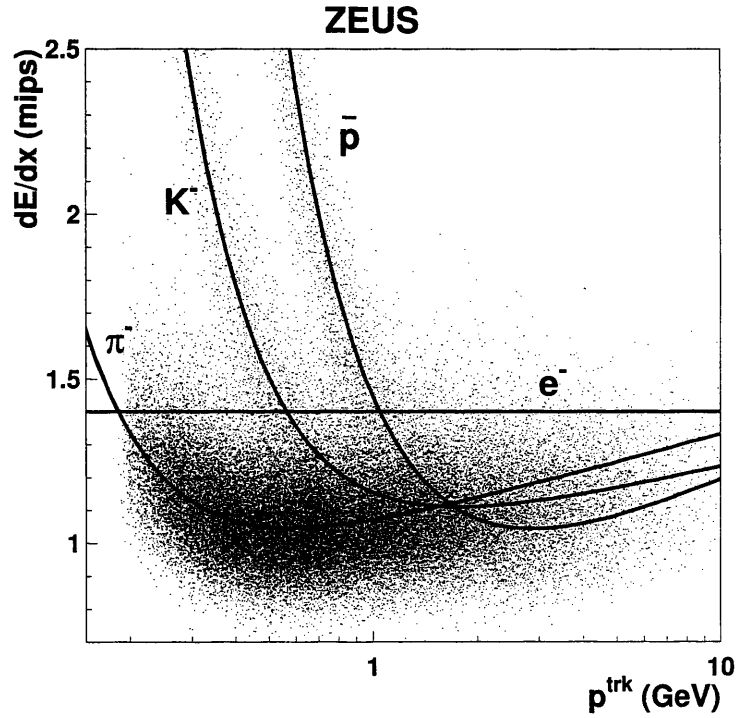


Figure 3.9: *The energy lost by different particles, as reconstructed by the CTD, as a function of the particle momentum [67].*

3.5 The Uranium-scintillator Calorimeter (UCAL)

The ZEUS calorimeter (UCAL) [68] is a high-resolution compensating calorimeter. It completely surrounds the tracking devices and the solenoid, and covers 99.7% of the 4π solid angle. It consists of 3.3 mm thick depleted uranium plates (98.1% U^{238} , 1.7 % Nb, 0.2 % U^{235}) as absorbers alternated with 2.6 mm thick organic scintillators (SCSN-38 polystyrene) as active material.

The hadronic showers contain both hadronic and electromagnetic components whose proportions can fluctuate enormously (see Fig. 3.10). In order to take into

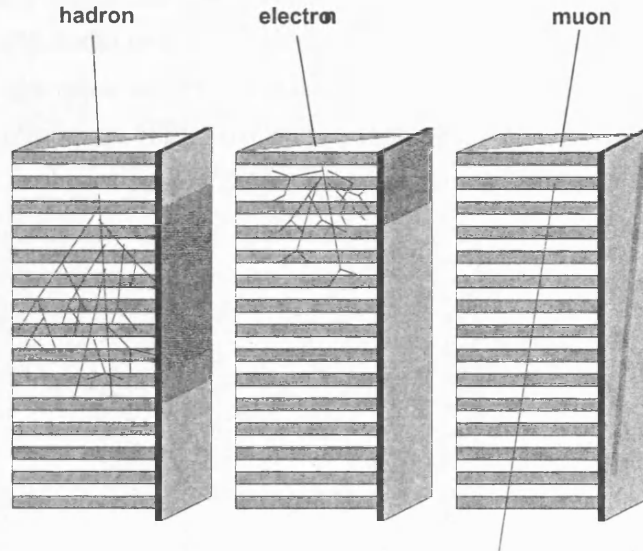


Figure 3.10: *Production of showers inside ZEUS calorimeter.*

account this phenomenon and therefore optimize the energy detection of both shower components, the uranium calorimeter was designed to be *compensating*, so as to obtain the same mean detector response from hadronic and electromagnetic showers of the same energy ($e/h=1$). Therefore the UCAL has different layers of depleted uranium and scintillator with thickness of 3.3 mm and 2.6 mm (Fig. 3.11).

Under test beam conditions [69], the electromagnetic resolution achieved is:

$$\frac{\sigma_E}{E} = \frac{18\%}{\sqrt{E}} \oplus 2\% \quad (3.6)$$

whilst the hadronic resolution is:

$$\frac{\sigma_E}{E} = \frac{35\%}{\sqrt{E}} \oplus 1\% \quad (3.7)$$

where E is the particle energy measured in GeV.

The UCAL is divided into three regions: the forward (FCAL), barrel (BCAL) and rear (RCAL) calorimeter. Since most of the final state particles in a lepton-

proton interaction at HERA are boosted to the forward (proton) direction, the three parts are of different thickness, the thickest being the FCAL ($\sim 7\lambda$), then the BCAL ($\sim 5\lambda$) and finally the RCAL ($\sim 4\lambda$), where λ is the interaction length. Each part of the calorimeter is divided into *modules*. The 23 FCAL modules and the 23 RCAL modules are rectangular, whereas the 32 BCAL modules which surround the cylindrical CTD are wedge-shaped covering 11.25° in azimuth. An FCAL module is shown in Fig 3.11. Each module consists of so called *towers* of

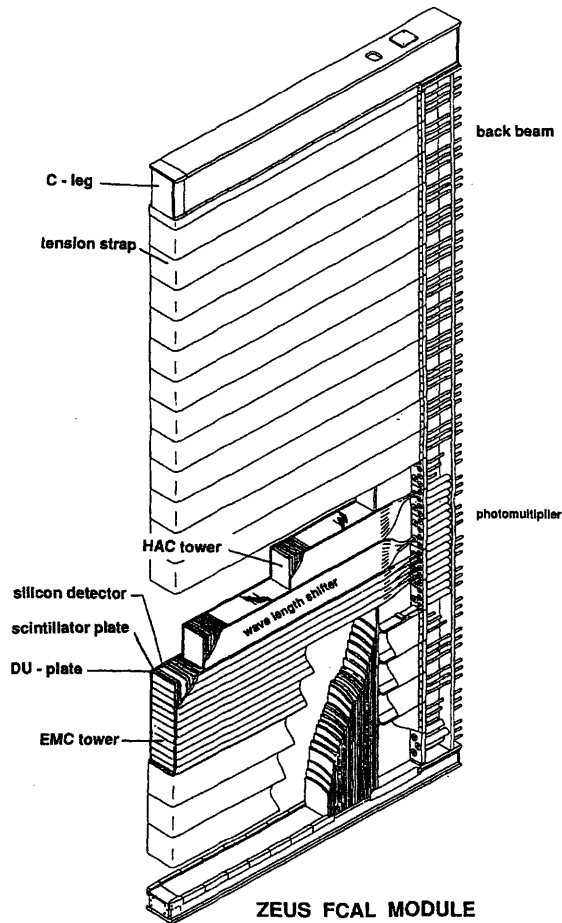


Figure 3.11: Section of an FCAL module.

20×20 cm which are subdivided longitudinally into one electromagnetic (EMC) and two (one in RCAL) hadronic (HAC) sections. The EMC sections are further transversely divided into four cells (only two in RCAL).

The FCAL EMC section per tower consists of the first 25 uranium-scintillator layers and has a depth of $25 X_0$, where X_0 is the radiation length. Each of the

two HAC sections per FCAL tower is 3.1λ deep and consists of 160 uranium-scintillator layers.

The BCAL EMC section is made of the first 21 uranium-scintillator layers, the two HAC sections of 98 layers. The resulting depth is $21 X_0$ for the electromagnetic section and 2.0λ for each hadronic section.

The RCAL towers consist of one EMC and only one HAC section. Therefore its depth is $26 X_0$ for the EMC part and 3.1λ for the HAC part.

Light produced in the scintillators is read out by 2 mm thick wavelength shifter (WLS) bars at both sides of the module, and brought to one of the 11386 photomultiplier tubes (PMT) where it is converted into an electrical signal. The summed information per cell is used for energy and time measurements. The UCAL provides accurate timing information, with a resolution of the order of 1 ns for particles with an energy deposit greater than 1 GeV. This information can be used to determine the timing of the particle with respect to the bunch-crossing time, and it is very useful for trigger purposes in order to reject background events, as will be illustrated later in the trigger section.

Calibration of the PMTs and the electronics is mainly performed using the natural radioactivity of the depleted uranium which produces a constant signal in the PMTs. The signal can be used to intercalibrate geometrically identical regions and to transport the absolute calibration scale determined in test beam measurement. In addition, laser, LED and test pulses are also used for the calibration. The achieved accuracy is better than 1%.

The Presampler [70] is a thin scintillator layer placed on the inner side of the forward and rear calorimeter (FCAL and RCAL) and is used to cover the forward and rear regions which cannot be covered by the barrel section (BCAL). It is used to estimate the shower dimensions and hence the energy loss in the passive material before entering the calorimeter.

3.6 The muon detectors

These detectors are specifically designed to measure penetrating tracks coming from the interaction region (*pointing tracks*) which can cross the whole calorimeter and the iron yoke. These tracks are identified mainly with muons which can traverse large amounts of material without being absorbed. Being much heavier

than the electrons and not interacting strongly, these particles lose energy only by ionization.

The momenta of muons can be very different, depending on their polar angle due to the boost in the forward direction. Muons with more than 10 GeV momentum are frequently produced in the forward region. In the barrel and rear regions, the average momentum of the muons is expected to be much lower. Therefore the muon detection system is split into two subdetectors, the Forward Muon Detector (FMUON) and the barrel and rear muon detectors (BMUON and RMUON respectively).

3.6.1 The Forward MUON detector (FMUON)

The muon detection in the forward region is important for the physics goals of HERA where important physical phenomena, like heavy quark or leptoquark production, produce leptons with small decay angles. Since the resolution and the acceptance of tracking detectors placed inside the calorimeter decreases at low angles, the FMUON is used to measure momenta up to 100 GeV with a resolution of 25% in the forward region independently of the inner region detectors. This detector is equipped with a trigger system which applies a momentum cut and requires a candidate track originating from the interaction point.

The FMUON consists of:

- a system of four limited streamer tube trigger planes (LT1 - LT4) [71], with digital ρ^2 and ϕ readout;
- two planes of limited streamer tubes with digital (ρ, ϕ) and analog ρ readout, in the large polar angle region (LW1 and LW2);
- four planes of drift chambers (DC1 - DC4) [72];
- two large toroidal iron magnets providing a magnetic field of 1.7 T for the momentum separation and measurement in the angular region $5^\circ < \theta < 16^\circ$.

The first limited streamer tube plane and the first drift chamber make up the FMUI detector, while the FMUO detector consists of the rest of the system (Fig. 3.12).

²The ρ coordinate defines the direction perpendicular to the beam line.

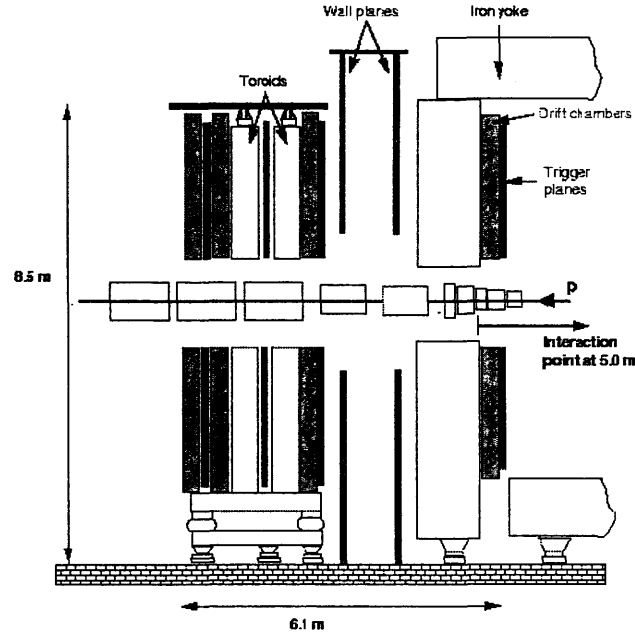


Figure 3.12: FMUON longitudinal section.

The Limited Streamer Tubes (LST) Planes

The aim of the limited streamer tubes (LST) is to trigger on muon candidates and to reconstruct their position in terms of the azimuthal and radial coordinates of the track. A trigger plane is made of four LST chambers, grouped in pairs in two half-planes. A quadrant consists of two layers of LST positioned horizontally inside a plastic sheet. The tubes of the two planes are slightly displaced (0.5 cm) in order to achieve a complete geometrical acceptance. Each quadrant is contained in an aluminium air tight box. On the outer side, copper strips are glued in polar geometry. The LSTs induce a signal in the copper strips if a particle crosses the plane. There are 132 radial ρ strips each 1.9 cm wide. They are divided along the bisector of the quadrant so that the simplest unit of the trigger plane to be read out is the octant. The number of ϕ strips is 32 per octant and each strip covers an interval of 1.4° in the azimuthal angle.

The Drift Chambers (DC)

The drift chambers are needed in order to obtain a good momentum resolution. Each plane consists of four chambers, grouped two by two in two half planes,

fixed on a support panel. The basic constituent of the chamber is the *cell*, made of four sense wires and of the layers needed to generate the appropriate electric field. The four sense wires are sent to a TDC, which convert them into a time distance, connected to the space distance by a known relation.

The Large Angle Coverage Planes (Limited Wall, LW)

The two large angle coverage planes (LW) are needed in order to achieve the desired geometrical acceptance also in the region left uncovered by the toroids ($16^\circ < \theta < 32^\circ$). Each plane consists of eight steel tight wrappings that contain a LST layer. The LST signal is induced on copper strips with a radial geometry, spaced at 0.7° in the ϕ coordinate and at 1.8 cm in the ρ coordinate. There are 64 ϕ strips per octant and 192 ρ strips per octant. The achieved resolution in the ρ coordinate, using a charge barycentre method, is ~ 1 mm.

3.6.2 The Barrel and Rear MUON detector (B/RMUON)

The barrel and rear muon detector [73] covers a very large area ($\sim 2000 \text{ m}^2$) and consists of LST *chambers* as the basic structure. The chambers covering the inner barrel part between the CAL and the iron yoke are called BMUI while the chambers situated outside the yoke are denoted as BMUON. The rear region is divided into RMUI and RMUO chambers in a similar way (see Fig. 3.13).

The chambers have different shapes and dimensions depending on their location, but their nominal structure is the same. The supporting structure of each chamber is an aluminium honeycomb frame 20 cm thick in the rear chambers and 40 cm in the barrel. Two plates of LST are placed on both sides of the honeycomb. The two layers on the same side of the chamber are displaced by 8.3 mm in order to minimize dead areas for particles traversing at 90° with respect to the wire plane. Each LST is made of a plastic sheet with eight cells. Each cell contains a copper-beryllium wire of $100 \mu\text{m}$ diameter, the distance between two sense wires being 1 cm.

Each LST plane is equipped on one side by 13 mm wide readout strips with 15 mm pitch that run orthogonal to the wires. In the BMUI and BMUO chambers the LSTs are parallel to the beam direction while in RMUI and RMUO they are horizontal (parallel to the x -axis). With the analog strip readout the achievable spatial resolution on the coordinate orthogonal to the wires is $200 \mu\text{m}$ while it is

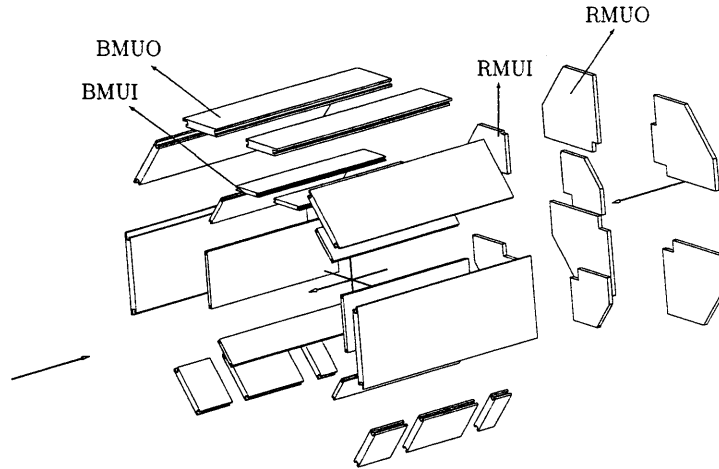


Figure 3.13: Layout of the barrel and rear muon detector.

700 μm for the coordinate parallel to the wires.

3.6.3 The Backing Calorimeter (BAC)

The Backing Calorimeter (BAC) [74] uses the return iron yoke as an absorber to form an additional tracking calorimeter using aluminium proportional tubes operating in an $\text{Ar} - \text{CO}_2$ atmosphere. The BAC vetoes showers leaking out of the CAL allowing the selection of event samples with a resolution corresponding to the intrinsic resolution of the CAL. It can distinguish between hadron showers and muons and provides muon identification and trigger capabilities in the bottom yoke and other areas where no muon chambers are present.

The BAC is built from modules inserted into the yoke (see Fig. 3.5) consisting of 7-8 tubes of a cross section of 11×15 mm and a length between 1.8 and 7.3 m. Modules are equipped with 50 cm long aluminium cathode pads in addition to the gold plated tungsten wires of $50 \mu\text{m}$ diameter. The wires are read out on one side and provide both analogue and digital signals whereas the pads have only an analogue read-out.

Energy is measured by summing up the analogue signals in towers of a width of 25 -50 cm (2-4 modules) over the full depth of the BAC. The pads of 2-4 neighbouring modules are added up to pad towers with an area of $50 \times 50 \text{ cm}^2$ (4

modules) similar to the wire towers. They provide also patterns of hit positions in the BAC to reconstruct muon trajectories.

The spatial resolution of the BAC is ~ 1 mm perpendicular to the wires, whereas the resolution parallel to the wires is defined mainly by the pad size. The energy resolution determined by test beam measurements is:

$$\frac{\sigma_E}{E} = \frac{1.1}{\sqrt{E}} \quad (3.8)$$

where E is the particle energy in GeV.

3.7 The luminosity measurement

The luminosity measurement at ZEUS is done by studying the production rate of photons through the Bethe-Heitler process [75]:

$$e + p \rightarrow e' + p + \gamma, \quad (3.9)$$

where the photon is emitted from the electron at very small angles with respect to the ingoing lepton direction (negative z). The cross section for this process at the leading order (LO) is expressed as:

$$\frac{d\sigma}{dk} = 4\alpha_e r_e^2 \frac{E'}{kE} \left(\frac{E}{E'} + \frac{E'}{E} - \frac{2}{3} \right) \left(\ln \frac{4E_p E E'}{M m k} - \frac{1}{2} \right) \quad (3.10)$$

where E and E_p are the energies of the lepton and proton beams respectively, E' is the outgoing electron energy, k is the photon energy, M and m are the proton and electron masses while r_e^2 represents the classical electron radius. Higher-order corrections in the above cross section calculation are less than 0.5%.

The luminosity monitor consists of a photon and a lepton calorimeter [76], located along the beam pipe at $z = -(104 - 107)$ m and $z = -35$ m, respectively (Fig. 3.14). To protect the photon calorimeter against synchrotron radiation, it has been shielded by a carbon-lead filter. The resulting calorimeter resolution, (with E in GeV), is:

$$\frac{\sigma_E}{E} = \frac{0.25}{\sqrt{E}}. \quad (3.11)$$

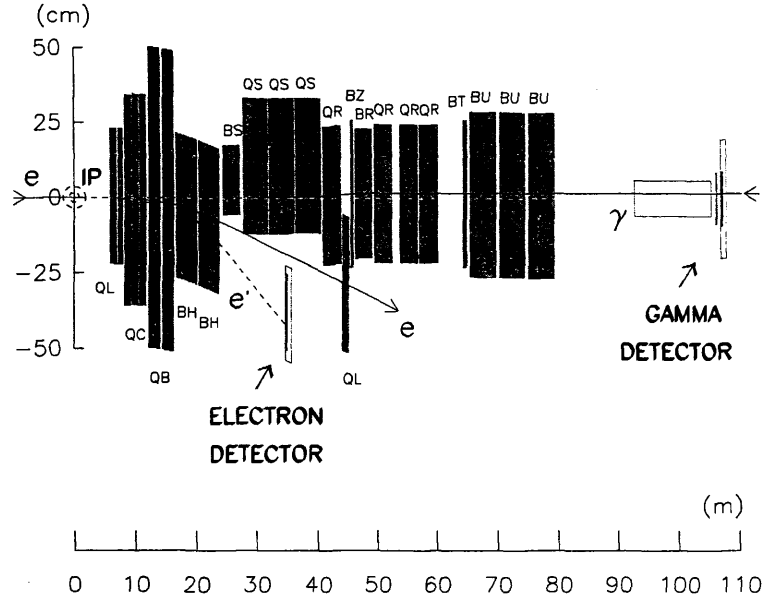


Figure 3.14: The layout of the ZEUS Luminosity Monitor. The nominal interaction point is located at (0,0).

The bremsstrahlung event rate is determined by counting the number of photons above a fixed energy threshold, and not by the simultaneous identification of the lepton and the photon, because of the dependence of the lepton calorimeter acceptance on the beam position and angle. The luminosity is then extracted using:

$$L = \frac{R_{ep}(E_\gamma > E_\gamma^{th})}{\sigma_{ep}^{acc}(E_\gamma > E_\gamma^{th})}, \quad (3.12)$$

where $\sigma_{ep}^{acc}(E_\gamma > E_\gamma^{th})$ is the cross section corrected for the detector acceptance, $R_{ep}(E_\gamma > E_\gamma^{th})$ is the photon rate and E_γ^{th} is the photon threshold.

3.8 Background

The background event rate at ZEUS can be much higher than the ep interaction rate, especially in the machine startup phases, depending on the beam-pipe vacuum conditions. The main background sources which have to be removed are:

- gas interactions inside the beam pipe: when the beam particles interact with the residual gas inside the beam pipe. If this interaction happens near

the detector, the interaction products can be detected by ZEUS.

- halo muons: the hadronic interactions of the beam protons can subsequently produce muons through pion or kaon decays; these muons go into the halo beam and are therefore called *halo muons*.
- cosmic muons: these are muons coming from the cosmic showers generated in the atmosphere which can be detected by ZEUS.

The background is dramatically reduced by the trigger, which is tuned to discriminate against it. The background coming from the interaction of the particles with the beam gas is limited through the VETOWALL device, an iron wall 87 cm thick and $800 \times 907 \text{ cm}^2$ placed at $z = -7.5 \text{ m}$ from the interaction point. It is instrumented with two scintillator hodoscopes, one for each side of the wall, which can identify the beam-gas-interaction events. A $95 \times 95 \text{ cm}^2$ gap window is left uncovered around the beam-pipe.

The trigger system, described in the next chapter, takes into account the information coming from the calorimeter, SRTD (a hodoscopic scintillator placed around the beam pipe in front of the RCAL) and C5 (a HERA collimator equipped with scintillator counters placed behind the RCAL at 1.2 m from the nominal interaction point in the electron beam direction).

The temporal information from the ZEUS calorimeter is calibrated in order to have no temporal gap for the particle in the interaction region. The timing difference between the FCAL and RCAL measurements can be used to reject the beam gas events, since the products from the beam gas interactions hit the RCAL $\sim 10 \text{ ns}$ before hitting the FCAL. The calorimeter temporal resolution, for energy E greater than few GeV, is better than 1 ns. The same method is used to tag the cosmic muons, studying the temporal difference between the upper and lower side of BCAL.

3.9 The ZEUS trigger system

The bunch crossing frequency at ZEUS is $\sim 10 \text{ MHz}$, corresponding to a time gap of 96 ns between two consecutive collisions. The rate is dominated by the interaction of the proton beam with the residual gas which contributes about 10-100 kHz, depending upon the vacuum levels in the beam-pipe up to 100 m

upstream of ZEUS. This frequency has to be reduced at a level compatible with the offline data storage without losing interesting physics events (few Hz).

The approach adopted for the ZEUS data acquisition is a three level trigger system with increasing complexity of the decision making algorithm and decreasing throughput rate (Fig. 3.15).

- *first level trigger (FLT)*; is a hardware based trigger which uses programmable logic to make a quick rejection of background events. The FLT reduces the input rate of 100 kHz to an output rate of 1 kHz. As it is not possible to take a decision within the bunch crossing time, the data are pipelined until the trigger decision is taken.

Individual component decisions use a subset of the total data, and are made within 1.0-2.5 μs . The global first level trigger (GFLT) calculations take up to 20 bunch crossings and the FLT delivers the abort/accept decision after 4.4 μs .

Typical criteria used by the FLT in taking the trigger decision are the approximate “crude” event vertex position, the transverse energy of the event, and energy sums in sections of the calorimeter. The FLT has a good efficiency for ep physics ($\sim 100\%$), but still has a very low purity ($\sim 1\%$).

- *second level trigger (SLT)*; the SLT is a parallel processor utilising a network of transputers. It reduces the FLT output rate of ~ 1 kHz to an output rate of ~ 100 Hz. As in the FLT, the outputs of the component SLT decisions are passed to the global SLT (GSLT) where the event decision is made. The GSLT makes its decision after 5.2-6.8 ms. The decision is based upon limited charged particle tracking, vertex determination, calorimeter timing and $E - P_z$ and scattered electron tagging.

Data from an event accepted by the SLT trigger is sent directly from the component to the event builder (EVB). The EVB stores the data from the components until the third level trigger (TLT) is ready to process it, and combines the data from different components into one consistent record: the event. One event is stored in a single record of the ADAMO [77] database tables.

- *third level trigger (TLT)*; is a software trigger which is sent asynchronously

with the bunch crossing on a dedicated PC farm. At this stage an approximate version of the event reconstruction software is run, including tracks and interaction vertex reconstruction. The TLT has been designed to cope with an input rate of 100 Hz from the SLT at design luminosity. The output rate is reduced to about 5 Hz.

After accepting an event, the TLT sends the data via optical link to the DESY computer centre, where the events are written onto disk to be available for further offline reconstruction and data analysis.

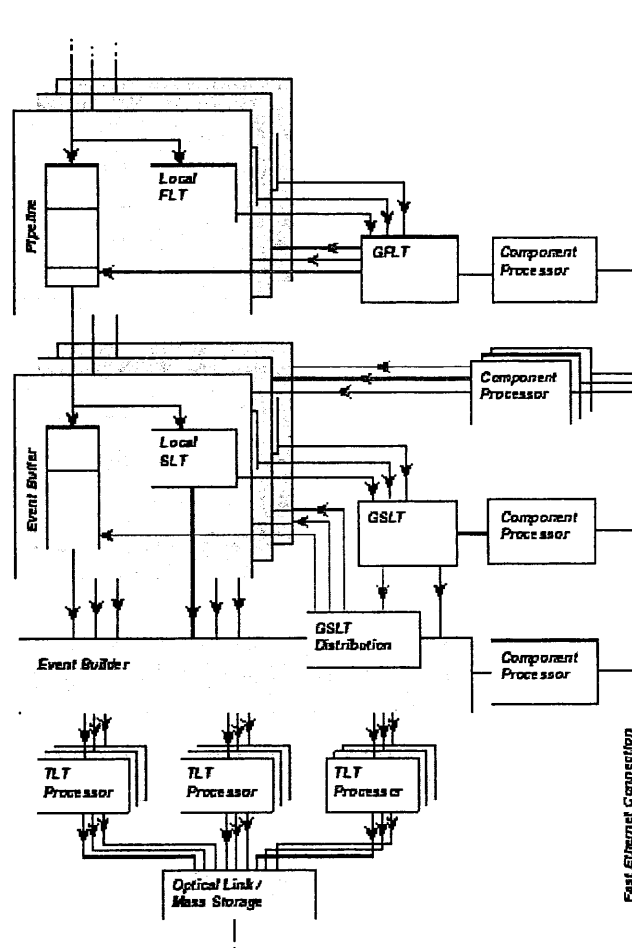


Figure 3.15: ZEUS trigger chain

Chapter 4

The ZEUS Microvertex Detector (MVD)

During the 2000-2001 shutdown, planned for the luminosity upgrade, a silicon microvertex detector (MVD) was installed in ZEUS.

The MVD, placed between the beam pipe and the inner volume of the CTD, provides an improvement in the global precision of the tracking system and allows the identification of events with secondary vertices originating from the decay of particles with long lifetime ($c\tau \gtrsim 100\mu\text{m}$). This device helps the study of hadron decays containing heavy quarks such as charm and beauty, or tau leptons thanks to an improvement in the track resolution with the possibility to resolve secondary vertices.

The main analysis topics which can be substantially improved through the use of the MVD are [79]:

- *Charm and beauty in photoproduction.* Measuring the rate of events containing charm (and beauty) in direct photoproduction, it is possible to study the gluon content of the proton.
- *Charm and beauty in Deep Inelastic Scattering.* The measurement of the proton structure function F_2^{charm} will cover a kinematic range beyond the one accessible so far from ZEUS using D^* meson tagging. This analysis is currently characterized by a low efficiency, around 1%, with 30% purity and hence very limited statistics. The introduction of the MVD will allow charm tagging with an efficiency between 10% and 30% and with a purity

greater than 30%. The proton structure function F_2^{beauty} will be extracted for the first time using ZEUS data.

- *New physics.* The possibility to identify tracks originating from secondary vertices and the tracking resolution improvement will allow a better reconstruction of the events containing electrons with very high Q^2 which are scattered in the forward region.

The technical requirements which were taken into account during the design of the MVD are:

- angular coverage around the interaction point between $10^\circ < \theta < 160^\circ$;
- measurement of three points for each track in two independent projections;
- $20 \mu m$ intrinsic hit resolution;
- separation of two tracks up to $200 \mu m$;

The main limitations are due to the small amount of space available between the CTD (radius=18.2 cm, see Chapter 3) and the beam pipe. The following description summarizes the main characteristics of the MVD, in its two components covering the central (BMVD) and forward (FMVD) region (see Fig. 4.1).

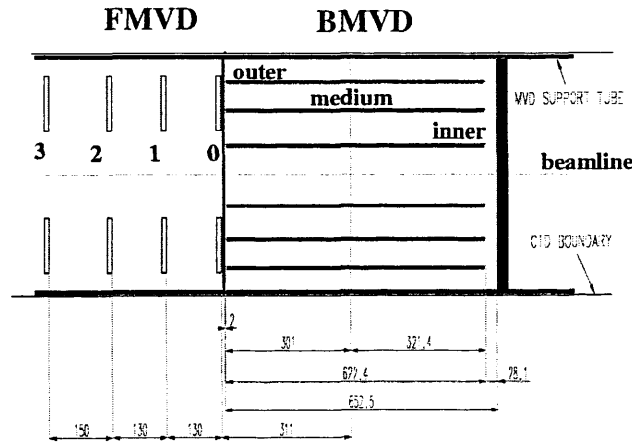


Figure 4.1: *Longitudinal MVD section. There are 3 layers in the barrel region and the 4 wheels in the forward section.*

4.1 Barrel and forward micro vertex detector

The barrel section of the MVD is 64 cm long (see Fig. 4.1) and is sub-structured in three layers to allow high efficiency in the pattern recognition and to make an estimate of the track momentum in the trigger phase.

The first layer of silicon detectors follows the elliptical path around and along the beam pipe and it is placed at a variable radius between 3 and 5 cm from the CTD axis (see Fig. 4.2). The beam pipe is not centred with respect to

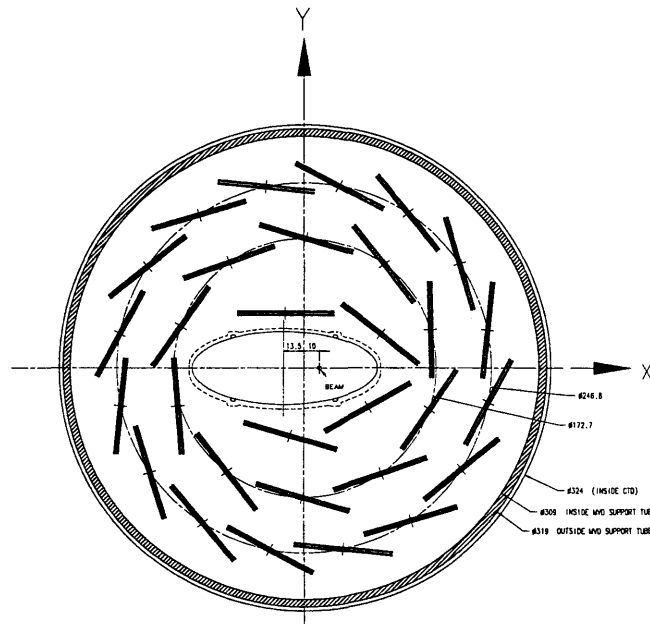


Figure 4.2: *BMVD section: 3 superlayers around beam pipe are shown.*

the CTD axis and the nominal interaction point is shifted towards the centre of HERA (along the x axis) by about 4 mm in order to accommodate the primary synchrotron radiation spread inside the beam-pipe volume. The second and third layer are placed along a circular path at $r \sim 8.6$ cm and $r \sim 12.3$ cm. On average a track crosses 2.8 layers. The resolution on the impact parameter, based on Monte Carlo studies, is shown in Fig. 4.3. These resolution studies are for tracks perpendicular to the beam pipe ($\eta = 0$) which cross all three layers, as a function of track momentum.

The BMVD is equipped with 600 silicon strips sensors (see Appendix B) mounted

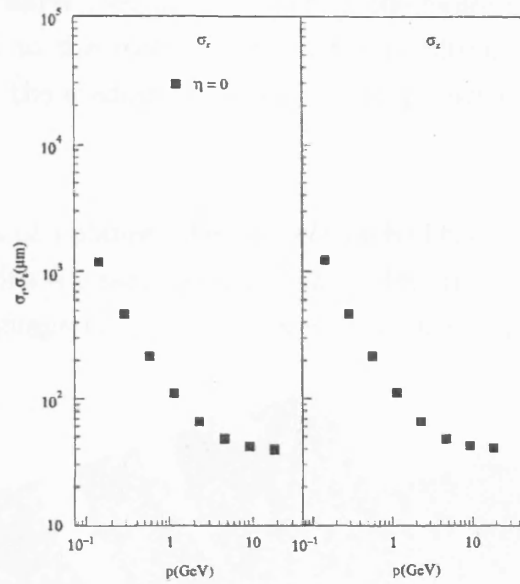


Figure 4.3: Impact parameter resolution on tracks at $\eta = 0$ as a function of the momentum. The measurements are for tracks crossing 3 layers of half modules [80].

on 30 carbon fibre structures called *ladders* (Fig. 4.4); two layers of sensors are placed parallel and perpendicular to the beam line in order to measure $r - \phi$ and $r - z$ coordinates. Each layer is made of two single-sided silicon strip planes

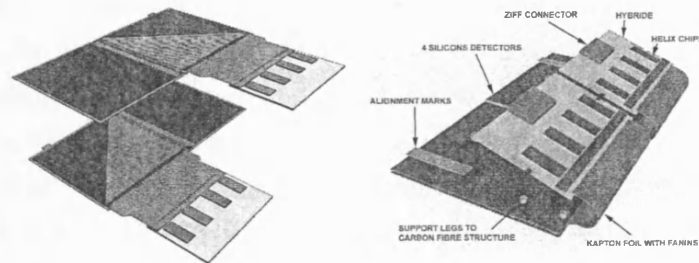


Figure 4.4: Half modules and ladders mounted on the support.

(320 μm thickness) with p^+ strips implanted in a n -type bulk. The strip pitch is 20 μm ; every 6th strip has an AC coupling with a read out line made by an aluminium strip through a dielectric material ($\text{SiO}_2 - \text{SiN}_4$). Two sensors are glued together, electrically connected with a copper path excavated in a Upilex

foil of $50\mu\text{m}$ of thickness (see fig. 4.4). From the figure it can be seen that the sensor is connected to the readout device; the resulting surface covered by the two sensors and by the readout system is called a “half-module” and is $6.15\text{ cm} \times 6.15\text{ cm}$.

The FMVD consists of 4 planes called *wheels*, each of them is made of two layers of 14 silicon sensors with the same technical characteristics of the barrel sensors but with a trapezoidal shape (Fig. 4.5). This device allows the acceptance to extend

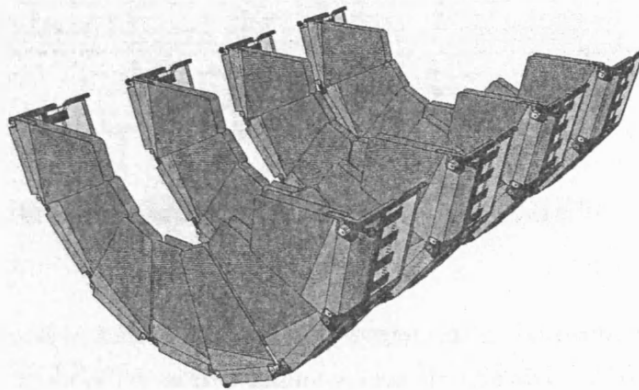


Figure 4.5: *FMVD 4 wheels.*

in pseudorapidity up to $\eta = 2.6$, a region where tracking information has yet to be used in ZEUS. Each wheel has inner and outer sensors. They are mounted back to back. An inner and outer wheel sensor form a sector. The crossing angle between the strips in the inner and outer sensor is $\sim 13^\circ$ ($180^\circ/14$). Inside a layer of sensors the adjacent sensors are slightly overlapped in order to minimize the dead regions. The four wheels are positioned at $z=32, 45, 47$ and 75 cm ; the first wheel is linked to the structure supporting the BMVD. A more detailed description can be found in [81].

4.2 Readout electronics

The MVD silicon sensors are read by the analog chip HELIX3.0 [82] (see fig. 4.6); the chip integrates 128 channels with a charge-sensitive preamplifier followed by a shaper which produces a Gaussian signal with a time peak of $50 - 70\text{ ns}$. The

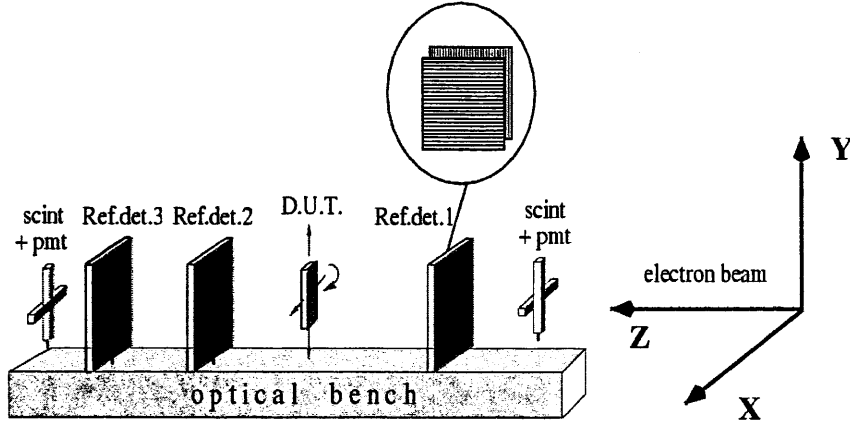


Figure 4.7: *Schematic view of the device used with the test beam.*

squared average noise of each strip. The impact position reconstruction was calculated using three different algorithms:

- *Eta Algorithm*: it is based on the assumption that most of the charge is collected by the two strips closest to the impact position. If Q_{left} (Q_{right}) is the charge collected on the left (right) side of the impact position, P is the readout pitch and x_{left} (x_{right}) is the position on the left (right) strip, the x_{eta} can be defined as:

$$x_{eta} = P \cdot f(\eta) + x_{left} \quad (4.1)$$

with:

$$\eta = \frac{Q_{right}}{Q_{right} + Q_{left}}, \quad f(\eta) = \frac{1}{N} \int_0^\eta \frac{dN}{d\eta'} d\eta'. \quad (4.2)$$

- *Double Centroid Algorithm*: it reconstructs the impact position using the strip collecting the highest charge and the two nearest strips. Once the gravity centre C_{left} (C_{right}) between the central and the left (right) strip is calculated, the hit position will be:

$$x_{DC} = \frac{C_{left}/dr + C_{right}/dl}{dr + dl}, \quad \text{where} \quad dl = \frac{C_{left}}{C_{right}} = 1/dr. \quad (4.3)$$

- *Head-Tail Algorithm*: for large incidence angles, the charge generated by a particle is spread over many strips. In this case, the charge collected by the central strip of the cluster does not contain precise information about the position. The head-tail algorithm uses the information from the external strips on both sides to solve this problem. The *head* (*tail*) strip is that with the lowest (highest) identification number (integer number defining the strip position inside a sensor) which collects a charge three times higher than the noise level.

The hit position will be given by:

$$x_{HT} = \frac{x_h + x_t}{2} + \frac{Q_t + Q_h}{2Q_{AV}} \cdot P \quad (4.4)$$

where $x_h(x_t)$ is the head (tail) strip position and Q the charge. Q_{AV} is the average pulse height for each strip inside the cluster.

Figure 4.8 shows the intrinsic resolution as a function of the incident angle, measured with the three different algorithms. The intrinsic spatial resolution reaches $13\mu m$ for tracks perpendicular to the sensor surface.

4.4 Radiation monitor

The main radiation sources in the MVD area are the synchrotron radiation and the radiation caused by beam losses. The MVD is expected to be operative for at least 5 years. During this period, the foreseen integrated radiation dose is ~ 0.5 kGy. The MVD detector and all the readout electronics were designed to work without a change in the signal-noise ratio, up to an integrated dose of 3 kGy. In order to keep the radiation dose under control, a radiation monitoring system (RadMon) generates warning signals when there is high radiation and generates a dump signal to the electron kicker. This RadMon is also used to calculate the time integrated total dose.

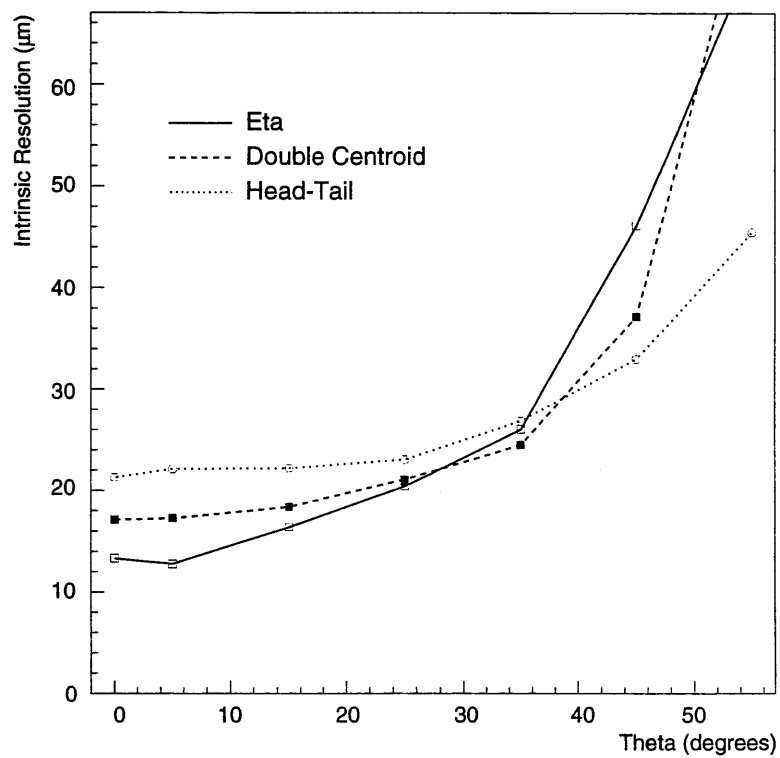


Figure 4.8: *Intrinsic resolution as a function of the incident angle, measured with the three different algorithms [85].*

Chapter 5

Physics simulation and NLO QCD predictions

The use of simulation programmes is important in physics analysis. A better understanding of the data and the detector behaviour can be achieved by simulating the detector response to physics events. Moreover, the theoretical models implemented in the simulations can be tested by comparisons to real data.

The simulation of physics events at HERA is done in two main steps. First, the ep scattering process is simulated using an *event generator*. This programme, following the prescriptions of the theoretical models implemented in it, provides a complete list of the four-momenta of the final state particles. In the second step, all the detector and the trigger systems are simulated, in order to determine their response to the particles produced in the physical process.

These simulations are based on Monte Carlo (MC) techniques, which are an essential tool in understanding the complexity of high energy physics processes and of particle detectors.

5.1 General structure of an event generator

The factorization theorem for hard processes [86] is the main theoretical justification for the approach adopted by QCD Monte Carlo event generators. Following the prescriptions of the theorem, an ep scattering process, characterized by a hard scale, can be factorized into the following separate stages (Fig. 5.1):

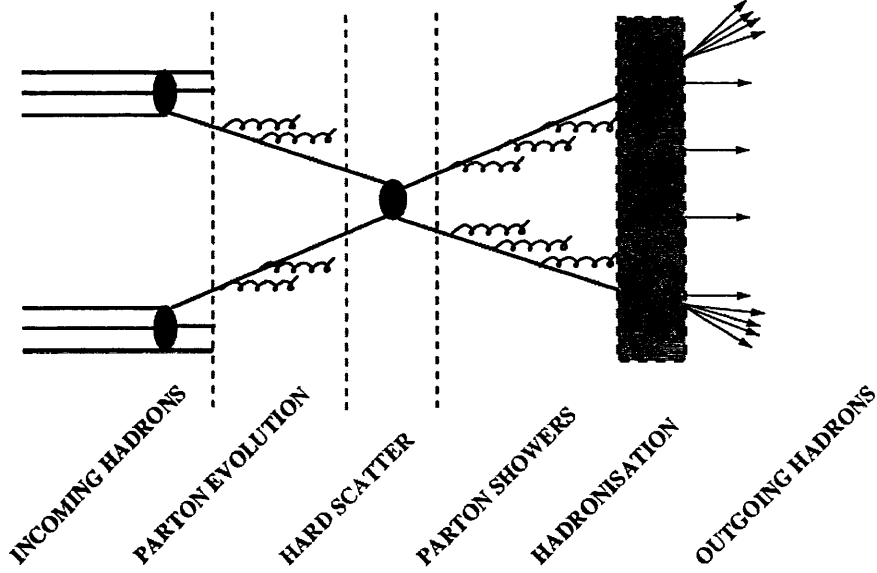


Figure 5.1: General structure of the leading-order plus parton-shower PYTHIA MC generator.

- *hard sub-process*: it is the interaction between a parton, extracted from the proton, and the photon, or a photon constituent in resolved photon events. This process can be calculated in a fixed order perturbative expansion if it involves a hard scale μ ($\mu \gg \Lambda_{QCD}$), as seen in Chapter 1;
- *initial and final state radiation*: in processes involving charged and coloured objects, the topology of an event can be strongly influenced by the emission of gluons and photons in the initial or final state. These perturbative corrections are usually modelled by the so called *parton shower method*: the radiation is simulated by an arbitrary number of branchings of one parton into two, like $e \rightarrow e\gamma$, $q \rightarrow qg$, $q \rightarrow q\gamma$, $g \rightarrow q\bar{q}$. The kernel $P_{a \rightarrow bc}(z)$ of a branching gives the probability distribution of the energy sharing, with daughter b taking a fraction z and daughter c the remainder $(1-z)$ of the initial energy E_a . The two daughters may branch in turn, producing other partons, and so on. Via *initial state radiation* a parton, having low space-like virtuality, radiates time-like partons, increasing its space-like virtual mass. On the other hand, in *final state radiation* an outgoing virtual parton with large time-like mass generates a shower of partons of lower virtuality. The

shower evolution is stopped at some fixed scale μ_0 , typically of the order of 1 GeV;

- *hadronization*: it is the process in which colourless hadrons are formed starting from coloured partons. It is a non-perturbative phenomenon, involving soft processes where pQCD is not applicable. Therefore simulation programmes model the hadronization process using phenomenological inputs. The main hadronization models now available are the cluster model, implemented in HERWIG (see section 5.2) and the Lund string model, implemented in PYTHIA (see section 5.3);
- *beam remnant*: the interacting partons carry only a fraction of the initial beam energy, the rest is taken by the beam remnant. If the shower initiator is coloured, so is the beam remnant, which is therefore connected to the rest of the event and has to be fragmented and reconstructed coherently.

5.2 The HERWIG Monte Carlo

The HERWIG [87] Monte Carlo programme is a general-purpose particle physics event generator which can simulate lepton-lepton, lepton-hadron and hadron-hadron interactions. It has a relatively small number of free parameters, a large predictive power, and is as independent as possible of non-perturbative parameters.

The initial and final state radiation is factorized as successive branching processes in which the energy fractions are distributed according to the Altarelli-Parisi splitting functions. The full available phase-space is restricted to an angular ordered region, as a result of interference, and leading infrared singularities are correctly taken into account.

In the case of final state radiation, at each branching the angle between the two emitted partons is smaller than that of the previous branching. In the case of initial state radiation, the angular ordering applies to the angle θ_i between the incoming hadron and the emitted parton i . The scale of α_s at each branching is set at the relative transverse momentum of the two emitted partons. In the case of heavy flavour production, the mass of the quark modifies the angular-ordered phase-space depleting the soft radiation in the direction of the heavy quark. The emission within a cone with an opening angle m_Q/E_Q , where m_Q and E_Q are

the mass and the energy of the heavy quark, vanishes. This angular screening determines the shape of the heavy flavour jet.

A large variety of electroweak and QCD processes can be simulated using HERWIG. The factorization scale μ^2 of the hard subprocess is given by:

$$\mu^2 = \frac{2\hat{s}\hat{t}\hat{u}}{\hat{s}^2 + \hat{t}^2 + \hat{u}^2}, \quad (5.1)$$

where \hat{s} , \hat{t} and \hat{u} are the Mandelstam variables. The resulting cross section for light flavour production diverges in the limit $P_T \rightarrow 0$, therefore a cut on the minimum transverse momentum of the produced partons has to be applied.

HERWIG uses the Equivalent Photon Approximation (EPA) (see Chapter 1) to generate the spectrum of the photon radiated from the incoming lepton in ep scattering. The boson-gluon fusion process in heavy flavour production uses the exact cross section of the process $ep \rightarrow Q\bar{Q}X$ as fully calculated by Schuler [88]. In the case of resolved photon processes, the programme allows, at each branching, the possibility for a dynamical $\gamma \rightarrow q\bar{q}$ anomalous splitting; the factorisation scale for anomalous splittings is chosen to be consistent with that for hadronic photon events.

In the hadronization process, three types of non-perturbative contributions have to be considered: the representation of the incoming partons as constituents of the incoming particles, the conversion of the outgoing partons into hadrons, and the description of the soft underlying event due to the presence of spectator partons. The incoming parton treatment is related to the factorization theorem of collinear singularities. A phenomenological input structure function describes the distribution of the parton longitudinal momentum fractions, whilst the transverse momentum distribution is characteristic of the size of the hadron.

Concerning the formation of hadrons from the outgoing partons, below the time-like cutoff scale Q_0 , perturbative QCD predicts [89] that in hard processes the confinement of partons is local in colour and independent of the hard scale μ . The cluster hadronization model used in HERWIG is assumed to satisfy these requirements. After the perturbative parton branching processes, all the outgoing gluons are split non-perturbatively into light (u or d) quark-antiquark or diquark-antidiquark pairs, the splitting into diquarks being suppressed with respect to that into quarks. Quarks are then combined with their nearest neighbours to form colour singlet clusters, whose mass distribution is peaked at low values and

falls rapidly for large masses. The clusters formed in this way are fragmented into hadrons following some prescriptions. If a cluster is too light to decay into two hadrons, it is taken to represent the lightest single hadron of its flavour, and its mass is shifted to the right value by an exchange of momentum with a neighbouring cluster. The clusters which are massive enough decay isotropically into pairs of hadrons and following rules that bring about the formation of an unbiased selection of decay products conserving flavour. The small fraction of clusters having masses too high for isotropic two-body decay are fragmented using an iterative fission model, until the masses of the products are below the fission threshold. This mechanism is not unlike string fragmentation (see section 5.3).

The spectators remaining from the incoming particles in hadron-hadron and lepton-hadron collisions are included in beam clusters. In the formation of those clusters, the colour connection between the spectators and the initial state parton shower is cut by the forced emission of a quark-antiquark pair. In a lepton-hadron collision, the soft underlying event is represented by a soft collision between the beam cluster and the adjacent cluster, produced in the forced emission.

5.3 The PYTHIA Monte Carlo

The PYTHIA [90] Monte Carlo is a general-purpose event generator, sharing many common features with HERWIG, but having also some significant differences, in particular in the treatment of the non-perturbative processes. The PYTHIA philosophy, in fact, is to describe also the hadronization processes in as much detail as possible.

PYTHIA and HERWIG also differ in the description of the hard sub-process. In particular, in photoproduction events PYTHIA uses the Weizacker-Williams approximation to generate the spectrum of the photons radiated from the incoming lepton, whereas HERWIG uses the equivalent photon approximation (see section 5.2). Another difference is the scale μ^2 of the hard scattering $1 + 2 \rightarrow 3 + 4$; PYTHIA sets μ^2 to the transverse mass m_T of the two outgoing partons, m_3, m_4 :

$$\mu^2 = \frac{1}{2}(m_3^2 + P_{T_3}^2 + m_4^2 + P_{T_4}^2) = \frac{1}{2}(m_3^2 + m_4^2) + \frac{tu - m_3^2 m_4^2}{s}, \quad (5.2)$$

whereas the scale used by HERWIG was given by Eq. 5.1.

The parton shower process implementation is similar to that of the HERWIG Monte Carlo, but in PYTHIA the parton emissions are ordered only according to the virtuality of the radiated partons. The perturbative parton radiation is stopped at some cutoff scale Q_0^2 , of the order of 1 GeV^2 .

The main difference between PYTHIA and HERWIG is the hadronization model. In PYTHIA fragmentation is performed by the JETSET programme, which implements the *Lund string fragmentation model* [91]. The string model is based on the starting assumption of a linear confinement picture. According to this model, the energy stored in the colour dipole field between a charge and an anticharge increases linearly with the separation between the charges. This assumption is supported by lattice QCD studies performed on one of the simplest possible systems, the colour-singlet $q\bar{q}$ in 2-jet event.

As q and \bar{q} move apart from their common production vertex, the physical picture is that of a colour flux tube, with transverse dimensions of the typical hadronic sizes (1 fm), being stretched between the q and the \bar{q} . If the tube is uniform along its length, this leads to a confinement picture with a linearly rising potential. The simplest way to obtain a Lorentz covariant and causal description of the energy flow due to this confinement is by the use of the dynamics of massless relativistic strings with no transverse degrees of freedom. As q and \bar{q} move apart the potential energy stored in the string increases, and the string may break producing a new $q'\bar{q}'$ pair. The original system therefore splits into two colour-singlet systems $q\bar{q}'$ and $\bar{q}q'$. Further breakings may occur if the invariant mass of either of these string pieces is large enough. The string break-up process proceeds until on-mass-shell hadrons remain.

In the generation of quark-antiquark pairs from string break-ups quantum mechanical tunnelling is used, leading to a flavour-independent Gaussian spectrum from the transverse momentum p_T of the $q'\bar{q}'$ pair. Since the string has no transverse excitation this p_T is locally compensated between the quark and antiquark. The p_T of the hadron is made up of the p_T of the quark and antiquark forming it. The tunnelling picture also implies a suppression of heavy quark production so heavy quarks are not expected to be produced in the soft fragmentation, but only in the perturbative parton shower branching $g \rightarrow q\bar{q}$. A tunnelling mechanism can also be used to explain the production of baryons.

The different string breakings are causally disconnected. This means that, for

example, starting from a system made up of a quark moving in the $+z$ direction and an antiquark moving in the $-z$ direction, the formation of mesons can be described in the following way: by a string break-up, the production of a $q_1\bar{q}_1$ pair leads to the formation of a $q\bar{q}_1$ meson, leaving behind an unpaired quark q_1 . A second pair $q_2\bar{q}_2$ may now be produced, to give a new meson with flavours $q_1\bar{q}_2$, etc. This process can be iterated until all energy is used, with some modifications near the \bar{q} -branch to make the total energy and momentum consistent.

The case of several partons moving apart from a common origin is more complicated. For a $\bar{q}qg$ event, a string is stretched from the q to the \bar{q} end via a gluon, so that the gluon has two string pieces attached. The string fragments into two $\bar{q}q$ pairs, boosted with respect to the centre-of-mass frame of the original $q\bar{q}$ system, and into one hadron straddling both string pieces.

5.4 The detector simulation

All the event generators supported in ZEUS, like PYTHIA and HERWIG, are gathered in a software programme called AMADEUS. The user can choose the event generator, which gives as output all the four-momenta of the particles produced in the hard scattering process and all the relevant kinematic variables. The data produced by an event generator are the input to the ZEUS detector and the trigger simulation programme, MOZART [92]. MOZART is based on the GEANT [93] package, whose kernel contains a description of all the detector components, including the material they are made of, their shapes and positions. The programme traces the particles through the whole detector, simulating its response and taking into account physics processes such as energy loss, multiple scattering and particle decays in flight.

The events then pass through the CZAR [77] package, that simulates the trigger logic as implemented in the data taking.

As a final step, the generated sample is processed by the ZEUS reconstruction programme, ZEPHYR. This programme reconstructs the event variables, like particle momenta and energies, treating the data and the Monte Carlo in the same way. All the information coming from the different detectors making up ZEUS are taken as inputs by ZEPHYR.

ZEUS data are organized using the ADAMO [77] management system and used

for the data storage in memory or on external media and for their documentation. Access to the data by users is done with the EAZE programme. The ZEVIS event display generates bi-dimensional graphical representations of the real or simulated events. A diagram of the ZEUS reconstruction scheme for data and Monte Carlo is shown in fig. 5.2.

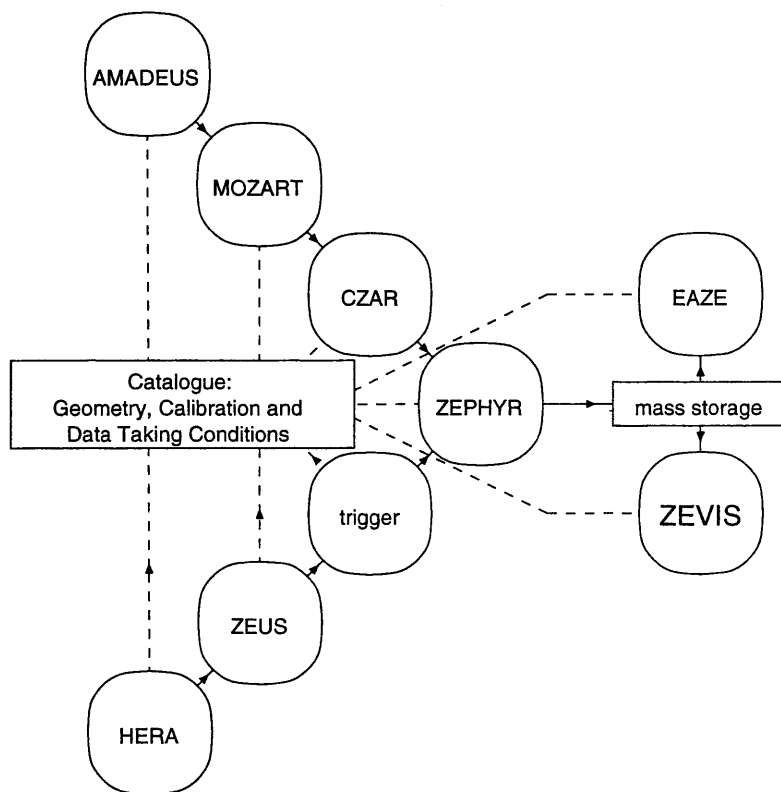


Figure 5.2: *A schematic diagram of ZEUS data and Monte Carlo reconstruction chain.*

5.5 Monte Carlo samples

In this section, a brief description of all the Monte Carlo samples generated for the simulation of the data used in this thesis is given.

5.5.1 Beauty event simulation

The production of beauty quarks in an event proceeds through different sub-processes. The main contribution to the cross section is given by the *direct*

photon process, which at LO reduces to boson-gluon fusion $\gamma g \rightarrow Q\bar{Q}$.

Contributions to the cross section also come from *resolved photon* processes. A class of these events is known as *beauty excitation*, in which a beauty quark is extracted from the photon or from the proton.

Monte Carlo samples simulating all these sub-processes have been generated, the respective cross sections and the integrated luminosities generated are reported in Table 5.1

Four different samples were generated using the PYTHIA Monte Carlo, simulating direct, resolved and excitation processes. The sub-processes simulated in each sample were:

- ***b* in direct γ :**

$$\gamma g \rightarrow b\bar{b};$$

- ***b* in resolved γ :**

$$q\bar{q} \rightarrow b\bar{b}; \quad gg \rightarrow b\bar{b};$$

- ***b* excitation in γ :**

$$bq \rightarrow bq; \quad bg \rightarrow bg;$$

- ***b* excitation in p :**

$$b\gamma \rightarrow b\gamma; \quad bg \rightarrow bg; \quad bq \rightarrow bq; \quad b\bar{b} \rightarrow b\bar{b}.$$

In the event generation, the *b*-quark mass was set to $m_b = 4.5$ GeV. The parton densities used for the proton and the photon were CTEQ5L [97] and GRVG-LO [98], respectively. The events were generated with no requirements on the presence of muons or jets. The beauty quarks were not forced to decay into muons: as a consequence, in the beauty Monte Carlo samples the fraction of beauty quarks decaying into muons is given by the fraction implemented in the simulation. This choice was made in order to generate a Monte Carlo sample suitable for the evaluation of the beauty photoproduction cross section without requesting the semi-leptonic decay into muons.

5.5.2 Charm event simulation

The production mechanisms of $c\bar{c}$ quark pairs are identical to those of $b\bar{b}$. Charm can be produced in direct photon processes, like boson gluon fusion, and in resolved processes. Also charm excitation in the photon and in the proton gives a sizeable contribution to the cross section. The charm photoproduction cross section is expected to be two orders of magnitude larger than that of beauty; the resolved processes are expected to give a larger contribution than in the case of beauty. Resolved processes are in fact more important for lower masses of the produced quarks.

Monte Carlo samples simulating charm photoproduction have been generated using PYTHIA. The cross sections and the integrated luminosities generated are shown in Table 5.1. As in the case of beauty, four samples were generated, simulating different sub-processes. For each sample, the simulated interactions are the same as described above in the case of beauty, with b quarks replaced by charm quarks.

In the event generation the mass of the c quark was set to $m_c = 1.35$ GeV and the charm quarks were forced to decay into muons. An event was included in the simulation if at least one muon and two jets were found in the final state satisfying the following requirements:

- **muons:** the muon was asked to be in the acceptance region of the muon chambers:

$$p_T^\mu > 2 \text{ GeV} \quad \text{or} \quad p_z^\mu > 3 \text{ GeV} \quad \text{or} \quad p_z^\mu < -1.5 \text{ GeV}$$

and

$$10^\circ < \theta^\mu < 170^\circ .$$

- **jets:**

$$E_T^{jet1} > 4.5 \text{ GeV}, \quad E_T^{jet2} > 3.5 \text{ GeV}, \quad -3 < \eta^{jet1,2} < 3.$$

These are well away from the final cuts and were used for the purpose of efficient generation.

5.5.3 Light quark event simulation

In light quark photoproduction, due to the low mass of the produced quark, resolved photon processes are expected to be dominant. The cross section is much larger than that of charm photoproduction, and therefore also of beauty. Monte Carlo samples simulating light flavour photoproduction in direct and resolved photon processes have been generated. The cross sections and the integrated luminosities generated are reported in Table 5.1, where the light flavours are indicated by l . The production of heavy quarks was forbidden in the event generation. The subprocesses simulated in each sample were:

- q in direct γ :

$$q\gamma \rightarrow qg$$

$$g\gamma \rightarrow q\bar{q}$$

- q in resolved γ :

$$qq' \rightarrow qq' \text{ (QCD)}$$

$$q\bar{q} \rightarrow q'\bar{q}'$$

$$q\bar{q} \rightarrow gg$$

$$gg \rightarrow qq$$

$$gg \rightarrow q\bar{q}$$

$$gg \rightarrow gg.$$

As in the case of charm, cuts have been applied on the generated events in order to reduce the size of the data to be analysed, keeping only those of interest for the analysis. As will be shown in detail in Chapter 6, a possible source of background for the analysis reported here is two-jet events, in which a light particle (usually a pion, kaon or proton) is misidentified as a muon by the muon chambers. The probability of such a particle reaching the muon detectors is very low, but its production cross section is much higher than that of beauty quarks, and therefore it is necessary to estimate the probability of these particles giving a fake muon signal. Hence, the generated light quark events were required to have at least two jets in the final state, and a high momentum particle in the acceptance region of the muon chambers. The cuts were:

- at least one track in the angular region:

$$10^\circ < \theta < 170^\circ$$

and satisfying the following momentum cuts:

$$P_T > 1.35 \text{ GeV} \quad \text{or} \quad P > 2.5 \text{ GeV};$$

- at least two jets, reconstructed by the KTCLUS algorithm (see Chapter 7) and satisfying the following requirements:

$$E_T^{jet1,2} > 5.25 \text{ GeV} \quad \text{and} \quad -3 < \eta^{jet1,2} < 2.7;$$

5.6 NLO QCD predictions

In this thesis the measured beauty photoproduction cross sections are compared to NLO QCD predictions based on the programme FMNR by Frixione et al. [99]. The programme gives as output the NLO cross sections for $b\bar{b}$ photoproduction at the parton level, without hadronization and decay of the produced particles. In

process	σ [mb]	number of events	L [pb^{-1}]
b in direct γ	4.1×10^{-6}	1649526	402
b in resolved γ	7.1×10^{-7}	274990	389
b exc. in γ	1.3×10^{-6}	549930	410
b exc. in p	4.1×10^{-7}	174993	427
c in direct γ	1.5×10^{-4}	519933	388
c in resolved γ	1.2×10^{-5}	99971	1866
c exc. in γ	2.6×10^{-4}	403803	332
c exc. in p	5.6×10^{-5}	52026	281
l in direct γ	2.3×10^{-4}	7972365	195
l in resolved γ	1.3×10^{-3}	9934961	80

Table 5.1: Cross sections and luminosities of the PYTHIA MC sample used in this thesis.

the data, beauty cross sections using events in which the heavy quarks produce jets and decay into muons are measured. Therefore, in order to compare the measurements to the NLO predicted cross sections, the NLO prediction needs an implementation of fragmentation and hadronization, and in some cases the measurements have to be extrapolated.

The FMNR programme provides two- and three-parton final states in photoproduction. The calculation is performed in the *massive scheme* where only light quarks (u , d , s) and gluons are active partons in the initial state. This is implemented using a modified version of the $\bar{M}S$ subtraction scheme [94] in which heavy quark effects decouple in processes involving momenta much smaller than the heavy quark mass. This approach was favoured over the *massless approach*, where the heavy flavours are treated as active massless initial partons above some energy thresholds (see Chapter 2) due to theoretical limitations. The programme generates sequences of correlated events. These sequences are chosen to cancel out divergences in the cross section calculation.

For the calculations of ep collisions, the *Weizsäcker-Williams function* [95] is used to simulate the energy distribution of the quasi-real photon flux from the electron.

To extract dijet plus muon photoproduction beauty quark cross section predictions, a dijet plus muon final state is selected by application of the KTCLUS jet finder algorithm (see section 7) to the parton final state of the FMNR calculation.

The muon selection requires the hadronisation of the parton final state. This is done in analogy to the approach chosen in the Monte Carlo event simulation (see section 5.3). The hadronisation of beauty is carried out according to the total $B \rightarrow \mu X$ branching ratio where the muon momentum in the B hadron rest frame is extracted from PYTHIA [96].

The following parameter set is used for the calculation:

- Proton PDF: CTEQ5M
- Photon PDF: GRV-HO
- beauty quark mass: 4.75 GeV
- factorisation and renormalisation scales are set to the transverse mass of the beauty quark pair which is proposed by the authors for $b\bar{b}$ cross sections:

$$\mu_R = \mu_F = \langle m_T \rangle = \sqrt{\frac{1}{2} ((P_T^b)^2 + (P_T^{\bar{b}})^2) + m_b^2} \quad (5.3)$$

where $P_T^{b(\bar{b})}$ is the transverse momentum of the beauty (anti-beauty) quark in the laboratory frame.

- $\Lambda_{QCD} = 0.226$ GeV according to the value of α_s used in the CTEQ5M PDF
- Peterson fragmentation with $\epsilon = 0.0035$
- B hadron branching ratio into muons: 0.217

The dominant systematic error on the NLO QCD dijet plus muon photoproduction beauty quark cross section prediction originates from the chosen factorisation and renormalisation scales and the beauty quark mass. The influence from the proton PDF, fragmentation and Λ_{QCD} are negligible when added in quadrature. The systematic error from scales and beauty quark mass variation is taken as the systematic error of the NLO QCD predictions which will be used to compare to the measured cross sections of this thesis (see Chapter 11).

Chapter 6

Analysis overview

Before entering into the details of the analysis, this chapter gives an overview on some key aspects of the measurements. A brief introduction to the characteristics of the beauty-flavoured hadrons is given. The choice of semi-muonic decay channel to measure beauty production is motivated and the expected typical final state topology is sketched. After a description of potential background processes, the beauty-sensitive observables used in this measurement are defined and discussed. The chapter concludes with a summary of the analysis strategy.

6.1 Definition of the measurement

The ZEUS collaboration measured beauty production in events with jets and muons [42, 45] and found agreement with NLO QCD calculations. In those analyses, the beauty component was separated from the backgrounds due to charm and light flavours by exploiting the transverse momentum of the muon relative to the axis of the associated jet, P_T^{rel} . Due to the large b mass P_T^{rel} is expected to be larger on average in the case of muons from semi-leptonic b decays than for muons originating from charm and light flavours (see section 6.5.1).

An alternative method to extract the beauty and the charm content of a sample with jets and muon is to use the impact parameter, δ , of the muon that is expected to be large for B decays due to their large lifetime (see section 6.5.2). The H1 collaboration has recently published an analysis based on a combination of P_T^{rel} and δ [100] in which good agreement was found with ZEUS results, except for a possible excess at low P_T of the muon. Other hints for a possible excess in beauty

production at low P_T are given by double-tag analyses [50, 51, 52].

This thesis presents the first measurement of b production in HERA-II data. The process $ep \rightarrow e' b \bar{b} X \rightarrow e' jj \mu X'$ is studied. The beauty content of a sample with two jets and a muon (see Chapter 7 for the applied selection) was measured using a combination of P_T^{rel} and δ providing a measurement of differential cross sections for beauty production.

6.2 Beauty flavoured hadrons and their semi-muonic decay

Due to colour confinement, a measurement of b quark production can only be performed indirectly, as only hadron-level observables are accessible by experiments. A brief description of the main characteristics which play an important role in the discrimination of beauty hadrons from charm and light-flavoured hadrons follows.

Due to the difference in quark masses, beauty flavoured hadrons are considerably heavier than hadrons with only light valence quarks u , d and s . There is also a sizeable mass difference between charm and beauty hadrons. The masses of beauty mesons are typically around 5.3 GeV (see Tab. 6.1). This can be compared to, e.g. the D^0 meson with a mass of 1.8 GeV and the light meson π^0 with $m_\pi \sim 0.135$ GeV.

hadron	quark content	mass (MeV)	τ (ps)	$c \tau$ (μm)
B^0	bd	5279.4 ± 0.7	1.542 ± 0.016	462
B^\pm	bu	5279.1 ± 0.5	1.674 ± 0.018	502
B_s^0	bs	5369.6 ± 2.4	1.461 ± 0.057	438
Λ_b^0	bdu	5624 ± 9	1.229 ± 0.080	368
D^0	cu	1864.1 ± 1.0	0.4117 ± 0.0027	123
D^\pm	cd	1869.3 ± 0.5	1.051 ± 0.013	315
D_s^\pm	cs	1968.5 ± 0.6	0.490 ± 0.009	147
Λ_c^+	cud	2284.9 ± 0.6	0.200 ± 0.006	60

Table 6.1: *Examples of beauty and charm-flavoured hadrons and their properties [101].*

Another property of beauty particles is their long lifetime. While beauty meson

lifetimes are of the order of 1.5 ps (see Tab. 6.1), the lifetime of, for example the D^0 meson, is 0.4 ps, which translates into proper decay lengths $c\tau$ of 450 μm and 120 μm respectively. This reflects the different sizes of the Cabibbo-Kobayashi-Maskawa (CKM) matrix elements $|V_{ij}|$ corresponding to the dominant decays $b \rightarrow cW^-$ and $c \rightarrow sW^+$:

$$|V_{cb}| = 0.0412 \pm 0.0020, \quad |V_{cs}| = 0.224 \pm 0.016 \quad [101]. \quad (6.1)$$

Although beauty flavoured hadrons are long-lived particles compared to other strongly decaying particles, the time scale of the decay, which is of the order of 10^{-12} s, is too short to observe beauty hadrons directly. Only the decay products are accessible experimentally.

The production of beauty at HERA is strongly suppressed; the relative production ratios are:

$$\sigma_{uds} : \sigma_c : \sigma_b \sim 2000 : 200 : 1 \quad (6.2)$$

The main reason for beauty suppression is a phase-space factor; there is a kinematic threshold for b production due to its mass. The fraction of the four-momentum of the proton carried by the gluon participating in the hard interaction, x_g , is given by:

$$x_g \geq \frac{m_Q^2}{E_\gamma \times 920 \text{ GeV}} \quad (6.3)$$

where m_Q indicates the beauty mass and E_γ is around 10-20 GeV. Charm production requires $x_g \geq 10^{-4}$, whilst for beauty $x_g \geq 10^{-3}$; Fig. 6.1 indicates the x_g region where b is produced, characterised by a low gluon density inside the proton. Hence as beauty production in ep collisions is a relatively rare process, a clean experimental signature is highly desirable. Such a signature is provided by high-energy leptons from the decay of beauty flavoured hadrons. For this analysis the semi-muonic decay mode is chosen.

Since $|V_{ub}| = 0.0036 \pm 0.0007$ [101] is much smaller than $|V_{cb}|$ (see Eq. 6.1), b quarks predominantly decay into c quarks via the emission of a virtual W . The W produces two fermions $f\bar{f}'$, with a $(10.57 \pm 0.22)\%$ probability [101]; these are a muon μ and a muon-neutrino ν_μ (Fig. 6.2(a)). In addition to these direct

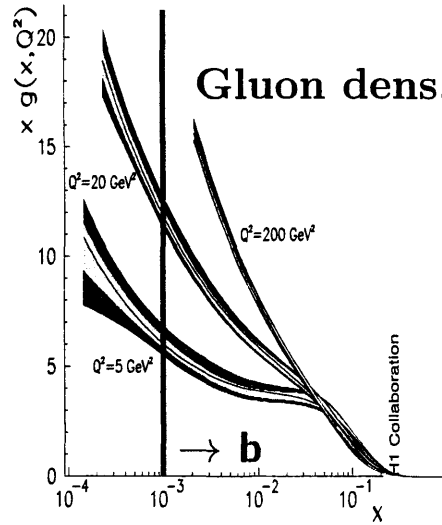


Figure 6.1: Gluon density distribution as a function of x . The threshold for beauty production is shown [102].

(prompt) decays there is also muon production from b decays through *cascade processes* as shown in Fig. 6.2(b), where the charm quark originating from the b quark decays muonically.

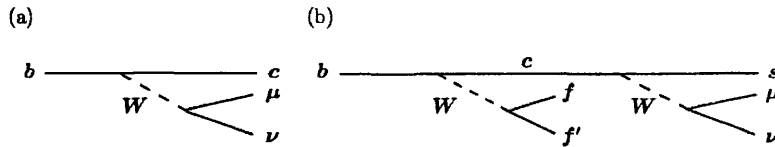


Figure 6.2: Muonic b quark decay: (a) prompt, (b) charm cascade.

As seen in Chapter 2 a simple and widely used model for the formation of heavy hadrons is independent fragmentation according to the *Peterson Fragmentation function* [103]

$$D_q^h(z) \sim \frac{1/z}{(1 - 1/z - \epsilon_q/(1-z))^2}, \quad (6.4)$$

where z denotes the fraction of the quark momentum carried by the hadron. The free parameter ϵ_q needs to be determined experimentally.

An extraction of ϵ_q needs independent information from both the parton and the

hadron levels. At ep colliders this is difficult because the parton level centre-of-mass energy is, a priori, not known and, therefore, the reaction kinematics are not sufficiently constrained. Instead, measurements at e^+e^- colliders are used as experimental input to the fragmentation model. These measurements yield significantly lower ϵ values for beauty compared to charm, e.g. $\epsilon_b=0.0033$ [104] and $\epsilon_c=0.040$ [104]. These ϵ_q values result from a fixed order (α_s^2) QCD fit to heavy hadron spectra measured at the LEP e^+e^- collider. As can be seen in Fig. 6.3 $D_b^h(z)$ peaks at higher z values than $D_c^h(z)$, i.e. the fragmentation is *harder* for b quarks than in the charm case.

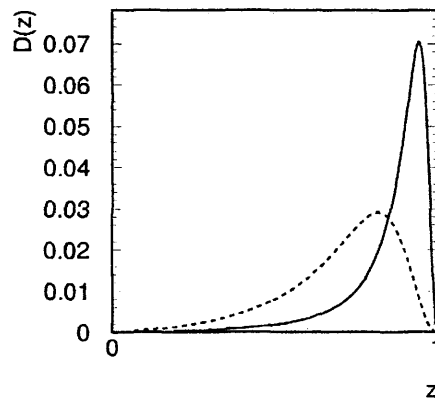


Figure 6.3: *Peterson fragmentation function from beauty (full line) and charm (dashed line), where the values for the fragmentation parameter ϵ have been chosen according to [104].*

6.3 Choice of decay channel

In this analysis, the semi-muonic decay mode is chosen to measure the beauty production cross section. The branching ratio of about 10% is acceptably large and the decay muon provides a clean experimental starting point. In contrast to other final state particles, which in general are stopped within the calorimeter, the muon typically traverses the inner detector region as a minimal ionising particle and, if its momentum is sufficiently large ($P_T \gtrsim 2$ GeV), can be detected in the muon chambers.

The prompt muon from the beauty decay (Fig. 6.2(a)) provides direct access to the decay kinematics. Also, performing an inclusive muon analysis avoids combinatorial background, which in general is an issue in the measurement of hadronic decay modes. Part of the decay information, however, is lost in this approach, because the hadronic decay products are not explicitly reconstructed and the muon neutrino unavoidably escapes detection.

Processes with a b quark in the final state will always contain at least one other hard parton. If the momenta of the outgoing partons are not too low, each of them will form a hadronic jet. In this analysis, jet formation is needed to estimate the flight direction of the semi-muonically decaying beauty hadron, and the selection is based on events with two or more jets with (at least) one of them containing a muon.

It will be discussed below that the MVD [105] is an indispensable tool for this measurement. The muon, therefore, is required to be found within the MVD polar acceptance, i.e. in the central part of the ZEUS detector. In this region a reliable detection in the muon chambers is expected for muon transverse momenta $P_T \gtrsim 2$ GeV.

Figure 6.4 shows an event display of a signal candidate selected from ZEUS 2004 data, where the final state topology of two jets and two associated muons is clearly visible.

6.4 Background processes

Performing a selection of dijet events with a central high P_T muon will not result in a pure signal sample. There are various background processes producing similar final state topologies which are discussed below.

Semi-Muonic Charm Decays

In principle, the production mechanisms for charm and beauty production are the same, and charm hadrons also decay semi-leptonically with branching ratios of the order of 10% [101]. As a consequence, semi-muonic charm decays are expected

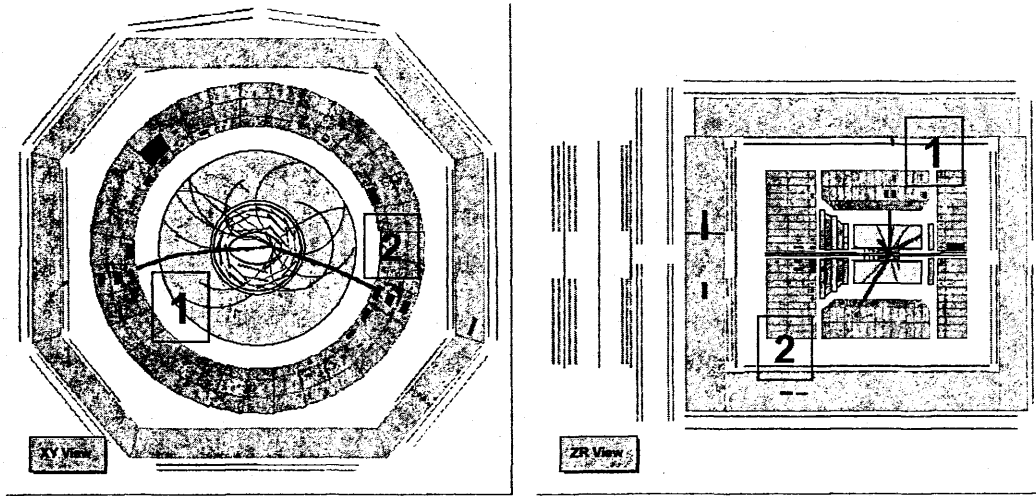


Figure 6.4: *ZEUS beauty candidate event with 2 jets and 2 associated muons. The muons have impact parameters relative to the beam spot of 250 and 330 μm as well as high P_T^{rel} with respect to the jets of 1.24 and 2.05 GeV. The dimuon pair has an invariant mass of 5.5 GeV.*

to produce final state topologies similar to those of signal events. Furthermore, the charm production cross section considerably exceeds the beauty production cross section. A good separation of charm and beauty events, therefore, is one of the crucial requirements for a measurement of beauty production. Possible starting points for the definition of observable quantities to distinguish between charm and beauty are the differences in mass, lifetime and fragmentation.

Heavy Vector Meson Decays

Muon pair production from the decay of heavy vector mesons, in particular the process $J/\psi \rightarrow \mu^+\mu^-$, has to be considered as a background source. In contrast to semi-muonic hadron decays, however, all hadronic activity is due to the underlying event and is not directly connected to the decay itself. A study of the final state topologies for muonic J/ψ decays using Monte Carlo simulated events suggests that two central hadronic jets with one of them containing a high- P_T muon is an unlikely configuration. The relative contribution from this source to the final analysis sample is estimated to be below 1% and is thus neglected.

Cosmic Muons

High-energy muons from cosmic-rays (*cosmic muons*) penetrate the outer detector shielding at a rate of about 1 kHz. If a cosmic muon crosses the central detector region close to the nominal interaction point then it can be mis-interpreted as an *ep* event with one or two identified muons in the final state. There is, however, no timing correlation with the colliding HERA beams. Cosmic muons are thus in general isolated with little additional detector activity and, therefore, do not fulfil the requirement of at least two reconstructed hadron jets. Only in rare cases where a cosmic muon is recorded at the same time as an *ep* event (*overlay event*) might the final state topology be similar to a semi-muonic beauty decay. Based on filter algorithms designed to suppress non-*ep* muon background, the background from this source was found to be negligible. A visual inspection of a part of the analysis event sample confirms this.

Background from mis-identified hadrons

In this analysis, muon identification is based on a signal in the barrel region of the calorimeter associated with a reconstructed signal in the muon chambers. All other detectable particles are expected to be stopped within the calorimeter. Hadrons coming from the interaction region, however, also produce in rare cases a signal in the central muon system. In this way any process producing two or more jets and including central, high P_T hadrons might contribute to the signal sample. Such hadrons, mainly kaons and pions, have a small probability to reach the muon chambers and to be reconstructed as a muon. Nevertheless, since they are produced in large numbers in ZEUS events, some of them can actually give a wrong signal in the muon chambers (*fake muons* or *mistag*).

It should be noted that, while a muonic background can be associated to a specific physics process which can be studied separately using dedicated Monte Carlo event samples, this in general is not the case for fake muons.

The particle hitting the muon chambers could also be a secondary muon, originating from different processes:

- *punch – through*: hadrons passing through the calorimeter can interact and produce secondary particles that hit the muon detectors; this source of background is reduced by requiring a good position and momentum matching between the segment in the muon detector and the CTD track;

- *sail – through*: in some cases, hadrons can pass through the whole detector without being stopped, and then reach the muon chambers being mistagged as muons;
- *decay – in – flight*: muons can come from particle decays, like $\pi^\pm \rightarrow \mu^\pm \nu$, or $k^\pm \rightarrow \mu^\pm \nu$. Such muons typically have low momenta and therefore the request for a hard muon reduced this kind of background. Moreover, these events are rejected also by requiring the muon to come from the interaction vertex.

The procedure used in this analysis to quantify the fraction of light quark events as well as charmed events in the final data sample will be explained in detail in Chapter 10.

6.5 Analysis observables

As discussed above, the selection of dijet events with an identified muon results in a data sample containing both signal and background events. An event-by-event separation of signal and background turns out to be impossible, but the fraction f_b of beauty events can be determined on a statistical basis. The contributing processes can be modelled using, for example, Monte Carlo event generators and their relative contributions can be obtained from a likelihood fit to the shape of distributions of suitably defined observables.

The definition of signal-sensitive observables is based on the large mass or the long lifetime of beauty flavoured hadrons. In this analysis, two different observables are used, namely the muon transverse momentum relative to an associated jet, P_T^{rel} , and the muon signed impact parameter δ , both of which will be described in detail in the following sections.

6.5.1 Mass signature: the P_T^{rel} method

Beauty production is found to give a significantly harder transverse momentum spectrum than charm production. This is partly due to the larger beauty mass, but differences in the hadron production kinematics and the harder beauty fragmentation compared to charm are also relevant. As already mentioned in section 3.1, using combined information from calorimeter and muon chambers

to experimentally identify muon candidates implies a minimum transverse momentum requirement of about 2 GeV, resulting in a considerable enrichment of signal events with respect to the charm background (Figure 6.5 a)).

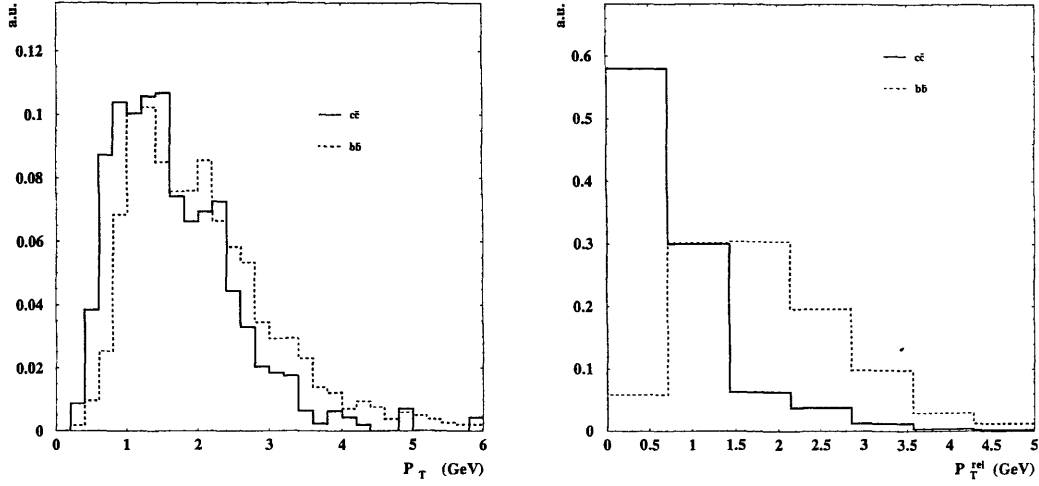


Figure 6.5: Normalized distributions of (left) the transverse momentum and (right) the transverse momentum relative to the direction of the parent hadron for muons from charm decays (full line) and beauty decays (dashed line) as predicted by PYTHIA.

However, for a quantitative extraction of the signal contribution of the sample better observables can be found, which are not only based on the muon momentum but also consider the parent hadron.

While the muon momentum component parallel to the flight direction of the parent hadron also depends on the hadron production kinematics, the transverse momentum of the decay muon relative to the hadron direction,

$$P_{t,true}^{rel} = |\vec{P}_{t,true}^{rel}| = \left| \frac{\vec{P}_{t,true} \times \vec{P}_{hadron}}{\vec{P}_{hadron}} \right|, \quad (6.5)$$

reflects the hadron mass in a more direct way. In fact the $P_{t,true}^{rel}$ distribution is closely related to the muon momentum spectrum in the rest frame of the decay hadron, the kinematic end point being the same for both quantities (see fig. 6.6). This results in clearly different spectra for beauty and charm decays (Fig. 6.5 b)). Approximating the hadron direction by a suitably defined jet-based reference

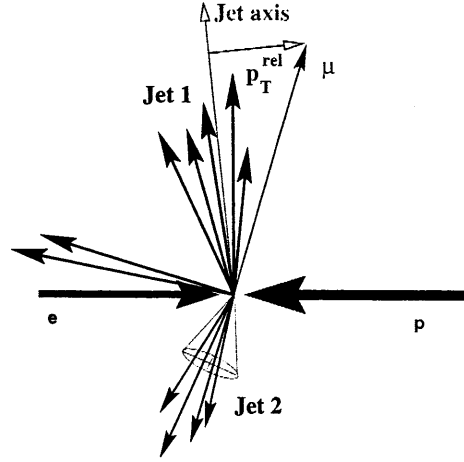


Figure 6.6: *The transverse muon momentum P_T^{rel} relative to an associated jet.*

axis, the corresponding experimental observable is defined as:

$$P_T^{\text{rel}} = |\vec{P}_T^\mu| \cdot \sin \left(\arccos \left(\frac{\vec{P}_T^\mu \cdot \vec{P}_T^{\text{jet}}}{|\vec{P}_T^\mu| \cdot |\vec{P}_T^{\text{jet}}|} \right) \right) \quad (6.6)$$

There is an alternative definition, used in this analysis, for this quantity where the muon transverse momentum is subtracted from the jet and the transverse momentum of the muon relative to the new jet axis, $P_T^{\text{rel}, \text{jet}-\mu}$, is calculated

$$P_T^{\text{rel}, \text{jet}-\mu} = |\vec{P}_T^\mu| \cdot \sin \left(\arccos \left(\frac{\vec{P}_T^\mu \cdot (\vec{P}_T^{\text{jet}} - \vec{P}_T^\mu)}{|\vec{P}_T^\mu| \cdot |\vec{P}_T^{\text{jet}} - \vec{P}_T^\mu|} \right) \right). \quad (6.7)$$

By subtracting the muon transverse momentum from the jet to form the new reference axis, the calculated $P_T^{\text{rel}, \text{jet}-\mu}$ spectrum is shifted to larger values, allowing a better discrimination of signal-background down to low P_T^{rel} values. The characteristics of the $P_T^{\text{rel}, \text{jet}-\mu}$ shape with respect to the originating quark flavour remains the same as for the first definition.

6.5.2 Lifetime signature: the impact parameter method

The large decay length of beauty hadrons arising from their long lifetime can also be used to define beauty-sensitive observables. Table 6.1 lists the *proper decay*

length $c\tau$ for various hadrons, where τ denotes the lifetime in the rest frame of the decaying hadron, but in the laboratory frame the decay length l , which is experimentally accessible, also depends on the hadron *boost*, $\beta\gamma = |p|/m$, via

$$l = c\tau\beta\gamma. \quad (6.8)$$

The probability that an individual hadron of characteristic decay length l traverses at least a laboratory distance L between its production and decay is given by

$$P(L) = \exp(-L/l). \quad (6.9)$$

For experimental reasons, in this analysis, the lifetime information is extracted only in a plane perpendicular to the beam axis. Therefore, only the $r\phi$ -projection

$$L_t = L \sin\theta, \quad (6.10)$$

where θ denotes the polar angle of the decaying hadron, is relevant here.

The *impact parameter* of a particle coming from the hadron decay is the closest distance in the $r\phi$ plane, between the decay particle's trajectory and the production point of the decaying hadron and is given by

$$\delta_{true} = L_t \sin\alpha. \quad (6.11)$$

Here α is the angle in the $r\phi$ -plane between the hadron direction and the direction of the decay particle. The factor, $\sin\alpha$, approximately compensates the boost dependence of L_t .

The lifetime difference between charm and beauty-flavoured hadrons leads to significantly different decay muon δ_{true} spectra, the large δ_{true} region is dominated by beauty events. This is shown in figure 6.7. In order to reconstruct an experimental observable corresponding to δ_{true} , the hadron production vertex is taken to be the reconstructed primary event vertex (the estimated beam spot was taken for this analysis, see Chapter 8) and the flight direction of the decaying hadron is approximated by a jet-based reference axis as already discussed for the P_T^{rel} in the previous subsection. While δ_{true} is by definition a positive quantity, it turns out to be useful to define a sign for the corresponding experimental observable. The resulting *signed muon impact parameter*, δ , is defined as follows:

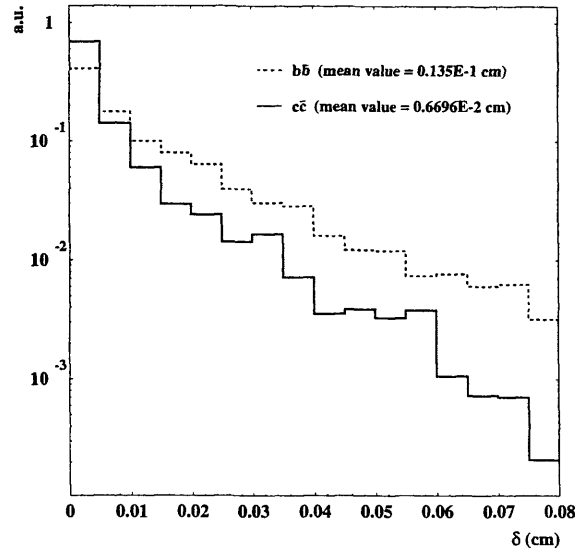


Figure 6.7: *Normalized distributions of the impact parameter for muons originating from charm decays (full line) and beauty decays (dashed line) as predicted by PYTHIA .*

- The magnitude of the impact parameter is given by the $r\phi$ distance of closest approach of the reconstructed muon track to the reconstructed beam spot, $|dca|$ (see Fig. 6.8).
- In order to give a sign to the $|dca|$ quantity the muon track is associated to the nearest jet; the sign is positive if the intercept of the muon track with the jet in the $r\phi$ -projection is downstream of the primary vertex, and negative otherwise (see Fig. 6.8).

For muons originating from the primary vertex the δ spectrum will be symmetric around zero, the width of the distribution reflecting the finite track and vertex reconstruction resolutions. Decays of long-lived particles are characterised by an excess at positive δ values. The region at large positive impact parameters is expected to be dominated by muons from beauty decays.

The impact parameter method is based on the reconstruction of the muon track and the event primary vertex which is assumed to be the production vertex of the heavy hadron. In contrast to an explicit decay length analysis, no knowledge of the hadron decay vertex is required and, therefore, a reconstruction of secondary

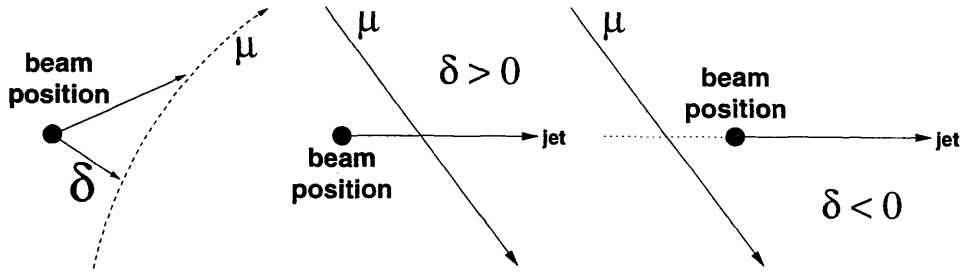


Figure 6.8: Sketch of the impact parameter, δ , of a muon track. If the muon track intercepts the jet axis downstream the primary vertex (beam position, see Chapter 8) the impact parameter has positive sign, otherwise it is negative.

event vertices is not necessary. Moreover the impact parameter depends only weakly on the boost of the decaying hadron. In this sense δ probes the proper lifetime of the decaying hadron in a more direct way than the decay length, which is proportional to the hadron boost (see Eq. 6.11).

6.6 Experimental requirements and analysis strategy

In order to use the observables defined in the previous section to determine the beauty content of a selected sample of dijet events containing a muon candidate, all quantities entering the calculation of P_T^{rel} and δ need to be reconstructed with sufficient precision. This turns out to be an experimental challenge, especially for the impact parameter analysis. The typical δ_{true} values of $140 \mu\text{m}$ and $70 \mu\text{m}$ for muons from beauty and charm decays respectively (see Fig. 6.7) require an impact parameter resolution of the order of $100 \mu\text{m}$ in order to separate the signal from the charm background via this observable. The intrinsic $r\phi$ hit resolution of the central drift chambers is about $150 \mu\text{m}$, the vertex detector is clearly needed for an impact parameter based measurement of beauty production. In this analysis, the MVD information is used in the reconstruction of both the muon track and the primary event vertex. The jet reference axis is used in the calculation of both δ and P_T^{rel} . The P_T^{rel} resolution depends directly on how well the jets reflect the direction of the heavy hadron. In the impact parameter distribution a degraded jet angle resolution will lead to an increased number of signal events

with large δ_{true} reconstructed with negative sign, thus making long lifetime effects indistinguishable from badly modelled resolution. For the P_T^{rel} analysis, also a good modelling of the energy flow within the jet is of relevance.

To summarise, the analysis is based on the following procedure: dijet events containing a central, high- P_T muon candidate are selected, considering in particular high quality requirements for the reconstruction of the muon track, the jet axis and the primary event vertex. This is done for ZEUS data taken during 2004 and for Monte Carlo simulated events modelling the signal and relevant background processes. The relative contributions of the different processes are obtained from χ^2 fits to the muon δ and P_T^{rel} spectra, taking the normalization from the data. Correcting for luminosity, detector acceptance and selection efficiency, the relative beauty contribution is transformed into a beauty cross section which can, in turn, be compared with theoretical predictions.

While P_T^{rel} has been used already in a previous measurements of beauty production at ZEUS [42, 45, 106], the measurement presented in this thesis is the first to be based on the impact parameter method and to use the MVD. As δ and P_T^{rel} probe beauty in a fairly independent way (see Chapter 10), this combination is expected to result in a measurement which is clearly improved with respect to analyses based on only one of the observables, providing also a vital cross-check for the validity of the P_T^{rel} method used so far.

Chapter 7

Event reconstruction and selection

In this chapter all the relevant steps of the selection of the events used in this analysis are described. The experimental signature of events for this analysis is the presence of at least two jets in the final state, coming from the hadronization of the b quarks, and at least one high transverse momentum muon, used to tag beauty via its semi-leptonic decay (see Chapter 6).

First, the reconstruction method for the kinematic variables of interest, like jet and muon parameters, and kinematic variables used to distinguish the photoproduction and deep inelastic scattering regimes, is illustrated. Then, the trigger chain used for the online selection of the event sample is described. Finally the cuts applied to the data to obtain the final photoproduction sample are illustrated, together with the comparison between data and Monte Carlo.

7.1 Reconstruction of tracks and vertices

VCTRAK [107] is the package used in ZEUS for the reconstruction of tracks and primary and secondary vertices inside the detector. Its development, begun in 1990, is still undergoing developments because of the different configurations of the ZEUS tracking system. All reconstructed tracks use mostly hits from the CTD although information coming from other tracking devices (MVD, SRTD, RTD and FTD1) are taken into account.

For this thesis information coming from the MVD is essential to study the decays

of particles containing heavy quarks. The decay length in the transverse plane of a generic particle of mass m , mean lifetime $c\tau$, and transverse momentum P_T is approximately given by:

$$\lambda_{xy} = P_T \frac{c\tau}{m}.$$

Therefore decays of hadrons with a momentum of a few GeV can clearly be discriminated from the primary vertex if $c\tau$ is large enough (of the order of $10^2 \mu m$). For this analysis the measurement of the impact parameter of tracks originating from b decays requires a precise reconstruction of the tracks and of the primary vertex of the event. The reconstruction of the tracks and vertices by VCTRAK can be summarised in three basic steps:

- pattern recognition
- track fit
- vertex finding

which will be discussed in detail in this chapter.

7.1.1 Pattern recognition

Due to the axial magnetic field around the interaction region, the particle trajectory is to first approximation a cylindrical helix with axis along Z . In the pattern recognition phase in order to describe the helix in 3 dimensions the following parameters are used (see Fig. 7.1):

- two parameters in the XY plane: (a_1, a_2)
- two parameters in the sZ plane: (p_1, p_2) , where s is the path length. For a 2D s path along the circumference, $Z = p_1 + sp_2$, where $p_1 = z$ at (x_0, y_0) and $p_2 = \cot \theta$.

The reference point for the trajectory corresponds to the outer hit in (x_0, y_0) . For more details about this parametrization see Appendix A.

This method of track parametrization is faster than the 5-parameter fit used in the final track reconstruction; the speed of the execution is important in this phase because this algorithm is also implemented at the third level trigger where it is necessary to process a huge quantity of information (all possible hit combinations)

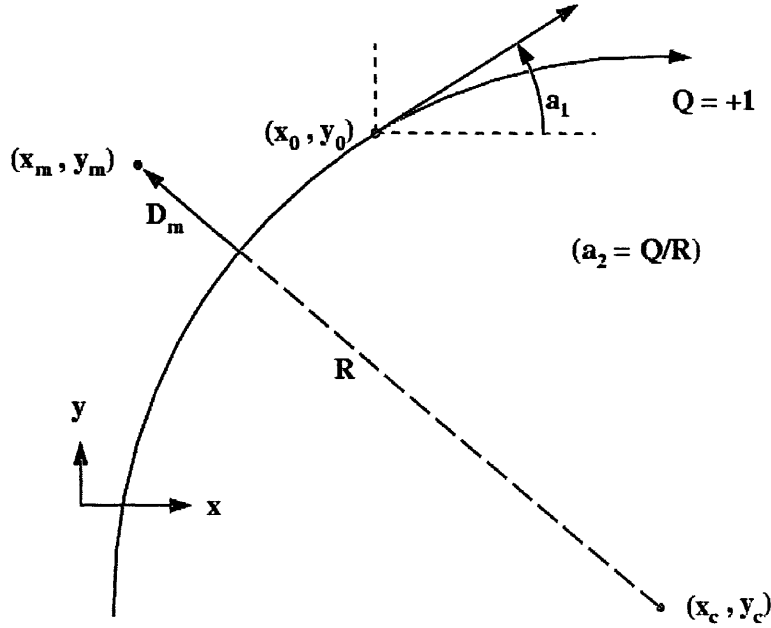


Figure 7.1: *Parametrization used in Pattern Recognition in VCTRAK. The reference point for the trajectory is (x_0, y_0) ; (a_1, a_2) are the two fit parameters in the XY plane.*

in a limited amount of time.

Pattern recognition begins at the outer point of the tracking detectors and goes inward, i.e. it starts in the outer SuperLayer (SL9) of the CTD and follows inward through the MVD module layers. Of all track segments found, only track segments with at least 4 hits are kept (see Fig. 7.2). In the figure the CTD sense wires, placed along a slightly curved path (open ellipses) to solve the “ghost hits” ambiguity [108], are also shown.

7.1.2 Track fit

In the region around the interaction point the magnetic field generated by the solenoid is almost parallel to the CTD axis leading to a parametrization like the one sketched in Fig. 7.3; at this stage the helix is described by 5 parameters calculated with respect to a reference point (X_{ref}, Y_{ref}) :

1. ϕ_H , azimuthal angle of the helix tangent at the distance of closest approach

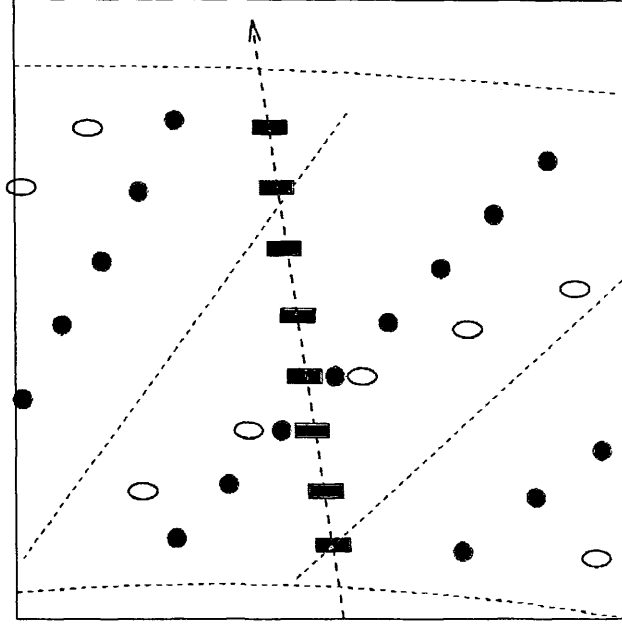


Figure 7.2: *Example of a track segment inside the CTD built using 8 hits.*

to the straight line $x = y = 0$;

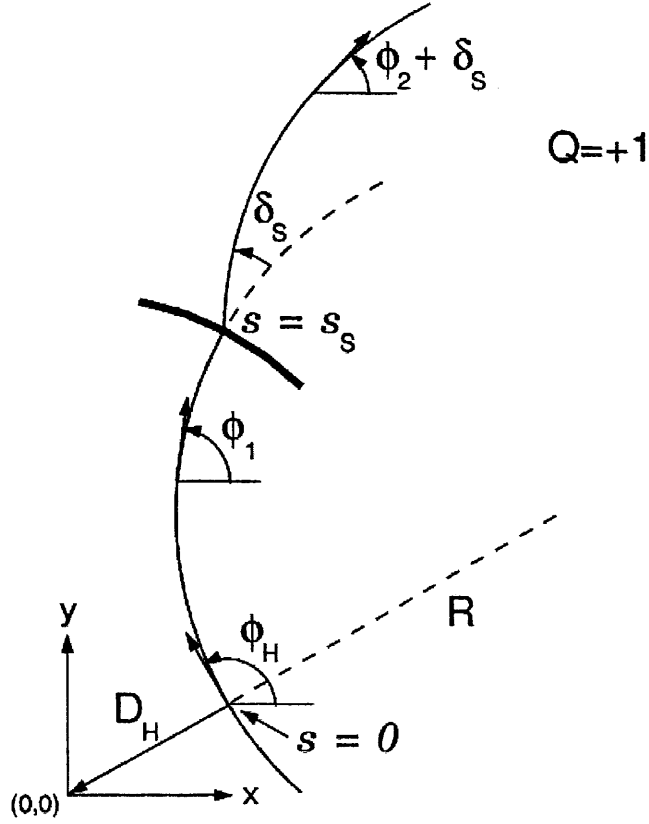
2. Q/R , where Q indicates the track charge (sign) and R the local curvature radius;
3. QD_H , distance of closest approach to the straight line $x = y = 0$;
4. Z_H , z coordinate of the track at the distance of closest approach to the straight line $x = y = 0$;
5. $\cot \theta_H$, where θ_H is the polar angle of the track.

The coordinates of the closest approach to the reference point can be written as:

$$\begin{cases} X_H = X_{ref} + QD_H \sin \phi_H \\ Y_H = Y_{ref} - QD_H \cos \phi_H \\ Z_H \end{cases} \quad (7.1)$$

The path length of a generic trajectory in the XY plane is given by:

$$s(\phi) = -QR(\phi - \phi_H) . \quad (7.2)$$

Figure 7.3: *VCTRACK parametrization used in the track fit.*

The coordinates at a generic point of the helix can be parameterized as:

$$\begin{cases} X = X_H + QR(-\sin \phi + \sin \phi_H) \\ Y = Y_H + QR(+\cos \phi - \cos \phi_H) \\ Z = Z_H + s(\phi) \cot \phi . \end{cases} \quad (7.3)$$

The three-momentum components are given by:

$$(p_x, p_y, p_z) = (p \cos \phi \sin \theta, p \sin \theta \sin \phi, p \cos \theta) . \quad (7.4)$$

7.1.3 Vertex finding

The track parameters obtained in the fit phase are the starting point for the vertex finding. The goal of the pattern recognition phase for the vertices is to find the primary vertex. Each vertex is defined by the trajectories of the tracks

“forced” to its position. A detailed description of this process can be found in [109]. The VCTRAK package can be run in two modes:

- A) **“primary vertex only” mode** which does not reconstruct secondary vertices.
- B) **“multi-vertex” mode** which finds a primary vertex compatible with the existence of secondary vertices. The execution time is obviously longer but there are some advantages:
 - many events in which the primary vertex is not revealed in the A) mode now can be reconstructed (usually they are events with a low multiplicity of primary tracks and many secondary tracks).
 - The primary vertex is identified in a “cleaner” way because tracks contaminating the primary vertex reconstruction now are associated to secondary vertices.

7.1.4 MVD information

At the end of 2002 a new version of VCTRAK including the MVD information became available; the improvements with respect to the old version which used only CTD information are the following:

- track finding efficiency: using the MVD already in the pattern recognition stage, an efficiency improvement of $\sim 3\%$ can be obtained (from 93.5 % using only CTD information to $\sim 97\%$ including also the MVD information)
- trajectory precision: MC studies have shown that the precision in the trajectory determination is significantly improved, as can be noticed in Fig. 7.4 where the distribution of the variable QD_H , and the z coordinate of closest approach, Z_H , are plotted
- vertex finding: the primary vertex resolution is improved as well as the efficiency in the identification of secondary vertices. In Fig. 7.5 a) c) e) the primary vertex resolution in the different x , y and z components using CTD only information is shown whilst Fig. 7.5 b) d) f) show the same resolutions using also the MVD hit information.

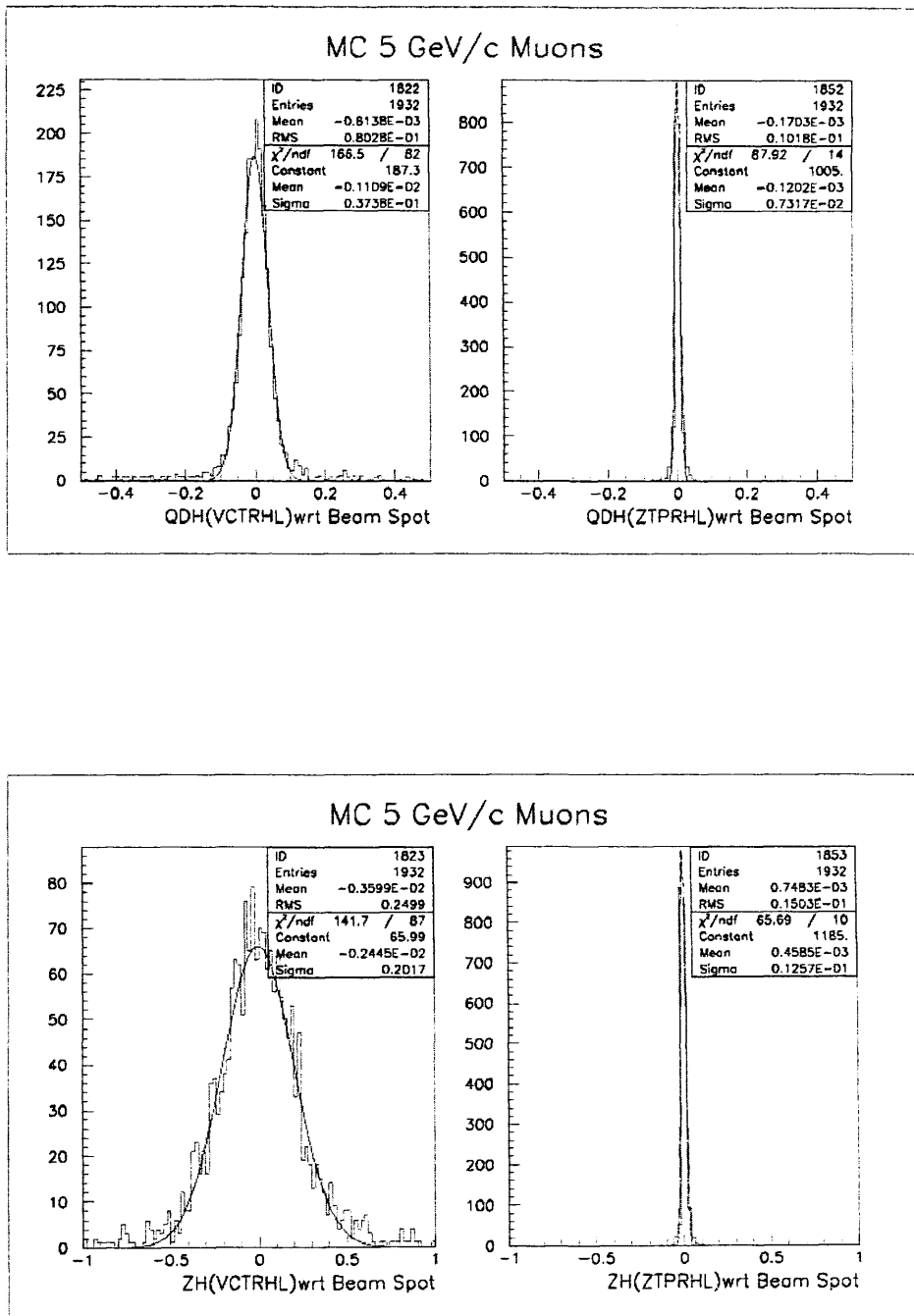


Figure 7.4: Distributions of the coordinates QD_H (top) and Z_H (bottom) of distance of closest approach (in cm) used in the fit; in the left column plots only the CTD info was used, in the right column MVD hit info was also taken into account [110].

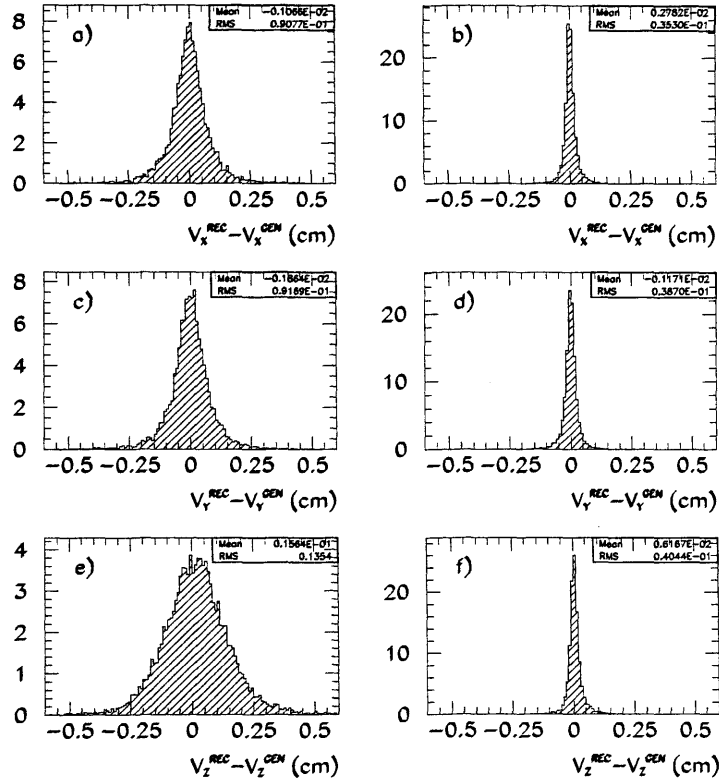


Figure 7.5: Distributions of the primary vertex coordinates in a beauty photoproduction Monte Carlo event sample; on the left column (a), c) and e)) only the CTD information was used. In the right column (b), d) and f)) the MVD hit information was also taken into account [111].

7.2 Beam spot

For this thesis, the precision on the reconstruction of the primary vertex plays an important role, affecting the measurement of the impact parameter of the tracks considered. In order to achieve the best resolution for the x and y coordinates, an average vertex position was determined on a run-by-run basis, i.e. the beam spot was re-calculated averaging the primary vertex positions for all the events in a run, after applying some quality cuts on the tracks participating in the fit and background reduction cuts. A detailed description of this procedure is given in Chapter 8.

7.3 Jet algorithm

The features of the jets in a hadronic final state are related to those of the partons from which they originate. However, jets are complex objects, and they are not uniquely defined in QCD: their definition relies on the algorithms used to reconstruct them. In the Snowmass workshop in 1990 [113] some criteria were fixed to be satisfied by every jet reconstruction algorithm. In particular, two requirements have to be fulfilled, in order to define an *infrared* and *collinear-safe* algorithm, reconstructing jets in the proper way:

- the results must be independent of the fact that one parton can split into two partons moving collinearly, or, from the experimental point of view, that a particle can release energy in two adjacent calorimeter cells. This dependence in fact causes collinear divergences in the theoretical calculations, which disappear if no distinction is made between two particles having energy $E_1 + E_2 = E$ and one single particle of energy E , moving in the same direction. From the experimental point of view, this means that the results are independent from the detector *granularity*;
- the results must be independent of the emission of very low energy particles; this fact causes infrared divergences in the theoretical calculations, removed by integration. In experiments these small energy deposits are related to the noise of the detector, removed by using thresholds or corrected by suitable algorithms.

Jet algorithms for the analysis of photoproduction processes have to fulfill two further requirements: they have to treat the proton and, if present, the photon remnant in a proper way, that means, the remnants have to be separated from the jets and not influence their search. Moreover, in photoproduction processes in general the laboratory frame is different from the frame of physical interest (i.e. the γp centre-of-mass frame). Nevertheless, the interesting frames are usually Lorentz boosted along the beam direction with respect to the laboratory frame. Therefore the jet algorithm has to be independent of this kind of transformation: this can be done by reconstructing jets using their transverse energy in a pseudorapidity-azimuth plane ($\eta - \phi$).

In ZEUS jet reconstruction is performed through *cone* and *clustering* algorithms. The clustering approach has the advantages of unambiguously assigning objects, i.e. the treatment of overlapping jets is clear, and the assignment of hadrons to jets can be done using the same procedure both in theoretical calculations and in experiments. This is the reason why here a clustering algorithm has been used to reconstruct jets, namely the k_T algorithm [114], as implemented in the KTCLUS [115] library.

The resolution variable used by the k_T algorithm to identify the jets is the relative transverse momentum, k_T , between particles. The use of this variable follows from the fact that, with the present understanding of perturbative QCD, the jets are not sprays of hadrons confined in cones of fixed angle. Soft hadrons produced coherently by the fragmentation of hard partons should be assigned to the jet of the hard parton nearest in angle, independently of the actual value of its angular distance [115][116]. This means that the jets have an effective radius depending on the hardness of the jet itself and on the colour flow of the hard subprocess.

The clustering procedure of the k_T algorithm is performed using the following iterative procedure:

1. the collision final state is described through a set of four-momentum objects p_i . The initial p_i can be the single particle four-momenta or the energy deposits inside the calorimeter (which can be improved using the information reconstructed by the tracking devices). The masses of these objects $m_i = \sqrt{p_i^2} \ll |p_{Ti}|$, where p_{Ti} is the transverse momentum of the i^{th} -object. The algorithm recursively groups pairs of objects to form

new objects, merging objects with almost parallel momenta. A parameter R characterises the measurement of the “distance” between two candidate objects to be merged. Every i^{th} -object is characterised by its pseudorapidity $\eta_i = -\log(\tan \frac{\theta_i}{2})$, its azimuthal position ϕ_i and transverse energy E_T^i .

2. For each object it is possible to define:

$$d_i = E_{T,i}^2, \quad (7.5)$$

which measures the distance from the beam-axis and for each pair:

$$d_{ij} = \frac{\min(E_{T,i}^2, E_{T,j}^2) [(\eta_i - \eta_j)^2 + (\phi_i - \phi_j)^2]}{R^2} \quad (7.6)$$

where $R = 1$ is assumed in this thesis.

3. The quantity:

$$d_{min} = \min(d_i, d_{ij}) \quad (7.7)$$

is determined.

4. If $d_{min} = d_{ij}$, the i and j objects are recombined into a new R object. The recombination scheme used in this thesis, known as “E-scheme”, combines the 4-momenta of i and j like:

$$P_k = P_i + P_j \quad (7.8)$$

and produces massive jets.

5. If $d_{min} = d_i$, the i^{th} -object is removed from the list and is added to the final jet list.
6. Re-start from step 2.

This procedure is re-iterated until all the starting objects are processed.

7.4 Reconstruction of the hadronic system

The measurement of particle energy is fundamental for the reconstruction of the event properties. The energy resolution of the CAL (see Eqs. 3.6, 3.7 in Chapter 3) goes like $\sigma(E)/E \sim a/\sqrt{E} \oplus b$ improving as the particle energy increases, whilst the resolution of the tracking system behaves like $\sigma(p_T)/p_T \sim a \cdot p_T \oplus b \oplus c/p_T$ leading to better energy estimation for lower energy particles (see Fig. 7.6). The

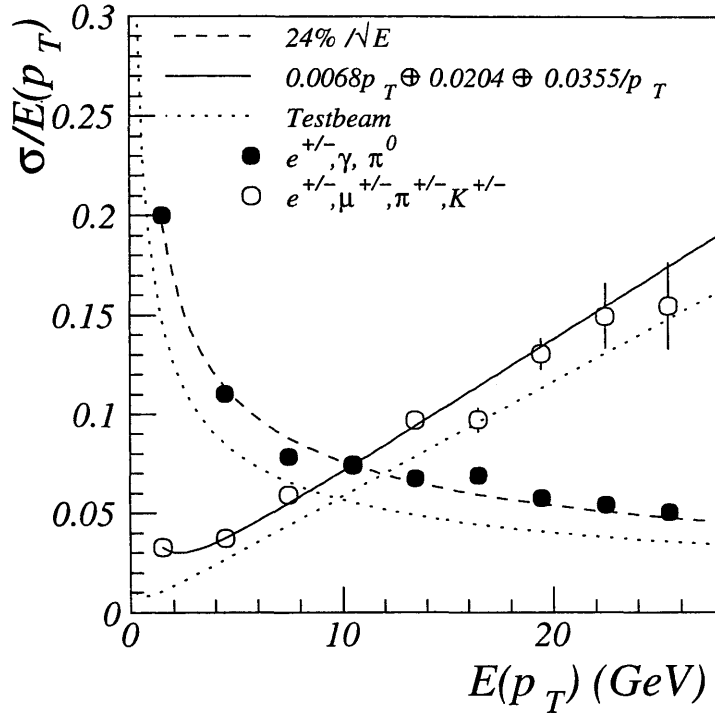


Figure 7.6: Resolution from single particle MC simulation. The track transverse momentum resolution in the CTD (open markers) and the CAL energy resolution (full markers) are shown [112].

relationship between the CTD and BCAL resolution for electrons and charged hadrons, as recently measured, is also shown in Fig. 7.7 a) and 7.7 b), respectively, as a function of the polar angle. The range chosen lies within the BCAL and away from its edges. The BCAL energy resolution for electrons, in the energy range shown, is $\sigma(E_e) \approx 0.193E_e^{1/2}$ [117], where E_e is the electron's energy in GeV and the relationship assumes 1 X_0 of dead material. The equivalent formula for the hadronic energy resolution is $\sigma(E_h) \approx 0.35E_h^{1/2}$, where E_h is the hadron's energy in GeV. The CTD energy resolution for both electrons and charged hadrons

is given by $\sigma(E) \approx 0.0058E^2 \sin \theta \oplus 0.0065 \oplus 0.0014/\sin \theta$, where E is the charged particle's energy in GeV and θ , its polar angle. The poorest CTD resolution corresponds to $\theta \approx \pi/2$, where the energy of electrons O(10 GeV) and hadrons O(15 GeV), or higher, begins to be better resolved by the BCAL.

To benefit from the most accurate energy determination in both energy ranges, the track reconstruction and the CAL energy measurement are combined into *energy flow objects* (EFOs) [112]. The tracking information is mainly used below 10-15 GeV and the calorimetry energy measurement above to form four-vectors representing the oriented energy deposit of particles traversing the detector.

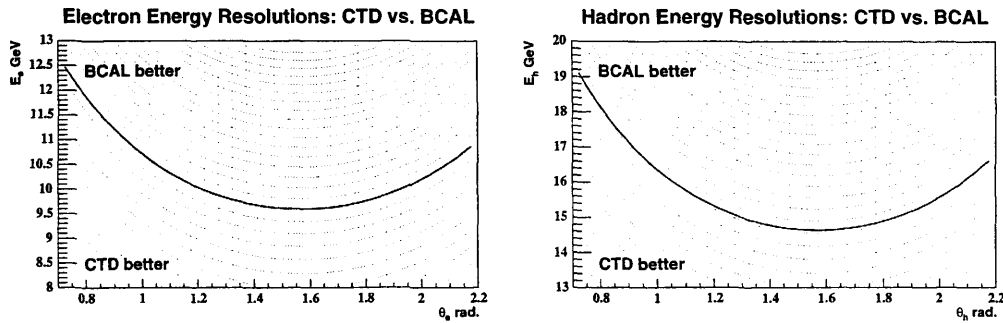


Figure 7.7: The relative resolution of the CTD and BCAL for reconstructing the energy of (a) an electron, E_e and (b) a charged hadron, E_h , as a function of E_e and E_h and polar angle, θ_e and θ_h , for electrons and hadrons, respectively. The contours show the rate at which one reconstruction improves the other [117].

7.4.1 Reconstruction of Energy Flow Objects (EFOs)

The use of EFOs is justified by the fact that the hadronic energy has both a charged particle and a neutral particle component. Both are measured by the calorimeter, but a large fraction of the charged particles are also measured by the tracking detectors. In many cases, especially when the charged particles have low energies, or when they cross a large thickness of dead material before being detected, the resolution of the tracking devices is better than that of the calorimeter.

The use of the EFOs rather than the usual energy deposits in the calorimeter is also driven by the design of the ZEUS calorimeter (see Chapter 3), which

is divided in three parts, the forward (FCAL), barrel (BCAL) and rear (RCAL) calorimeter. This spatial separation is a serious complication for a local clustering algorithm in handling the energy deposits of a single particle which is not confined within a single part of UCAL, since the energy will be split in two or more clusters. Because of these complications, the EFO clustering algorithm is done in two steps [112]:

- the first stage of the clustering procedure is performed in each calorimeter layer separately. Each cell with sufficient energy is considered a candidate to be connected with one of its neighbours. The connection is made with the nearest neighbour with the highest energy or with the highest energy cell next to the neighbour. This procedure is repeated for each cell and produces a unique assignment of a cell to a so-called *cell island* (see Fig. 7.8).

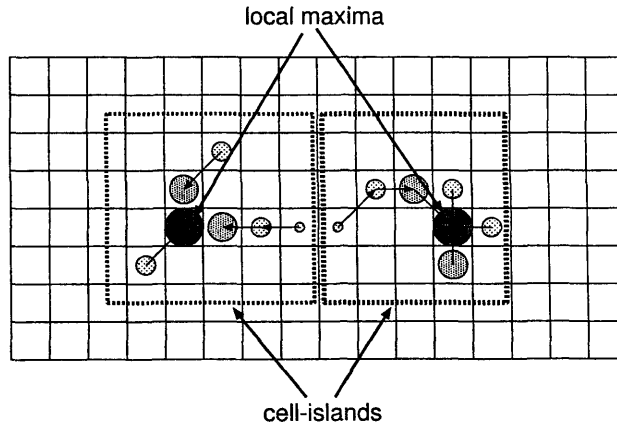


Figure 7.8: A schematic diagram showing how cell-islands are formed.

- The second stage of the clustering procedure collects the cell islands belonging to a shower of a single particle or a jet of particles into a so-called *cone island*. The matching of cell islands starts from the outermost hadronic layer of the calorimeter and proceeds inwards. The angular separation between cell islands of different layers is calculated in $\theta - \phi$ space and translated to a probability according to a distribution determined by a single pion MC. Links with high probability are accepted provided that the probability is larger than a threshold. Once the linking procedure has been completed, the cone islands are generated by combining all calorimeter cells

which point to the same cone island in the electromagnetic layer.

The cone island centre is calculated as the energy weighted mean of the cell centres which have been corrected for the imbalance of the two photomultiplier measurements per cell. The energy weight is determined logarithmically rather than linearly to cope with the observed systematic bias due to the varying cell projectivity resulting from the CAL geometry.

For the track reconstruction (see Sec. 7.1), vertex fitted tracks with hits in at least 4 superlayers are selected in the transverse momentum range $0.1 < P_T^{track} < 20$ GeV. If the track has hits in more than 7 superlayers, the upper transverse momentum cut is raised to $P_T^{track} < 25$ GeV. The tracks are extrapolated to the inner CAL surface taking into account the magnetic field geometry and further into the CAL by a linear approximation using the track momentum vector at the CAL surface.

The matching of a track to a cone island uses the distance-of-closest-approach (DCA) method. A match is assigned between the extrapolated track and the

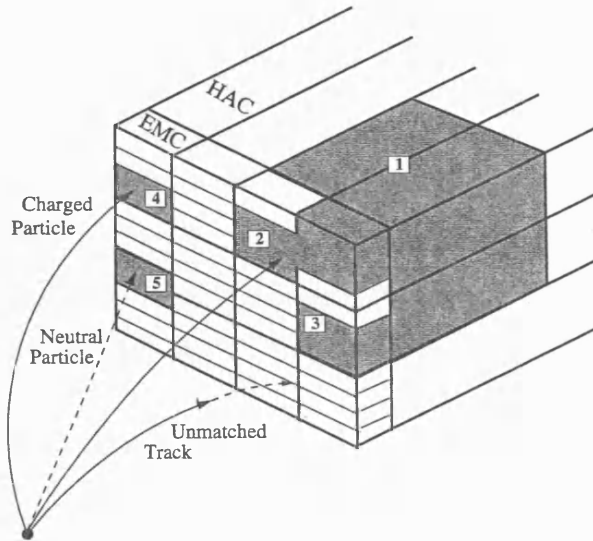


Figure 7.9: *Reconstruction of EFOs by a match between CAL cells clustered into cone islands (HAC cell 1 and EMC cell 2 and 3 are joined to form a cone island) and tracks. The different match categories of a charged particle (track is matched to cone island 4), neutral particle (no track is matched to cone island 5) and unmatched track are shown.*

cone island centre (see. Fig. 7.9) if the distance is closer than the cone island

radius or a minimal radius of $r_{min} = 20$ cm optimized using MC simulations to maximize the track-island matching efficiency for single particle CAL clusters:

$$DCA \leq \max(r_{min}, r_{island}) . \quad (7.9)$$

The set of associated track-islands, the EFOs, are then processed according to the following criteria:

- good tracks not associated to any calorimetric object are counted as charged particles, and the CTD information is used. The particle is assumed to be a pion;
- calorimeter objects not associated with any track are counted as neutral particles and the calorimeter information is chosen;
- for calorimeter objects associated with more than three tracks the calorimetric information is chosen.

In the case of one-to-one track-island matching, the track information is used instead of that from the UCAL if these two requirements are fulfilled: the energy deposit in the calorimeter has to be due to the associated track alone, and the momentum resolution of the track has to be better than the energy resolution of the corresponding calorimetric object (see Fig. 7.6), i.e. if both the following requests are satisfied:

- the track momentum exceeds the energy measurement in the CAL within the resolution on the measured ratio E_{cal}/p :

$$E_{cal}/p < 1.0 + 1.2 \cdot \sigma(E_{cal}/p) , \quad (7.10)$$

where $\sigma(E_{cal}/p) = \sigma(E_{cal}/p^2)\sigma(p) \oplus (1/p)\sigma(E_{cal})$.

- That:

$$\sigma(p)/p < \sigma(E_{cal})/E_{cal} , \quad (7.11)$$

where $\sigma(p)$ and $\sigma(E_{cal})$ are the resolutions of the momentum from the tracking and the energy in the CAL respectively.

Since muons are minimum ionising particles (MIPs) and lose their energy predominantly by ionisation, the measured energy in the CAL is not proportional

to the momentum. Therefore, EFOs having the properties of a muon are treated differently and the tracking information is favoured over the energy measurement if:

- $E_{cal} < 5 \text{ GeV}$;
- $E_{cal}/p < 0.25$;
- $P_T < 30 \text{ GeV}$.

The more complicated 1-to-2, 1-to-3, 2-to-1 and 2-to-2 track-island matches are treated similarly to the 1-to-1 match, substituting the UCAL energy and the CTD momentum with the sum of the energies of the islands and the sum of the momenta of the tracks respectively.

Finally, in the case where a single track is matched to two or more islands, and the energy of the UCAL is favoured, the more precise angular information of the track is used.

7.4.2 Correction of the cone islands

Comparisons between data and MC simulations have shown discrepancies in the reconstruction of EFOs using calorimetric islands [118, 119]. The following corrections have therefore been applied to the EFOs:

Energy loss in inactive material: Energy losses due to dead material are generally difficult to fully implement into the MC simulation. A detailed dead material map is available and has been used to write correction algorithms. The material constituting the beam pipe, the tracking devices and the solenoid correspond to a number of radiation lengths varying from 1 to 3 in the central part of the detector (see Fig. 7.10) and the energy loss of the particles, especially of those having low momenta, can be significant in such a thickness. Since energy losses due to the presence of dead material are difficult to include with sufficient precision in the detector simulation, the correction is done offline, and it is parametrized as a function of the energy and of the polar angle of the particles.

Calorimeter geometry: The zones of the cracks between the calorimeter sectors are not well simulated and corrections are introduced offline.

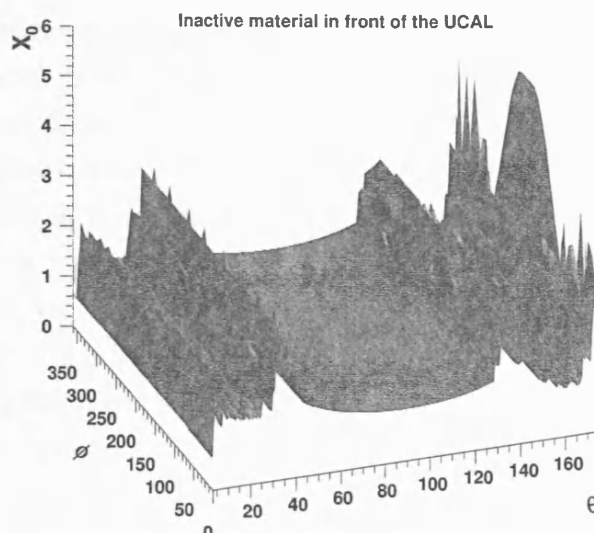


Figure 7.10: *Distribution of the inactive material in front of the UCAL in units of the radiation length, X^0 , in the $\theta - \phi$ plane, as implemented in the simulation of the detector [118].*

Energy overestimation of low momentum hadrons: Protons and pions with momenta below ~ 1 GeV lose energy mainly through ionisation without hadronic interactions. In this case, the CAL is no longer compensating ($e/h \sim 0.6$). This effect causes an overestimation of the energy of low-momentum hadrons which has to be corrected.

7.4.3 Correction for the presence of a muon

Muons are particles which do not release all their energy in calorimeters (*minimum ionizing particles, mips*). Therefore if the energy as reconstructed by the UCAL is used, rather than the information from the CTD, the obtained energy of a jet containing a muon will be systematically lower than the true value. As mentioned in section 7.4.1, the EFO algorithm should in principle distinguish muons from the other particles, and use tracking rather than calorimeter information for their reconstruction. Nevertheless, since this step is crucial for an accurate reconstruction of the jet, another correction has been introduced in order to modify the EFO parameters when the main algorithm does not succeed in the correct identification of the muon.

First the muon reconstruction algorithms find the candidate muons and perform

the matching between the segments in the muon chambers and the tracks in the inner tracking devices, including also the momentum of the particles. Some minimal cuts on the candidate quality are applied: the muons are required to have a momentum greater than 2 GeV, as measured by the CTD (a particle with lower momentum cannot reach the outer muon chambers) and a matching probability greater than 0.01 is required. Once the EFO containing the good quality muon has been identified, its energy deposit is analysed. The EFO energy is considered compatible to that of a mip if it is between 50% and 150% of the energy predicted for a mip in the same angular range (in Fig. 7.11 the energy released by a mip in the UCAL as a function of the polar angle θ is shown). Then, the following

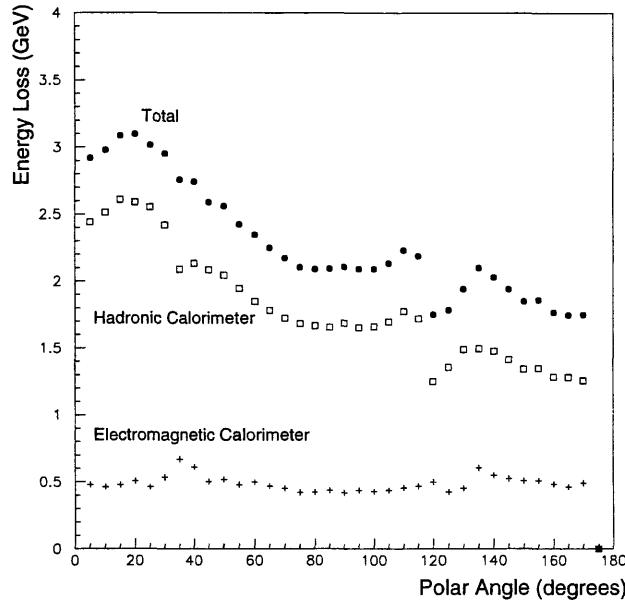


Figure 7.11: *Energy loss of a muon in the CAL as a function of the polar angle θ (full circles) and the energy fractions in the electromagnetic (crosses) and hadronic (open squares) calorimeter sections [119].*

correction criteria are used:

- If the EFO uses the track information for the energy determination, no action is taken.
- If the EFO uses the CAL measurement for the four-vector determination and the energy of the EFO is between 50% and 150% of the predicted energy loss of a muon, the EFO four-vector is determined from the reconstructed muon properties, as given by the CTD.

- If the EFO uses the CAL measurement for the four-vector determination and the energy of the EFO is larger than 150% of the predicted energy loss of a muon $E_{EFO} > 1.5E_{MIP}$, a new EFO corresponding to the reconstructed muon is added and the mip contribution is subtracted from the initial EFO. Now, the muon contribution to the hadronic system is correctly reconstructed.
- If the EFO uses the CAL measurement for the four-vector determination and the energy of the EFO is less than 50% of the predicted energy loss of a muon $E_{EFO} < 0.5E_{MIP}$, the EFO four-vector is determined from the reconstructed muon properties, as given by the CTD.

Jet parameters and the hadronic final state are in general now better reconstructed, using corrected EFOs rather than CAL cells.

In Fig. 7.12 and 7.13 the transverse energy, E_T^{jet} , and pseudorapidity, η^{jet} , are compared to the reconstructed quantities. The two reconstructed jets with highest transverse energy are matched with the true jets requiring the distance between the jets in the $\eta - \phi$ plane:

$$d_{\eta\phi} = \sqrt{(\eta_{jet}^{rec} - \eta_{jet}^{true})^2 + (\phi_{jet}^{rec} - \phi_{jet}^{true})^2} \quad (7.12)$$

to be less than 0.7. The true jets were reconstructed starting from the B hadrons. The reconstructed and the true variables are well correlated.

7.5 Muon reconstruction

Due to the different structure of the BRMUON and FMUON detectors (see Chapter 3) two different muon reconstruction packages were used in this analysis, one for the muon identification in the forward region, MPMATCH [120], and one for muons in the barrel and rear region, BREMAT [121]. These two algorithms will be briefly described in this section, more details can be found in [120, 121].

7.5.1 Forward muon reconstruction: MPMATCH

The MPMATCH package has the main purpose of matching segments reconstructed by the FMUON detector with tracks reconstructed by the inner track-

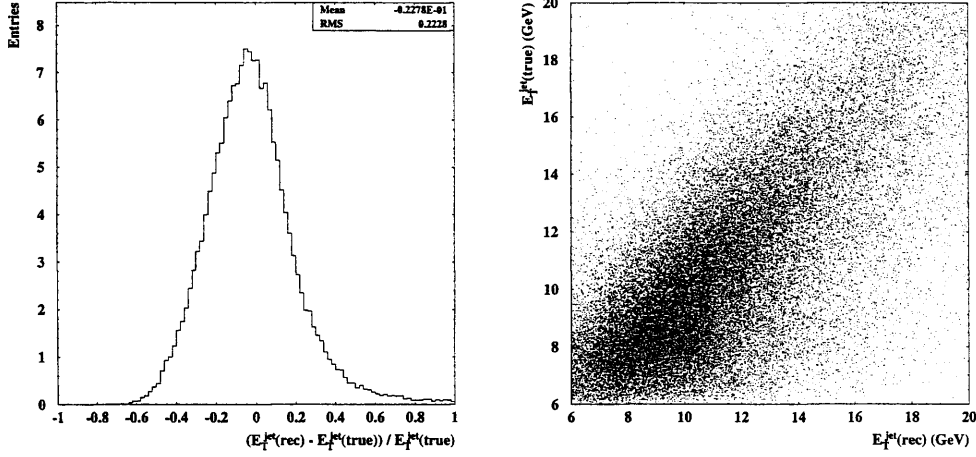


Figure 7.12: The resolution, $(E_T^{jet}(rec) - E_T^{jet}(true)) / E_T^{jet}(true)$ (left) and $E_T^{jet}(rec)$ vs $E_T^{jet}(true)$ (right), plotted for a beauty MC sample. The reconstructed $E_T^{jet}(rec)$ is calculated taking as input the EFOs, after applying all the corrections described in the text. The sample was obtained by mixing Monte Carlo samples (direct, resolved and excitation) normalising them according to their predicted luminosities.

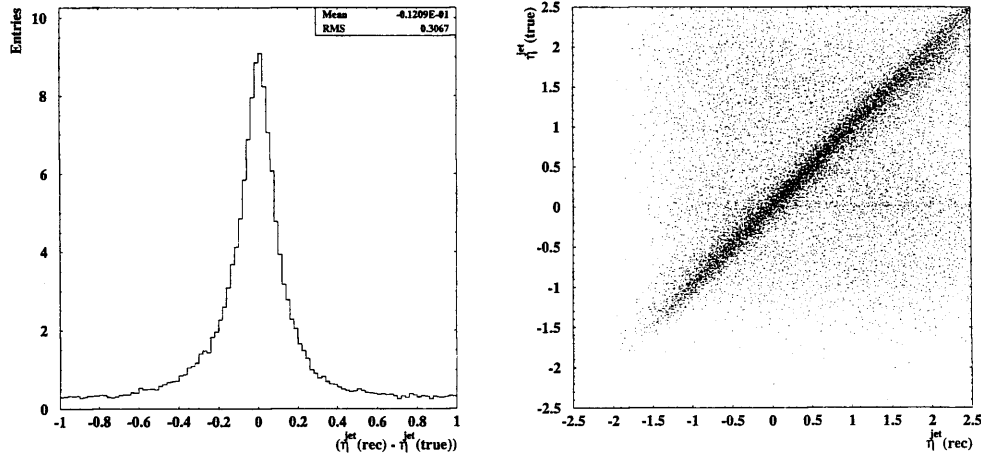


Figure 7.13: The resolution, $(\eta_{jet}^{rec} - \eta_{jet}^{true})$ (left) and η_{jet}^{rec} vs η_{jet}^{true} (right), plotted for a beauty MC sample. The reconstructed η_{jet}^{rec} is calculated taking as input the EFOs, after applying all the corrections described in the text. The sample was obtained by mixing Monte Carlo samples (direct, resolved and excitation) normalising them according to their predicted luminosities.

ing devices, mainly the CTD (see section 3.4). It has been developed for the selection and the reconstruction of a clean muon sample in inelastic events with non-isolated muons, and therefore the angular coverage is limited to the overlapping region between the FMUON and the CTD.

An FMUON track is defined by five parameters in the ZEUS reference frame:

$$(x, y, dx/dz, dy/dz, Q/p). \quad (7.13)$$

The search for a match starts from a FMUON reconstructed track. A θ and ϕ “road” is opened around the track, and tracks from the CTD are considered inside the road. The FMUON track, with its parameters and its covariance matrix, is then extrapolated backwards to the z coordinate measured by the CTD, using the GEANE [122] package. Then, a fit between the extrapolated FMUON track and the CTD track parameters is performed using a Kalman filtering technique [123]. If in the CTD there is more than one track inside the road, a choice based on the χ^2 probability is made so that just one track is retained. The procedure is then repeated for all available FMUON tracks. Once a match is found, a vertex fit is done, extrapolating the FMUON track towards the z of the reconstructed vertex, and performing a fit between the parameters of the extrapolated track and those of the CTD track, the x and y coordinates of the reconstructed vertex and the direction and momentum of the track.

7.5.2 Barrel and rear muon reconstruction: BREMAT

The *Barrel and Rear MATching* package, BREMAT [121], is used to match segments reconstructed in the barrel and rear muon detectors to tracks measured in the inner tracking detectors, mainly the CTD. The limited streamer tubes, and the associated strips, used in the BRMUON detector have a resolution of the order of ~ 1 mm on both coordinates they measure, x and y (see section 3.6.2). Moreover the momentum resolution for most of the muons is dominated by multiple scattering in the iron yoke placed between the inner and the outer chambers. The most powerful way to reconstruct muons in this context requires that measurement errors, multiple scattering and energy losses are correctly taken into account, and this is the technique used by BREMAT.

The main purpose of this algorithm is to find candidate muons, associating inner detector tracks to segments in the muon chambers and providing the resulting matching χ^2 . The main input to the algorithm is the MBXYSG table [124], containing the information on the reconstructed segments in the BRMUON chambers, and the VCTRHL table [125], containing the parameters of the tracks reconstructed by the inner detectors. When a segment in the muon chambers is found, BREMAT looks for candidates to be associated to it in the list of all the tracks reconstructed by the inner tracking devices, predominantly the CTD. A loose preselection is done on the tracks to be associated to the muon chamber segments:

- the momentum p of the track has to be $p > 1$ GeV; this is a minimal request for tracks that have crossed all the calorimeter before being identified by the chambers;
- the polar angle θ of the track has to be $\theta > 20^\circ$ (to ensure good acceptance of the CTD);
- the track has to start from CTD superlayer 1 and to extend at least to superlayer 3 (see section 3.4); since SL 3 covers up to $\theta = 18.4^\circ$ this cut is roughly equivalent to the previous one.
- the impact parameter of the track, D_H , has to be $|D_H| < 10$ cm;
- the z coordinate at the point of closest approach to the reference point $(x, y) = (0, 0)$ has to be $|z_H| < 75$ cm;
- $\chi_{track}^2/n.d.f. < 5$;
- $\Delta \leq 150$ cm, where Δ is the distance between the central point on the BRMUON segment and the straight line obtained by extrapolating the CTD track to the calorimeter entrance.

Tracks passing the preselection are extrapolated through the calorimeter using the GEANE [122] package. The extrapolation of the parameters and error matrix of the candidate track proceeds from the outer surface of the inner tracking devices, through the calorimeter up to a reference surface on the inner muon chambers, where matching is done.

For the best treatment of the low-momentum muons, the track extrapolation is

done outwards, starting from the inner region, since such muons suffer large energy losses compared to the initial energy. With the GEANE package, tracks that completely lose their energy before reaching the chambers are also simulated.

The output track parameters and error matrix at the reference surface are usually referred to as *predictions*. The predicted variables and error matrix are obtained in a convenient Cartesian parametrization, related to the local coordinate frame of each sector. The slopes of the track x' and y' are also given in order to determine the predicted direction of the particle. The fifth coordinate is Q/p , that can be measured by the BRMUON detector just in the case the muon reaches the outer chambers.

Naming ϵ_{M_i} and ϵ_{P_i} , respectively, the measured and the predicted track parameters at the reference surface, the residuals are defined as $\delta_i = \epsilon_{M_i} - \epsilon_{P_i}$. If the coordinates of the Cartesian parametrization are written as $(x, y, x', y', Q/p)$ the matching χ^2 is given by:

$$\chi^2 = \sum_{i,j} S_{ij}^{-1} \delta_i \delta_j \quad (7.14)$$

where the sum goes from 1 to $n = 4$ or 5, depending on whether the momentum is included or not in the χ^2 , and S^{-1} is the inverse of the covariance matrix of the residuals:

$$S_{ij} = \sum_{k,l} S_{ij}^{-1} T_{ik} (\sigma_{track}^2)_{kl} T_{lj}^T + (\sigma_{random}^2)_{ij} + (\sigma_{BRMU}^2)_{ij} \quad (7.15)$$

with $k, l = 1, \dots, n$; T is the transport matrix, between the start and the stop of the swim, σ_{track}^2 is the error matrix of the inner detector track, σ_{random}^2 is the error matrix due to multiple scattering and energy loss, and σ_{BRMU}^2 the error matrix of the BRMUON segment from the MBXYSG table. The first two terms are calculated by steps during the GEANE extrapolation using the detailed geometry of the ZEUS detector and the magnetic field map. BREMAT makes a loose cut on the matched tracks, considering as matching the tracks having $\chi^2 < 100$.

The resolution of muon P_T and η , together with the correlation between their true and reconstructed variables are shown in Fig. 7.14 and 7.15. The resolution on these quantities is reasonable.

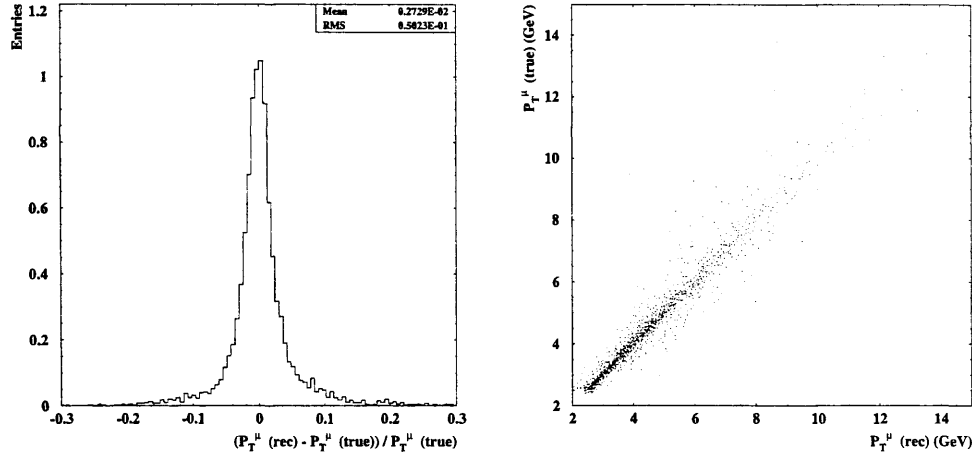


Figure 7.14: The resolution, $(P_T^\mu(\text{rec}) - P_T^\mu(\text{true})) / P_T^\mu(\text{true})$ (left) and $P_T^\mu(\text{rec})$ vs $P_T^\mu(\text{true})$ (right), plotted for a beauty MC sample. The reconstructed $P_T^\mu(\text{rec})$ is calculated taking as input the EFOs, after applying all the corrections described in the text. The sample was obtained by mixing Monte Carlo samples (direct, resolved and excitation) normalising them according to their predicted luminosities.

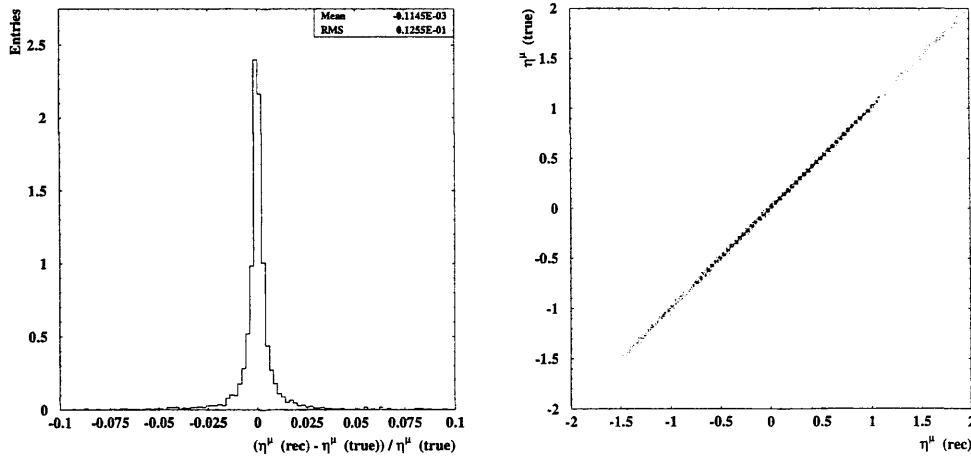


Figure 7.15: The resolution, $(\eta^\mu(\text{rec}) - \eta^\mu(\text{true})) / \eta^\mu(\text{true})$ (left) and $\eta^\mu(\text{rec})$ vs $\eta^\mu(\text{true})$ (right), plotted for a beauty MC sample. The reconstructed $\eta^\mu(\text{rec})$ is calculated taking as input the EFOs, after applying all the corrections described in the text. The sample was obtained by mixing Monte Carlo samples (direct, resolved and excitation) normalising them according to their predicted luminosities.

7.6 Trigger chain for online data selection

The trigger chain used to select dijet events is described in detail in this section. The detector simulation takes into account the simulation of the trigger system therefore the same trigger preselection is also applied to the MC samples. The selection requires trigger slots on the third level which are combinations of event quantities calculated on the third level and first and second level trigger slots. The trigger selection consists of at least one of the following third level trigger slots (inclusive *OR* of the three slots):

TLT HFL 5: Inclusive Dijets

- two jets with $E_T > 4.5$ GeV and $|\eta| < 2.5$
- CAL: $p_z/E < 0.95$
- CAL: $E - p_z < 100$ GeV.

TLT HFL 13: Inclusive Semi-Leptonic Muon

- at least one forward or barrel/rear muon found on the SLT
- at least one barrel/rear muon
- muon reconstructed by a hit in barrel/rear muon chambers with matching CTD track by GLOMU [126]
- CAL: total $E_T > 9$ GeV.

TLT HFL 25: Muon plus Dijets

- at least a forward or barrel/rear muon found on the SLT
- a hit in barrel/rear muon chambers with matching CTD track by GLOMU
- two jets with $E_T > 3.5$ GeV and $|\eta| < 2.5$
- CAL: $p_z/E < 1.0$
- $E - p_z < 100$ GeV.

7.7 Offline data selection

Having selected events using the trigger chain described above, the final data sample is chosen by applying cuts on the variables of interest for the analysis. Some of these, for example the calorimetric variables, need to be corrected before cutting on them, in order to make them more similar to the kinematic region of the measurement. The motivations and details of the corrections will be described below. Our aim is to obtain, after applying all the cuts, a clean dijet sample with an enriched $b\bar{b}$ component.

7.8 Photoproduction selection

The photoproduction regime is defined for photon virtualities $Q^2 < 1 \text{ GeV}^2$ (see Chapter 1). Two techniques have been used to veto events from the DIS regime.

7.8.1 Veto on reconstructed electrons

To select only photoproduction events, candidates from the DIS regime have to be rejected. In DIS events the electron is scattered at a sizeable angle in contrast to photoproduction events where the scattered electron escapes undetected inside the beam pipe. Therefore, to select only photoproduction events, events with a reconstructed electron in the final state are rejected. The SINISTRA package [127] is used in this thesis to analyse energy deposits in the electromagnetic and hadronic parts of the CAL and distinguishes between electromagnetic and hadronic clusters. The algorithm proceeds in two steps: first, SINISTRA takes as input the energies of the calorimeter cells, and, using a neural network, gives as output the probability for each cluster to be electromagnetic or hadronic. Then, the second part of the algorithm selects the scattered electron from the list of the candidates.

The algorithm can be used in different ways; for the analysis reported here, the choice has been made to require the candidate positron to be reconstructed only by the UCAL, with no request of an associated track in the CTD. The motivation behind this choice is the fact that the DIS cross section falls rapidly as the Q^2 of the event increases. Therefore, in most of the DIS background events the outgoing lepton is scattered at a very small angle, and is hence detected by the

UCAL but not by the CTD, since it falls outside its coverage region.

SINISTRA gives as output the lepton candidate having the highest probability to be the scattered positron, provided its probability, $Prob_{el}$, is greater than 0.9. For this candidate also the energy deposited in the calorimeter, E_{el} , and the inelasticity, y_{el} , are given as output by the algorithm. The event is rejected if:

$$E_{el} > 5 \text{ GeV} \quad \text{and} \quad y_{el} < 0.9. \quad (7.16)$$

The request on y_{el} is made to reduce the risk of rejecting photoproduction events wrongly identified as DIS. Final state pions, electrons or photons, present in a photoproduction event, can be misidentified as the scattered lepton. In this case, however, the reconstructed y_{el} , is typically very large. Therefore, events with an electromagnetic deposit of considerable energy but high y_{el} are included in the analysis as photoproduction events.

7.8.2 Reconstruction of y with the Jaquet-Blondel method

Since identified DIS electrons are rejected in the selection and photoproduction events do not contain a reconstructed electron, the inelasticity has to be reconstructed using only the CAL and CTD measurements. The *Jaquet-Blondel* method [128] uses EFOs (see section 7.4.1) to reconstruct the inelasticity by:

$$y_{JB} = \frac{\sum_i (E_i - p_{z,i})}{2E_e}, \quad (7.17)$$

where E_i are the energies and $p_{z,i}$ the momenta parallel to the beam pipe of each reconstructed EFO, respectively. E_e is the energy of the incoming electron.

The corrections on the reconstructed EFOs (see section 7.4.2, 7.4.3) significantly improve the consistency between the reconstructed and the true y_{JB} [119]. After the complete event selection, the comparison shows a remaining difference between true and reconstructed y_{JB} (see Fig. 7.16) for the beauty quark sample consistent with the previous studies. In DIS events, the electron energy contributes to this measurement even if the electron is not identified yielding a fake y_{JB} of ~ 1 . A cut on y_{JB} is therefore applied to reject background from residual DIS:

$$y_{JB} < 0.8. \quad (7.18)$$

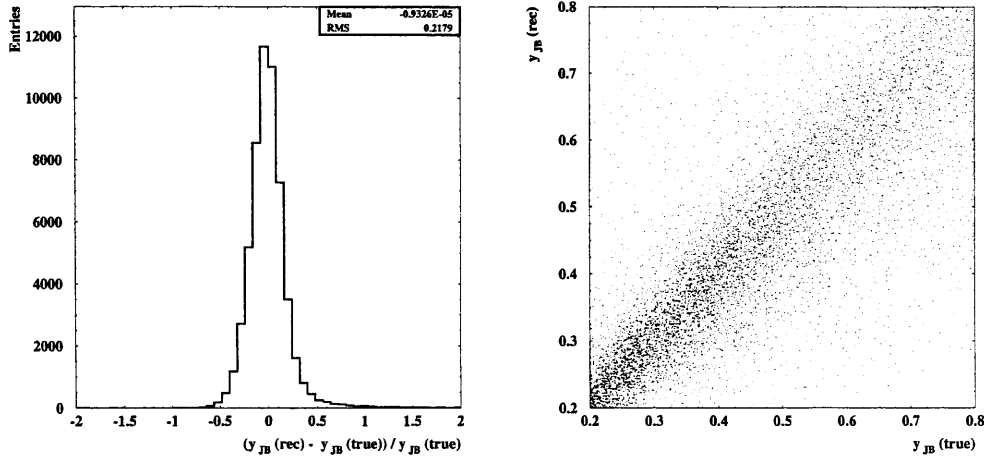


Figure 7.16: The resolution, $(y_{JB}(\text{rec}) - y_{JB}(\text{true})) / y_{JB}(\text{true})$ (left) and $y_{JB}(\text{rec})$ vs $y_{JB}(\text{true})$ (right), plotted for a beauty MC sample. The reconstructed y_{JB} is calculated taking as input the EFOs, after applying all the corrections described in the text. The sample was obtained by mixing Monte Carlo samples (direct, resolved and excitation) normalising them according to their predicted luminosities.

In Fig. 7.17, the y_{JB} distributions for a beauty MC sample before and after the selection cuts are shown.

7.9 Final selection

Summarizing the complete selection, events from the data and MC samples are required to fulfil the following cuts as well as the trigger preselection (see Sect. 7.6):

Photoproduction Selection

- rejection of the event if an electron is reconstructed with:

$$Prob_{el} > 0.9$$

$$E_{el} > 5 \text{ GeV}$$

$$y_{el} < 0.9$$

as described in section 7.8.1.

- cut on inelasticity using the Jaquet-Blondel method: $0.2 < y_{JB} < 0.8$ (see section 7.8.2).

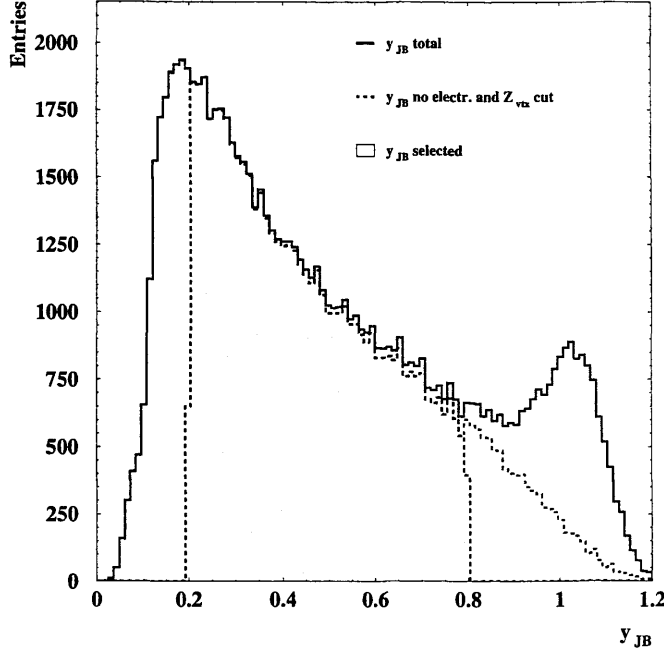


Figure 7.17: Distribution of y_{JB} for beauty PYTHIA MC. The sample was obtained by mixing Monte Carlo samples (direct, resolved and excitation) normalising them according to their predicted luminosities. The continuous line shows the total distribution of this variable in the photoproduction event sample considered, no cuts are applied. The dashed line indicates the events selected with no electron found in the event and a cut on the z vertex coordinate $|z_{vtx}| < 40$ cm. The final subsample of events considered is indicated by the dashed area.

Muon Selection

- At least one muon is reconstructed by the general muon reconstruction with:

$$P_T^\mu > 2.5 \text{ GeV}$$

$$|\eta^\mu| < 2.5.$$

These cuts on the muons were driven by the necessity to enrich the signal content of the sample, and to select a region where the muon detectors are well understood.

Jet Selection

- at least two jets are reconstructed by the KTCLUS algorithm using corrected EFOs; the following cuts were applied in order to select a region

where their reconstruction is well under control:

$$P_T^{jet1} \geq 7 \text{ GeV}$$

$$P_T^{jet2} \geq 6 \text{ GeV}$$

$$|\eta^{jet1,2}| < 2.5.$$

Jet-Muon association

- at least one muon associated to a jet:

$$P_T^{jet} \geq 6 \text{ GeV}$$

$$(P_T^{jet} - P_T^\mu) \geq 2 \text{ GeV}.$$

The second cut is applied to reject one-track jets produced by cosmic muons.

Additional cuts

On an event-basis the following cuts were required, mainly to reject beam-gas contamination:

vertex

- For the event, a vertex was required with: $|z_{vertex}| < 40 \text{ cm}$.

corrected EFOs Since beam-gas events are characterized by energy deposits around the beam-pipe region and possibly unbalanced P_T , the following cuts using tracking-CAL (EFOs) information were applied:

- $P_T/E_T < 0.5$
- $E_{T,rings} \geq 10 \text{ GeV}$ (E_T calculated excluding the two FCAL inner rings)
- $P_T \leq 10 \text{ GeV}$.

tracks As the beam-gas events can have a large number of tracks not-pointing to the vertex, the following cuts were applied:

- number of vertex-fitted tracks > 2
- $\frac{\text{total number of tracks}}{\text{number of vertex-fitted tracks}} \leq 10.0$.

About 1% of events have more than one muon-jet association.

7.9.1 Control distributions

Control distributions of the jet-muon quantities fundamental for this analysis are shown in Fig. 7.18. In all cases, the beauty (b), charm (c) and light flavour (lf) Monte Carlo samples after the event selection, scaled using the corresponding $P_T^{rel}-\delta$ fit results (see Chapter 10), are compared to the distribution from the data sample. Good agreement between data and Monte Carlo simulation is observed, validating the procedure adopted in this thesis to extract the beauty fraction.

In Fig. 7.19 control distributions for several event variables, after the applied selection, are shown; the Monte Carlo provides a good description of the data, proving the calorimetric and tracking variables used are well under control. As the tracking system plays a key role in this analysis, a closer look at CTD-MVD related quantities is shown in the control distributions of Fig. 7.20. In Fig. 7.20 a) and d) a shift in the distribution of the z coordinate of the primary vertex and in the z coordinate of distance of closest approach, respectively, is observed. The remaining variables are in general well described by MC, except the distribution of the impact parameter of the tracks (Fig. 7.20 c)) calculated with respect to the reference point $x = y = 0$. This disagreement in shape between data and MC will be discussed in detail in Chapter 9.

7.10 Muon efficiency corrections

The detector simulation is an important ingredient for the cross section measurement. Monte Carlo event samples simulating the actual detector output are used to determine the acceptance of the event reconstruction and selection. The implementation of the forward and barrel/rear muon chamber efficiencies in the detector simulation is not currently available. Therefore their efficiency simulation has to be corrected in the Monte Carlo samples on an event-by-event basis. These corrections are determined by the comparison of muon reconstruction efficiencies from simulated events with data events for well-understood samples [129, 53].

The decay $J/\psi \rightarrow \mu^+\mu^-$ (see Fig. 7.21) is chosen due to its simple and easily selectable topology of two isolated muons, where one muon is triggered and the efficiency of the other is measured.

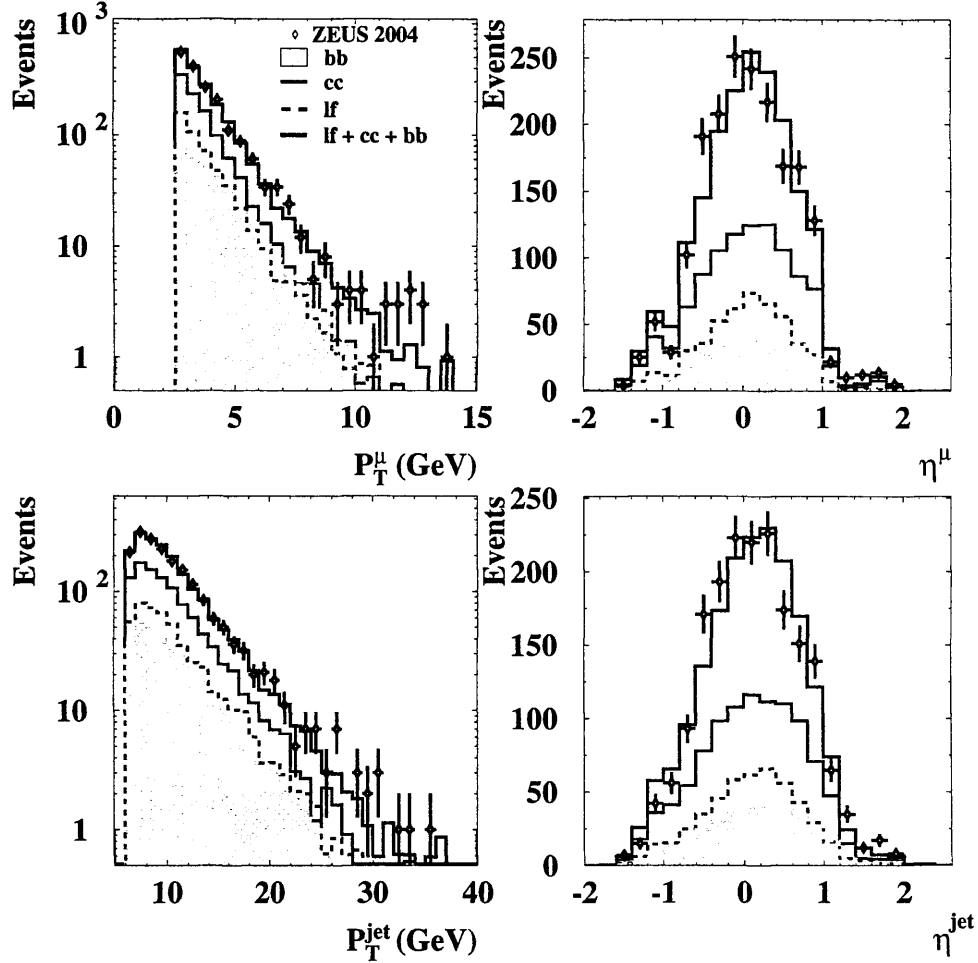


Figure 7.18: Control plots for the muon and jet (associated to the muon) variables. In the upper plots, the muon momentum, P_T^μ , (left) and pseudorapidity, η_μ , (right) are displayed. The lower plots show the analogous variables related to the jet associated to the muon, P_T^{jet} (left) and η_{jet} (right). In all the plots the data (dots) are compared to the fitted distribution (black continuous line) obtained by summing the beauty and charm-plus-light-flavour contributions in the fractions given by the $P_T^{\text{rel}} - \delta$ fit (see Chapter 10). The fitted distribution is area-normalized to the data. The dashed area represents the contribution coming from beauty events.

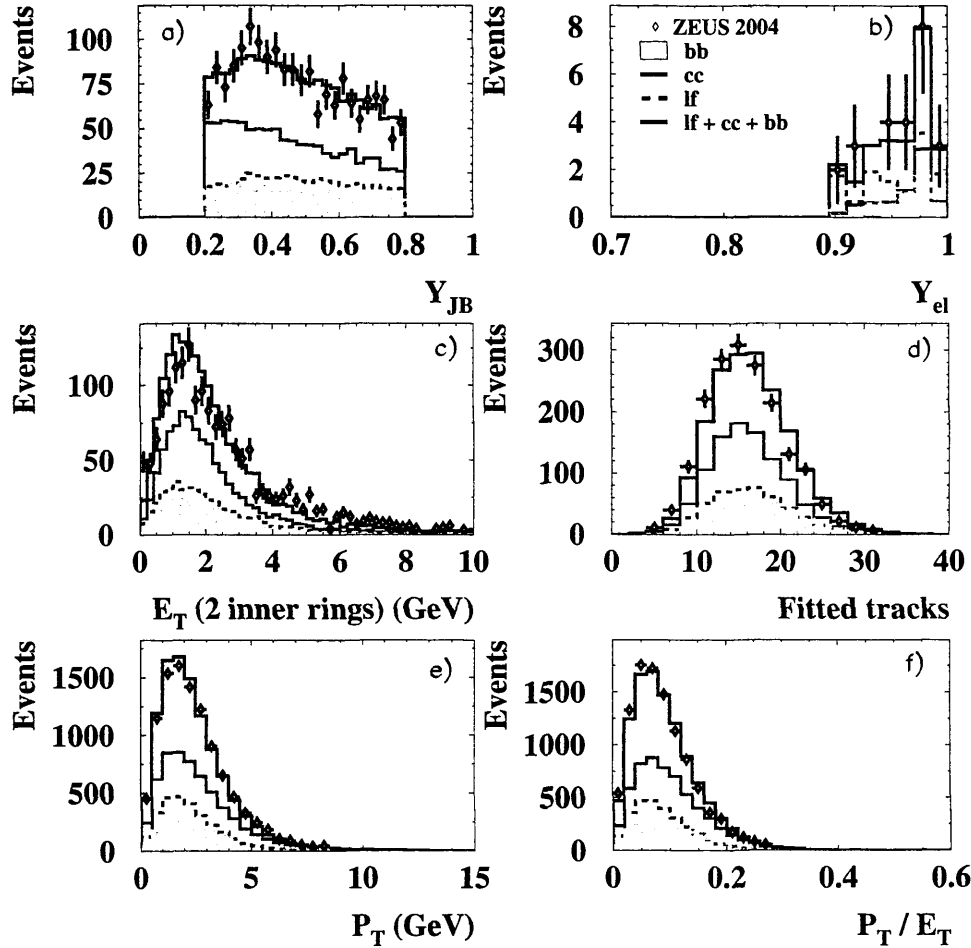


Figure 7.19: Control plots for several event variables. In a) Y_{JB} , b) Y_{el} , c) E_T of the two FCAL inner rings, d) number of fitted tracks, e) P_T of the event and f) P_T/E_T of the event. In all the plots the data (dots) are compared to the fitted distribution (black continuous line) obtained by summing the beauty and charm plus light flavour contributions in the fractions given by the $P_T^{rel} - \delta$ fit (see Chapter 10). The fitted distribution is area-normalized to the data. The dashed area represents the contribution coming from beauty events.

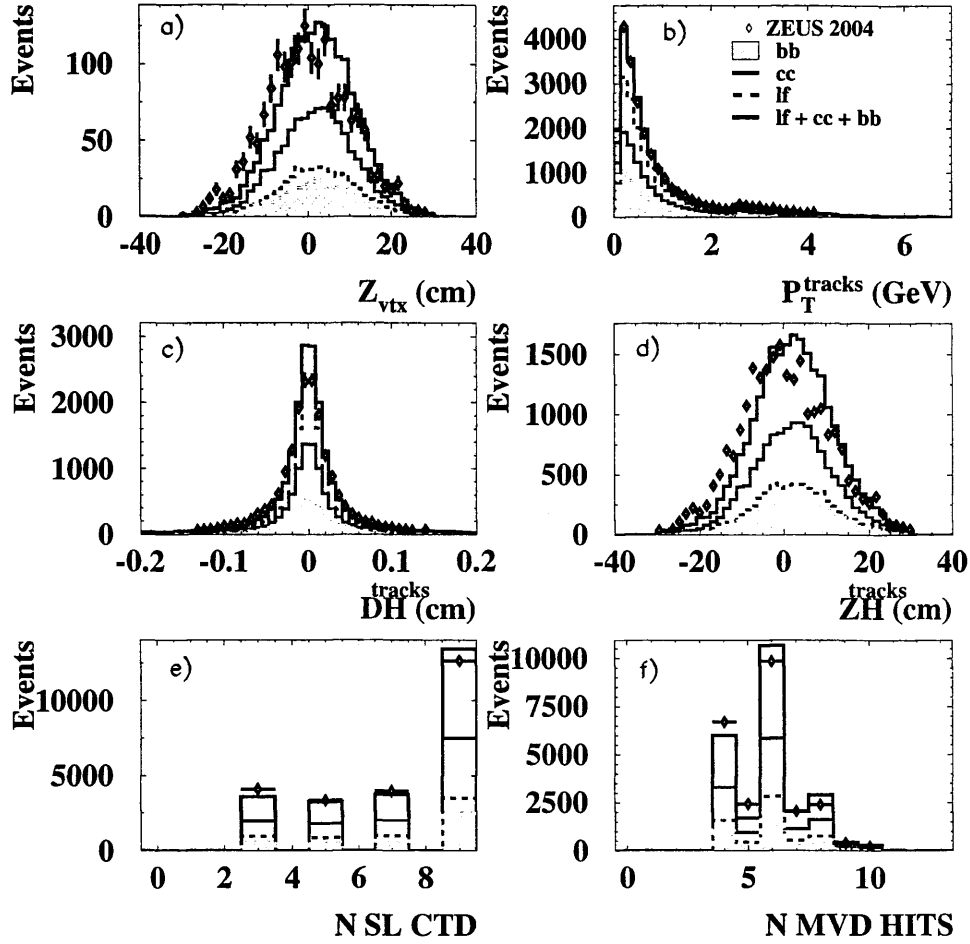
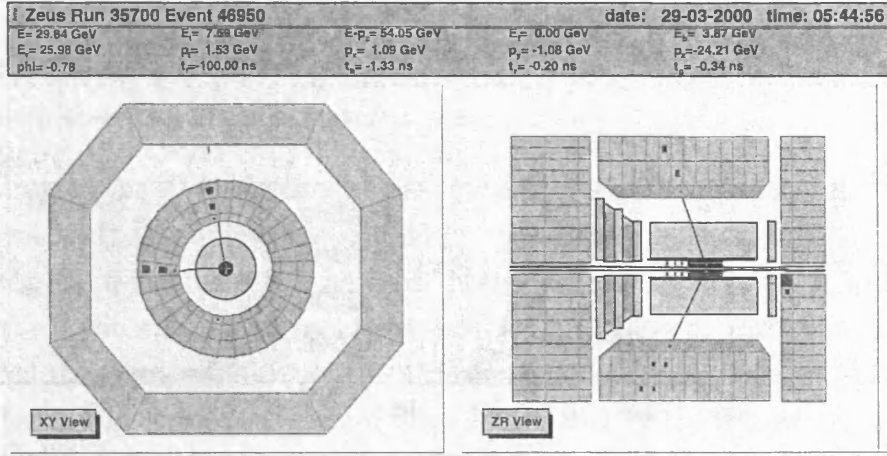


Figure 7.20: Control plots for track-related variables. In a) Z coordinate of the primary vertex, b) P_T of the tracks, c) distance of closest approach DH of the track to $x = y = 0$ in the transverse plane, d) Z coordinate of closest approach to $x = y = 0$, e) number of Super Layers of the CTD crossed by the tracks and f) number of MVD hits used in the reconstruction of the track. In all the plots the data (dots) are compared to the fitted distribution (black continuous line) obtained by summing the beauty and charm plus light flavour contributions in the fractions given by the $P_T^{\text{rel}} - \delta$ fit (see Chapter 10). The fitted distribution is area-normalized to the data. The dashed area represents the contribution coming from beauty events.

Figure 7.21: Event display of a $J/\psi \rightarrow \mu^+\mu^-$ event.

A clean J/ψ sample is selected using the following cuts:

- cut on global event timing determined from the CAL relative to the bunch crossing: $|T_g| \leq 10$ ns
- cut on the vertex position:
 - $|z_{vertex}| \leq 50$ cm
 - non-zero vertex in x and y : $x_{vertex} \neq 0$ cm, $y_{vertex} \neq 0$, i.e. vertex reconstruction
$$\sqrt{x_{vertex}^2 + y_{vertex}^2} \leq 3$$
 cm
- maximal number of vertex tracks: $\eta_{vertex-track} \leq 2$, i.e. elastic J/ψ , no other activity in the event
- at least one dimuon system with:
 - different charge of the two muons
 - invariant mass: $2 \text{ GeV} \leq m_{\mu^+\mu^-} \leq 4 \text{ GeV}$; the large mass window also takes muons from other useable processes (for example Bethe-Heitler processes) into account. The background is sufficiently suppressed by the complete selection.
 - angular distance between the two muons: $\Delta R = \sqrt{\Delta\eta^2 + \Delta\phi^2} > 0.5$

- angular distance in θ between the two muons: $\Delta\theta = \sqrt{(\theta_{\mu 1} - (\pi - \theta_{\mu 2}))^2} > 0.0157$ and ϕ : $\Delta\phi = \sqrt{(\sqrt{(\theta_{\mu 1} - \theta_{\mu 2})^2} - \pi)} > 0.0157$ to reject perfectly back-to-back muons from cosmic rays

In the case of the J/ψ selection, if one of the muons of the dimuon pair triggered the event, only the other can be used for the efficiency determination. If both triggered the event, both can be used. Starting from the first muon which triggered the event, the second should be included in the event. But the second also triggered the event, resulting in the inclusion of the first. As both muons include the other in the correction, each of them is unbiased by the trigger and both can be included.

The individual efficiencies ϵ are determined by the fraction of muons reconstructed by BREMAT and MPMATCH and the muons reconstructed by MV ¹ [130].

$$\epsilon_{FMU} = \frac{N_{MV \wedge (MPMATCH \vee MUFO)}}{N_{MV}} \quad (7.19)$$

$$\epsilon_{BMU} = \frac{N_{MV \wedge BREMAT}}{N_{MV}} \quad (7.20)$$

The application of the efficiency correction, c , to MC events is defined as:

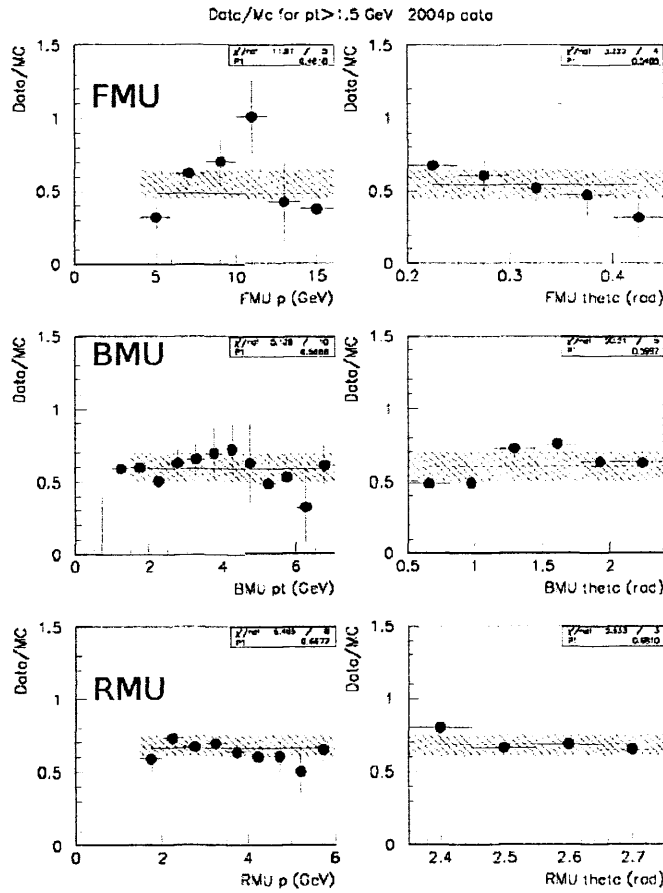
$$c = \frac{\epsilon^{data}}{\epsilon^{MC}} \quad (7.21)$$

and it has to take into account the characteristics of each individual reconstructed muon. Depending on the combination of the algorithms which reconstruct the muon, the correction, c , is determined from the data and MC efficiencies ϵ_i^j where i is BREMAT or MPMATCH and j is data or MC corresponding to the transverse momentum, P_T^μ , and the pseudorapidity, η , of the reconstructed muon. In Fig. 7.22 all the corrections applied are summarized for the forward, barrel and rear region of the detector, their mean values adopted for this analysis are reported in Table 7.1.

¹Reconstruction algorithm suitable for the isolated muon identification; it matches the CAL cell pattern to CTD tracks, exploiting also HES mip and B/RMUON information if available.

FMU	BMU	RMU
0.55 ± 0.10	0.60 ± 0.10	0.68 ± 0.07

Table 7.1: Values of the muon efficiency corrections applied in the analysis.

Figure 7.22: Muon efficiency corrections for the forward, barrel and rear regions. In the left-hand column the corrections are shown as a function of the momentum p and in the right-hand column the corrections are shown as a function of θ [129].

Chapter 8

Primary vertex determination

A precise reconstruction of the primary vertex position is fundamental for the measurement of the track impact parameter. If the primary vertex spread in the transverse plane (XY) is smaller than its reconstruction resolution, the accuracy on its position determination can be improved by replacing its value on an event-by-event basis with its average over many events. This average is technically named *beam spot*. In this Chapter the beam spot determination is described together with studies regarding its stability with time and longitudinal position in order to check if corrections are needed to take these effects into account.

8.1 Event selection and beam spot position

The expected transverse width of the HERA beams at the interaction point is $\sigma_x \simeq 110 \mu m$ and $\sigma_y \simeq 30 \mu m$. Therefore the beam position in x and y , determined run-by-run from an average of reconstructed event vertices, provides quite a precise and unbiased estimate of the event vertex in the transverse plane. The reliability of the beam spot measurement depends on the statistics of the sample used, therefore an inclusive sample for each run of 2004 data was used. It is important at this stage to select ep events rejecting the background (beam gas events) which detrimentally affect the determination of the real beam position. The following requirements were applied to the sample [131]:

- RCAL time - FCAL time > -8 ns. This cut reduces proton beam-gas events and proton beam halo muons.

- CAL $E_T > 5$ GeV and CAL $P_T < 5$ GeV. This cut reduces proton beam-gas events. Here E_T is the transverse energy in the calorimeter, whilst P_T is the sum of the momentum vectors of all CAL deposits projected onto the xy plane.
- At least one good quality track, i.e. a track which crosses at least 3 CTD superlayers and is reconstructed using at least 4 MVD clusters. This cut rejects the off-momentum positron events.

For each 2004 data run the beam spot position was determined applying a Gaussian fit to the primary vertex coordinate distributions (see Fig. 8.1). Different fit ranges were tested ($\pm 2\sigma$, ± 4 bins from the mean, free fit range), obtaining differences in the mean positions of the order of few μm , meaning that the systematic effect from the chosen fit procedure is of the same order as the statistical uncertainties. In this thesis a $\pm 2\sigma$ fit range was used.

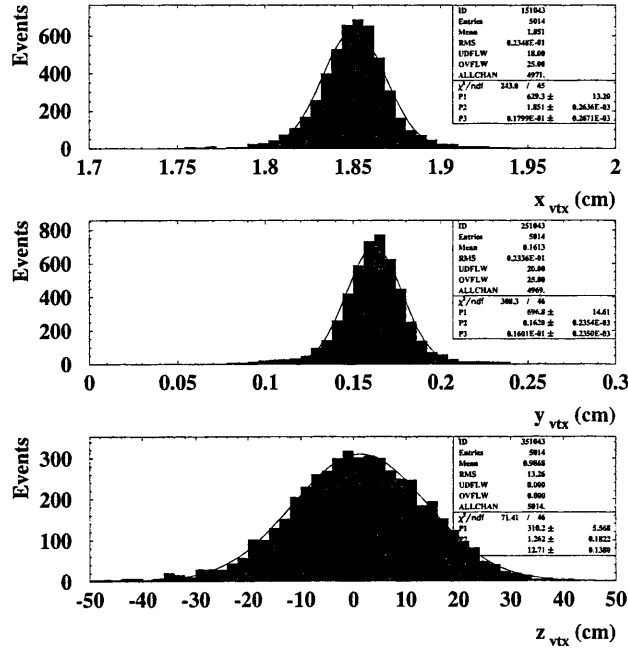


Figure 8.1: Distribution of the primary vertex coordinates in an example run (~ 5000 events were selected after applying the background rejection and quality cuts). A Gaussian fit was used to extract the mean beam spot values, restricting the fit range to $\pm 2\sigma$.

The large width of the z distribution in fig. 8.1 is dominated by the proton bunch length. This fit procedure was applied to all 2004 runs with at least 1000 events. The typical sigmas of the x and y distributions are ~ 180 and 170 microns, respectively, whilst the errors on their mean values are of the order of a few microns.

The VCTRAK (see Chapter 7) vertexing package used for the beam spot determination in this analysis (see section 7.1) was compared with other measurements using different vertexing routines. In Fig. 8.2 the comparison between the used package and the KFTRAK [132] vertexing package is shown. The selection cuts adopted were equivalent; the comparison shows a good agreement in both the calculated x and y positions in a subsample of the 2004 data.

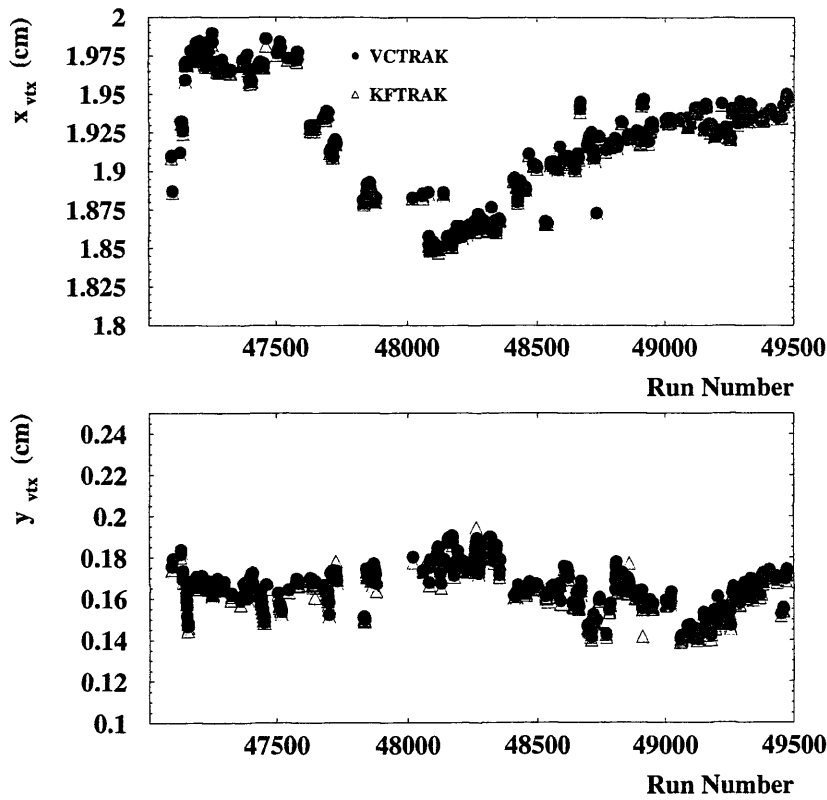


Figure 8.2: Comparison between the beam spot measurements obtained using the VCTRAK vertexing package (circles) and KFTRAK vertexing package (triangles) in a subsample of the 2004 data sample.

8.2 Time and z dependence

During the 2004 data taking the beam spot was not always in the same position, as shown in Fig. 8.3 [133] where the HERA and H1 measurements are reported. The vertical and horizontal positions of the beams vary significantly. The beam orbits can change between the fills due to the fact that the magnets GO/GG [61] move, being subject to magnetic forces. Also temperature effects can occur in the magnetic bridges leading to a shift up to 1 mm. The orbits can drift inside each fill as well; the reasons are again temperature effects induced by the magnet bridges and also luminosity, background and polarization tuning.

The time and longitudinal dependence of the beam spot are shown in the following subsections.

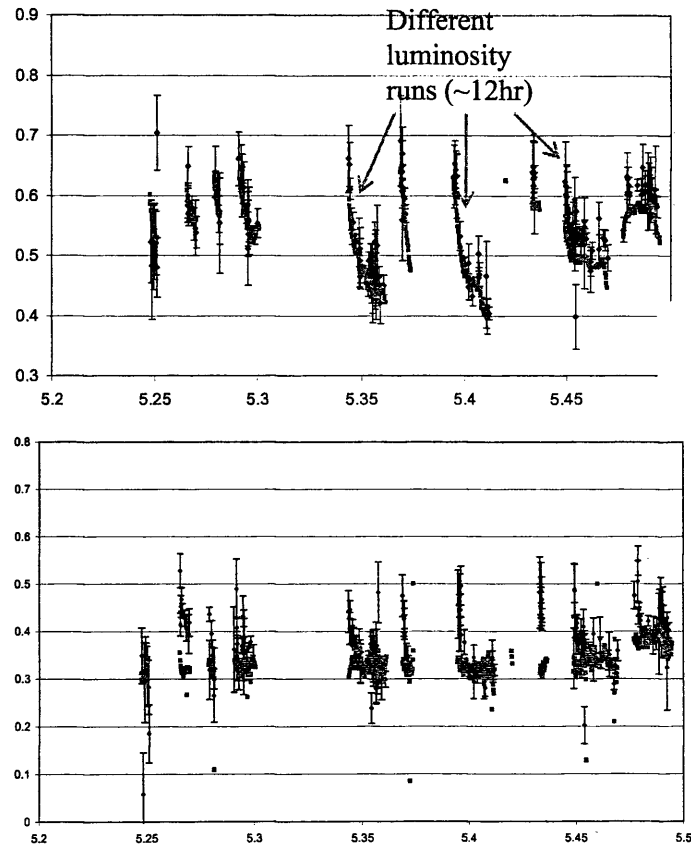


Figure 8.3: *HERA (grey) and H1 (black) vertical (top) and horizontal (bottom) beam position measurements (in mm) as a function of time (months). The periodic structure of the plot reflects the different machine fills.*

8.2.1 Time dependence

The average position of the primary vertex described in section 8.1 can drift during a fill (see Fig. 8.3). It is useful to remove the effects that this drifting in time of the beam coordinates can produce on the ZEUS data. For this purpose a subsample of the inclusive 2004 data sample was used, limiting the study to large statistics consecutive runs inside the same fill. In Fig. 8.4 the primary vertex coordinates are plotted as a function of the *Run Number* (time-dependent); the observed variation inside each run was of the order of $\sim \pm 20 \mu\text{m}$ for both the x and y coordinates. Since these variations are small compared to the sigmas of

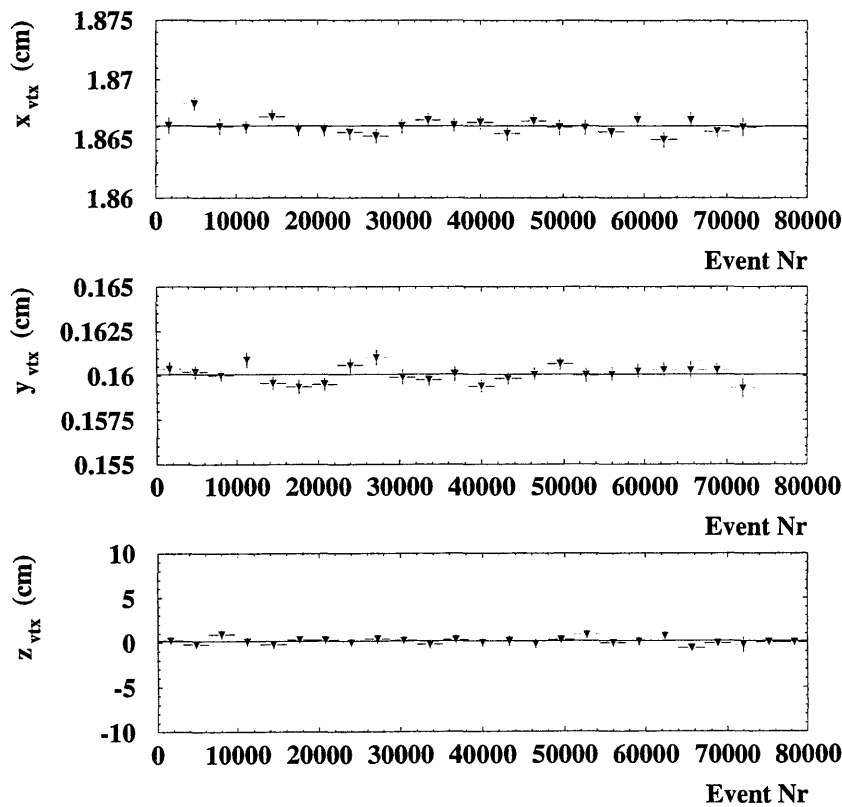


Figure 8.4: *Distribution on the vertex position in x (top, left), y (top, right) and z (bottom) in bins of approximately 500 events for one single 2004 run. Each of the measurements (triangles) corresponds to 200 events. The variation observed in x and y is of the order of $\sim \pm 20 \mu\text{m}$.*

the beam spot coordinates distributions (see Fig. 8.1) we decided to not correct

for this effect.

8.2.2 Z dependence

The beam and detector axes are not parallel along the longitudinal direction, producing a dependence of the primary vertex X, Y positions on the Z coordinate. Using the same subsample of consecutive runs of the previous section, this dependence was studied. In Fig. 8.5 the effect is shown for an example run; this time the variation can reach $\sim \pm 200 \mu\text{m}$, which translates into a beam tilt of a few mrad; therefore this effect is not negligible and for this thesis a correction is needed and is applied on the beam spot coordinates. After fitting the distribution

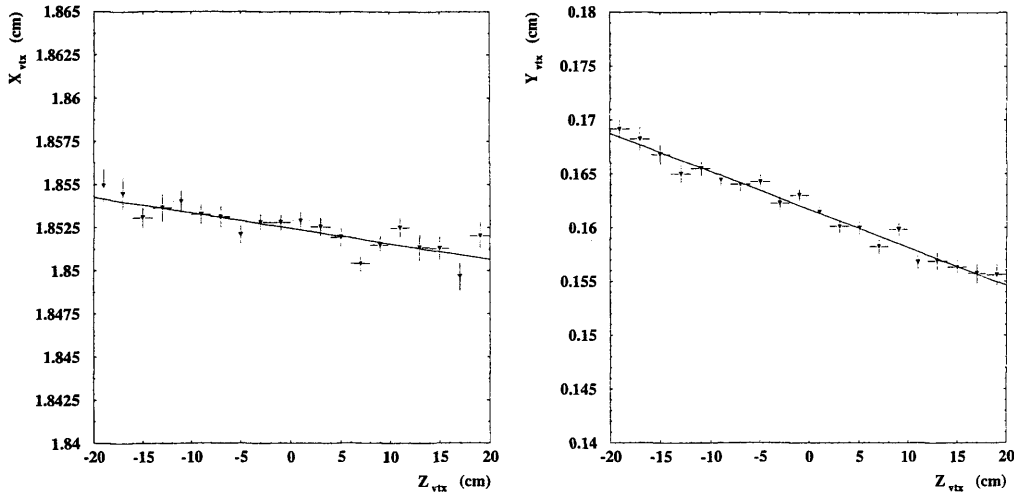


Figure 8.5: *Straight line fit for the x vs z (left) and y vs z (right) distributions. Only the central region around the mean value of the Z coordinate ($|Z| < 20$ cm) is shown.*

of Fig. 8.5 with a straight line, the tilt-parameters (Fig. 8.6 right and 8.7 right) were used to correct for the primary vertex position on an event basis.

The new coordinate positions can then be written as:

$$X_{\text{beamspot}}^{\text{corrected}} = X_{\text{beamspot}} + a1_x \cdot (Z_{\text{primaryvtx}} - Z_{\text{beamspot}}) \quad (8.1)$$

$$Y_{\text{beamspot}}^{\text{corrected}} = Y_{\text{beamspot}} + a1_y \cdot (Z_{\text{primaryvtx}} - Z_{\text{beamspot}}) \quad (8.2)$$

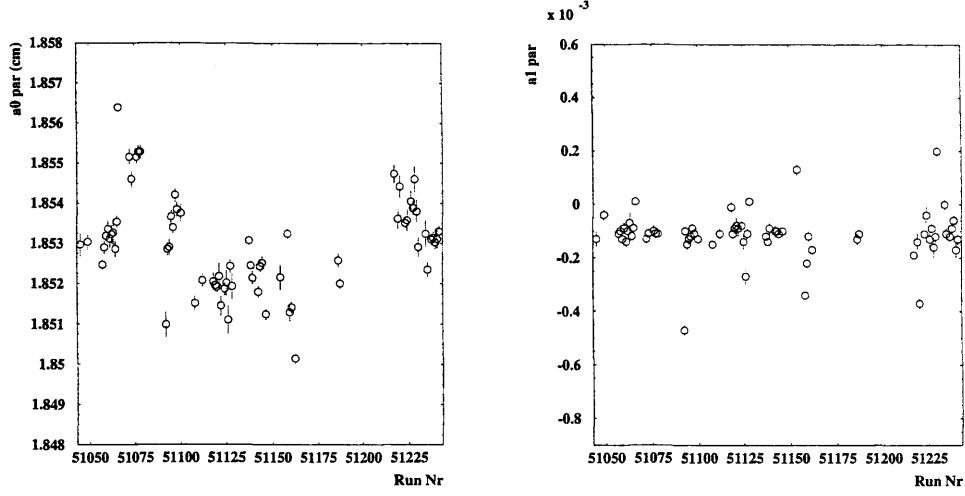


Figure 8.6: *Fit parameters for the x coordinate. On the left the off-set, on the right the slope coming from a linear fit.*

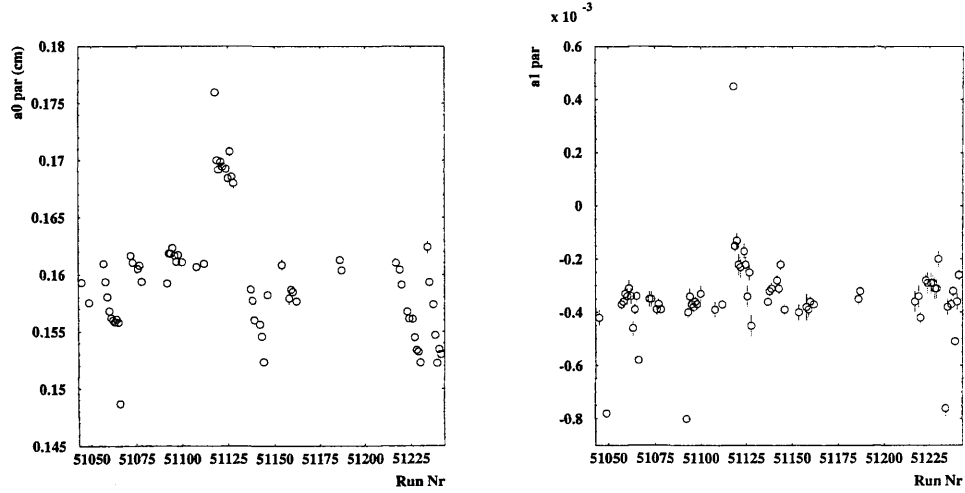


Figure 8.7: *Fit parameters for the y coordinate. On the left the off-set, on the right the slope coming from a linear fit.*

8.3 Summary

The beam spot coordinates were determined for the entire 2004 data set. The impact parameters of the tracks were calculated with respect to this average value instead of the primary vertex of the event as determined by the reconstruction package.

In Figures 8.8 and 8.9 all 2004 primary vertex x and y coordinate positions are

shown, together with their size (sigmas of the fitted distributions). In this analysis the beam-tilt corrections seen in the previous section were applied.

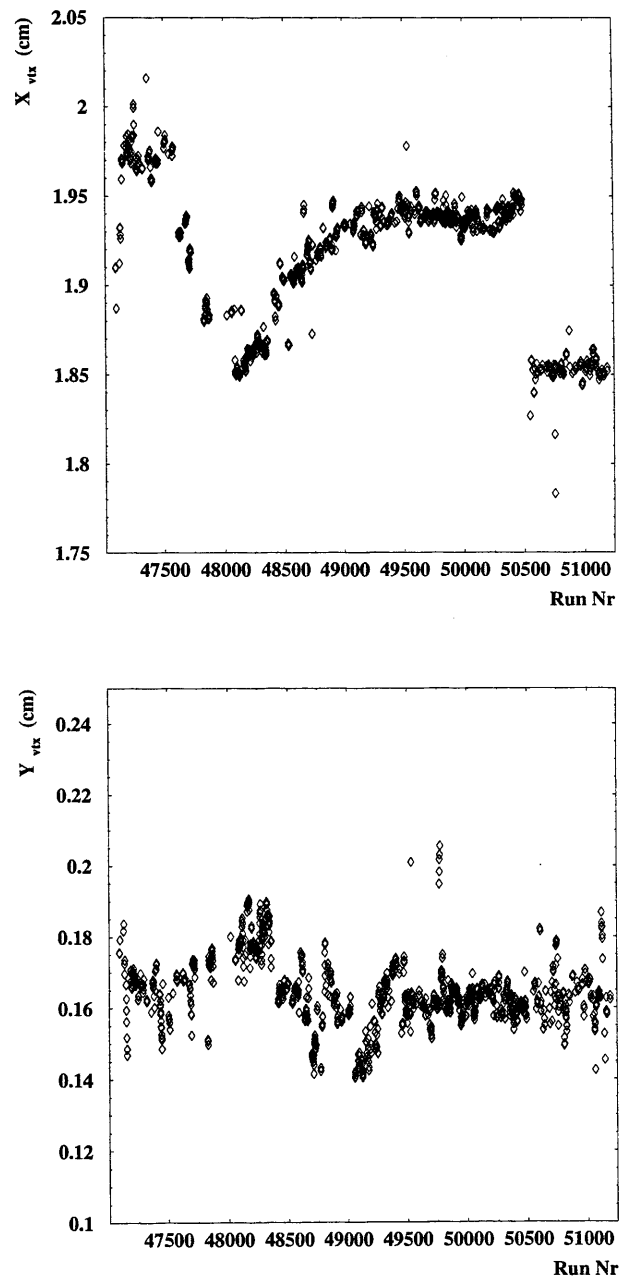


Figure 8.8: *The x (top) and y (bottom) coordinates of the beam spot for all 2004 data.*

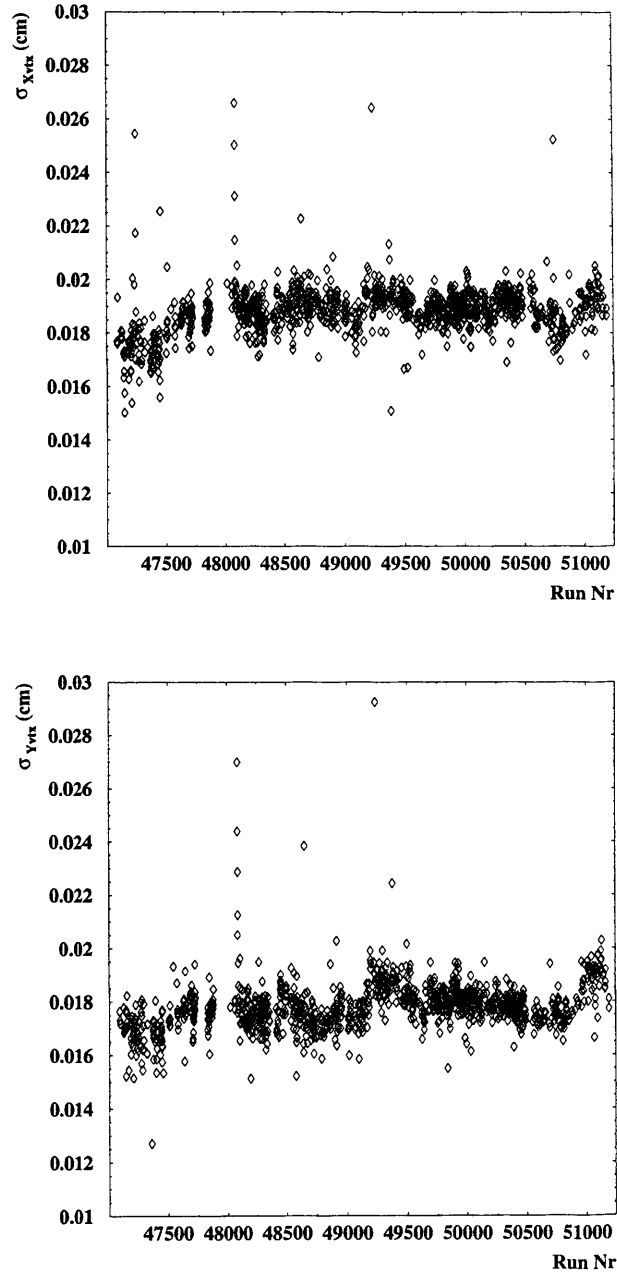


Figure 8.9: *The x (top) and y (bottom) size of the beam spot for all 2004 data.*

Chapter 9

Smearing of the Monte Carlo impact parameter distribution

The extraction of the b fraction using the impact parameter technique relies on the Monte Carlo description of these quantities. Background studies have been performed to improve their knowledge. The dependence from Monte Carlo has been reduced by using an independent data sample to assess the efficiency of b tagging. In this chapter, the impact parameter of all tracks for a dijet event sample from 2004 data has been compared with an inclusive sample of light flavour.

9.1 Selection

An inclusive sample of dijet events was selected with the same cuts as in the analysis (see Chapter 7), but omitting the muon requirements (and muon triggers). Photoproduction events are selected with two high P_T jets in the final state, and all tracks in the sample have to fulfil the following quality cuts:

- Number of CTD Super Layers crossed ≥ 3
- Number of MVD clusters used in the track reconstruction ≥ 4
- $P_T > 0.5$ GeV.

The tracks are associated with the closest jets cutting on the variable $\Delta R_{jet-track} < 1$, defined as:

$$\Delta R_{jet-track} = \sqrt{(\phi^{jet} - \phi^{track})^2 + (\eta^{jet} - \eta^{track})^2} . \quad (9.1)$$

As seen in Chapt. 7, the resolution of the tracking system can be expressed as:

$$\sigma(P_T)/P_T = aP_T \oplus b \oplus c/P_T , \quad (9.2)$$

where the first two terms are related to the intrinsic track and hit resolution, whilst the third term is related to the multiple scattering. It is therefore useful to analyse the impact parameter spectrum in different P_T bins. In Fig. 9.1 the distribution of the MC impact parameter is compared with all of the 2004 data sample in different P_T bins, from 0.5 to 5.0 GeV. In general the data impact parameter distribution is significantly wider than that in the MC. There are several reasons for this disagreement:

- the dead material is not simulated accurately enough in the Monte Carlo;
- the intrinsic hit and track resolutions implemented in the Monte Carlo simulation do not correctly reflect the real tracking detector resolution;
- the current implemented version of the alignment of the Micro Vertex Detector has still to be improved.

9.2 Double convolution fit

In order to determine the correct smearing to apply to the MC, different functional forms (e.g. Gaussian, double Gaussian, Breit-Wigner, convolution of Gaussian with exponential) were fitted to the negative side of the data distribution (the total distribution is slightly asymmetric towards positive values due to physics processes like K decays). The best fit to the data is found to be a double convolution of MC with a Gaussian and a Breit-Wigner:

$$F^1(x) = \int dz F(z) \mathbf{B}(x - z) \quad (9.3)$$

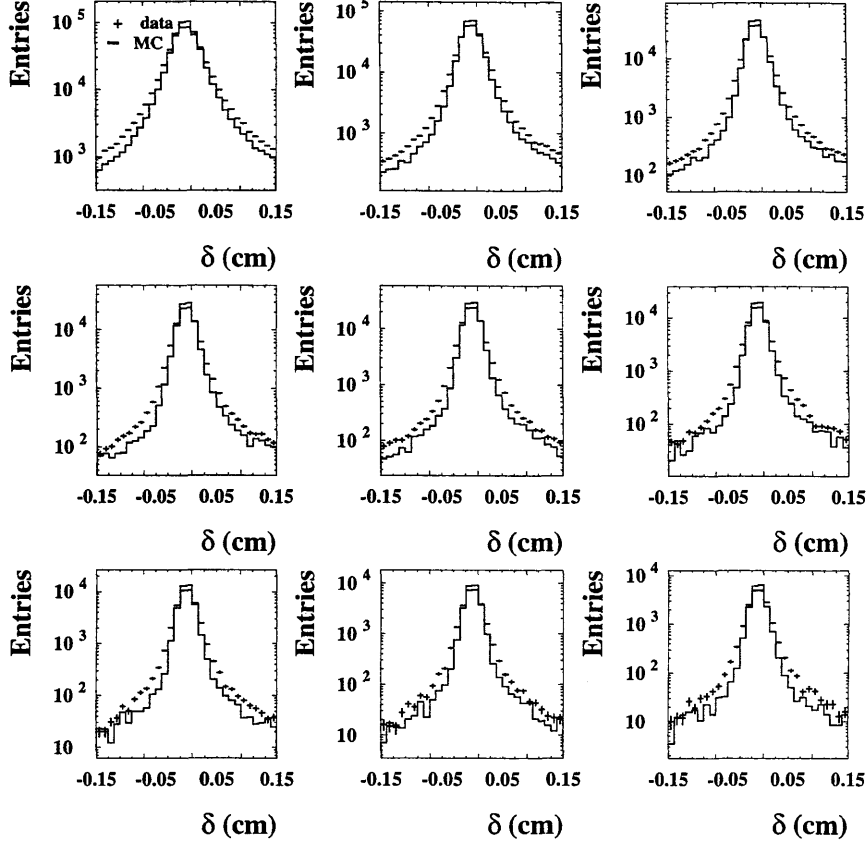


Figure 9.1: The MC impact parameter distributions (histograms) compared with 2004 data (black crosses), in different P_T bins (the P_T range considered is $0.5 < P_T < 5$ GeV, the P_T bin size is 0.5 GeV).

$$F^2(x) = \int dy \int dz F(z) \mathbf{B}(y - z) \mathbf{G}(x - y) \quad (9.4)$$

where B indicates the Breit-Wigner function and G is the Gaussian function. In order to determine the precise values for the widths of the two distributions, different combinations of the σ of the Gaussian and the Γ of the Breit-Wigner distributions were tested in order to find the minima. In Fig. 9.2 the χ^2 of the fit for the different P_T bins is plotted as a function of the Gaussian σ and the Breit-Wigner Γ . From Fig. 9.2 it can be seen that the χ^2 is approximately constant as a function of the Gaussian σ , whilst it shows a strong dependence on the Breit-Wigner Γ . The minima were determined considering two-dimensional

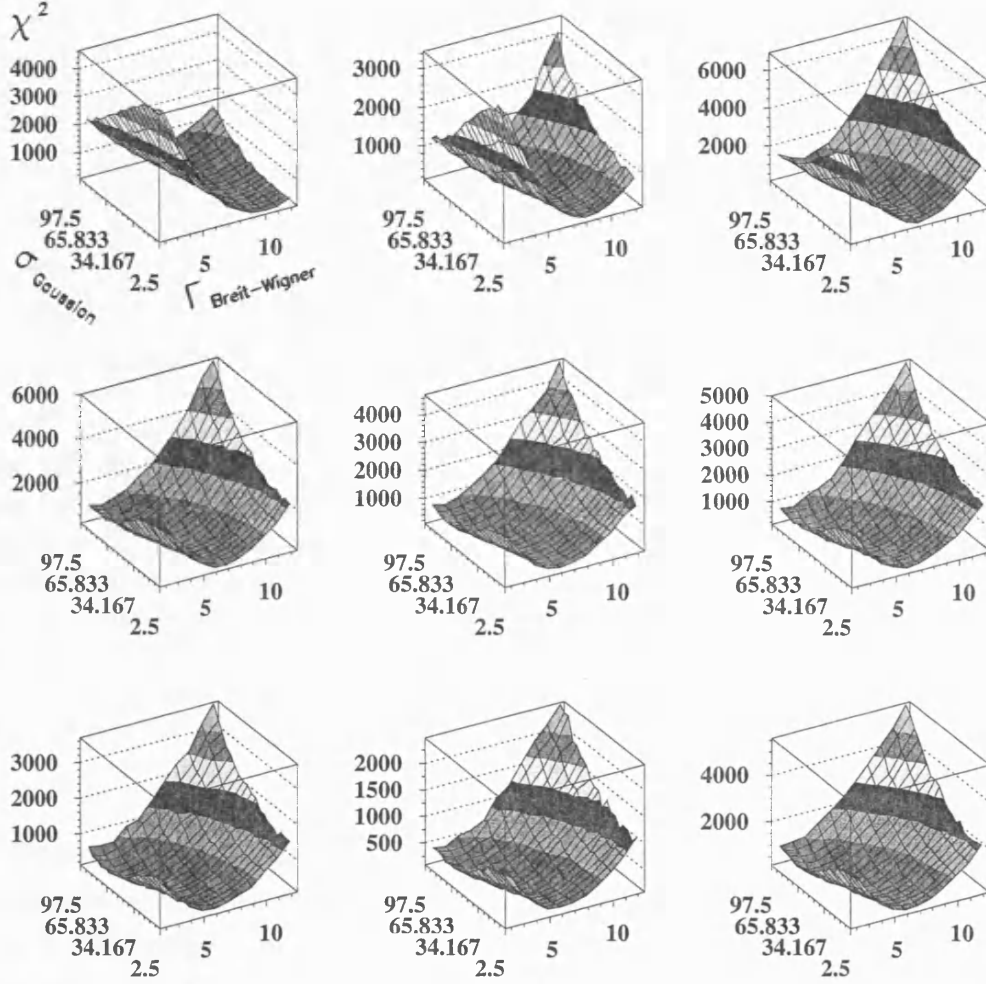


Figure 9.2: χ^2 of the fit plotted as a function of the σ of the Gaussian ($\times 10^{-4}$ cm) and the Γ of the Breit-Wigner ($\times 10^{-3}$ cm) in the different P_T bins specified in Fig. 9.1.

distributions; the χ^2 of the fit was plotted as a function of the Gaussian width keeping the gamma of the Breit-Wigner constant at its minimum; the Gaussian width was determined by fitting the local minimum area with a parabolic fit. The same procedure was adopted to extract the minimum of the χ^2 as a function of the gamma of the Breit-Wigner. An example of these distributions (the first P_T bin is considered) can be seen in fig. 9.3. The minima of these distributions

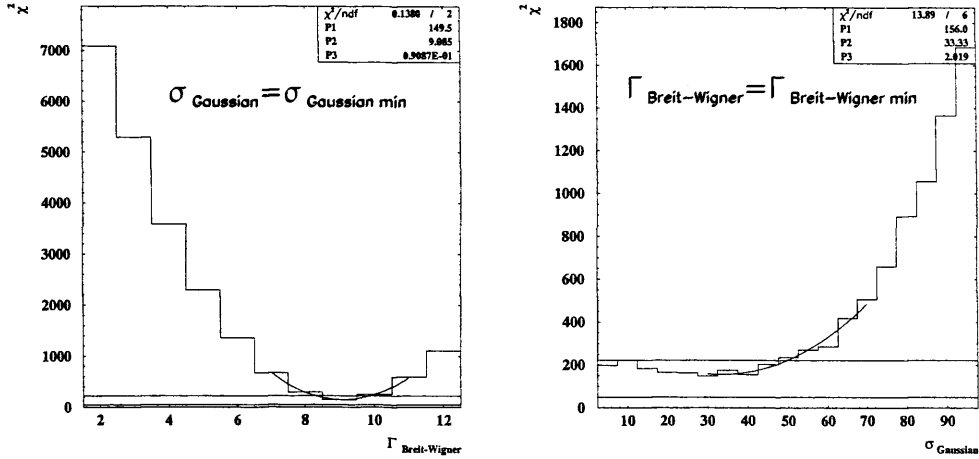


Figure 9.3: Example of a two-dimensional plot of the χ^2 distribution in the first bin of P_T of Fig. 9.2. On the right the distribution of the χ^2 is plotted as a function of the Gaussian σ ($\times 10^{-4}$ cm), keeping the value of the Breit-Wigner Γ constant at its minimum. On the left the distribution of the χ^2 is plotted as a function of the Breit-Wigner Γ ($\times 10^{-3}$ cm), keeping the value of the Gaussian σ constant at its minimum. In both distributions a horizontal line at $\chi^2 = 50$ is drawn, corresponding to the expected χ^2 if the fit and the errors were correct. Another line at $\chi^2 = \chi_{min}^2 \times 1.5$ is drawn.

were determined also using a Bayesian approach adopting a uniform prior; this method is in fact less sensitive to fluctuations, binning and local minima [134].

In Fig. 9.4 the different contour plots of the paraboloid distributions of Fig. 9.2 can be seen with the localization of the minima using the Bayesian approach as well as the likelihood method. The level lines of the contour plots are drawn between $\chi^2 = 50$ and $\chi_{min}^2 \times 1.5$.

The distributions of the above minima as a function of p_T , have been fitted using a combination of an exponential and constant function in the case of Breit-Wigner and with a constant term for the Gaussian; the results of the fit in fig. 9.5 can be written as:

$$\Gamma_{BW}(P_T) = \exp(a + b \cdot P_T) + c \quad (9.5)$$

$$\sigma_{Gauss}(P_T) = d \quad (9.6)$$

where the Breit-Wigner parameters $a = 3.0275$, $b = -2.2336$ and $c =$

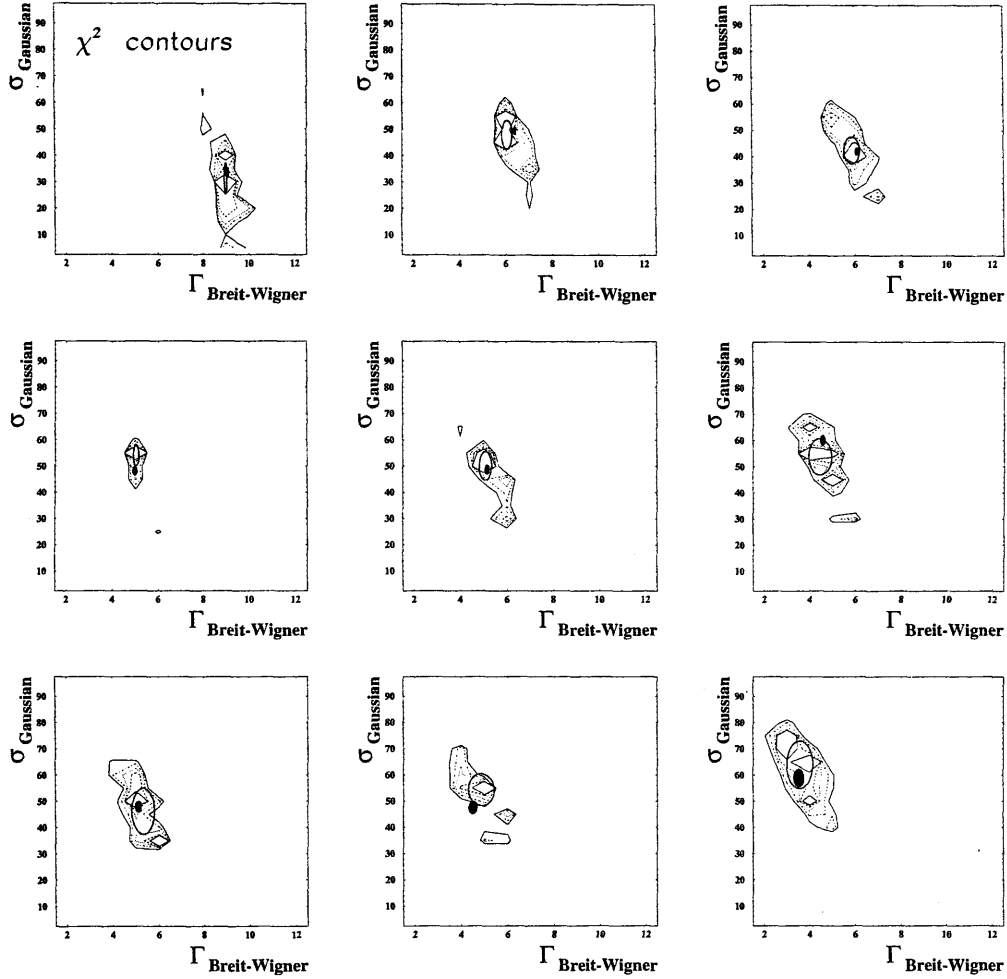


Figure 9.4: Contour plots of the 2d-histograms of fig. 9.2. The χ^2 distributions as a function of the Breit-Wigner width ($\times 10^{-3}$ cm) and Gaussian width ($\times 10^{-4}$ cm) are plotted in bins of P_T . The contour lines refer to iso- χ^2 regions between $\chi^2 = 50$ and $\chi^2_{min} \times 1.5$. The minima obtained using the Bayesian approach are identified by the empty ellipses, the minima extracted using the likelihood method are identified by the full dark ellipses.

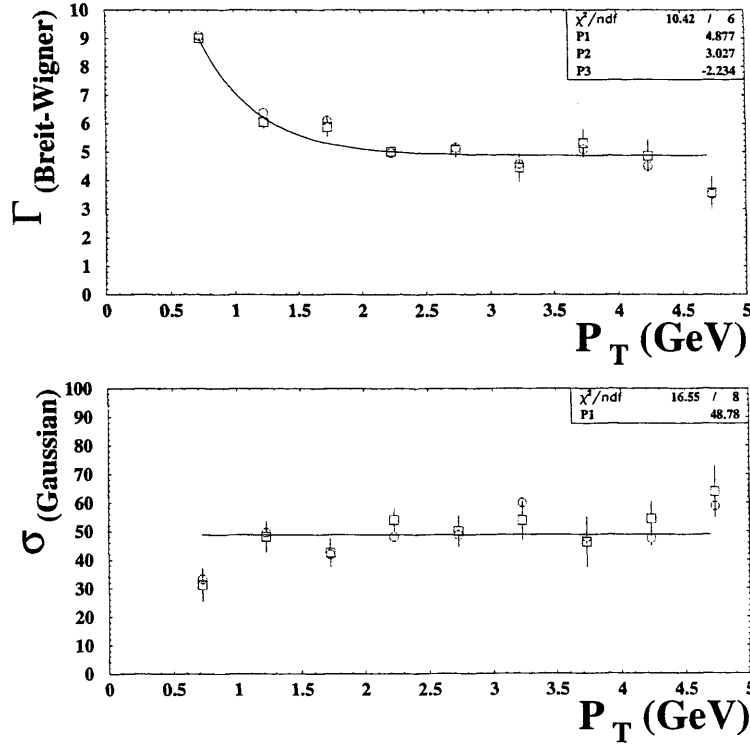


Figure 9.5: *Distribution of the Breit-Wigner gamma ($\times 10^{-3}$ cm, top) and Gaussian sigma ($\times 10^{-4}$ cm, bottom) in bins of P_T . The distributions were fitted with a combination of an exponential (top) and a constant function and with a constant function (bottom). Both the minima estimated using a likelihood (circles) and bayesian (squares) approach are shown.*

4.8768×10^{-3} cm, whilst the constant Gaussian fit parameter $d = 0.0048781$ cm. These values are used to correct the impact parameter measurements as follows:

$$IP_{smeared} = IP_{original} + sme_{BW} + sme_{Gauss} \quad (9.7)$$

where:

$$sme_{BW} = N_{RAN}^{BW}(N_{RAN}^{UNI}) \times (\exp(a + b \cdot P_T) + c) \times const. \quad (9.8)$$

and

$$sme_{Gauss} = d \times N_{RAN}^{GAUSS}. \quad (9.9)$$

In Eq. 9.8 N_{RAN}^{BW} is a random number generated with Γ_{BW} equals 1, whilst N_{RAN}^{UNI} is a uniformly generated random number from 0 to 1. In Eq. 9.9, N_{RAN}^{GAUSS} is

a random number generated according to a Gaussian distribution with σ_{Gauss} equals 1.

9.3 After smearing

Applying the above corrections to the inclusive MC sample, the distributions shown in fig. 9.1 transform as shown in fig. 9.6. Now the Monte Carlo generally

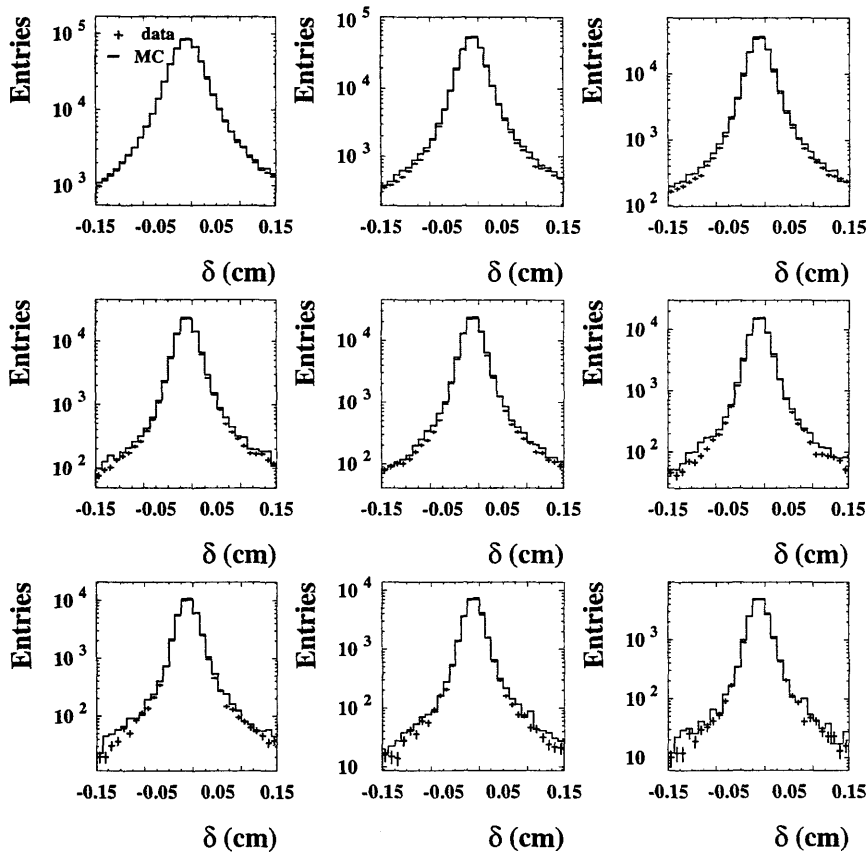


Figure 9.6: The MC impact parameter distributions (histograms) compared with 2004 data (black crosses), in different P_T bins, after the Monte Carlo smearing has been applied (the P_T range considered is $0.5 < P_T < 5$ GeV, the P_T bin size is 0.5 GeV).

describes appropriately the impact parameter distribution of the data in all P_T bins. Small discrepancies can still be observed in the tails of the distributions; an

improvement in the agreement could be achieved using the new MVD alignment. The same smearing parameters were applied to the muon Monte Carlo samples used for the analysis (see Chapt. 7).

Chapter 10

Extraction of the beauty fraction

In this Chapter the methods used to extract a beauty fraction from the selected data sample are outlined. The P_T^{rel} and δ fit are separately presented and their combined fit is then shown. The resulting b fraction will be used to calculate the cross sections as described in Chapter 11.

10.1 Extraction of the beauty fraction from the

P_T^{rel} fit

The determination of the beauty fraction in the data relies on the difference between the shapes of the P_T^{rel} distributions of the beauty (b), charm (c) and light quark (lf) components. The P_T^{rel} shape of the data results from the sum of various contributions, simulated by the different Monte Carlo components. A fit on the P_T^{rel} variable can distinguish between these contributions.

The P_T^{rel} distributions of beauty, charm and light flavours are the sums of different sub-processes: direct photoproduction, resolved photoproduction, excitation in the photon and in the proton, for beauty and charm, direct and resolved photoproduction for light flavours. These sub-processes have to be mixed in a proper way in order to obtain a single P_T^{rel} distribution for each component. These components have then been summed up, weighting them according to their luminosities:

$$N_i^f = \frac{\sum_{j \in fproc} \mathcal{L}_j^{-1} N_i^j}{\sum_{j \in fproc} \mathcal{L}_j^{-1}} \quad (10.1)$$

where N_i^f is the number of events in the i^{th} bin of the P_T^{rel} distribution of flavour f (f can refer to beauty, charm or light flavours), \mathcal{L}_j is the integrated luminosity generated for each subprocess and N_i^j is the i th bin content of the P_T^{rel} distribution relative to the sub-process j . Therefore each sub-process is taken into account considering both its cross section and the statistics available. The resulting plots, adopting the binning used in the fit, are shown in fig 10.1.

A fit to the data was then performed, using the following function:

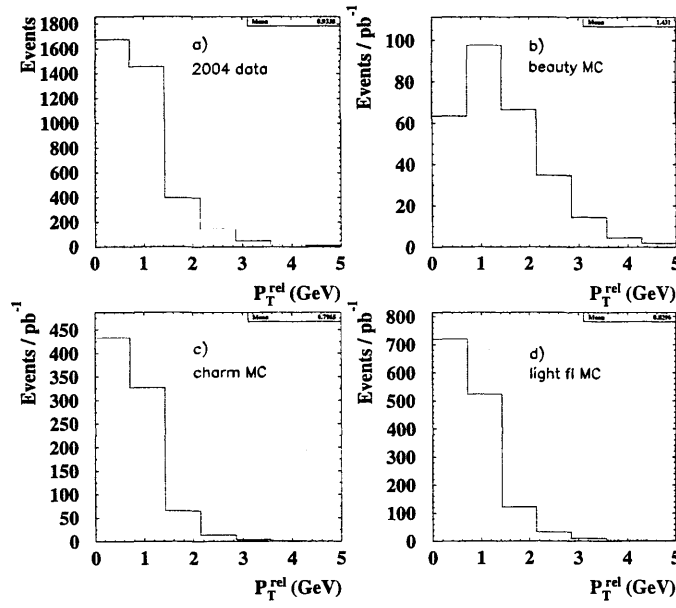


Figure 10.1: P_T^{rel} distribution for a) data and b) beauty, c) charm and d) light flavour Monte Carlo samples. All the MC samples are a mixture of the different direct, resolved and excitation processes and are normalized according to their luminosity.

$$N_i^{fit} = \frac{f_b N_i^b + f_c N_i^c + f_{lf} N_i^{lf}}{f_b + f_c + f_{lf}}, \quad (10.2)$$

where N_i^b , N_i^c , N_i^{lf} and N_i^{fit} are the contents of the i^{th} bin in the beauty, charm, light flavour and summed P_T^{rel} distributions. The free parameters of the fit, f_b , f_c and f_{lf} , can be interpreted as the relative fractions of beauty, charm and light

flavour events in the data, providing they sum up to 1. A χ^2 function

$$\chi^2 = \frac{\sum_i (N_i^{data} - N_i^{fit})^2}{\sigma_i^2 \cdot d.o.f.}, \quad (10.3)$$

was constructed and minimised, using a FORTRAN program, to perform the fit. In 10.3 N_i^{data} is the i^{th} bin content of the P_T^{rel} distribution of the data and σ_i is the error on the i^{th} bin content. σ_i is the result of different contributions, added in quadrature:

- the error on the data, given by the square root of the bin content, if the bin content is greater than 5, otherwise by the value given by Poisson statistics;
- the error on the Monte Carlo, given by the square root of the bin content, taking properly into account the applied weights. This error is of particular importance for the light flavour component, as it has the lowest statistics (see Chapter 5).

The FORTRAN program, using the MINUIT [136] package, varies the free parameters of the fit, f_b , f_c and f_{lf} , in order to find the values giving the lowest χ^2 . For each choice of the triplets (f_b , f_c , f_{lf}) χ^2 is evaluated, and the triplet corresponding to the minimum value is chosen. In a first loop, the percentages are varied in steps of 1 unit, until a minimum χ^2 value is found. In a second step, the percentages are varied in steps of 0.1 units in a restricted interval around the previously determined minimum. No more loops are performed, considering the error affecting the determination of the beauty percentage coming from the fit. Before showing the results of the fit, P_T^{rel} corrections were taken into account as described in the next section.

10.2 P_T^{rel} corrections

The P_T^{rel} method relies on the Monte Carlo description of this quantity. Background studies are needed [119][42] to improve the knowledge of the distribution of this variable. In order to reduce the dependence on the Monte Carlo, the data sample is used to determine the corrections.

An inclusive sample of dijet events was selected with the same cuts as in the analysis except for the muon requirement and muon triggers (the same samples

were used for smearing studies; see Chapter 9).

All the tracks passing the cuts are associated with a jet according to a track-jet distance $\Delta R(\text{track-jet}) < 1$ in the $\eta - \phi$ plane and the track P_T^{rel} is calculated. In Fig. 10.2 the P_T^{rel} distribution of the ratio $data/MC$ measured for the total cross section is shown. The same correction factors were measured for each muon P_T bin (fig. 10.3).

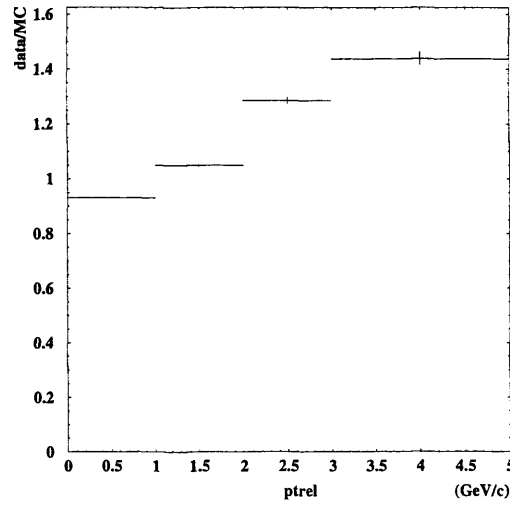


Figure 10.2: P_T^{rel} ratio $data/MC$.

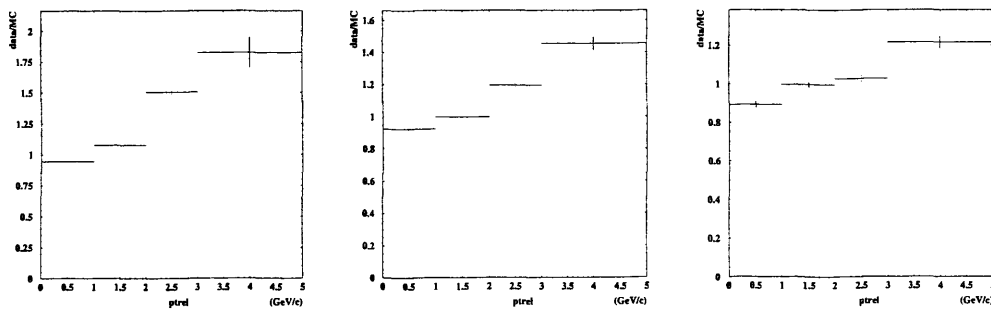


Figure 10.3: Ratio between data and MC in each muon P_T bin.

The distributions of P_T^{rel} after applying half of the correction to the charm (50%) and the full correction to the light flavour PYTHIA samples are shown in fig. 10.4. No corrections were applied to the b sample as this was assumed to be well

reproduced by the MC. As it is not possible to obtain a pure charm sample from the data, the P_T^{rel} shape for charm cannot be directly determined as in the light flavour case. Therefore, it was decided to apply an intermediate value for these corrections between light flavours and beauty, taking then into account a large variation of this estimate in the systematic uncertainties.

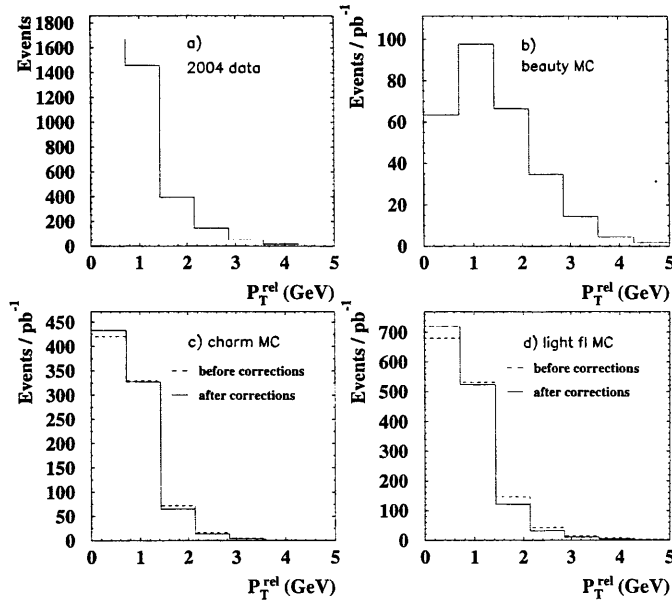


Figure 10.4: P_T^{rel} distribution for the data a) and Monte Carlo beauty b), charm c) and light flavour d) samples. All the MC samples are a mixture of the different direct, resolved and excitation processes and are normalized according to their luminosity. The charm and light flavour MC are corrected for the P_T^{rel} shape corrections.

10.2.1 P_T^{rel} fit

After applying the P_T^{rel} corrections to the charm and light flavour MC samples, the distributions of Fig. 10.4 were fitted to the data as described in section 10.1; the result of the fit is shown in Fig. 10.5. The beauty, charm and light flavour fractions extracted are:

$$f_b = 0.208 \pm 0.098 \quad (10.4)$$

$$f_c = 0.619 \pm 0.457 \quad (10.5)$$

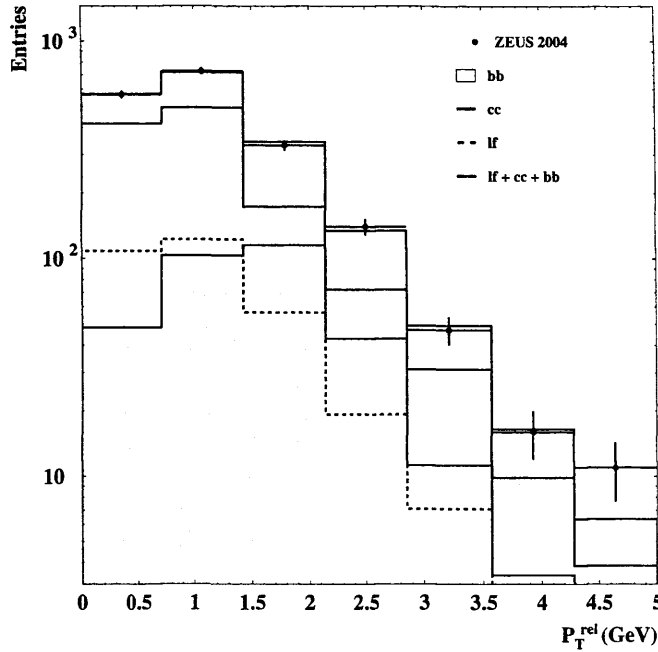


Figure 10.5: *Result of the single P_T^{rel} fit. The different Monte Carlo contributions are shown and their sum is compared with the 2004 data sample.*

$$f_{lf} = 0.173 \pm 0.468. \quad (10.6)$$

The charm and light flavour fractions are not meaningful since their errors are highly correlated, the two samples having similar P_T^{rel} shapes. For the beauty fraction, there is an agreement within the statistical error with the previous ZEUS results, obtained with a 2-parameter fit without use of MVD information [42]. This result was expected since the applied kinematic and muon cuts were the same except for the track quality requirement for the muons.

10.3 Impact parameter fit

Using the same sample, an analogous fit was used to extract the beauty fraction exploiting the different impact parameter shapes of the beauty, charm and light flavour samples. For each muon candidate the $r\phi$ impact parameter δ (Chapter 6) is calculated using MVD improved tracks and beam spot information.

The reference axis, which is needed to define the sign of δ , is taken to be the

direction of the muon jet xy -momentum vector provided by the jet algorithm, from which the muon momentum has been subtracted ($\vec{p}^{\text{subtracted}} = \vec{p}^{\text{jet}} - \vec{p}^{\mu}$). Figure 10.6 shows the reconstructed muon impact parameter spectrum for the ZEUS data and for the beauty, charm and light flavour Monte Carlo samples (normalized according to their luminosities). The distribution in the unphysical regions of negative δ reflects the finite resolution of the impact parameter reconstruction. As shown in Figure 10.6 (a), the data distribution is not symmetric around $\delta=0$, the excess at positive values indicating a relevant contribution from long-lived particle decays. This can already be taken as a qualitative proof of the existence of a lifetime signal due to charm and beauty contribution to the sample.

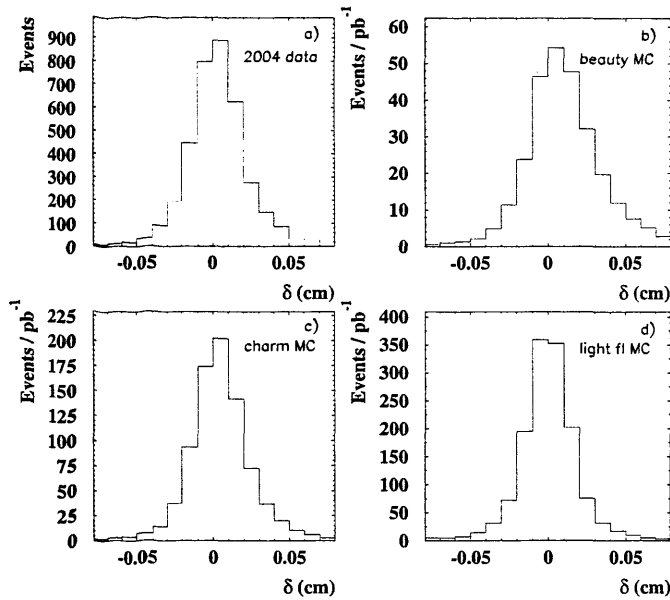


Figure 10.6: *Impact parameter distribution for the data a) and Monte Carlo beauty b), charm c) and light flavour d) samples. All the MC sample are a mixture of the different direct, resolved and excitation processes and are normalized according to their luminosity.*

To exploit this asymmetry to produce a quantitative measurement, the fit procedure as described in section 10.1 for P_T^{rel} is applied to the impact parameter distribution using as further input the δ spectra obtained from the beauty, charm and fake muon MC samples. The slight δ asymmetry for the fake muon sample

could arise from in-flight decays of light mesons.

At this stage, the impact parameter distribution alone cannot be used to extract a meaningful beauty fraction (see Fig. 10.10 in the next section) , since the shapes of the Monte Carlo distribution are not sufficiently different. A better understanding of the MVD, will allow future measurements of the beauty fraction using only this quantity. For the time being the impact parameter information can be used in combination with the P_T^{rel} technique as described below.

10.3.1 Combined fit

The separation power of the two observables can be combined in a two-dimensional fit. The (δ, P_T^{rel}) distributions used as input to the fit are shown in Fig. 10.7. In each plot of Fig. 10.7 the P_T^{rel} distribution is plotted for each bin

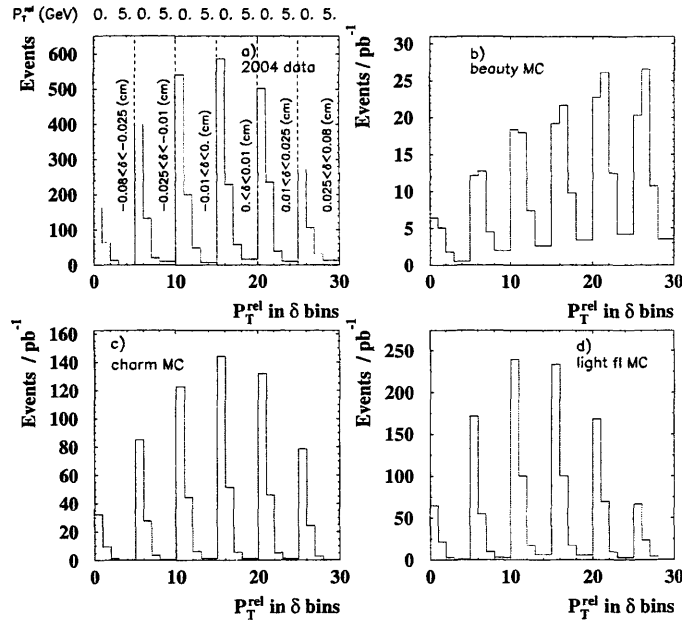


Figure 10.7: Combined (P_T^{rel}, δ) distributions for the data a) and Monte Carlo beauty b), charm c) and light flavour d) samples. All the MC samples are a mixture of the different direct, resolved and excitation processes and are normalized according to their luminosity.

of δ . In other words, in the first bins of the distribution (from 0 to 5 GeV) the P_T^{rel} distribution corresponding to the first bin of the impact parameter is plotted

and this procedure is done for all 6 δ bins considered.

As can be seen in Fig. 10.8 there is no strong correlation between the two observables and, for beauty decays, it is not too likely to find muons with both a very large impact parameter and a high P_T^{rel} .

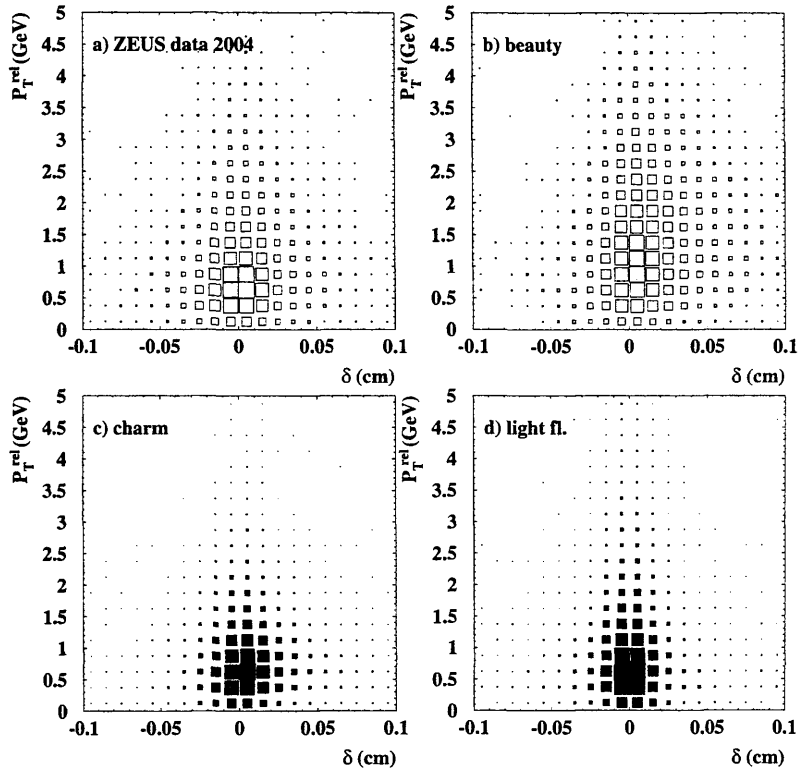


Figure 10.8: Correlation plot P_T^{rel} vs δ for a) data b) beauty c) charm and d) light flavours.

The signal can be enriched by selecting events from the tail of either observable but these two beauty-enriched event samples will be largely independent from each other. Thus, a significant improvement of the measurement can be expected if one uses the two-dimensional distribution in the fit instead of fitting the two observable spectra separately. The result of the two-dimensional fit is shown in fig 10.9.

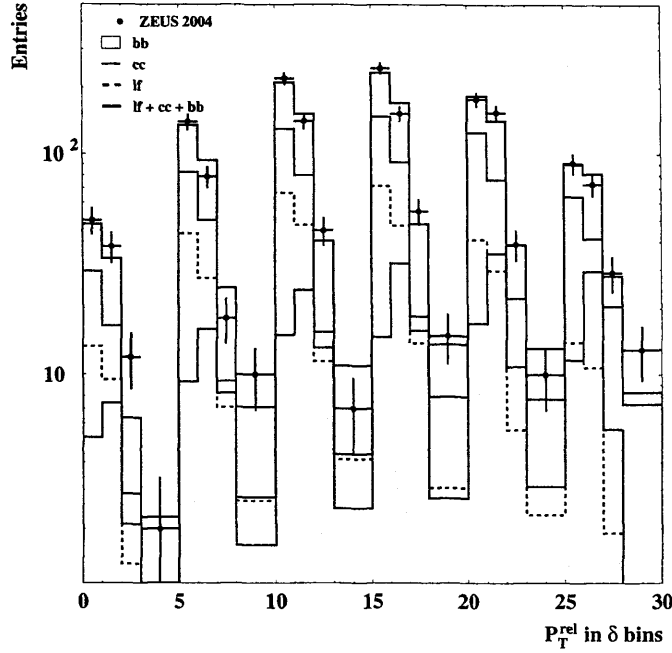


Figure 10.9: *Result of the two-dimensional fit. The different Monte Carlo contributions are shown and their sum is compared with the 2004 data sample.*

The fit yields the following sample decomposition:

$$f_b = 0.185 \pm 0.026 \quad (10.7)$$

$$f_c = 0.552 \pm 0.091 \quad (10.8)$$

$$f_{lf} = 0.262 \pm 0.095 \quad (10.9)$$

with a $\chi^2/n.d.f.$ of 23.6/22.

In fig. 10.10 the results of the two dimensional fit are shown together with the results obtained using the single P_T^{rel} and impact parameter fit. The triangle in the picture defines the physical region in which $0 < f_b < 1$, $0 < f_c < 1$; the ellipses represent the contours of the 68% χ^2 probability in the beauty and charm fraction plane. The result of the one-dimensional fits are compatible, though less precise, with those of the two-dimensional fit. The two variables give complementary information since the P_T^{rel} alone fit is able to distinguish the b component from c and light flavour but not to separate c and light flavour, while the δ -alone fit gives a good determination of the lf fraction but strongly anti-correlated fractions

of b and c . In fig. 10.11 a) and b) the P_T^{rel} and impact parameter distributions

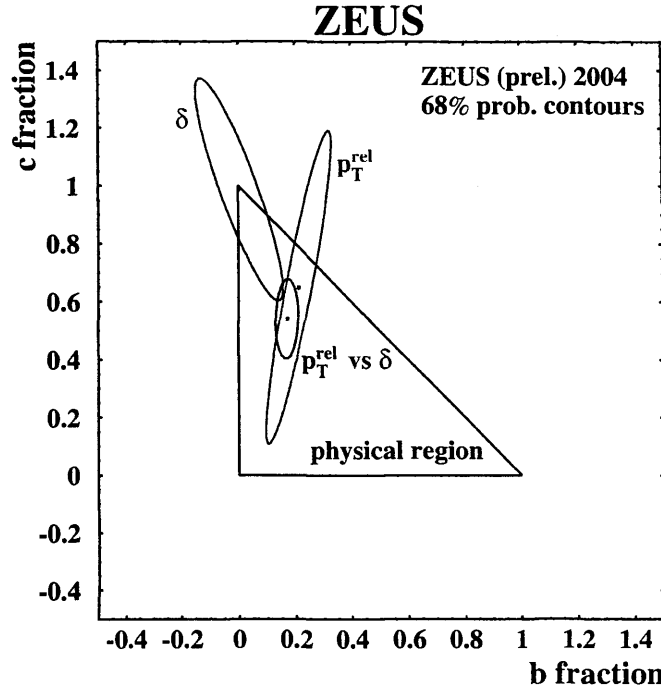


Figure 10.10: Contours of 68% probability in the plane defined by the beauty and the charm fractions. The blue line shows the contour from the two-dimensional P_T^{rel} -impact parameter distribution. The green and red lines show the contour for the one dimensional distributions in P_T^{rel} and impact parameter respectively. The triangle shows the physical region in which f_b , f_c and f_l are positive.

using the fractions obtained from the 2d-fit (Eq. 10.8, 10.9, 10.9) are shown.

The data shapes are well reproduced by the MC contribution resulting from the 2-dimensional fit.

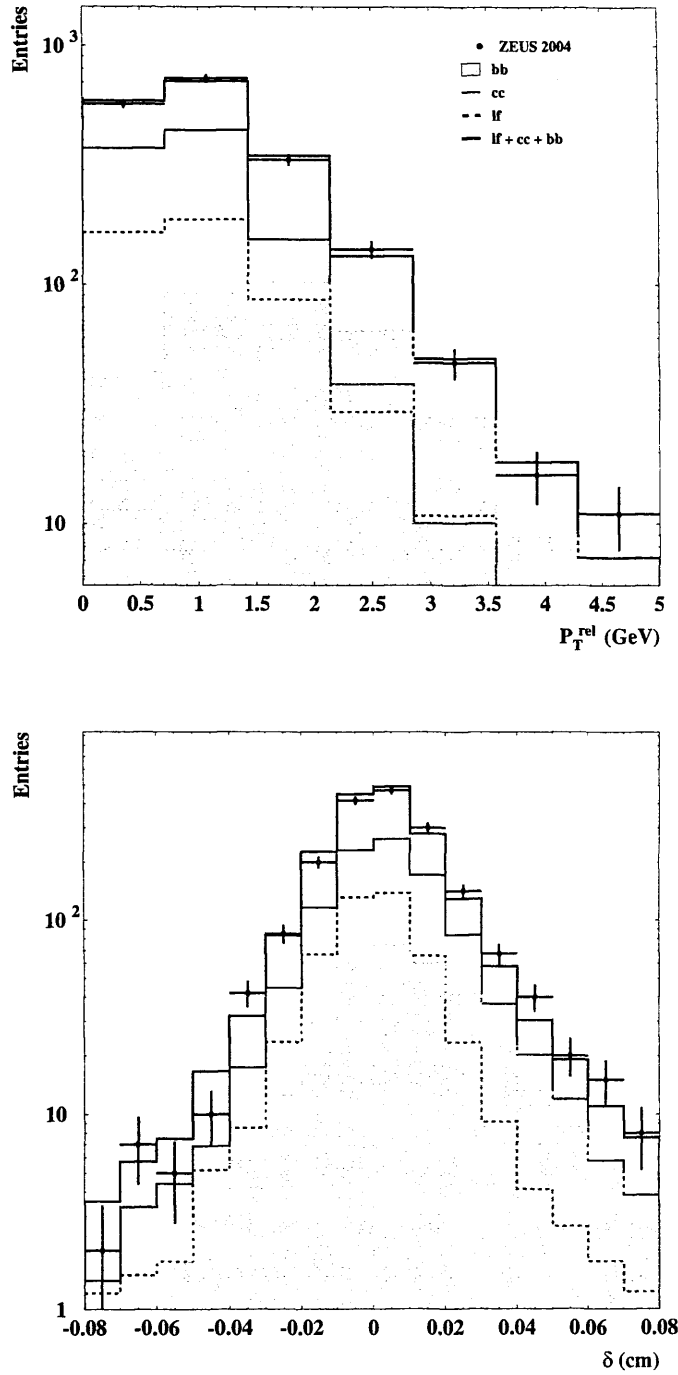


Figure 10.11: *Distribution of P_T^{rel} (top) and δ (bottom) for the data and for the MC mixture of beauty, charm and light flavours. The different MC components are also shown independently. The dashed area indicates the beauty contribution, the continuous grey line is charm, the dashed line is the light flavours and the continuous black line is the sum of the MC contributions. The black dots are the data.*

Chapter 11

Cross section measurement

This chapter describes the measurement of the beauty production cross section based on the event selection discussed in Chapter 7 and following the methods and strategy outlined in Chapter 6. The visible cross section is defined and its measurement is presented. After a discussion of the systematic errors the chapter concludes with a discussion of the cross section results.

11.1 Definition of the visible cross section

The cross section definition is adopted from [42]:

$$\sigma^{vis}(ep \rightarrow b(\bar{b})X \rightarrow \mu^\pm X) = \frac{f_b N_\mu}{2\epsilon\mathcal{L}}. \quad (11.1)$$

Here, N_μ is the number of muon candidates selected from ZEUS data (for an integrated luminosity \mathcal{L}) from which a fraction, f_b , is due to beauty production and ϵ denotes the efficiency for a $b\bar{b}$ event with primary or secondary muon in the visible kinematic range to fulfil the selection and trigger requirements. The factor 2 accounts for the fact that the experiment measures muons from b and \bar{b} decays. The visible kinematic range is defined by the transverse momentum and the pseudorapidity of the muon,

$$P_T^\mu > 2.5 \text{ GeV}, \quad \text{and} \quad -1.6 < \eta^\mu < 2.3. \quad (11.2)$$

The chosen kinematic region is given by

$$Q^2 < 1 \text{ GeV}^2, \quad \text{and} \quad 0.2 < y < 0.8, \quad (11.3)$$

selecting two jets with

$$P_T^{jet1,2} > 7,6 \text{ GeV}, \quad |\eta^{jet1,2}| < 2.5. \quad (11.4)$$

According to the PYTHIA simulation, the visible photoproduction range corresponds to 5% of the total phase space for semi-muonic beauty decays.

The selected ZEUS data sample ($\mathcal{L}=33 \text{ pb}^{-1}$) consists of 1806 muon candidates.

11.2 Visible and differential cross sections

The number of beauty events is corrected to a cross section using the acceptance determined from MC. The acceptance acc is defined as the ratio between the number of muons originating from b quarks reconstructed in the detector and those generated ($acc = N_{rec}^\mu / N_{gen}^\mu$). In order to have a rough estimate of the goodness of the selected samples, the efficiency, ϵ , and purity, P have been measured using

$$\epsilon = \frac{N^{rec \cap gen}}{N_{gen}}$$

$$P = \frac{N^{rec \cap gen}}{N^{rec}}$$

where $N^{rec \cap gen}$ is the number of muons reconstructed and generated in the same bin. The efficiency in this case is the probability to reconstruct a muon in the same bin as the bin it was generated in. Purity represents the fraction of muons which were generated in that bin with respect to the number of reconstructed muons in that bin. The total acceptance, purity and efficiency are reported in Table 11.1, and the same quantities as functions of P_T^μ and η^μ are shown in Fig. 11.1 and 11.2.

The acceptance, obtained from the beauty signal Monte Carlo, was corrected for the muon chamber efficiencies, measured in an independent sample (see section 7.10). The beauty fraction was determined in each bin of the distribution under consideration with an independent two-dimensional fit.

acceptance	purity	efficiency
0.201 ± 0.004	0.655 ± 0.020	0.131 ± 0.003

Table 11.1: *Total acceptance, purity and efficiency for the selection applied in the analysis.*

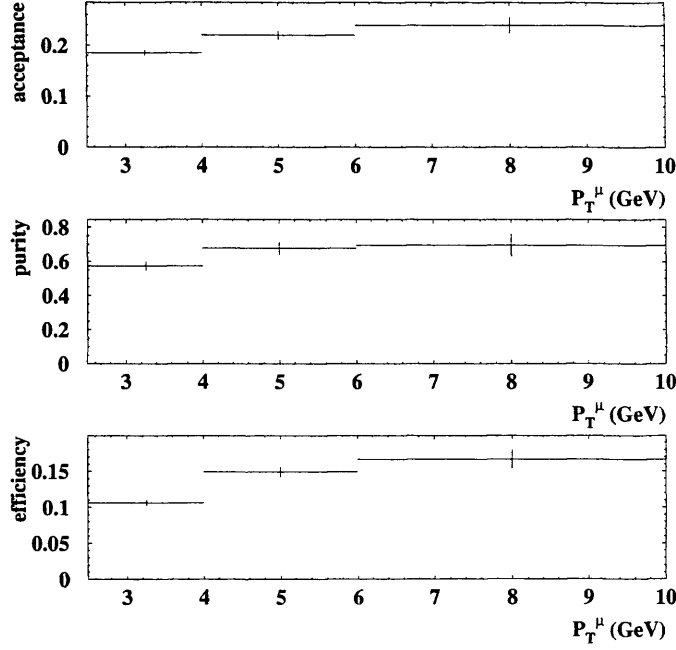


Figure 11.1: *Acceptance (top), purity (middle) and efficiency (bottom) distributions as a function of P_T^μ .*

The measured cross section for the process $ep \rightarrow e'b\bar{b}X \rightarrow e'jj\mu X'$ in the kinematic range $Q^2 < 1 \text{ GeV}^2$, $0.2 < y < 0.8$, $P_T^{j1,j2} > 7,6 \text{ GeV}$, $\eta_{j1,j2} < 2.5$, and $-1.6 < \eta_\mu < 2.3$ is:

$$\sigma_{tot} = 50.4 \pm 7.3 \pm 10 \text{ pb} \quad (11.5)$$

which is in agreement with the predictions by NLO QCD corrected for hadronization [42]:

$$\sigma_{NLO \text{ QCD} \times \text{had}} = 41.5_{-8.9}^{+13.9} \text{ pb}. \quad (11.6)$$

In fig. 11.3 the differential cross sections as a function of P_T^μ is shown. The measurement is compared to ZEUS HERA I data [42] and to the NLO QCD pre-

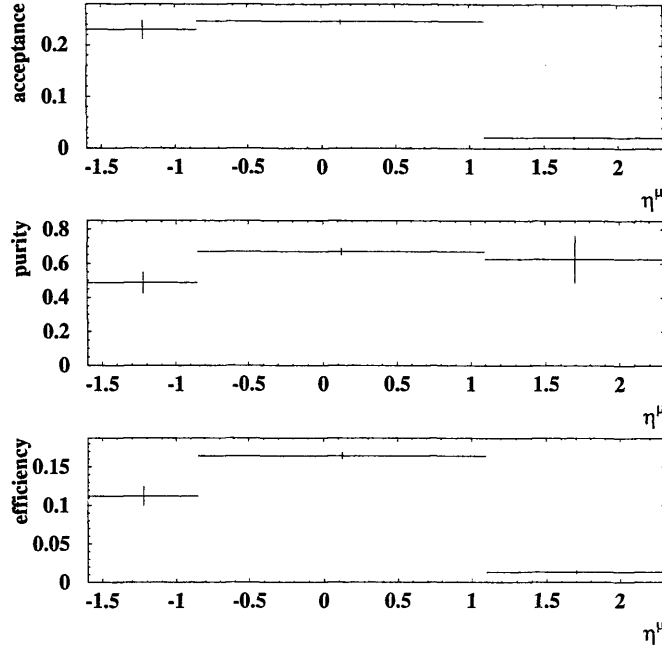


Figure 11.2: *Acceptance (top), purity (middle) and efficiency (bottom) distributions as a function of η^μ .*

diction from the FMNR [99] programme (corrected for jet hadronization effects). This measurement is in good agreement with the HERA-I results that were obtained from a luminosity ~ 3 times larger, and using P_T^{rel} to separate b from c and light flavour, fixing the charm-to-1f ratio from external measurements. An external constraint of the charm contribution is not needed in this analysis since f_c is extracted within the same data.

In a similar analysis, the H1 collaboration [100] found a two-standard deviation excess with respect to the NLO calculation for the lowest muon transverse momenta (in the range $2.5 < P_T^\mu < 3$ GeV). The present measurement does not show any excess in this P_T^μ region.

In Fig. 11.4 the differential cross section as a function of η^μ is shown. In this case a comparison with previous HERA I results was not possible due to the different range considered for this variable. A summary of the differential cross section values as a function of P_T^μ and η^μ is reported in Table 11.2.

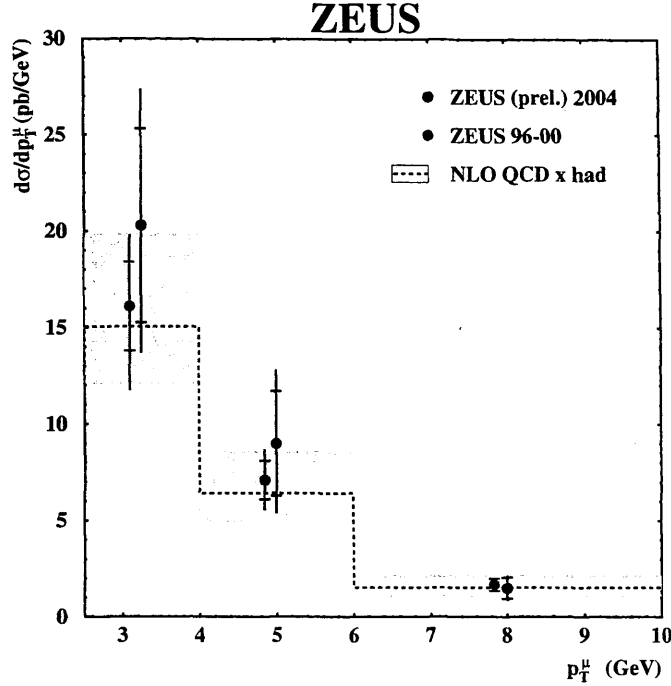


Figure 11.3: *Differential cross section as a function of the muon P_T for $Q^2 < 1 \text{ GeV}^2$, $0.2 < y < 0.8$, $P_T^{\text{jet}1,2} > 7,6 \text{ GeV}$, $\eta_{\text{jet}1,2} < 2.5$ and $-1.6 < \eta_\mu < 2.3$. The black circles show the results from this analysis while the grey circles show the previous HERA-I measurement. The inner error bars are statistical uncertainties while the external bars show the statistical and systematical uncertainties summed in quadrature. The band represents the NLO QCD prediction and hadronisation.*

11.3 Systematic errors

The systematic errors arising from the event reconstruction and the beauty fraction extraction using the P_T^{rel} and impact parameter methods are determined by varying the following procedures and corrections.

- **smearing function variation:** in Chapter 9 the correction applied to the impact parameter shape of MC was described. The widths of the functions (Breit Wigner and Gaussian) used to fit the data distribution were varied by $\pm 20\%$ which translates into a variation of the total cross section of $-8.1, +12\%$.
- **P_T^{rel} shape correction:** the correction for the difference in the shape of the light flavour MC samples and the data is also applied for 50% to the charm

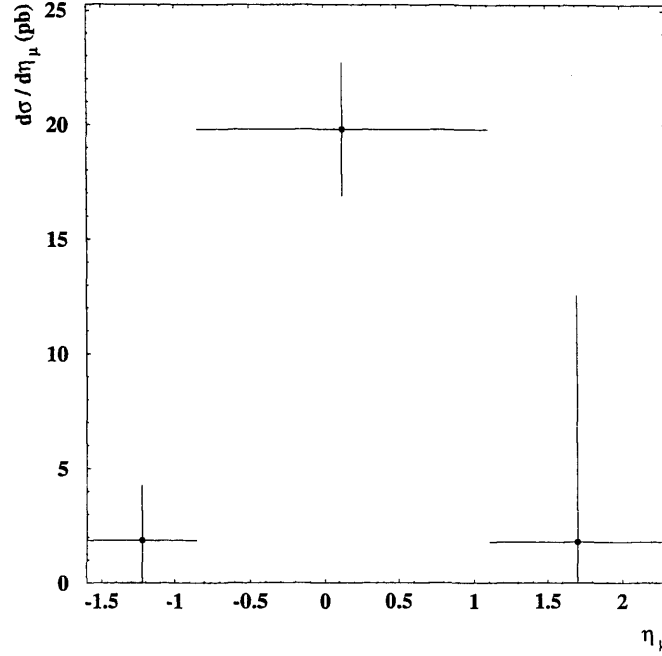


Figure 11.4: *Differential cross section as a function of the muon η for $Q^2 < 1 \text{ GeV}^2$, $0.2 < y < 0.8$, $P_T^{j1,j2} > 7, 6 \text{ GeV}$, $\eta_{j1,j2} < 2.5$ and $-1.6 < \eta_\mu < 2.3$. Only the statistical error is included in the error bars.*

MC samples (see Chapter 11). As a systematic check, the P_T^{rel} correction is applied to 100% and not at all to the charm MC sample. The effect on the total cross-section is -9.8% , $+9.4\%$. The corrections on both charm and light flavour samples were also varied by $\pm 20\%$ of their value translating in a cross section variation of -5.1% , $+4.9\%$.

- Muon efficiency corrections: A variation of $\pm 15\%$ has been considered by examining the distribution of the muon reconstruction efficiencies (see Fig. 7.22).

$\eta^\mu bin$	$d\sigma/d\eta^\mu$ (pb)	$P_T^\mu bin$ (GeV)	$d\sigma/dP_T^\mu$ (pb/GeV)	$d\sigma/dP_T^\mu$ (pb/GeV)(NLOQCDxhad)
-1.6,-0.85	1.9 ± 2.4	2.5,4.	$20.3 \pm 5.0^{+5.0}_{-4.3}$	16.0 ± 3.9
-0.85,1.1	19.8 ± 2.9	4.,6.	$9.0 \pm 2.7^{+2.7}_{-2.4}$	6.8 ± 1.8
1.1,2.3	1.8 ± 10.8	6.,10.	$1.5 \pm 0.6^{+0.3}_{-0.3}$	1.6 ± 0.5

Table 11.2: *Summary of the differential cross section values obtained as a function of P_T^μ and η^μ .*

The effect on the total beauty quark photoproduction cross section from dijet plus muon events is -13.0% , $+17.6\%$ and reflects the statistics of the isolated dimuon sample used to calculate the corrections.

- Luminosity: the integrated luminosity collected by the ZEUS experiment in 2004 is known with an error of $\pm 5\%$; this error is reflected in a cross section variation of -4.7% , $+5.3\%$.
- FLT track acceptance correction: in 2004 the First Level Trigger track veto efficiency was not properly described in the Monte Carlo since the Central Tracking Detector of ZEUS was operated at 95% of its High Voltage nominal value. A rough estimate of a correction factor of 1.05 ± 0.05 was obtained from independent studies [137] corresponding to a cross section variation of $\pm 5\%$.

The total systematic error is the sum in quadrature of the individual changes in total and differential cross sections.

All systematic checks have been determined for the total cross section and for all bins of the differential cross sections and are summarized in table 11.3.

systematic check	$\Delta\sigma(\%)$
$\Gamma(BW) \pm 20\%$	-4.9 +7.3
$\sigma(Gauss) \pm 20\%$	-4.4 +5.8
$\Gamma, \sigma \pm 20\%$	-8.1 +12.0
$\Gamma \pm 20\%, \sigma \mp 20\%$	-8.1 +12.0
Ptrel corr. lf,cc $\pm 20\%$	-5.1 +4.9
Ptrel corr. cc $\pm 100\%$	-9.8 +9.4
μ eff. corr. $\pm 15\%$	-4.7 +5.3
lumi $\pm 5\%$	-4.7 +5.3
FLT track acc. corr. 1.05 ± 0.05	-5.0 +5.0

Table 11.3: *Summary of the systematic errors taken into account.*

The dominant systematic error arises from the muon efficiency corrections and from the smearing function widths.

11.4 Discussion of results

The first measurement of beauty photoproduction from HERA II data has been presented. The muon impact parameter, measured with the new ZEUS silicon microvertex detector, was combined with the P_T^{rel} variable to improve the determination of the beauty content in a dijet-plus-muon sample. The production cross section for the process $ep \rightarrow e'b\bar{b}X \rightarrow e'jj\mu X'$ in the kinematic range $Q^2 < 1 \text{ GeV}^2$, $0.2 < y < 0.8$, $p_T^{j1,j2} > 7,6 \text{ GeV}$, $\eta_{j1,j2} < 2.5$, and $-1.6 < \eta_\mu < 2.3$ was found to be compatible with the previous ZEUS results obtained from HERA I data using only the P_T^{rel} method.

Good agreement with an NLO QCD prediction was also found in all the P_T^μ bins considered.

The method used has the advantage of allowing the extraction of both b and c fractions using a combined P_T^{rel} and δ fit, without relying on external measurements to constrain the charm contribution.

In 2005 ZEUS collected $\sim 200 \text{ pb}^{-1}$, therefore a more precise measurement will be soon produced. As the ZEUS Micro Vertex Detector is aligned using cosmics, higher reconstruction resolution is achieved for tracks coming from the vertical direction with respect to the detector [138]. Constraining the impact parameter measurement (calculated in this thesis in the transverse plane) in the projection which presents the higher resolution (y -projection) will therefore lead to higher precision in the beauty fraction. Recently, an MVD alignment using ep data has become available; the higher statistics of the sample used and its azimuthal uniformity will improve the impact parameter resolution and it will be used in future analyses.

Appendix A

Vertex fitting mathematics

A.1 Introduction

A detailed description of the vertex fitting mathematics can be found in [139]. In this appendix, the main characteristics of the two methods used by VCTRACK, the “simple” fit used in the pattern recognition and the “full” fit, are described. The local parameters q_i , defined in the next section, are named “perigee parameters” and describe the trajectories of the track near the origin which can be considered a first approximation of the primary vertex or the secondary vertices corresponding to short lifetime particles; the relation between the q_i parameters, the vertex position V and the momenta P_k of the tracks pointing to the vertex becomes easy if the curvature effect can be linearly approximated to first order. These perigee parameters carry important physics information: the impact parameter and a good approximation of the track direction in the vertex region. Moreover, using the perigee parametrization, the full fit (in which the track momenta are re-computed forcing the tracks to originate from the fitted vertex) can be reduced to a faster easy fit which estimates the vertex position without the necessity to re-adjust the track parameters.

A.2 Vertex fit: general theory

The goal of a tridimensional full vertex fit is to obtain the vertex position V and the track momentum vectors p_i ($i=1,n$) at the vertex, together with the associated covariance matrices. The vertex fit input information is the set of 5 parameters

q_i necessary to describe tridimensional tracks and the covariance matrices C_i of the track parameters with respect to a certain reference point (see fig. A.1).

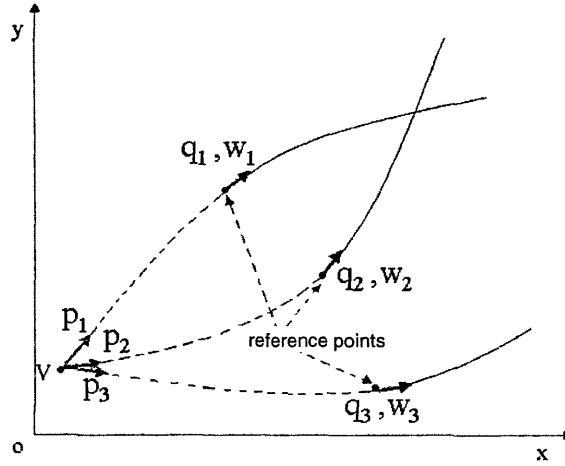


Figure A.1: Relation between q_i and (V, P_i) in the vertex fit.

The i^{th} track is characterised by the 5 parameters q_{ij} ¹ and the associated weights matrix W_i (which represents the inverse of the covariance matrix C_i^{-1}) with respect to a generic reference point. The q_{ij} will be then expressed as a function of the vertex position $V = (x_V, y_V, z_V)$ and of the track momentum at the vertex $V = (x_V, y_V, z_V)$ and of the track momentum at the vertex p_{im} ($m=1,3$), therefore $q_{ij} = F_j(V, p_i)$. the goal is to find V and p_i which minimize the χ^2 .

$$\chi^2 = \sum_i \Delta q_i^T W_i \Delta q_i \quad (A.1)$$

where

$$\Delta q_i = q_i^{measured} - F(V, p_i). \quad (A.2)$$

For small δV and δp_i variations, it is possible to linearize the functions F :

$$F(V^0 + \delta V, p_i^0 + \delta p_i) = F(V^0, p_i^0) + D_i \delta V + E_i \delta p_i \quad (A.3)$$

¹ q_{ij} indicates the j^{th} q parameter ($j=1,5$) of the i^{th} helix.

The D_i and E_i matrices are expressed as:

$$(D_i)_{jn} = \frac{\partial F_j(V, p_i)}{\partial V_n}, \quad (A.4)$$

$$(E_j)_{jm} = \frac{\partial F_j(V, p_i)}{\partial p_{im}}, \quad (j = 1 \sim 5, n = 1 \sim 3, m = 1 \sim 3) \quad (A.5)$$

In this way, substituting A.3 in A.1, the χ^2 can be re-written as:

$$\chi^2 = \sum_i (\delta q_i - D_i \delta V - E_i \delta p_i)^T \times w_i \times (\delta q_i - D_i \delta V - E_i \delta p_i) \quad (A.6)$$

where $\delta q_i = q_i^{measured} - F(V, p_i)$. Minimizing the χ^2 with respect to V :

$$\left(\sum_i D_i^T W_i D_i \right) \delta V + \sum_i (D_i^T W_i E_i) \delta p_i = \sum_i D_i^T W_i \delta q_i. \quad (A.7)$$

Minimizing the χ^2 with respect to p_i :

$$(E_i^T W_i D_i) \delta V + (E_i^T W_i E_i) \delta p_i = E_i^T W_i \delta q_i. \quad (A.8)$$

The formentioned equations can be re-written as:

$$\begin{cases} A \delta V + \sum_i B_i \delta p_i = T \\ B_i^T \delta V + C_i \delta p_i = U_i \end{cases} \quad (A.9)$$

where

$$A = \sum_i D_i^T W_i D_i, B_i = D_i^T W_i E_i, C_i = E_i^T W_i E_i, \quad (A.10)$$

$$T = \sum_i D_i^T W_i \delta q_i, U_i = E_i^T W_i \delta q_i. \quad (A.11)$$

Therefore the vertex position will be:

$$\delta V = \left(A - \sum_i B_i C_i^{-1} B_i^T \right)^{-1} \left(T - \sum_i B_i C_i^{-1} U_i \right). \quad (A.12)$$

It can be noticed that:

$$\left(A - \sum_i B_i C_i^{-1} B_i^T \right)^{-1} \quad (A.13)$$

is the covariance matrix $\text{Cov}(V, V)$ associated to δV . At this stage, for n tracks,

the system can be re-written using matrices:

$$\begin{pmatrix} A & B_1 & B_2 & \dots & \dots & B_n \\ B_1^T & C_1 & 0 & \dots & 0 & \\ B_2^T & 0 & C_2 & 0 & \dots & 0 \\ \cdot & \cdot & 0 & \cdot & \dots & 0 \\ \cdot & \cdot & 0 & \cdot & \dots & 0 \\ \cdot & \cdot & 0 & \cdot & \dots & 0 \\ \cdot & \cdot & 0 & \cdot & \dots & 0 \\ B_n^T & 0 & 0 & 0 & \dots & C_n \end{pmatrix} \cdot \begin{pmatrix} \delta V \\ \delta p_1 \\ \delta p_2 \\ \cdot \\ \cdot \\ \cdot \\ \cdot \\ \delta p_n \end{pmatrix} = \begin{pmatrix} T \\ U_1 \\ U_2 \\ \cdot \\ \cdot \\ \cdot \\ \cdot \\ U_n \end{pmatrix}. \quad (\text{A.14})$$

The standard least square method of the vertex fitting is based on the inversion of these matrices $(3n+3) \times (3n+3)$ (or $(4n+3) \times (4n+3)$ matrices where the effect of the multiple scattering is taken into account introducing an extra parameter for each track [140]). The number of operations needed is proportional to n^3 (where n is the track number).

The method used by ZEUS instead, described in the next section, uses smaller matrices and the computing time is approximately proportional to n , therefore it is particularly suitable to be applied in case of high track multiplicity. Another advantage using this method is that the Coulomb multiple scattering is taken into account only in the preliminary phase and not considered in the fit procedure.

Since the forementioned A, B_i, C_i, T e U_i matrices are kept in memory, it is easy to add or remove a track from the vertex without having to perform the calculation procedure from the beginning.

A.3 The “perigee” parametrization

$$q=(\epsilon, z_p, \theta, \phi_p, \rho)$$

The goal of this parametrization is to describe in a precise and easy way the particle trajectory in the region of the predicted vertex. The extrapolation of the track in the vertex region is performed only once.

The magnetic field is assumed to be along the z axis: a “perigee” P is defined as the point of minimum approach of the helicoidal trajectory to the z axis. If the origin O is chosen near the interaction point, this point will be close to the primary vertex and to the secondary vertices generated from the decays of short

lifetime particles (see Fig. A.2).

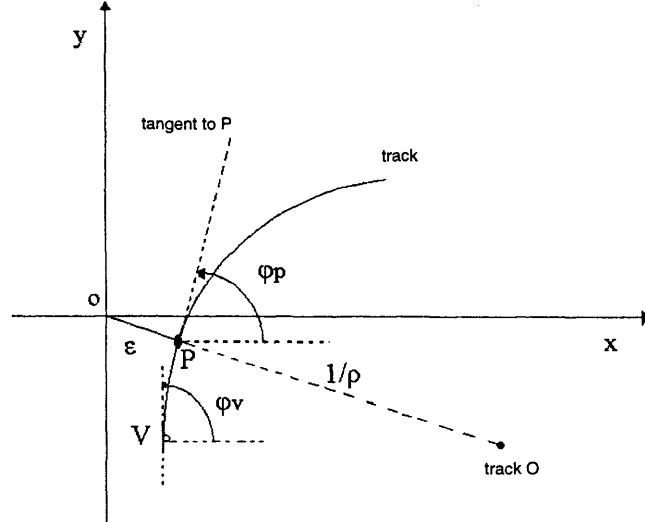


Figure A.2: *Perigee parameters in the $x - y$ projection.*

In figure A.2 P is defined in the x - y plane by the trajectory azimuthal angle ϕ_P at that point and by the value of $\epsilon \equiv OP$. The 3-dimensional description of P is completed by the z_P coordinate, the polar angle θ of the trajectory with respect to the z axis and by the ρ curvature ($1/|\rho|$ is the radius of curvature in the x - y projection and the sign of ρ is defined as positive if the trajectory follows an anticlockwise direction). At this stage the trajectory near P can be parametrized as:

$$\begin{cases} x = \epsilon \sin \phi_P + L \cos \phi_P - \frac{L^2 \rho}{2} \sin \phi_P \\ y = \epsilon \cos \phi_P + L \sin \phi_P - \frac{L^2 \rho}{2} \cos \phi_P \\ z = z_P + L \cot \theta \end{cases} \quad (\text{A.15})$$

where L is the distance from P along the trajectory in the x - y plane. The L^2 terms are small if the L is small with respect to the radius of curvature. In order to use this parameterization for the vertex fit, it is necessary to define these parameters as functions of the vertex parameters, i.e. (x_V, y_V, z_V) of the V vertex and the track parameters $p = (\theta, \phi_V, \rho)$ in V . The θ and ρ quantities remain unchanged if we pass from V to P . If the quantities $Q = x_V \cos \phi_V + y_V \sin \phi_V$ and $R = y_V \cos \phi_V - x_V \sin \phi_V$ are introduced, at the first order in ρ we have:

$$\begin{cases} \epsilon = -R - \frac{Q^2 \rho}{2} \\ z_P = z_V - Q(1 - R\rho) \cot \theta \\ \phi_P = \phi_V - Q\rho \end{cases} \quad (\text{A.16})$$

Therefore the matrices of derivatives (computed at the first order since at this level a better precision is not necessary) in the equations A.3 and A.6 can be written as:

$\partial \downarrow / \partial \rightarrow$	x_V	y_V	z_V	θ	ϕ_V	ρ
ϵ	s	-c	0	0	Q	$-Q^2/2$
z_p	-tc	-ts	1	$-Q(1+t^2)$	-Rt	-QRt
ϕ_p	$-\rho c$	$-\rho s$	0	0	1	-Q
	D matrix			E matrix		

Table A.1: *D and E matrix components.*

where $c \equiv \cos \phi_V$, $s \equiv \sin \phi_V$, $t \equiv \cot \theta$.

If a secondary vertex has to be found far away from the primary (this is the case for long-lived particles), the perigee parameters can be computed with respect to a certain origin. The parametrization precision is acceptable when the vertex is placed in an interval within $\sim 15-20$ mm around the origin chosen for the perigee calculation. Therefore most of the secondary vertices created by short lifetime particles can be determined using the parametrization of the tracks reconstructed with respect to the “main” origin, without the necessity to re-parameterize with respect to an origin expressly modified.

It is easy to calculate the impact parameter D_0 in the x-y projection with respect to the fitted vertex, starting from (ϵ, ϕ_p) and (x_V, y_V) :

$$D_0 = \epsilon - (x_V \sin \phi_p - y_V \cos \phi_p). \quad (\text{A.17})$$

It is necessary to define the expressions to propagate the error matrices from the reference point (see Fig. A.2) to the perigee region. If the track original parameters are expressed in polar coordinates, i.e. $(\Phi, z, \theta, \phi, \rho)$ for a fixed value of $r = \sqrt{x^2 + y^2}$ (where θ and ϕ are the polar angles tangent to the track, r is the distance between the origin and the reference point, see Fig. A.2, in the x-y plane), and if ϵ is small with respect to r and r is small with respect to the radius

of curvature:

$\partial \downarrow / \partial \rightarrow$	Φ	z	θ	ϕ	ρ
ϵ	r	0	0	$-r$	$-r^2$
z_p	0	1	$-r/\cos^2\theta$	0	0
ϕ_p	0	0	0	1	r

In this propagation the radius r is assumed to be inside the beam-pipe region, therefore multiple scattering (m/s) can be neglected. If material is present between r and the vertex (placed at a certain r'), it is necessary to propagate the track from r to r' and then include the m/s due to the presence of the material in the covariance matrix; the last procedure will be the extrapolation of the error matrix to the vertex region applying the A.15, substituting r with r' .

A.4 The “simple” vertex fitting

Using the perigee parametrization, it is possible to obtain an easier algorithm to estimate the vertex position without re-fitting the track parameters. In this algorithm, the variation of the transverse errors along the track is neglected near to the perigee region and $p = (\theta, \Phi_V, \rho)$ is considered constant. Therefore the 5×5 covariance matrix (which is the inverse of W matrix in A.1) is reduced to the C' sub-matrix which corresponds to the ϵ and z_p variables, the 5×3 D matrix of equation A.2 is transformed into the 2×3 D' sub-matrix which contains the (ϵ, z_p) derivatives with respect to (x_V, y_V, z_V) . If W' is the inverse of C' and $q' = (\epsilon, z_p)$, the equations A.3 and A.6 can be reduced to:

$$F(V^0 + \delta V, P_i^0) = F(V^0, p_i^0) + D'_i \delta V, \quad (\text{A.18})$$

$$\chi^2 = \sum_i (\delta q'_i - D'_i \delta V)^T \cdot W'_i \cdot (\delta q'_i - D'_i \delta V). \quad (\text{A.19})$$

The A.7 and A.12 equations becomes:

$$\left(\sum_i D_i^T W'_i D'_i \right) \delta V = \sum_i D_i^T W'_i \delta q'_i, \quad (\text{A.20})$$

$$\delta V = \left(\sum_i D_i^T W_i' D_i' \right)^{-1} \left(\sum_i D_i^T W_i' \delta q_i' \right) = A^{-1} T. \quad (\text{A.21})$$

It is convenient to choose V^0 (i.e. the V first approximation) as the origin, therefore $\delta V = V$ and $\delta q_i' = q_i'$. If $x_{pi} = (x_p, y_p, z_p)$ are the coordinates of the perigee P of the i^{th} track, we will have:

$$\begin{cases} x_{pi} = \epsilon_i \sin \phi_{pi} \\ y_{pi} = -\epsilon_i \cos \phi_{pi} \\ z_{pi} = z_{pi} \end{cases} \quad \text{or} \quad x_{pi} = D_i'^{-1} q_i'. \quad (\text{A.22})$$

If $w_i = D_i'^T W_i' D_i'$, the A.19 and A.21 equations can be re-written as:

$$\chi^2 = \sum_i (x_{pi} - V)^T w_i (x_{pi} - V), \quad (\text{A.23})$$

$$V = \left(\sum_i w_i \right)^{-1} \left(\sum_i w_i x_i \right). \quad (\text{A.24})$$

The V error matrix is simply $(\sum_i w_i)^{-1}$. Computing V through A.24, the two factors on the right can be saved; therefore when the χ^2 is calculated, through the A.23 equation, the single track contribution is considered independent; in this way it is possible to decide whether or not to use that specific helix in the fit. If for instance the k^{th} track contributes too much to the χ^2 , the vertex can be re-estimated subtracting the w_k and $w_k x_{pk}$ from the two previous memorized factors, Eq. A.24, without starting the computing procedure from the beginning. In a similar way to the previous case, the beam position information can be introduced by adding C_b^{-1} to $\sum_i w_i$ and $C_b^{-1} b$ to $(\sum_i w_i x_{pi})$ in A.24.

Appendix B

General characteristics of a silicon strip detector

A silicon strip sensor can be obtained by dividing a $p - n$ junction into small segments which act as independent electrodes. The depletion region represents the sensitive volume in which the electron-hole pairs are collected after the ionization, since only in this region is an electric field present. When a charged particle crosses this region inside the silicon volume, electron-hole pairs are generated along the ionization path. The holes and the electrons drift towards the p^+ and p^- zones respectively, causing a change in the induced charge on the surface and hence creating a short current pulse on the electrodes.

The *reverse bias voltage*, V_{dep} , necessary to extend the depletion region over the whole sensor volume, is:

$$V_{dep} = \frac{t^2}{2\epsilon_{Si}\rho\mu_e}$$

where t is the thickness of the sensor, ϵ_{Si} is the dielectric constant of the doped silicon, ρ is the silicon resistivity and μ_e represents the electron mobility.

Due to the electric configuration, the depletion region is characterized by the dynamic capacity of the junction:

$$C_{junc} = \frac{dQ}{dV} = \epsilon_{Si} \cdot \frac{A}{W(V_{bias})}$$

where A is the area of the depletion region, $W(V_{bias})$ is its width when the V_{bias} voltage is applied. This means the detector acts like a parallel plate capacitor

with the two electrodes at a distance W . In general :

$$C_{junc}(V_{bias}) = A \cdot \sqrt{\frac{\epsilon_{Si} q N_D}{2 \cdot (V_{bias} + V_{bi})}} \quad \text{for } V_{bias} \leq V_{dep} \quad \text{and} \quad (\text{B.1})$$

$$C = C_{geom} = \epsilon_{Si} \cdot \frac{A}{t} \quad \text{for } V_{bias} > V_{dep} . \quad (\text{B.2})$$

In the first formula, N_D indicates the donor concentration and V_{bi} the induced voltage difference creating the equilibrium between the two n and p -type materials.

Bibliography

- [1] CDF Collab., F. Abe et al., Phys. Rev. D61 32001 (2000),
D0 Collab., D. Abbott et al., Phys. Rev. Lett. 85 5068 (2000).
- [2] L3 Collab., *Measurement of the Cross Section for Open-Beauty Production in Photon-Photon Collisions at LEP*, Submitted to Phys. Lett. B.
- [3] P. Nason, S. Dawson and R. K. Ellis, Nucl. Phys. B327 49 (1989) and
erratum ibid. B355 260 (1990);
W. Beenakker et al., Nucl. Phys. B351 507 (1991);
M. Mangano, P. Nason and G. Ridolfi, Nucl. Phys. B373 295 (1992).
- [4] M. Gell-Mann, Phys. Lett. 8 214 (1964);
G. Zweig, CERN Rep. 8182/TH 401.
- [5] E.D. Bloom et al., Phys. Rev. Lett. 23 930 (1969).
- [6] ZEUS Collab., S. Chekanov et al., Phys. Rev. D70 052001 (2004).
ZEUS Collab., S. Chekanov et al., Eur. Phys. J. C32 1 (2003).
- [7] B.R. Martin, G. Shaw, *Particle Physics*, Wiley 1992.
- [8] TASSO Collab., R. Brandelik et al., Phys. Lett. B86 243 (1979).
- [9] ZEUS Collab., M. Derrick et al., Phys. Lett. B316 412 (1993).
ZEUS Collab., M. Derrick et al., Zeit. Phys. C72 3 399 (1996).
- [10] H1 Collab, I. Abe et al., Nucl. Phys. B407 515 (1993).
H1 Collab, T. Ahmed et al., Nucl. Phys. B439 471 (1995).
H1 Collab, S. Aid et al., Nucl. Phys. B470 3 (1996).
- [11] V. N. Gribov, L. N. Lipatov, Sov. J. Nucl. Phys. 15 438 (1972);
L. N. Lipatov, Sov. J. Nucl. Phys. 20 96 (1975).

- [12] I. I. Balitsky and Lipatov, Sov. J. Nucl. Phys. 28 822 (1978);
E. A. Kuraev, L. N. Lipatov and V. S. Fadin, Sov. J. Nucl. Phys. JETP 44 443 (1976).
- [13] M. Sutton, *Charm in Dijet Photoproduction at HERA*, PhD thesis (1998).
- [14] C. F. von Weizsacker, Z. Phys. 88 612 (1934);
E. J. Williams, Phys. Rev. 45 729 (1934).
- [15] J. F. Owens, Phys. Rev. D21 52 (1980).
- [16] ZEUS Collab., M. Derrick et al., Phys. Lett. B322 287 (1994).
- [17] ZEUS Collab., M. Derrick et. al., Phys. Lett. B384 401 (1996).
- [18] S. W. Herb et al., Phys. Rev. Lett. 39 252 (1977).
- [19] H. Wohri and C. Lourenco, Nucl. Part. Phys. 30 S315 (2004).
- [20] R. K. Ellis and P. Nason, Nucl. Phys. B312 551 (1989).
- [21] S. Dawson, P. Nason and R. K. Ellis, Nucl. Phys. B303 607 (1988).
- [22] M. L. Mangano, P. Nason and G. Ridolfi, Nucl. Phys. B373 295 (1992).
- [23] S. Frixione et al., Phys. Lett. B348 633 (1995).
- [24] S. Frixione et al., Nucl. Phys. B454 3 (1995).
- [25] M. Drees and R.M. Godbole, Phys. Rev. D39 169 (1989).
R.K. Ellis and Z. Kunszt, Nucl. Phys. B303 653 (1998).
- [26] M. Cacciari, M. Greco and P. Nason, CERN Report (1998) CERN-TH-98-77, hep/ph/9803400.
- [27] M. Cacciari and M. Greco, Phys. Rev. D55 7134 (1997).
- [28] M. Cacciari, "Hadronic Production of Heavy Quarks", DESY 97-156. To appear in the Proceeding of the Ringberg Workshop "New trend in HERA Physics", 25-30 May 1997.

- [29] M. Cacciari, S. Frixione and P. Nason, JHEP 0103 006 (2001).
A.D. Martin et al., Eur. Phys. J. C39 155 (2005).
S. Kretzer et al., Phys. Rev. D69 114005 (2004).
- [30] H. Wohri and C. Lourenco, J. Phys. G30 S315 (2004).
- [31] C. Albajar et al., Z. Phys. C61 41 (1994).
- [32] P. Nason, S. Dawson and R.K. Ellis, Nucl. Phys. B303 607 (1988);
P. Nason, S. Dawson and R.K. Ellis, Nucl. Phys. B327 49 (1989).
- [33] C. Albajar et al., Phys. Lett. B256 121 (1991).
- [34] CDF Collab., F. Abe et al., Phys. Rev. Lett. 71 500 (1993).
CDF Collab., F. Abe et al., Phys. Rev. Lett. 71 2396 (1993).
CDF Collab., F. Abe et al., Phys. Rev. Lett. 68 3403 (1992).
CDF Collab., F. Abe et al., Phys. Rev. Lett. D50 4252 (1994).
CDF Collab., F. Abe et al., Phys. Rev. Lett. 69 3704 (1992).
CDF Collab., F. Abe et al., Phys. Rev. Lett. 71 2537 (1993).
- [35] D0 Collab., S. Abachi et al., Phys. Rev. Lett. 74 3548 (1995).
D0 Collab., S. Abachi et al., Phys. Rev. Lett. B370 239 (1996).
- [36] S. Frixione et al., *Heavy quark Production*, hep-ph/9702287.
- [37] M. Cacciari et al., J. High Energy Phys. 0407 033 (2004).
- [38] <http://www-cdf.fnal.gov/physics/new/bottom/030904.blessed-bxsec-jpsi>
and <http://www-cdf.fnal.gov/bishai/papers/wandc.pdf>
- [39] S. Frixione et al., J. High Energy Phys. 0308 007 (2003).
- [40] H1 Collab., C. Adloff et al., Phys. Lett. B467 156 (1999) [Erratum-ibid. B518 331 (2001)].
- [41] ZEUS Collab., J. Breitweg et al., Eur. Phys. J. C18 625 (2001).
- [42] ZEUS Coll., S. Chekanov et al., Phys. Rev. D70 012008 (2004).

- [43] T. Sjöstrand, Comput. Phys. Commun. 82 74 (1994); E. Norrbin and T. Sjöstrand, Eur. Phys. J. C17 137 (2000).
- [44] H1 Collab., A. Aktas et al., hep-ex/050210.
- [45] ZEUS Collab., S. Chekanov et al., Phys. Lett. B599 173 (2004).
- [46] B.W. Harris and J. Smith, Phys. Rev. D57 2806 (1998).
- [47] H. Jung, Comput. Phys. Commun. 86 147 (1995).
- [48] H1 Collab., DESY 06-039.
- [49] H. Jung and G.P. Salam, Eur. Phys. J. C19 351 (2001).
- [50] H1 Collab., A. Aktas et al., Phys. Lett. B621 56 (2005).
- [51] ZEUS Collab., contrib. to EPS03, paper no. 575.
- [52] ZEUS Collab., contrib. to EPS05, paper no. 269.
- [53] A. Longhin, *Measurement of beauty production at HERA with a $D^* + \mu$ tag*, PhD thesis (2003).
- [54] ZEUS Collab., *The ZEUS Detector, Status Report 1993*, U. Holm ed. (1993).
- [55] HERA - *A proposal for a large electron-proton colliding beam facility at DESY*, report DESY HERA 81/10, July 1981.
- [56] G. Ingelman, A. De Roeck, R. Klanner, *Proceeding of the Workshop Future Physics at HERA*, DESY (1995-1996).
- [57] U. Schneekloth, DESY-HERA-98-05.
- [58] D. Bailey et al., *Study of beam-induced backgrounds in the ZEUS detector from 2002 HERA running* (unpublished), 2002, available on [http : //www-zeus.desy.de/ kuze/zeusbg/](http://www-zeus.desy.de/~kuze/zeusbg/) . ZEUS-Note 02-018.
D. Bailey et al., *Study of beam-induced backgrounds in the ZEUS detector from 2002 HERA running (Addendum 1)* (unpublished), 2002, available on [http : //www-zeus.desy.de/ kuze/zeusbg/](http://www-zeus.desy.de/~kuze/zeusbg/) . ZEUS-Note 02-020.
D. Bailey et al., *Study of beam-induced backgrounds in the ZEUS detector from 2002 HERA running (Addendum 2)* (unpublished), 2003, available on [http : //www-zeus.desy.de/ kuze/zeusbg/](http://www-zeus.desy.de/~kuze/zeusbg/) . ZEUS-Note 02-027.

- [59] DESY HERA 81-10 (81, REC. AUG.) 292p.
- [60] M. Seidel, DESY HERA-00-01.
- [61] B. Parker et al., *HERA Luminosity Upgrade Superconducting Magnet Production at BNL*, BNL-68284.
- [62] E. Hilger, *Zeus Coordinate System*, ZEUS-Note 86-17.
- [63] N. Harnew et al., Nucl. Instr. Meth. A279 290 (1989).
B. Foster et al., Nucl. Phys. Proc. Suppl. B32 81 (1993).
B. Foster et al., Nucl. Instr. Meth. A338 254 (1994).
- [64] R. Hall Wilton et al., *The CTD Tracking Resolution* (unpublished), ZEUS-Note 99-024 (1999).
- [65] E. Maddox, *Study of heavy quark production at HERA using the ZEUS microvertex detector*, PhD thesis (2004).
- [66] K. Kleinknecht, *Detectors for particle radiation*, Cambridge Press.
- [67] ZEUS Collab., J. Breitweg et al., Eur. Phys. J. C18 625 (2001).
- [68] M. Derrick et al., Nucl. Instr. Meth. A309 77 (1991);
A. Andersen et al., Nucl. Instr. Meth. A309 101 (1991);
A. Caldwell et al., Nucl. Instr. Meth. A321 356 (1992);
- [69] A. Bernstein et al., Nucl. Instr. Meth. A336 23 (1993).
- [70] A. Barbenger et al., Nucl. Instr. Meth. A382 419 (1996).
- [71] G. Battistoni et al., Nucl. Instr. Meth. 176 297 (1980).
- [72] A. Margotti, Diploma thesis, University of Bologna, (1990).
- [73] G. Abbiendi et al., Nucl. Instr. Meth. A333 342 (1993).
- [74] T. Jezynski et al., Proc. SPIE 5484 180 (2004).
K. T. Pozniak et al., Proc. SPIE 5484 186 (2004).
- [75] H. Bethe and W. Heitler, Proc. Roy. Soc. Lond. A146 83 (1934).

- [76] J. Andruszkow et al., *Acta Phys. Polon B*32 2025 (2001).
- [77] S.M. Fisher, P. Palazzi, *ADAMO Reference Manual for Version 3.3*. CERN ECP, available on:
[http : //adamo.web.cern.ch/Adamo/refmanual/Document.html](http://adamo.web.cern.ch/Adamo/refmanual/Document.html).
- [78] ZEUS Collab., M. Derrick et al., *Phys. Lett. B*297 404 (1992).
ZEUS Collab., M. Derrick et al., *Phys. Lett. B*322 287 (1994).
- [79] A. Garfagnini, *The ZEUS Micro Vertex Detector*, *Nucl. Instr. and Meth.* A435 34 (1999).
- [80] V. Chiochia, *Measurement of beauty quark production in deep inelastic scattering at HERA*, DESY-THESIS-03-031.
- [81] C. Coldewey, *Nucl. Instr. and Meth.* A447 44 (2000).
- [82] M. Feuerstack-Raible, *Overview of microstrip readout chips*, *Nucl. Instr. and Meth.* A447 (2000), proceedings VERTEX 99;
W. Fallot-Burghardt et al., *HELIX! User Manual V2.1*, 03/02/1999, HD-ASICS-33-0697.
- [83] A. Polini, *apblib: an Event Building and Buffering Package for the Microvertex and Global Tracking Trigger Online Environment*, ZEUS-Note 04-021.
- [84] B. West, *Charm and the Virtual Photon at HERA and a Global Tracking Trigger*, PhD thesis (2001).
- [85] V. Chiochia, *Nucl. Instr. Meth.* A501 60 (2003).
- [86] J.C. Collins, D.E. Soper and G. Sterman, *Nucl. Phys.* B308 833 (1988).
- [87] G. Marchesini et al., *Comp. Phys. Comm.* 67 465 (1992).
- [88] G. A. Schuler, *Nucl. Phys.* B299 21 (1988).
- [89] D. Amati and G. Veneziano, *Phys. Lett.* B83 87 (1979);
Yu. L. Dokshitzer and S.I. Troian, Leningrad Nuclear Physics Institute preprint N922 (1984);
Ya. I. Azimov et al., *Phys. Lett.* B165 147 (1985), *Z. Phys.* C27 65 (1985).

- [90] T. Sjöstrand et al., *Comp. Phys. Comm.* 135 238 (2001).
- [91] T. Sjöstrand, *Nucl. Phys.* 248 469 (1984).
- [92] *The ZEUS Detector Status Report 1993*, DESY 1993.
- [93] R. Brun, *Geant 3.13*, CERN DD/EE/84-1 (1987).
- [94] W.A. Bardeen et al., *Phys. Rev.* D18 3998 (1978).
- [95] C.F. Von Weizsaecker, *Z. Phys.* 88 612 (1934);
E.J. Williams, *Phys. Rev.* 45 729 (1934).
- [96] M. Corradi, M. Turcato, *Beauty production in dijet events*, ZEUS-Note 04-005.
- [97] H.L. Lai et al., *Eur. Phys. J.* C12 375 (2000).
- [98] M. Glück, E. Reya and A. Vogt, *Phys. Rev.* D46 1973 (1992).
- [99] S. Frixione et al., *Nucl. Phys.* B412 225 (1994).
- [100] H1 Coll., A. Aktas et al., *Eur. Phys. J.* C41 453 (2005).
- [101] S. Eidelman et al. (Particle Data Book), *Review of Particle Physics*, *Phys. Lett.* B592 1 (2004).
- [102] O. Behnke, *Beauty Production at HERA*, Ringberg Workshop 2005.
- [103] C. Peterson et al., *Phys. Rev.* D27 105 (1983).
- [104] P. Nason and C. Oleari, *Nucl. Phys.* B565 245 (2000).
- [105] A. Garfagnini, *Nucl. Instr. and Meth.* A461 (2001) 210.
- [106] ZEUS Collab, J. Breitweg et al., *Eur. Phys. J.* C18 625 (2001).
- [107] G. Hartner, *VCTRAK: Offline Output Information*, ZEUS-Note 97-064.
- [108] G. Hartner, *VCTRAK: ZEUS Track & Vertex Reconstruction*, 15.07.200.
- [109] G. Hartner, *VCTRAK Briefing: Program & Math*, ZEUS-Note 98-058.
- [110] G. Hartner, private communication.

- [111] S. Miglioranzi, *Sviluppo di algoritmi per la misura della produzione di quark b all'esperimento ZEUS ad HERA* (in Italian), Diploma thesis, Bologna University (2002).
- [112] G.M. Briskin, *Diffractional Dissociation in ep Deep Inelastic Scattering*, DESY-THESIS 1998-036.
- [113] J. Huth et al., *Proceedings of the PDF Summer Study on High Energy Physics*, 1990, ed. L. Berger, 134 (1992).
- [114] S. Catani, Yu.L. Dokshitzer and M.H. Seymour, Phys. Lett. B285 291 (1992).
- [115] S. Catani et al., Nucl. Phys. B406 186 (1993).
- [116] A. Bassetto, M. Ciafaloni and G. Marchesini, Phys. Rep. 100 202 (1983); Yu.L. Dokshitzer et al., *Basics of perturbative QCD*, Ed. Frontieres, Gif-Sur-Yvette, 1991.
- [117] T. Namssoo, *Three- and Four-Jet States in Photoproduction at HERA*, PhD thesis (2005).
- [118] A. Longhin, *Misura delle sezioni d'urto di fotoproduzione di Open Beauty ad HERA*. (In Italian, unpublished). Diploma Thesis Padova University (2000);
V. Chiochia, *Measurement of beauty quark production in deep inelastic scattering at HERA* (unpublished). DESY-THESIS-2003-031.
- [119] M. Turcato, *Measurement of beauty photoproduction at HERA* (unpublished), DESY-THESIS-2003-039.
- [120] L. Bellagamba, *MVMATCH: A package to match FMUON tracks with Central Detectors*, ZEUS-Note 96-051; M. Corradi, private communication, and http://www-zeus.desy.de/~corradi/ZEUS_ONLY/mpmatch/mpmatch2.html.
- [121] G. Abbiendi, *Global Tracking of muons in the Barrel and Rear region*, ZEUS-Note 99-063.
- [122] V. Innocente, M. Maire and E. Nagy, *GEANE: average tracking and error propagation package*, proceedings of MC91: Detector and event simulation in High Energy Physics, Amsterdam (1991).

- [123] R. E. Kalman, Transaction of the ASME-Journal of Basic Engineering 82 35 (1960);
R. Fruhwirth, Nucl. Instr. Meth. A262 444 (1987).
- [124] S. Limentani, M. Posocco and L. Stanco, *Muon Barrel Reconstruction*, ZEUS-Note 98-058.
- [125] G. F. Hartner et al., *VCTRAK(3.07/04): Offline Output Information*, ZEUS-Note 97-064.
G.F Hartner, *VCTRAK Briefing: Program and Math*, ZEUS-Note 98-058.
- [126] A. Bertolin, R. Brugnera, M. Turcato, *Study of GLOMU and BREMAT muon-finders efficiencies*, ZEUS-Note 05-022 (2005).
- [127] R. Sinkus, H. Abramowicz and A. Caldwell, Nucl. Instr. and Meth. A365 508 (1995).
- [128] F. Jaquet and A. Blondel, *Proceedings of the Study of an ep facility for Europe*, Ed. U. Amaldi, DESY 79/48, 391.
- [129] M. Corradi, private communication.
- [130] V. Kuzmin, Nucl. Instr. Meth. A435 (2000) 336.
- [131] E. Maddox, *Study of heavy quark production at HERA using the ZEUS microvertex detector* (unpublished). Amsterdam preprint, December 2004.
- [132] E. Maddox *A Kalman filter track fit for the ZEUS mirovertex detector*, ZEUS-Note 03-008 (2003).
- [133] U. Schneekloth *HERA Report*, talk ZEUS Collaboration Meeting, Padova October 2004.
- [134] G. D'Agostini, *Bayesian Reasoning in High Energy Physics: Principles and Applications*, CERN Yellow Report CERN-99-03.
- [135] M. Turcato, *Measurements of beauty photoproduction at HERA*, DESY-THESIS-03-039.
- [136] F. James, *MINUIT - Minimization Package Reference Manual - v94.1*.

- [137] A. Geiser, private communication.
- [138] R. Mankel, ZEUS Phys. Coord. talk (internal page), 07-02-2006.
- [139] P. Billoir, S. Qian, Nucl. Instr. Meth. A311 139 (1992).
- [140] D. H. Saxon, Nucl. Instr. and Meth. A234 258 (1985).